# Towards Upscaling of Microbial Electrosynthesis Reactors

Cabau Peinado, O.

**Citation (APA)**
Cabau Peinado, O. (2025). *Towards Upscaling of Microbial Electrosynthesis Reactors*. [Dissertation (TU Delft), Delft University of Technology]. https://doi.org/10.4233/uuid:39a2dfe3-689d-465d-b1ea-554d56987f3c

**Important note**
To cite this publication, please use the final published version (if applicable).
Please check the document version above.

# TOWARDS UPSCALING
## OF MICROBIAL ELECTROSYNTHESIS REACTORS

ORIOL CABAU PEINADO

# Towards upscaling of microbial electrosynthesis reactors

# Towards upscaling of microbial electrosynthesis reactors

**Dissertation**

for the purpose of obtaining the degree of doctor
at Delft University of Technology,
by the authority of the Rector Magnificus prof. dr. ir. T.H.J.J. van der Hagen,
chair of the Board for Doctorates,
to be defended publicly on
Friday 7 March 2025 at 10:00 o'clock

by

## Oriol CABAU PEINADO

Master of Science in Biotechnology,
Wageningen University & Research, the Netherlands

born in El Vendrell, Spain

This dissertation has been approved by the promotors.

Composition of the doctoral committee:

| | |
|---|---|
| Rector Magnificus | Chairperson |
| Dr. ir. A.J.J. Straathof | Delft University of Technology, promotor |
| Dr. L. Jourdin | Delft University of Technology, co-promotor |

*Independent members*

| | |
|---|---|
| Prof. dr. S. Puig Broch | Universitat de Girona, Spain |
| Prof. dr. J. Gescher | Technische Universität Hamburg, Germany |
| Prof. dr. ir. C.A. Ramírez Ramírez | Delft University of Technology |
| Dr. T.E. Burdyny | Delft University of Technology |
| Dr. ir. R. Kleerebezem | Delft University of Technology |
| Prof. dr. ir. L.A.M. van der Wielen | Delft University of Technology, reserve member |

*"Més lluny, heu d'anar més lluny*
*dels arbres caiguts que ara us empresonen,*
*i quan els haureu guanyat*
*tingueu ben present no aturar-vos"*

**Lluís Llach**

# Contents

# Summary

As of today, reducing the anthropogenic release of greenhouse gases might be considered as humankind's most pressing challenge. Moving away from fossil fuels to renewable energy technologies is an essential step, but will not suffice. The chemical industry is responsible for a significant 6.3% of all $CO_2$ emissions, thus fossil-free chemicals production is also required. To that end, carbon capture and utilization (CCU) offers a way to reduce emissions in industrial processes, while converting captured $CO_2$ into commodity and specialty chemicals. Under the umbrella of CCU technologies, microbial electrosynthesis (MES) offers a sustainable solution with minimal water usage and the capacity to increase the value of electrical energy produced from renewable sources.

The ability of microorganisms to accept and utilize electrons from an electrode to catalyze the reduction of $CO_2$ is the basis of MES processes. Whilst significant progress on understanding its fundamentals has been achieved, performance improvements have been modest. To reach industrial viability, a major breakthrough is needed. Unraveling multi-scale interactions between microbial, electrochemical and engineering parameters within MES systems will allow for the rational design of scalable bioreactors. Still, it remains widely unknown what is limiting current setups. The work presented in this thesis aims to identify, understand, and tackle major key process parameters, allowing for a step-by-step design approach to develop scalable MES bioreactors.

How microorganisms adapt to changing operational parameters and different reactor environments was investigated in **Chapter 2**. A general framework for modeling microbial kinetics within MES reactors was developed, and results showed that $CO_2$ availability may be a limiting factor in existing systems. An insufficient mass transfer capability led to partially limited biomass growth under reported operational conditions, either because of a low gas partial pressure or an inefficient gas delivery strategy. The dynamic reactor-scale model also revealed that in biofilm-driven reactors, a continuous operational mode markedly improved microbial growth and potentially led to denser biofilms and higher current densities. Simulations indicated distinct correlations between operational process conditions and critical performance indicators (e.g., productivity), underscoring existing process limitations and paving the way for future system optimization.

A major knowledge gap in MES is that biomass-specific rates such as microbial growth rates had not been experimentally elucidated and were thus unknown to date. In **Chapter 3**, a method using nitrogen balances and optical density to determine the amount of microorganisms in biofilm and in suspension at any given time was developed. This was necessary to allow further complex computational attempts, since biomass concentration was one of the major unmeasured variables within biofilm-based MES processes. Measured growth rates during the colonization stage ranged from 0.12 to 0.16 days$^{-1}$, values in accordance with the ones obtained in previous mathematical simulations. Interestingly, results showed that biomass-specific production rates were relatively low (0.37 mol$_C$ mol$_X^{-1}$ day$^{-1}$) when compared to syngas and chain elongation studies (up to 10 mol$_C$ mol$_X^{-1}$ day$^{-1}$). Thus, this comparative analysis highlighted that there is room to significantly improve metabolic rates in MES.

After gaining insight on what major factors limit MES performance, a novel directed-flow-through bioelectrochemical reactor (DFBR) with a serpentine flow-pattern entirely filled with a 3D carbon-based electrode was developed in **Chapter 4**. The elimination of free-flowing liquid in the cathode chamber allowed the DFBR design to substantially increase mass transfer as well as carbon and hydrogen utilization efficiencies. Results demonstrated a 3-fold higher volumetric current density (-28 ± 7 mA cm$^{-3}_{cathode}$) and productivity (43 ± 24 kg$_C$ m$^{-3}_{cathode}$ day$^{-1}$) than previously reported in biofilm-based MES studies. Most notably, volumetric productivities obtained were now comparable to lab-scale syngas fermentation, a technology that has been successfully scaled up to an industrial level. These findings serve as a milestone in developing MES and emphasize key design parameters for efficient bioelectrochemical $CO_2$ reduction. Furthermore, results obtained with the novel DFBR design proved that a knowledge-driven step-by-step approach allows for successful MES reactor development.

Collectively, this dissertation shows that it is possible to unravel the main limitations in currently used MES reactors. The subsequent utilization of such knowledge to design scalable reactors able to achieve industrially relevant performance is also demonstrated. Nonetheless, new challenges are sure to arise while further developing MES as a technology. Extensive research, accounting for a multiscale and multidisciplinary approach is therefore a must in order to bring MES to industrial production.

# Samenvatting

Tegenwoordig kan het verminderen van de door de mens veroorzaakte uitstoot van broeikasgassen worden beschouwd als de meest urgente uitdaging voor de mensheid. De transitie van fossiele brandstoffen naar hernieuwbare energie is een essentiële stap, maar zal niet voldoende zijn. De chemische industrie is verantwoordelijk voor een significante 6,3% van alle $CO_2$-uitstoot, wat betekent dat ook de productie van fossielvrije chemicaliën noodzakelijk is. Koolstofafvang en –gebruik (CCU) biedt hiervoor een manier om de uitstoot in industriële processen te verminderen, terwijl de opgevangen $CO_2$ wordt omgezet in basis- en speciale chemicaliën. Als een van de CCU-technologieën biedt microbiële elektrosynthese (MES) een duurzame oplossing met minimaal watergebruik en de capaciteit om de waarde van geproduceerde elektrische energie uit hernieuwbare bronnen te verhogen.

Het vermogen van micro-organismen om elektronen van een elektrode te accepteren en te benutten om $CO_2$-reductie te katalyseren, vormt de basis van MES-processen. Hoewel er aanzienlijke vooruitgang is geboekt in het begrijpen van de fundamentele aspecten, zijn de prestatieverbeteringen bescheiden gebleven. Om industriële haalbaarheid te bereiken, is een significante doorbraak nodig. Het ontrafelen van interacties op meerdere schalen tussen microbiële, elektrochemische en technische parameters binnen MES-systemen zal het mogelijk maken om rationeel ontworpen, schaalbare bioreactoren te ontwikkelen. Toch blijft het grotendeels onbekend wat de huidige systemen beperkt. Het werk dat in dit proefschrift wordt gepresenteerd is erop gericht om belangrijke procesparameters te identificeren, te begrijpen en aan te pakken, waardoor een stapsgewijze ontwerpmethode voor de ontwikkeling van schaalbare MES-bioreactoren mogelijk wordt gemaakt.

Hoe micro-organismen zich aanpassen aan veranderende operationele parameters en verschillende reactoromgevingen werd onderzocht in **Hoofdstuk 2**. Er werd een algemeen kader ontwikkeld voor het modelleren van microbiële kinetiek binnen MES-reactoren, en de resultaten toonden aan dat $CO_2$-beschikbaarheid een beperkende factor kan zijn in bestaande systemen. Een tekort aan massaoverdracht beperkte de biomassa-groei deels door lage partiële druk of inefficiënte gaslevering. Het dynamische reactorschaalmodel onthulde ook dat in biofilm-gebaseerde reactoren een constante doorstroom van medium de microbiële groei aanzienlijk verbeterde en mogelijk leidde tot dichtere biofilms en hogere elektrische stroomdichtheden. Simulaties gaven aan dat er duidelijke correlaties waren tussen operationele procescondities en kritieke prestatie-indicatoren (bijv. productiviteit), wat bestaande procesbeperkingen onderstreept en de weg vrijmaakt voor toekomstige systeemoptimalisatie.

Een belangrijke kenniskloof in MES is dat biomassa-specifieke snelheden, zoals microbiële groeisnelheden, tot nu toe niet experimenteel waren aangetoond en dus onbekend waren. In **Hoofdstuk 3** werd een methode ontwikkeld die gebruik maakt van stikstofbalansen en optische dichtheid om de hoeveelheid micro-organismen in biofilm en in suspensie op elk moment te kunnen bepalen. Dit was noodzakelijk om verdere complexe rekenkundige pogingen mogelijk te maken, aangezien biomassa-concentratie een van de belangrijkste niet-gemeten variabelen was binnen biofilm-gebaseerde MES-processen. Gemeten groeisnelheden tijdens de kolonisatiefase varieerden van 0,12 tot 0,16 dag$^{-1}$, waarden die in overeen kwamen met de waarden die in de eerdere wiskundige simulaties waren verkregen. Opvallend genoeg toonden de resultaten aan dat biomassa-specifieke productiesnelheden relatief laag waren (0,37 mol$_C$ mol$_X^{-1}$ dag$^{-1}$) in vergelijking met synthesegas- en ketenverlengingsstudies (tot 10 mol$_C$ mol$_X^{-1}$ dag$^{-1}$). Deze vergelijkende analyse toonde dus aan dat er ruimte is om de metabole snelheden in MES aanzienlijk te verbeteren.

Na inzicht te hebben verkregen in de belangrijkste factoren die de MES-prestaties beperken, werd in **Hoofdstuk 4** een nieuwe directe doorstroom bio-elektrochemische reactor (DFBR) met een slangachtig stroompatroon dat volledig gevuld was met een driedimensionale koolstof-gebaseerde elektrode ontwikkeld. Het elimineren van vrij stromende vloeistof in de kathodekamer stelde het DFBR-ontwerp in staat om de massaoverdracht en de koolstof- en waterstof-omzettingsgraad aanzienlijk te verhogen. Resultaten toonden een 3-voudig hogere volumetrische elektrische stroomdichtheid (-28 ± 7 mA cm$^{-3}_{kathode}$) en productiviteit (43 ± 24 kg$_C$ m$^{-3}_{kathode}$ dag$^{-1}$) dan eerder gerapporteerd in biofilm-gebaseerde MES-studies. Het meest opvallend was dat de behaalde volumetrische productiesnelheden nu vergelijkbaar waren met laboratoriumschaal synthesegasfermentatie, een technologie die met succes op industriële schaal is opgeschaald. Deze bevindingen vormen een mijlpaal in de ontwikkeling van MES en benadrukken belangrijke ontwerpparameters voor efficiënte bio-elektrochemische $CO_2$-reductie. Bovendien bewezen de resultaten die met het nieuwe DFBR-ontwerp werden behaald, dat een kennis gestuurde stapsgewijze aanpak succesvol is bij de ontwikkeling van MES-reactoren.

Als geheel laat dit proefschrift zien dat het mogelijk is om de belangrijkste beperkingen in de momenteel gebruikte MES-reactoren te ontrafelen. Het daaropvolgende gebruik van dergelijke kennis om schaalbare reactoren te ontwerpen die in staat zijn industriële relevante prestaties te bereiken, wordt ook aangetoond. Desalniettemin zullen er nieuwe uitdagingen ontstaan bij de verdere ontwikkeling van MES als technologie. Uitgebreid onderzoek, rekening houdend met een multidisciplinaire en multischaal benadering, is daarom vereist om MES op industriële schaal haalbaar te maken.

# Resum

Actualment, la reducció de les emissions antropogèniques de gasos d'efecte hivernacle es podria considerar com el repte més urgent per a la humanitat. Abandonar els combustibles fòssils i moure's cap a les tecnologies d'energia renovable és essencial, però no en serà pas suficient. La indústria química és responsable d'un significatiu 6,3% de totes les emissions de $CO_2$. Per aquesta raó, també serà necessari desenvolupar una producció de productes químics sense combustibles fòssils. En aquest sentit, la captura i utilització de carboni (CUC) ofereix una forma de reduir les emissions en els processos industrials, convertint el $CO_2$ capturat en productes químics. En el marc de les tecnologies CUC, l'electrosíntesi microbiana (ESM) ofereix una solució sostenible amb un ús mínim d'aigua i la capacitat d'incrementar el valor de l'energia elèctrica produïda a partir de fonts renovables.

La capacitat d'alguns microorganismes d'acceptar i utilitzar electrons d'un elèctrode per catalitzar la reducció de $CO_2$ és la base dels processos d'ESM. Tot i que en els últims anys el progrés cap a la comprensió dels seus fonaments bàsics ha estat significatiu, les millores en el seu rendiment han estat modestes. Per assolir la viabilitat industrial, serà necessari un gran avenç. Desxifrar les interaccions entre paràmetres microbians, electroquímics i d'enginyeria dins dels sistemes d'ESM permetrà el disseny racional de bioreactors escalables. Tanmateix, encara es desconeix àmpliament què limita els sistemes actuals. La recerca presentada en aquesta tesi té com a objectiu identificar, comprendre i abordar els principals paràmetres del procés, permetent una estratègia de disseny pas a pas per a desenvolupar bioreactors d'ESM escalables.

Al **Capítol 2** es va investigar com els microorganismes s'adapten a canvis en els paràmetres operatius i a diferents ambients dins els bioreactors. Es va desenvolupar un marc matemàtic generalista per modelar la cinètica microbiana dins dels reactors d'ESM, i els resultats van mostrar que la disponibilitat de $CO_2$ podria haver estat el factor limitant en els sistemes estudiats. Una capacitat de transferència de massa insuficient va provocar un creixement de biomassa parcialment limitat sota les condicions operatives reportades, ja sigui a causa d'una baixa pressió parcial de gas o una estratègia ineficaç de subministrament del mateix. El model dinàmic a escala de reactor també va revelar que en reactors que utilitzen biofilms, un mode d'operació continu millora notablement el creixement microbià, potencialment facilitant la formació de biofilms més densos i l'obtenció de densitats de corrent més altes. Les simulacions indiquen correlacions clares entre les condicions operatives del procés i els indicadors clau de rendiment (per exemple, la productivitat), destacant les limitacions existents del procés i obrint el camí per a una futura optimització del sistema.

Una gran llacuna en el coneixement de l'ESM és que les velocitats de reacció específiques de biomassa, com la velocitat de creixement microbià no s'havien obtingut experimentalment i, per tant, eren desconegudes fins ara. Per aquest motiu, al **Capítol 3** es va desenvolupar un mètode utilitzant balanços de nitrogen i densitat òptica per determinar la quantitat de microorganismes en biofilm i en suspensió en qualsevol moment donat. Això va ser necessari per permetre simulacions computacionals més complexes, ja que la concentració de biomassa era una de les principals variables no reportades per als processos d'ESM basats en biofilm. Les velocitats de creixement mesurades durant l'etapa de colonització van variar de 0,12 a 0,16 dies$^{-1}$, valors en acord amb els obtinguts en anteriors simulacions matemàtiques. Curiosament, els resultats van mostrar que les velocitats específiques de producció eren relativament baixes (0,37 mol$_C$ mol$_X^{-1}$ dia$^{-1}$) en comparació amb els estudis de syngas i fermentació d'àcids carboxílics (fins a 10 mol$_C$ mol$_X^{-1}$ dia$^{-1}$). Per tant, aquesta anàlisi comparativa va servir per destacar que hi ha marge per millorar significativament les velocitats de reacció metabòliques en processos d'ESM.

Després d'obtenir informació sobre els principals factors que limiten el rendiment dels processos d'ESM, al **Capítol 4** es va desenvolupar un nou reactor bioelectroquímic de flux dirigit (RBFD) amb un patró de flux serpentejant completament saturat amb un elèctrode 3D de carboni. L'eliminació del líquid amb moviment lliure a la cambra del càtode va permetre que el disseny RBFD augmentés substancialment la transferència de massa, així com les eficiències d'utilització de carboni i hidrogen. Els resultats van demostrar una densitat de corrent volumètrica (-28 $\pm$ 7 mA cm$^{-3}_{càtode}$) i una productivitat (43 $\pm$ 24 kg$_C$ m$^{-3}_{càtode}$ dia$^{-1}$) tres vegades superior a la reportada anteriorment en estudis d'ESM basats en biofilms. El més destacable és que les productivitats volumètriques obtingudes eren ara comparables a les obtingudes en fermentacions de syngas a escala de laboratori, una tecnologia que s'ha portat amb èxit a escala industrial. Aquests resultats són una fita en el desenvolupament de l'ESM i serveixen per ressaltar paràmetres de disseny clau per a una reducció bioelectroquímica de $CO_2$ eficient. A més, els resultats obtinguts amb el nou disseny RBFD van demostrar que una estratègia de disseny pas a pas permet un desenvolupament reeixit dels reactors d'ESM.

En conjunt, aquesta tesi mostra que és possible desxifrar les principals limitacions en els reactors d'ESM utilitzats actualment. També demostra que és possible el posterior ús d'aquest coneixement per a dissenyar reactors escalables capaços d'aconseguir rendiments rellevants a escala industrial. No obstant això, de segur sorgiran nous problemes i desafiaments en continuar desenvolupant la tecnologia d'ESM. Per tant, la investigació exhaustiva, amb un enfocament multiescalar i multidisciplinari, és imprescindible per portar l'ESM a escala industrial.
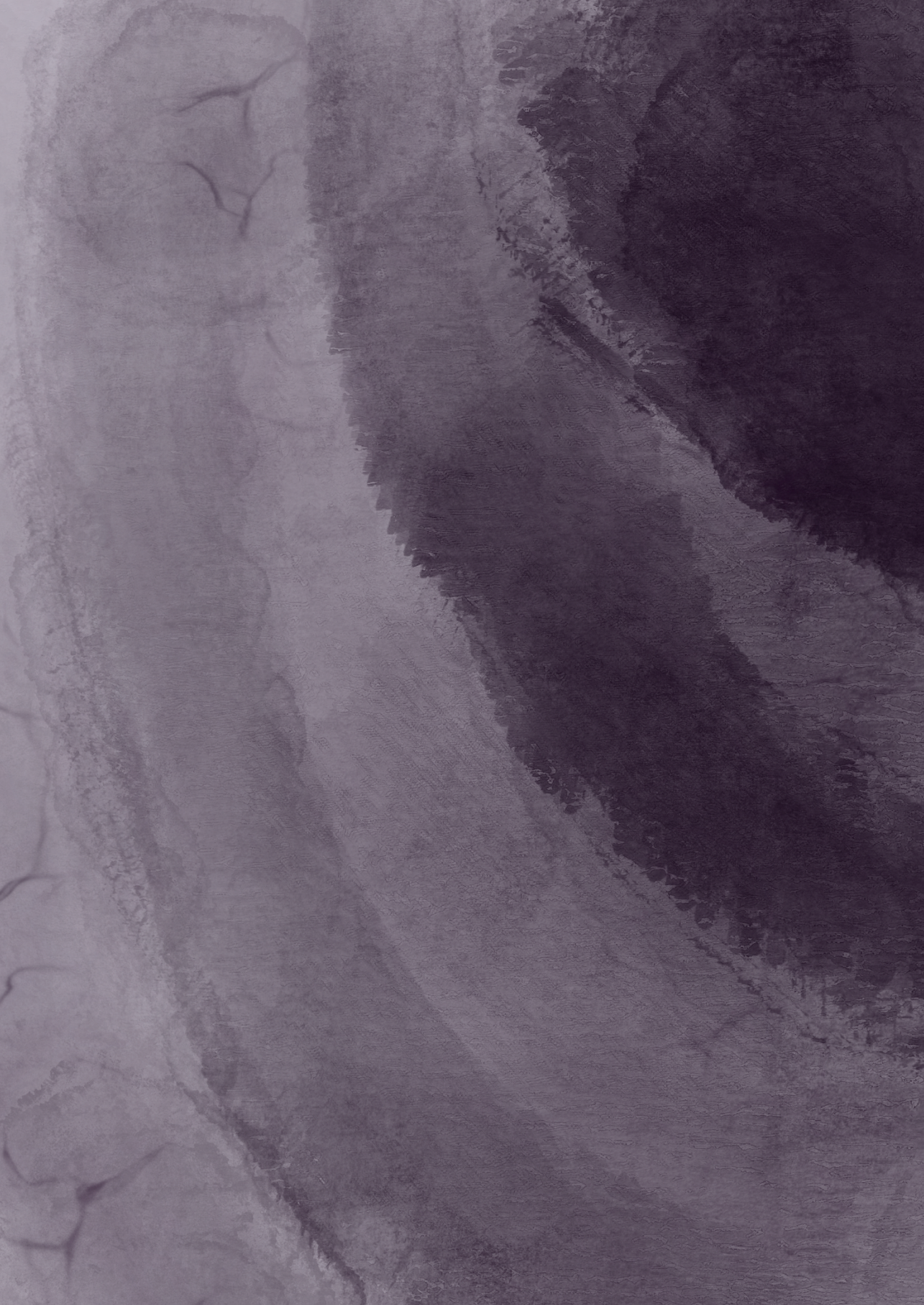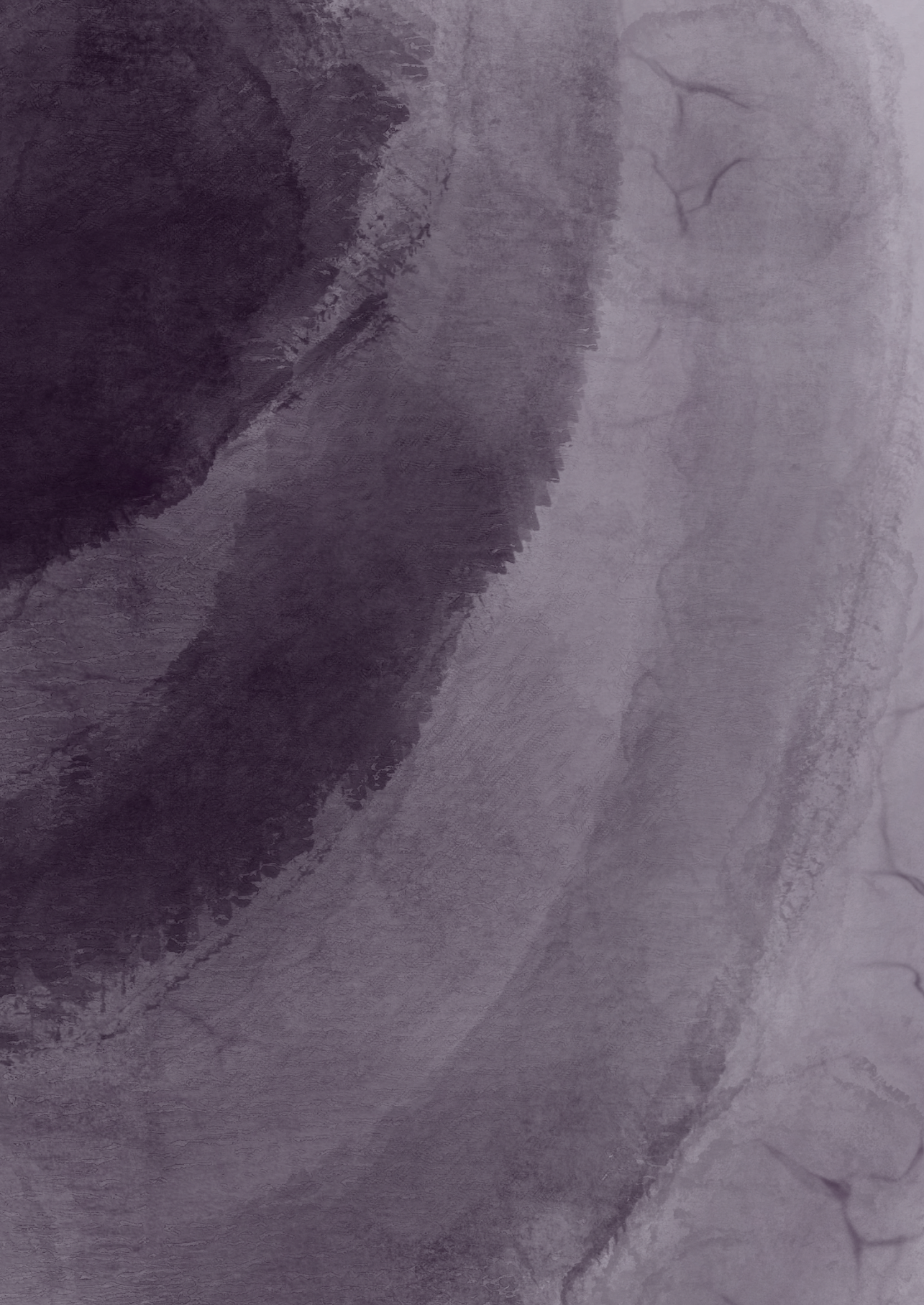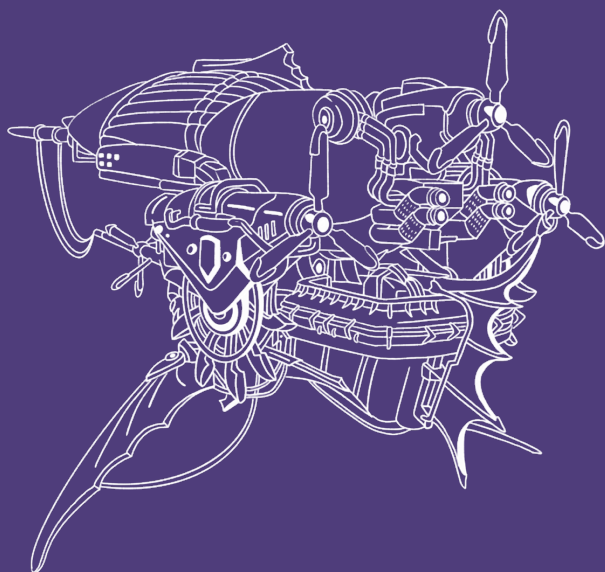
# Chapter 1

General introduction

## 1.1. Background and Context

Over the past two centuries, industrial revolutions and the subsequent transformation of many aspects of human life have dramatically increased humankind needs for energy [1]. While these transformative changes ushered an unprecedented increment of living standards, the energy required to sustain them has been predominantly derived from fossil fuels. The subsequent anthropogenic release of greenhouse gases precipitated a rapid increase in global temperatures, with profound implications for the planet's ecological, social, and economic fabric. This climate change stands as one of the most pressing and prominent challenge of our era. Even with its effects already visible, fossil fuel's usage may increase even further as growing economies continue their fast industrialization and strife for higher living standards in par with those of already fully developed countries [2]. To accommodate this change, a general and widespread implementation of renewable energy technologies will not suffice. Since the chemical industry accounts for a significant percentage of the usage of fossil fuels, and the associated $CO_2$ emission, the development of effective fossil-carbon-free commodity and specialty chemicals production platforms will also be required [2,3].

In response to these intertwined challenges, the concept of carbon capture and utilization (CCU) has emerged as an attractive idea not only to reduce the volume of emissions but also to obtain a benefit through the use of $CO_2$ in different industrial processes. Even though CCU methods will not suffice on their own, they can act as complementary key stones to renewable energy and carbon-free technologies [4]. Multiple routes can be taken for $CO_2$ conversion, pure biological approaches such as syngas fermentation, traditional catalytic synthesis like Fischer-Tropsch or direct electrochemical conversion as $CO_2$ electrolysis [5–7]. Regardless of the method used, converting $CO_2$ and utilizing it in alternative processes is a challenging endeavor, mainly due to its thermodynamically stable nature. At the moment, CCU technologies are still subject of extensive research aimed at the economic improvement of the processes, as well as technological development to achieve products with higher added value [8]. A relatively novel technology that has been getting increasing attention from multiple research groups and could potentially solve some of the aforementioned complications is the bioelectrochemical conversion of $CO_2$.

## 1.2. Microbial Electrosynthesis

Nevin et al. (2010) proved for the first time that some microorganisms, when allowed to take up electric power, can convert carbon dioxide and water into organic chemicals [9]. In subsequent years, several studies have shown the possibility of $CO_2$ conversion into different multi-carbon extracellular organic compounds such as butyrate, caproate, ethanol or butanol [10–12]. This discovery of so-called microbial electrosynthesis (MES) triggered the question whether MES could satisfy the growing demand for commodity chemicals, and increase the value of the electrical energy produced from renewable sources [13]. The low water usage and virtually unlimited carbon dioxide availability make MES a highly interesting candidate to become one of the sustainable technologies of the future [14,15].

### 1.2.1. Working Principle

Microbial electrosynthesis relies on the ability of microorganisms to accept and utilize electrons coming from a solid-state electrode to catalyze the reduction of $CO_2$ into industrially relevant products. Being an electrochemical process, a typical MES system consists of an anodic chamber where the oxidation reaction of a supplied electron donor takes place (e.g., water), a cathodic chamber where $CO_2$ reduction and microbial growth occur, and optionally a membrane that separates them both (**Figure 1.1**). The electrons produced during the oxidation half-reaction are transferred via an external circuit to the cathode surface where they are accepted, directly or indirectly, by the microorganisms to biocatalyze the reduction half-reaction. As indicated in **Box 1**, the reduction of $CO_2$ requires a driving force, therefore both electrodes are connected to an external power supply unit, which increases the electrons' potential in order to drive the catalysis [16].
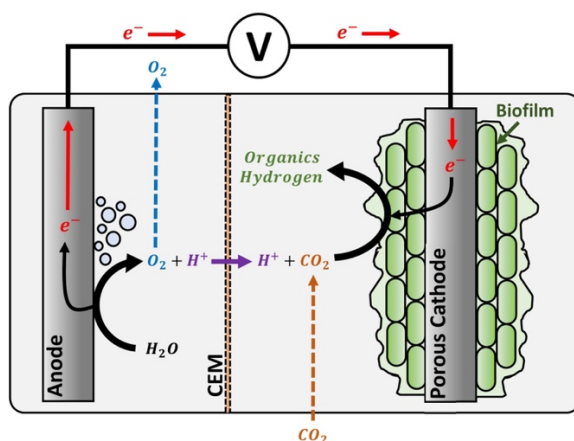


**Figure 1.1. Schematic representation of a typical MES cell.** CEM: cation exchange membrane.

---

**Box 1. Theoretical potential ($\Delta E^{01}_{cell}$) calculation for a typical MES to reduce CO₂ (as bicarbonate species).** Theoretical potential values for each half reaction were obtained from Hamelers et al. (2010) [17]. Values are presented vs. standard hydrogen electrode (SHE).
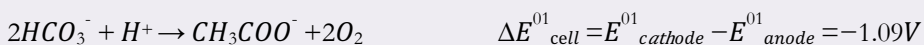
Assuming water oxidation as the anodic half-reaction:

$$4H_2O \leftrightarrow 2O_2 + 8H^+ + 8e^- \qquad\qquad E^{01}_{anode} = 0.81V$$

The most studied cathodic half-reaction on MES is the production of acetate ($CH_3COO^-$):

$$2HCO_3^- + 9H^+ + 8e^- \leftrightarrow CH_3COO^- + 4H_2O \qquad\qquad E^{01}_{cathode} = -0.28V$$

Overall reaction:

$$2HCO_3^- + H^+ \rightarrow CH_3COO^- + 2O_2 \qquad \Delta E^{01}_{cell} = E^{01}_{cathode} - E^{01}_{anode} = -1.09V$$

$\Delta E^{01}_{cell}$ is the minimum voltage required on the system at biochemical standard conditions (25°C, pH 7). The negative sign indicates that the overall reaction requires energy to be thermodynamically favorable, hence the addition of external energy is necessary.

Water oxidation, like shown in **Figure 1.1** and **Box 1**, is currently the most commonly used anodic half-reaction in MES systems. Alternative anodic reactions could be envisioned such as the biological oxidation of carbon-rich wastewater or the selective oxidation and chemical upgrading of complex molecules into industrially valuable compounds [18]. Protons that are produced at the anode will be consumed at the cathode. Cation-exchange membranes between anode and cathode can be used to minimize transport of other species than cations.

### 1.2.2. Microbial Production Platform

Acetate is a key intermediate in the bacterial anaerobic metabolism, and since the discovery of MES using an undefined mixed culture, several isolated homoacetogens species have been shown to be capable of catalyzing the reduction of CO₂ in an electrochemical setup [19]. When using mixed cultures in chemostat conditions under selective pressure, however, the most productive strains will grow and evolve, without the effort of keeping conditions aseptic.

In nature, when growing at favorable conditions (i.e., nutrient surplus, optimal temperature), bacterial cultures tend to stay in suspension. However, usually they are subjected to harsh environments, and a biofilm will be formed at the expense of a lower growth rate [20]. Regarding MES cultures, CO₂ is the only carbon source and reductive power can only be obtained from the solid-state electrode. At these

harsh conditions, cells tend to form cathodic biofilms as complex aggregates of microbial colonies attached to the surface of the electrode [21]. It is not clear if cells on a biofilm obtain reductive power via direct or indirect electron transfer mechanisms. However, if hydrogen would be abiotically produced at the cathode, it can be easily obtained by the attached cells [22,23]. A thick biofilm will have favorable, high production rates. Its formation has proven to be a difficult task, but improved performance of biofilm-based systems has been observed in the past years. Since the discovery of MES in 2010, the complexity of the product spectrum and the production rates have increased. Labelle et al. (2014) studied the effect of acidic pH on the acetate production of an *Acetobacterium* community biofilm [24]. Acetate and hydrogen production rates of 3.1 g L$^{-1}$ d$^{-1}$ and 2.6 g L$^{-1}$ d$^{-1}$ respectively, were obtained. Coulombic efficiency for acetate production was 40% at its peak. Bajracharya et al. (2015) used a mixed culture biofilm to produce acetate from $CO_2$. A maximum acetate production rate of 4.8 g L$^{-1}$ d$^{-1}$ was achieved, which is 20 times higher than the one obtained by Nevin et al. (2011) four years before [9,25]. Jourdin et al. (2018) developed a continuous system with a thick biofilm with a maximum acetate production rate of 9.8 g L$^{-1}$ d$^{-1}$. During the experiment, butyrate and caproate were also produced by the biofilm at production rates of 3.2 and 0.95 g L$^{-1}$ d$^{-1}$, respectively [11].

### 1.2.3. Energy Efficiency Losses

The costs of providing electricity are important for the economic feasibility of MES. Side processes that compete with the reduction of $CO_2$ to the desired end-products need to be accounted for as they reduce the amount of electricity used for product formation (Faradaic losses) [17,26,27]. These competitive processes are not limited to purely electrochemical ones such as the abiotic $H_2$ evolution or metal reduction at the cathode surface, but include biological ones as well, like methanogenesis and bacterial growth [28]. In addition to these side reactions, MES reactors can deviate from their theoretical ideal behavior in many other ways. This leads to the presence of overpotentials, a difference between the thermodynamically determined redox potentials and the actual potentials the system needs to catalyze the desired reactions [26,29]. These losses include activation, concentration, and ohmic overpotentials, which will be explained subsequently. When overpotentials are present, additional electrical energy is required to drive the catalysis and lower energy efficiencies are obtained (see **Box 2**) [16,26,29].

Any given chemical reaction needs an activation energy threshold to occur. This activation energy induces the so-called activation polarization, a non-ideal catalytic activity of the electrodes. Since the electrons have to be transferred from a solid-

state electrode to the reactant (i.e., the biofilm), these losses can occur when there is not enough electrode surface area, when temperature is not optimal or, for example, when the biofilm is not well enriched [26,29]. Activation losses show a non-linear behavior and are notably relevant at low current densities.

---

**Box 2. Cell voltage ($\Delta E_{cell}$) in a typical BES.**

The cell voltage ($\Delta E_{cell}$) of a typical BES is determined by the theoretical cell voltage ($\Delta E^{01}_{cell}$) lowered with losses that occur on the system. Calculation of the $\Delta E^{01}_{cell}$ has been previously explained in **Box 1**. Losses occurring in a BES are called overpotentials. Those include activation overpotential ($\Delta E_\eta$), concentration overpotential ($\Delta E_C$), and ohmic overpotential ($\Delta E_\Omega$).

$$\Delta E_{cell} = \Delta E^{01}_{cell} - \Delta E_\eta - \Delta E_C - \Delta E_\Omega$$

Both activation and concentration overpotentials can be seen as the overpotential of the anode ($\eta$) and the one of the cathode (c), as shown in the following equations:

$$\Delta E_\eta = \eta^{anode} + \eta^{cathode}$$

$$\Delta E_C = c^{anode} + c^{cathode}$$

Ohmic losses are proportional to the current (I) and ohmic resistances of the system ($\sum R_\Omega$):

$$\Delta E_\Omega = I \cdot \sum R_\Omega$$

---

On the other hand, concentration losses show a non-linear behavior and occur at high current densities, mainly due to mass transfer limitation of molecules by diffusion from or towards the electrode surface. This overpotential occurs when the diffusion rate of the reactant (e.g., $CO_2$, $H^+$) and the rate of the microbial metabolism are not equivalent. A concentration gradient of reactants and products is formed in the proximity of the electrode, limiting the maximal current consumption for the cathode and current production for the anode [26]. If the ratio between reduced and oxidized species at the cathode surface increases due to diffusion limitations, a drop in the cathode potential can occur [30,31].

In contrast to concentration and activation overpotentials, ohmic losses are due to electric resistances of the materials used in the reactor (e.g., reactor frame, electrolyte, wire connectors). All materials offer a certain resistance to charge flow (electric current), and this resistance is linear to this flow. Three main ohmic resistances can be found in a MES reactor; ionic resistances in the electrolyte and

through the membrane, electronic resistances on the electrode and current collectors, and contact resistances at the contacting interface of two electric connections [32]. In general, resistance offered by the electrodes and the current collector can be neglected when working with lab-scale reactors, but not when scaling up. This is especially true when working with carbon-based electrodes, since these materials have a higher internal resistance compared to that of a metal-based electrode and therefore can lead to significant losses at industrial scale [33,34]. Although these can become a problem when scaling-up a reactor, it is important to notice that ohmic losses due to ionic resistance of the electrolyte are usually more relevant at any point of the process development [32]. The resistance of a salt solution can be reduced to two main factors: the conductivity of the electrolyte and the distance between the electrodes.

## 1.3. Bioelectrochemical Reactor Design

While extensive research and significant progress in production rates and efficiencies have been achieved, as of today MES still needs considerably more research for industrial feasibility [35]. The vast majority of this research is performed at laboratory scale, with working volumes rarely exceeding the liter scale. Although these studies are beneficial for answering fundamental research questions, optimization and upscaling of MES reactors is a topic mostly overlooked. Most studies often aim to improve a single bottleneck of the system (e.g., higher rates, a better mass transfer, less membrane resistance) while the remaining ones are left as independent variables. However, basing the reactor design on only one or a few parameters may lead to reactors that are unfit for large scale [36]. A complete review of the literature is out of scope here, but several interesting reactor concepts and configurations are discussed in the following subsections, as well as their most relevant advantages and disadvantages.

### 1.3.1. Single-Chamber Reactors

Overpotential losses are one of the main causes for inefficiencies on bioelectrochemical reactors. Consequently, extensive research has been done on trying to decrease these in MES systems. An interesting design by Cheng et al. (2011) revolves around a membrane-less reactor with rotating half-disks as electrodes [37]. A stack of disks is rotated with half a disk submerged in the liquid phase and the other half exposed to the headspace gaseous phase. As a result of the reactor geometry and since both phases are separated, no pH gradient is possible between anode and cathode, hence overpotential produced by concentration polarization is significantly decreased. However, the high energy needed to rotate the disks is a

major concern when trying to scale-up this reactor. Unfortunately, due to polarity inversion each half-disk becomes alternatingly anode and cathode hence making it hardly applicable to MES. To tackle this problem, Hackbarth et al. (2023) developed a novel rotating disk membrane-less reactor [38]. Up to 14 working graphite electrode disks are used, corresponding to 1 m² of working electrode surface and a reaction liquid volume of up to 10 L. In contrast to the previous design by Cheng et al., the presence of counter electrode disks allows the avoidance of polarity inversion and enables the reactor to operate in either anodic or cathodic mode. As a proof-of-concept, a pure culture of *Kyrpidia spormannii* was cultivated for an aerobic MES process. Although the low applied current density of 3 µA cm⁻² resulted in low growth rates, after 24 days up to 87% of the cathode was covered with a biofilm. Organic production was not reported, yet their results suggest that such reactors could successfully be used to upscale niche aerobic processes (e.g., bioelectrochemical bioplastic production from $CO_2$).

The removal of the membrane that separates both cathode and anode compartments is a promising way of decreasing the extra resistance for proton diffusion. The use of single-chamber reactors can help to limit this effect, as shown by Xafenias et al. (2014) [39]. On their research, a membrane and a membrane-less reactor were compared on their methane and acetate production capabilities with water oxidation as the anodic reaction, showing a cathodic faradaic efficiency over 60% towards acetate when no membrane was used. However, they also observed that both systems produced different ratios of methane and acetate. The challenge of using membrane-less reactors due to side-processes and cross-over of $O_2$ has been observed in other experiments as well [40,41]. Aiming to solve this problem, Giddings et al. (2015) used a single-chamber reactor with an anode-on-top strategy, where the electrodes were placed one above each other instead of parallel to each other. By putting the anode above the cathode, cross-over of $O_2$ to the cathode side was minimized. Although an interesting way to decrease membrane resistance while avoiding oxygen microbial inhibition, significant hydrogen production was detected and faradaic efficiency towards acetate produced was below 50% [27].

### 1.3.2. In-situ Recovery Reactors

Product recovery in MES is a challenging endeavor as low organic titers and heterogenic product spectrums make the process not only technically challenging but also economically [42–44]. If carboxylates are produced, the acid species of the carboxylate is usually the main product of interest. Then, an acidification step is required downstream. One way to mitigate this is to utilize a three-chamber reactor that couples production and recovery in a single vessel. Using an additional anion

exchange membrane next to a cation exchange membrane, the carboxylates can cross to a middle chamber where they are protonated and can later be more easily recovered [45]. By using such a reactor, Gildemyn et al. (2015) recovered acetate as an acidified stream containing up to 13.5 g $L^{-1}$ acetic acid. However, the high distance between both electrodes induces high energy losses and will become an impediment when scaling-up. Uncharged acetic acid cross-over to the anode compartment and bicarbonate cross-over to the middle chamber is also of concern at industrial scale.

Accumulating acetic acid inhibits MES. Therefore, Bajracharya et al. (2017) recirculated the catholyte through an external anion exchange column [46]. This process was carried in a batch-wise mode over a 2-day period, while the MES reactor was operated in fed-batch mode. An eluent with a final concentration of 5 g $L^{-1}$ acetate was obtained, but an overall recovery of 70% and the long operational time required makes the economic feasibility of such setup unlikely. Nevertheless, the fact that acetate production (0.5 g $L^{-1}$ $day^{-1}$) remained unaltered after the recirculation might point towards a possible future viability of integrated extraction in MES.

### 1.3.3. Gas Diffusion Electrode Reactors

The design of large-scale MES reactors should take into account the rate of $CO_2$ diffusion from gas to liquid to microbes. In the field of chemocatalytic $CO_2$ electrolysis, the limiting mass transfer of $CO_2$ through a liquid phase has been solved by the use of electrodes with a conjunction of a solid, liquid and gaseous interface [47]. These gas diffusion electrodes (GDE) are typically composed of a hydrophobic gas diffusion layer, a current collector, and a catalyst layer. GDEs create a three-phase interface at the electrode surface, increasing $CO_2$ availability on the cathode surface and have been reported to increase $CO_2$ electroreduction several orders of magnitude [47–50]. In order to increase mass transfer over the cathode and improve reactor performance, several studies tested the possibility of using GDE for MES. Bajracharya et al. (2016) demonstrated the possibility of using a GDE for acetate production with improved mass transfer rate and a continuous supply of gaseous $CO_2$. An average, acetate production rate of 0.61 g $L^{-1}$ $d^{-1}$ was achieved with an 80% $CO_2$ gas mixture and faradaic efficiencies around 55% [51]. Another potential benefit of using GDEs is the possibility of reducing activation potentials at the cathode surface, thus decreasing losses through activation overpotential [52]. Although rates obtained with GDE are still low when compared with traditional MES, the possibilities to increase mass transfer and avoid high energy demanding

bubbling of the gas into the liquid phase make GDEs a promising solution when designing and optimizing a future reactor [48,53]. The use of an enriched biofilm could lead to an increment on rates, as well as the use of a different cathode material and/or structure.

Bian et al. (2018) used modified porous hollow fibers as GDEs for the production of acetate in a H-cell type MES reactor [54]. By functionalizing the hollow fiber membrane with carbon nanotubes, the specific surface area and $CO_2$ transfer capabilities of the resulting GDE were significantly increased. However, the acetate production rate remained low and only reached 0.021 g $L^{-1}$ $d^{-1}$ by the end of the experiment. The reactor was only operated for a week, making it hard to assess the overall performance of such modified GDEs. The used laboratory-type reactor architecture limits the direct assessment of such systems' potential industrial viability. Ohmic overpotential due to the anode-cathode distance will become an issue when upscaling, and better performances are needed to make the fabrication and use of such complex electrodes at larger scales viable. Nonetheless, these results serve as proof-of-concept for research with modified hollow fibers as GDEs.

In a recent development, a column-type membrane-less reactor for MES processes was patented [55]. The novel invention consists of a tubular GDE, hence without liquid between the $CO_2$-rich gas and the cathode, with a modified active layer as working electrode and an anode positioned perpendicular to it. The main product of the experiments were acetate, formate and methanol. However, low current densities (1-4 mA $cm^{-2}$) as well as modest production rates (2-7 g $L^{-1}$ $day^{-1}$) are reported, indicating major limitations in the system. A possibility is the $CO_2$ recirculation, as Kumar et al. (2021) claim that negligible amounts of $O_2$ are produced at the anode and that is why it is not separated from the $CO_2$ stream. However, this might imply that $O_2$ may still have reached the anaerobic microorganisms, resulting in lower rates due to inhibition. Also recently, Cui et al. (2023) reported an electrolytic bubble column with an external hollow fiber membrane gas–liquid contactor for the production of acetate from $CO_2$ [56]. The main column unit allows for a more efficient $H_2$ utilization by the suspended microorganisms, while the hollow fiber external contactor allows to recover the unused gas increasing overall reaction efficiency. They obtained an acetate titer and production rate of up to 34.5 g $L^{-1}$ and 1.15 g $L^{-1}$ $d^{-1}$, at an average faradaic efficiency of 64% into acetate. Even though the use of an external membrane unit might become an issue when upscaling, these results show the potential of such bubble column reactors for non-biofilm MES processes.

### 1.3.4. Flow-Through Reactors

In order to decrease mass transfer limitations, Jourdin et al. (2018) used a flat-plate double-chamber reactor where catholyte is forced through a 3-dimensional carbon-based porous electrode [11]. The flow-through configuration increases convective flow near the biofilm surface, resulting in faster mass transfer. The study achieved a maximum acetate production rate of 9.8 g $L^{-1}$ $d^{-1}$, but most relevant an increased conversion to longer carboxylic acids was also observed (3.2 g $L^{-1}$ $d^{-1}$ butyrate and 0.95 g $L^{-1}$ $d^{-1}$ caproate). The authors hypothesized that this increment on butyrate and caproate production rates was linked to the operation mode of their setup. By running the reactor in continuous mode, enhanced biofilm formation was observed, leading to a thick and uniform biofilm evenly spread throughout the porous electrode. Their results highlight the possibility to broaden the product spectrum and possible implementations of MES technology. In a subsequent study by the same group, modified operational parameters achieved increased selectivity towards longer carboxylic acids [57]. Using the same reactor, the study reports how adjusting the $CO_2$ loading rate and increasing the hydraulic retention time of the system triggers bioelectrochemical chain elongation. A selectivity increment of up to 63.6% total carbon into both butyrate and caproate was obtained while maintaining high production rates (9.8 g $L^{-1}$ $d^{-1}$ acetate, 5.7 g $L^{-1}$ $d^{-1}$ butyrate and 2.0 g $L^{-1}$ $d^{-1}$ caproate).

Recently, Chu and coworkers (2023) used a flow-electrode-based MES reactor, which was constructed using a liquid-type flow-electrode separated from the electrochemical cells [58]. Powder activated carbon was used as cathode material which was suspended in the catholyte and recirculated through the cathode chamber. A hollow serpentine channel was carved into a conductive graphite sheet and used as cathode compartment. The reactors were operated in batch mode with passive $CO_2$ supply from a gas bag and reported an acetate production rate of 16 g $m^{-2}$ $d^{-1}$ at -5 A $m^{-2}$, and an acetate concentration of about 1.5 g $L^{-1}$ both in the catholyte and extraction compartment. Baek and coworkers (2022) designed a zero-gap MES reactor configuration with a vapor-fed anode and a liquid catholyte, which they used for methane and acetate production from $CO_2$ [59]. The cathode chamber was filled with carbon felt and the catholyte forced through it. They operated their reactors in batch with both bicarbonate and sporadically sparged $CO_2$ as C-source, achieving methane and acetate production rates up to 12 and 55 g $m^{-2}$ $d^{-1}$, respectively, at 17.4 A $m^{-2}$.

Even though flat plates and laminar flow systems are highly suitable for upscaling, the results obtained with such reactors are not yet ready for industrial implementation. The distance between both electrodes is a big limitation of the

setup used in the studies, as even a few centimeters distance leads to high internal resistances. The time for complete microbial colonization of the working electrode is also a major concern when moving towards a full-scale production platform. Though these reactors claim the highest productivities achieved so far in a biofilm-based MES system, they are not yet at the level of already established gas fermentation technologies. For comparison's sake, typical production rates for ethanol in syngas fermentation are on the order of 4 g $L^{-1}$ $h^{-1}$ [60,61].

## 1.4. Upscaling of Microbial Electrosynthesis Reactors

As of now, MES systems are far from being scalable. According to a techno-economic analysis, under the current state-of-the-art performance and economic conditions MES is industrially non-viable [44]. Some relevant key factors associated with this low performance are insufficient product specificity, low production rates, high cell voltage, low energy conversion efficiency, and high capital costs [35]. The design of optimized reactor parameters is strongly underrepresented in literature, indicating that large advancements in process performance are still possible [62]. By focusing on improvements from a non-biological nature, mainly reactor design, quick advances towards a more feasible and scalable process could be achieved. As research on this topic is currently scarce, an increase in research on mass transfer, fluid dynamics and reactor cell geometry is required to obtain the necessary information for proper reactor design [63]. Besides, it is also unclear how to rationally upscale a MES reactor. Bioreactor design is a complex task as operational parameters need to be tailored to each specific process. The optimum conditions, with limited deviations from the best possible performance, can be difficult to achieve. It is therefore crucial to understand which are the limiting steps of each MES sub-process and adapt the design strategy accordingly. Hence, to push MES to an industrial level a deep understanding of all factors that limit reactor efficiency and a clever way to overcome scalability issues must be combined and applied during the design part.

## 1.5. Scope of this Thesis

The objective of this dissertation is to develop a scalable bioreactor that will allow for a reactor-scale performance of microbial electrosynthesis from $CO_2$ comparable to those of already established technologies. Microbial fundamentals are therefore out of the scope of this thesis. The literature review presented in this chapter highlights the main knowledge gaps that need to be addressed for successful and cost-effective upscaling of microbial electrosynthesis systems:

- A lack of understanding on how microorganisms respond to relevant operational parameters and reactor environments impedes designing successful microbial electrosynthesis processes.

- Microbial growth rates and microbial kinetics have not been experimentally elucidated, hindering process understanding and effective optimization.

- Reactor designs have not considered, assessed, and addressed all key process parameters and their intertwined interactions to achieve industrially relevant performances.

The work presented in this thesis addresses these knowledge gaps by combining mathematical modelling and experimental work.

Control over the desired bioelectrochemical reactions necessitates the proper adjustment of process parameters, thus creating a need for a deeper understanding of the complex interactions taking place within a MES reactor. To achieve this, **Chapter 2** introduces a reactor-scale computational model describing key processes occurring within a biofilm-based MES reactor. The presented model not only serves as a framework for future modelling studies but also allows for quick predictions of the overall performance of different reactor setups. Simulation results show clear links between critical performance indicators (e.g., productivity) and operational process conditions, highlighting prevailing process limitations and opening a door for future system optimization.

Microorganisms are essential in all biotechnological systems, and their proper determination is crucial not only for research purposes but for process development as well. However, biomass concentration is one of the major unmeasured variables within biofilm-based MES processes, hindering further complex computational attempts. Therefore, **Chapter 3** presents the results of a collaborative effort to develop a method to determine biomass concentration in biofilm-based MES systems. A simple method using nitrogen balancing and optical density allows for the determination of biofilm and planktonic cell concentrations at any given time. Biomass-specific growth rates and production rates of desired products are also derived, allowing for a more effective and comparable assessment of the performance of MES reactors.

Insight on which major factors currently limit the overall performance of MES allows for a more comprehensive reactor design strategy. To simultaneously tackle most relevant limitations, a novel directed flow-through bioreactor that can continuously reduce $CO_2$ is presented in **Chapter 4**. The new design outperforms

all previously reported MES reactors by achieving 3-fold increased productivities with high faradaic efficiencies. Results demonstrate the capability of MES to attain process performances comparable to those in gas fermentation technologies already present at industrial scale. These findings serve as a milestone in developing MES as a competitive technology and emphasize key design parameters for efficient electricity-driven microbial $CO_2$ reduction. Despite the need for further improvement, the combination of computationally derived knowledge on limiting parameters and a step-by-step design approach shows the scale-up capacity of MES reactors.

Finally, **Chapter 5** presents a general discussion on the main outcomes of this thesis. An outlook on future research, focusing on the next steps necessary to make MES upscaling a reality is also presented.

## 1.6. References

[1]     S. Chu, A. Majumdar, Opportunities and challenges for a sustainable energy future, Nature 488 (2012) 294–303. https://doi.org/10.1038/nature11475.

[2]     S.J. Davis, K. Caldeira, H.D. Matthews, Future $CO_2$ Emissions and Climate Change from Existing Energy Infrastructure, Science (1979) 329 (2010) 1330–1333. https://doi.org/10.1126/science.1188566.

[3]     M. Patel, M. Neelis, D. Gielen, J. Olivier, T. Simmons, J. Theunis, Carbon dioxide emissions from non-energy use of fossil fuels: Summary of key issues and conclusions from the country analyses, Resour Conserv Recycl 45 (2005) 195–209. https://doi.org/10.1016/j.resconrec.2005.05.002.

[4]     F.M. Baena-Moreno, M. Rodríguez-Galán, F. Vega, B. Alonso-Fariñas, L.F. Vilches Arenas, B. Navarrete, Carbon capture and utilization technologies: a literature review and recent advances, Energy Sources, Part A: Recovery, Utilization, and Environmental Effects 41 (2019) 1403–1433. https://doi.org/10.1080/15567036.2018.1548518.

[5]     A. Al-Mamoori, A. Krishnamurthy, A.A. Rownaghi, F. Rezaei, Carbon Capture and Utilization Update, Energy Technology 5 (2017) 834–849. https://doi.org/10.1002/ente.201600747.

[6]     R.M. Cuéllar-Franca, A. Azapagic, Carbon capture, storage and utilisation technologies: A critical analysis and comparison of their life cycle environmental impacts, Journal of CO2 Utilization 9 (2015) 82–102. https://doi.org/10.1016/j.jcou.2014.12.001.

[7]     F.D. Meylan, V. Moreau, S. Erkman, CO2 utilization in the perspective of industrial ecology, an overview, Journal of CO2 Utilization 12 (2015) 101–108. https://doi.org/10.1016/j.jcou.2015.05.003.

[8]     Z. Yuan, M.R. Eden, R. Gani, Toward the Development and Deployment of Large-Scale Carbon Dioxide Capture and Conversion Processes, Ind Eng Chem Res 55 (2016) 3383–3419. https://doi.org/10.1021/acs.iecr.5b03277.

[9]     K.P. Nevin, T.L. Woodard, A.E. Franks, Z.M. Summers, D.R. Lovley, Microbial Electrosynthesis: Feeding Microbes Electricity To Convert Carbon Dioxide and Water to Multicarbon Extracellular Organic Compounds, MBio 1 (2010). https://doi.org/10.1128/mBio.00103-10.

[10]    R. Ganigué, S. Puig, P. Batlle-Vilanova, M.D. Balaguer, J. Colprim, Microbial electrosynthesis of butyrate from carbon dioxide, Chemical Communications 51 (2015) 3235–3238. https://doi.org/10.1039/C4CC10121A.

[11]    L. Jourdin, S.M.T. Raes, C.J.N. Buisman, D.P.B.T.B. Strik, Critical Biofilm Growth throughout Unmodified Carbon Felts Allows Continuous Bioelectrochemical Chain Elongation from CO2 up to Caproate at High Current Density, Front Energy Res 6 (2018). https://doi.org/10.3389/fenrg.2018.00007.

[12]    S.M.T. Raes, L. Jourdin, C.J.N. Buisman, D.P.B.T.B. Strik, Continuous Long-Term Bioelectrochemical Chain Elongation to Butyrate, ChemElectroChem 4 (2017) 386–395. https://doi.org/10.1002/celc.201600587.

[13]    N.S. Lewis, D.G. Nocera, Powering the planet: Chemical challenges in solar energy utilization, Proceedings of the National Academy of Sciences 103 (2006) 15729–15735. https://doi.org/10.1073/pnas.0603395103.

[14]    K. Rabaey, R.A. Rozendal, Microbial electrosynthesis — revisiting the electrical route for microbial production, Nat Rev Microbiol 8 (2010) 706–716. https://doi.org/10.1038/nrmicro2422.

[15]    J. Desloover, J.B.A. Arends, T. Hennebel, K. Rabaey, Operational and technical considerations for microbial electrosynthesis, Biochem Soc Trans 40 (2012) 1233–1238. https://doi.org/10.1042/BST20120111.

[16]    T. Krieg, J. Madjarov, L.F.M. Rosa, F. Enzmann, F. Harnisch, D. Holtmann, K. Rabaey, Reactors for Microbial Electrobiotechnology, in: 2018: pp. 231–271. https://doi.org/10.1007/10_2017_40.

[17]    H.V.M. Hamelers, A. Ter Heijne, T.H.J.A. Sleutels, A.W. Jeremiasse, D.P.B.T.B. Strik, C.J.N. Buisman, New applications and performance of bioelectrochemical systems, Appl Microbiol Biotechnol 85 (2010) 1673–1685. https://doi.org/10.1007/s00253-009-2357-1.

[18]    F. Birk, H. Hausmann, M.A. Fraatz, A. Kirste, N.C. Aust, R. Pelzer, H. Zorn, Generation of Flavor-Active Compounds by Electrochemical Oxidation of ( *R* )-Limonene, J Agric Food Chem 70 (2022) 7220–7229. https://doi.org/10.1021/acs.jafc.2c01301.

[19]    C.W. Marshall, D.E. Ross, K.M. Handley, P.B. Weisenhorn, J.N. Edirisinghe, C.S. Henry, J.A. Gilbert, H.D. May, R.S. Norman, Metabolic Reconstruction and Modeling Microbial Electrosynthesis, Sci Rep 7 (2017) 8391. https://doi.org/10.1038/s41598-017-08877-z.

[20]    K.K. Jefferson, What drives bacteria to produce a biofilm?, FEMS Microbiol Lett 236 (2004) 163–173. https://doi.org/10.1111/j.1574-6968.2004.tb09643.x.

[21]    J. Yang, S. Cheng, C. Li, Y. Sun, H. Huang, Shear Stress Affects Biofilm Structure and Consequently Current Generation of Bioanode in Microbial Electrochemical Systems (MESs), Front Microbiol 10 (2019). https://doi.org/10.3389/fmicb.2019.00398.

[22] C.W. Marshall, D.E. Ross, E.B. Fichot, R.S. Norman, H.D. May, Electrosynthesis of Commodity Chemicals by an Autotrophic Microbial Community, Appl Environ Microbiol 78 (2012) 8412–8420. https://doi.org/10.1128/AEM.02401-12.

[23] H.D. May, P.J. Evans, E. V LaBelle, The bioelectrosynthesis of acetate, Curr Opin Biotechnol 42 (2016) 225–233. https://doi.org/10.1016/j.copbio.2016.09.004.

[24] E. V. LaBelle, C.W. Marshall, J.A. Gilbert, H.D. May, Influence of Acidic pH on Hydrogen and Acetate Production by an Electrosynthetic Microbiome, PLoS One 9 (2014) e109935. https://doi.org/10.1371/journal.pone.0109935.

[25] S. Bajracharya, A. ter Heijne, X. Dominguez Benetton, K. Vanbroekhoven, C.J.N. Buisman, D.P.B.T.B. Strik, D. Pant, Carbon dioxide reduction by mixed and pure cultures in microbial electrosynthesis using an assembly of graphite felt and stainless steel as a cathode, Bioresour Technol 195 (2015) 14–24. https://doi.org/10.1016/j.biortech.2015.05.081.

[26] B.E. Logan, B. Hamelers, R. Rozendal, U. Schröder, J. Keller, S. Freguia, P. Aelterman, W. Verstraete, K. Rabaey, Microbial Fuel Cells: Methodology and Technology, Environ Sci Technol 40 (2006) 5181–5192. https://doi.org/10.1021/es0605016.

[27] C.G.S. Giddings, K.P. Nevin, T. Woodward, Simplifying microbial electrosynthesis reactor design, Front Microbiol 6 (2015). https://doi.org/10.3389/fmicb.2015.00468.

[28] S. Bajracharya, R. Yuliasni, K. Vanbroekhoven, C.J.N. Buisman, D.P.B.T.B. Strik, D. Pant, Long-term operation of microbial electrosynthesis cell reducing CO2 to multi-carbon chemicals with a mixed culture avoiding methanogenesis, Bioelectrochemistry 113 (2017) 26–34. https://doi.org/10.1016/j.bioelechem.2016.09.001.

[29] P. Clauwaert, P. Aelterman, T.H. Pham, L. De Schamphelaire, M. Carballa, K. Rabaey, W. Verstraete, Minimizing losses in bio-electrochemical systems: the road to applications, Appl Microbiol Biotechnol 79 (2008) 901–913. https://doi.org/10.1007/s00253-008-1522-2.

[30] S. Kerzenmacher, Engineering of Microbial Electrodes, in: 2017: pp. 135–180. https://doi.org/10.1007/10_2017_16.

[31] B.E. Logan, Scaling up microbial fuel cells and other bioelectrochemical systems, Appl Microbiol Biotechnol 85 (2010) 1665–1671. https://doi.org/10.1007/s00253-009-2378-9.

[32] L. Carrette, K.A. Friedrich, U. Stimming, Fuel Cells: Principles, Types, Fuels, and Applications, ChemPhysChem 1 (2000) 162–193. https://doi.org/10.1002/1439-7641(20001215)1:4<162::AID-CPHC162>3.0.CO;2-Z.

[33] R.A. Rozendal, H.V.M. Hamelers, K. Rabaey, J. Keller, C.J.N. Buisman, Towards practical implementation of bioelectrochemical wastewater treatment, Trends Biotechnol 26 (2008) 450–459. https://doi.org/10.1016/j.tibtech.2008.04.008.

[34] X. Xie, G. Yu, N. Liu, Z. Bao, C.S. Criddle, Y. Cui, Graphene–sponges as high-performance low-cost anodes for microbial fuel cells, Energy Environ Sci 5 (2012) 6862. https://doi.org/10.1039/c2ee03583a.

[35] A. Prévoteau, J.M. Carvajal-Arroyo, R. Ganigué, K. Rabaey, Microbial electrosynthesis from CO2: forever a promise?, Curr Opin Biotechnol 62 (2020) 48–57. https://doi.org/10.1016/j.copbio.2019.08.014.

**1**

[36]     N.J. Claassens, C.A.R. Cotton, D. Kopljar, A. Bar-Even, Making quantitative sense of electromicrobial production, Nat Catal 2 (2019) 437–447. https://doi.org/10.1038/s41929-019-0272-0.

[37]     K.Y. Cheng, G. Ho, R. Cord-Ruwisch, Novel Methanogenic Rotatable Bioelectrochemical System Operated with Polarity Inversion, Environ Sci Technol 45 (2011) 796–802. https://doi.org/10.1021/es102482j.

[38]     M. Hackbarth, J. Gescher, H. Horn, J.E. Reiner, A scalable, rotating disc bioelectrochemical reactor (RDBER) suitable for the cultivation of both cathodic and anodic biofilms, Bioresour Technol Rep 21 (2023) 101357. https://doi.org/10.1016/j.biteb.2023.101357.

[39]     N. Xafenias, V. Mapelli, Performance and bacterial enrichment of bioelectrochemical systems during methane and acetate production, Int J Hydrogen Energy 39 (2014) 21864–21875. https://doi.org/10.1016/j.ijhydene.2014.05.038.

[40]     P. Clauwaert, W. Verstraete, Methanogenesis in membraneless microbial electrolysis cells, Appl Microbiol Biotechnol 82 (2009) 829–836. https://doi.org/10.1007/s00253-008-1796-4.

[41]     Q. Fu, Y. Kuramochi, N. Fukushima, H. Maeda, K. Sato, H. Kobayashi, Bioelectrochemical Analyses of the Development of a Thermophilic Biocathode Catalyzing Electromethanogenesis, Environ Sci Technol 49 (2015) 1225–1232. https://doi.org/10.1021/es5052233.

[42]     F. Demichelis, S. Fiore, D. Pleissner, J. Venus, Technical and economic assessment of food waste valorization through a biorefinery chain, Renewable and Sustainable Energy Reviews 94 (2018) 38–48. https://doi.org/10.1016/j.rser.2018.05.064.

[43]     P. Batlle-Vilanova, R. Ganigué, S. Ramió-Pujol, L. Bañeras, G. Jiménez, M. Hidalgo, M.D. Balaguer, J. Colprim, S. Puig, Microbial electrosynthesis of butyrate from carbon dioxide: Production and extraction, Bioelectrochemistry 117 (2017) 57–64. https://doi.org/10.1016/j.bioelechem.2017.06.004.

[44]     L. Jourdin, J. Sousa, N. van Stralen, D.P.B.T.B. Strik, Techno-economic assessment of microbial electrosynthesis from CO2 and/or organics: An interdisciplinary roadmap towards future research and application, Appl Energy 279 (2020) 115775. https://doi.org/10.1016/j.apenergy.2020.115775.

[45]     S. Gildemyn, K. Verbeeck, R. Slabbinck, S.J. Andersen, A. Prévoteau, K. Rabaey, Integrated Production, Extraction, and Concentration of Acetic Acid from $CO_2$ through Microbial Electrosynthesis, Environ Sci Technol Lett 2 (2015) 325–328. https://doi.org/10.1021/acs.estlett.5b00212.

[46]     S. Bajracharya, B. van den Burg, K. Vanbroekhoven, H. De Wever, C.J.N. Buisman, D. Pant, D.P.B.T.B. Strik, In situ acetate separation in microbial electrosynthesis from CO2 using ion-exchange resin, Electrochim Acta 237 (2017) 267–275. https://doi.org/10.1016/j.electacta.2017.03.209.

[47]     C. Gaudillere, L. Navarrete, J.M. Serra, Syngas production at intermediate temperature through H2O and CO2 electrolysis with a Cu-based solid oxide electrolyzer cell, Int J Hydrogen Energy 39 (2014) 3047–3054. https://doi.org/10.1016/j.ijhydene.2013.12.045.

[48] M.N. Mahmood, D. Masheder, C.J. Harty, Use of gas-diffusion electrodes for high-rate electrochemical reduction of carbon dioxide. I. Reduction at lead, indium- and tin-impregnated electrodes, J Appl Electrochem 17 (1987) 1159–1170. https://doi.org/10.1007/BF01023599.

[49] F. Bidrawn, G. Kim, G. Corre, J.T.S. Irvine, J.M. Vohs, R.J. Gorte, Efficient Reduction of CO[sub 2] in a Solid Oxide Electrolyzer, Electrochemical and Solid-State Letters 11 (2008) B167. https://doi.org/10.1149/1.2943664.

[50] S. Ma, M. Sadakiyo, R. Luo, M. Heima, M. Yamauchi, P.J.A. Kenis, One-step electrosynthesis of ethylene and ethanol from CO2 in an alkaline electrolyzer, J Power Sources 301 (2016) 219–228. https://doi.org/10.1016/j.jpowsour.2015.09.124.

[51] S. Bajracharya, K. Vanbroekhoven, C.J.N. Buisman, D. Pant, D.P.B.T.B. Strik, Application of gas diffusion biocathode in microbial electrosynthesis from carbon dioxide, Environmental Science and Pollution Research 23 (2016) 22292–22308. https://doi.org/10.1007/s11356-016-7196-x.

[52] H. Liu, B.E. Logan, Electricity Generation Using an Air-Cathode Single Chamber Microbial Fuel Cell in the Presence and Absence of a Proton Exchange Membrane, Environ Sci Technol 38 (2004) 4040–4046. https://doi.org/10.1021/es0499344.

[53] H. Rismani-Yazdi, S.M. Carver, A.D. Christy, O.H. Tuovinen, Cathodic limitations in microbial fuel cells: An overview, J Power Sources 180 (2008) 683–694. https://doi.org/10.1016/j.jpowsour.2008.02.074.

[54] B. Bian, M.F. Alqahtani, K.P. Katuri, D. Liu, S. Bajracharya, Z. Lai, K. Rabaey, P.E. Saikaly, Porous nickel hollow fiber cathodes coated with CNTs for efficient microbial electrosynthesis of acetate from CO $_2$ using *Sporomusa ovata*, J Mater Chem A Mater 6 (2018) 17201–17211. https://doi.org/10.1039/C8TA05322G.

[55] M. Kumar, Srikanth Sandipam, Suresh Kumar Puri, Sankara Sri Venkata Ramakumar, Ludovicus Diels, Lambertus Bouwman, Karolien Vanbroekhoven, Deepak Pant, Membrane-less reactor design and process for biotransformation of carbon dioxide., U.S. Patent No. 11,519,084, 2022.

[56] K. Cui, K. Guo, J.M. Carvajal-Arroyo, J. Arends, K. Rabaey, An electrolytic bubble column with an external hollow fiber membrane gas–liquid contactor for effective microbial electrosynthesis of acetate from CO2, Chemical Engineering Journal 471 (2023) 144296. https://doi.org/10.1016/j.cej.2023.144296.

[57] L. Jourdin, M. Winkelhorst, B. Rawls, C.J.N. Buisman, D.P.B.T.B. Strik, Enhanced selectivity to butyrate and caproate above acetate in continuous bioelectrochemical chain elongation from CO2: Steering with CO2 loading rate and hydraulic retention time, Bioresour Technol Rep 7 (2019) 100284. https://doi.org/10.1016/j.biteb.2019.100284.

[58] N. Chu, D. Wang, H. Wang, Q. Liang, J. Chang, Y. Gao, Y. Jiang, R.J. Zeng, Flow-Electrode Microbial Electrosynthesis for Increasing Production Rates and Lowering Energy Consumption, Engineering 25 (2023) 157–167. https://doi.org/10.1016/j.eng.2021.09.015.

**1**

[59]     G. Baek, R. Rossi, P.E. Saikaly, B.E. Logan, High-rate microbial electrosynthesis using a zero-gap flow cell and vapor-fed anode design, Water Res 219 (2022) 118597. https://doi.org/10.1016/j.watres.2022.118597.

[60]     L. Puiman, B. Abrahamson, R.G.J.M. van der Lans, C. Haringa, H.J. Noorman, C. Picioreanu, Alleviating mass transfer limitations in industrial external-loop syngas-to-ethanol fermentation, Chem Eng Sci 259 (2022) 117770. https://doi.org/10.1016/j.ces.2022.117770.

[61]     E. Almeida Benalcázar, H. Noorman, R. Maciel Filho, J.A. Posada, Modeling ethanol production through gas fermentation: a biothermodynamics and mass transfer-based hybrid model for microbial growth in a large-scale bubble column bioreactor, Biotechnol Biofuels 13 (2020) 59. https://doi.org/10.1186/s13068-020-01695-y.

[62]     F. Harnisch, D. Holtmann, Bioelectrosynthesis, Springer International Publishing, Cham, 2019. https://doi.org/10.1007/978-3-030-03299-9.

[63]     L. Jourdin, T. Burdyny, Microbial Electrosynthesis: Where Do We Go from Here?, Trends Biotechnol 39 (2021) 359–369. https://doi.org/10.1016/j.tibtech.2020.10.014.
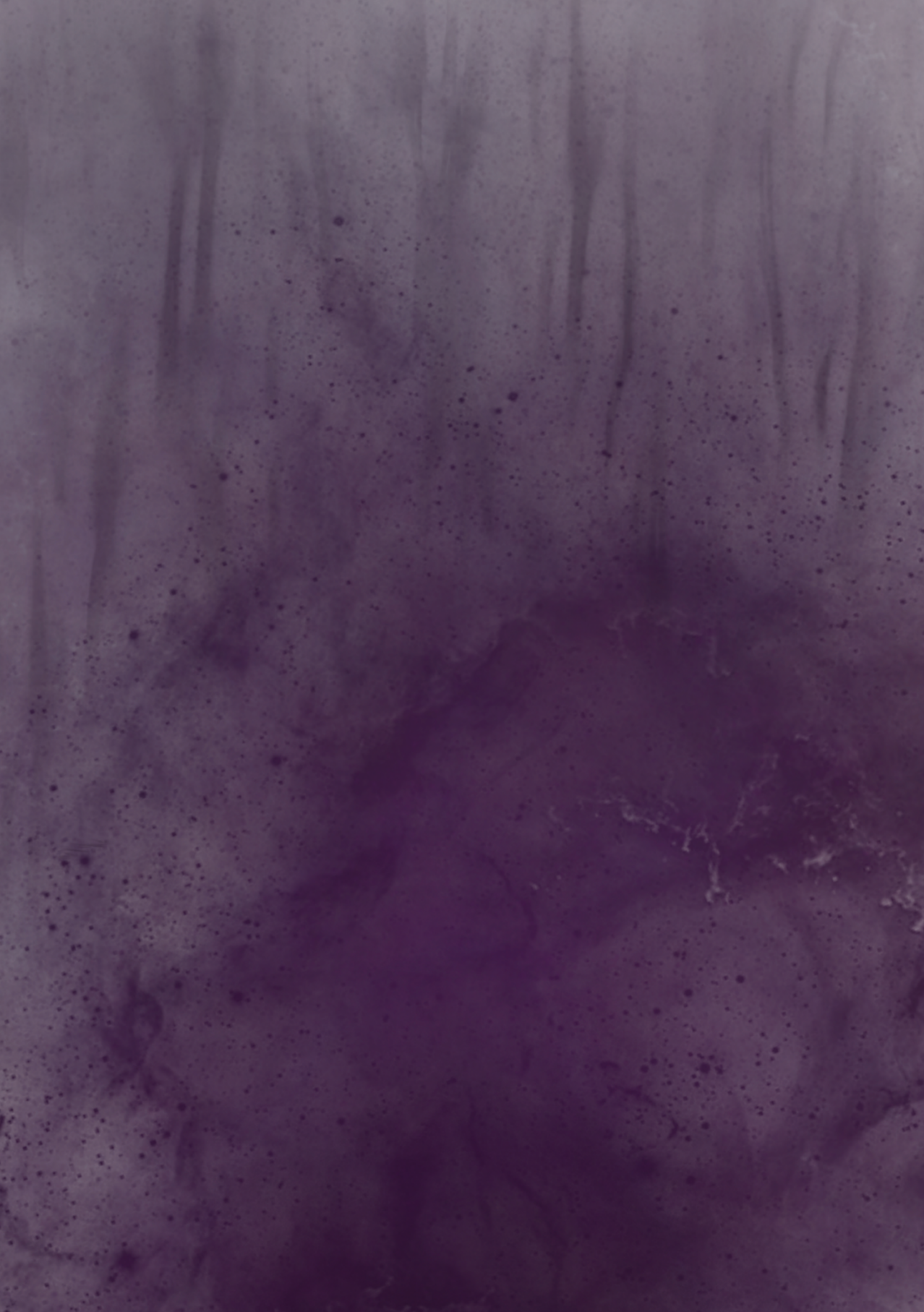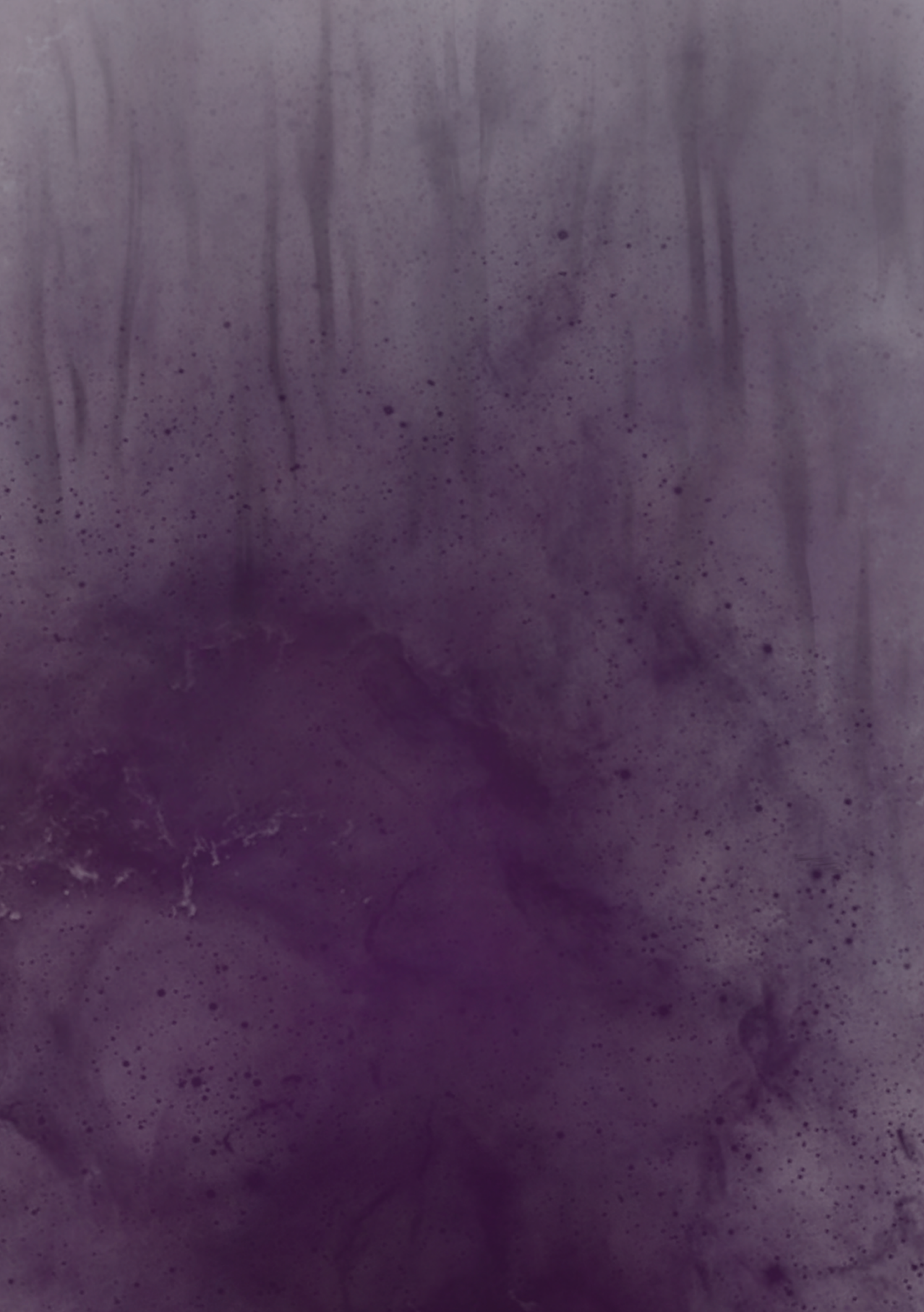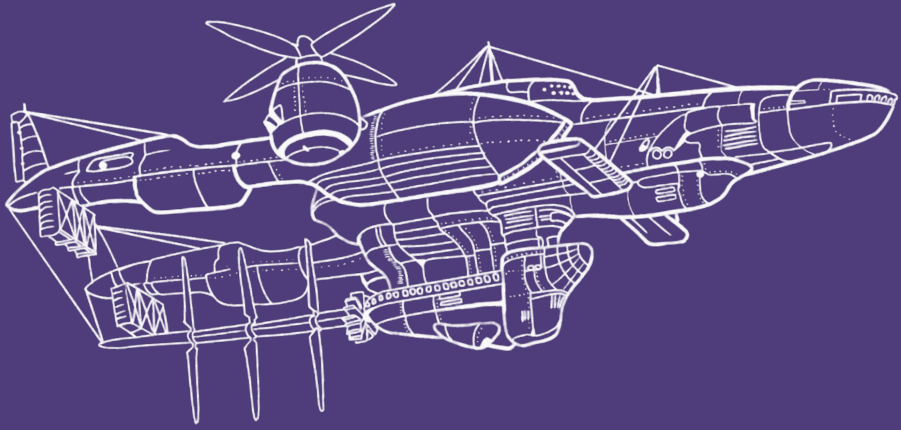
# Chapter 2

A general model for biofilm-driven microbial electrosynthesis of carboxylates from $CO_2$

## Abstract

Up to now, computational modeling of microbial electrosynthesis (MES) has been underexplored, but is necessary to achieve breakthrough understanding of the process- limiting steps. Here, a general framework for modeling microbial kinetics in a MES reactor is presented. A thermodynamic approach is used to link microbial metabolism to the electrochemical reduction of an intracellular mediator, allowing to predict cellular growth and current consumption. The model accounts for $CO_2$ reduction to acetate, and further elongation to n-butyrate and n-caproate. Simulation results were compared with experimental data obtained from different sources and proved the model is able to successfully describe microbial kinetics (growth, chain elongation, and product inhibition) and reactor performance (current density, organics titer). The capacity of the model to simulate different system configurations is also shown. Model results suggest $CO_2$ dissolved concentration might be limiting existing MES systems, and highlight the importance of the delivery method utilized to supply it. Simulation results also indicate that for biofilm-driven reactors, continuous mode significantly enhances microbial growth and might allow denser biofilms to be formed and higher current densities to be achieved.

**Keywords:** microbial electrosynthesis, bioelectrochemical system, microbial kinetics, mathematical model, $CO_2$ reduction, chain elongation

## 2.1. Introduction

Microbial electrosynthesis (MES) is based on the use of microorganisms that can reduce $CO_2$ to industrially relevant products (i.e., alcohols, carboxylic acids) by using electrons coming from a solid-state electrode [1–3]. MES is a promising technology to satisfy the growing demand for commodity and specialty chemicals, and has the potential to increase the value of the electrical energy produced from renewable sources [4]. Until now, research on MES has been primarily focused on developing the technology by means of studying its fundamentals (e.g., electron transfer mechanisms, metabolic routes used for reducing $CO_2$) and improving the efficiency of crucial components (e.g., microorganisms, cathode structure, and material) [5,6]. Even though significant progress has been achieved on these aspects, MES technology still needs to be pushed to higher performance to reach industrial viability [7]. In that sense, rate-limiting steps, scalability, and system optimization are key aspects that need to be assessed. Initial work in all those directions has been published in the last decade [8–11], but progress has been modest.

MES is a complex system that combines both electrochemistry and biotechnology. When trying to improve reactor performance, all physical, chemical, and biological processes occurring simultaneously have to be properly regulated. A major breakthrough would require a deeper understanding of this inherent complexity. To that end, computational models are a systematic approach that can be used for testing hypotheses and obtain knowledge on the described system, as pointed out by Korth and Harnisch (2017) in their detailed review on modeling microbial electrosynthesis [12].

When looking at the biocatalyst itself, metabolic modeling allows for an in-depth analysis of the molecular and biochemical mechanisms occurring within a particular microorganism. These complex mathematical expressions encompass all major metabolic pathways, and simulate them in perspective of the entire metabolic network. Pandit and Mahadevan (2011) used flux balance analysis to develop one of the first computational genome-scale metabolic models, and used it to characterize the role of bioelectrosynthesis in chemical production [13]. Their model was based on the genome of *Escherichia coli*, and showed that trade-offs between improving growth rates and yields could exist. Kracke and Krömer (2014) used elementary mode analysis to create multiple core networks of metabolic carbon pathways, and found that the yield obtained with electrical enhancement depends strongly on the electron transport mechanism [14]. Marshall et al. (2017) constructed three full genome-scale metabolic models that in combination with flux balance analysis, allowed them to predict the metabolic activity of different microbial communities

[15]. Their results identified the main metabolic pathways in those systems, as well as demonstrating the possibility of multiple species being active within a very limited space near an electrode. Metabolic network models are of great use when exploring suitable MES processes, as well as when studying the pathways present within a particular microorganism. However, these are complex mathematical expressions that require prior knowledge on the genome and transcriptome of the studied organism. Moreover, data on interactions between species in mixed microbial culture biofilms, biofilm structure, and mass transport phenomena are needed when extrapolating results to a biofilm superstructure. Since this information is largely unknown in MES to date, and metabolic models are mostly focused on microbial cells and their immediate surroundings, these models are hardly suited for a more generalized study at a reactor scale.

To date, few modeling studies have been published on microbial electrosynthesis and the dynamics between microorganisms and operating conditions. Kazemi et al. (2015) modeled a biofilm-based MES cathode with a pure culture producing acetate using a conductive biofilm approach [16]. The model allowed them to study current density and biofilm thickness on different $CO_2$ concentrations and applied cathodic potentials. Their model showed that high $CO_2$ concentrations decreased coulombic efficiency, while a higher cathodic potential increased the coulombic efficiency. Gadkari et al. (2019) performed a study of the interdependence of some operating parameters in a MES system using a bioanode [17]. They developed a two-chamber model with two cell populations, allowing them to analyze the effect of parameters such as initial substrate concentration and operation cycle time on MES performance. Their results showed that reducing the operation cycle time favored production rates, but decreased substrate utilization and coulombic efficiency. Abel and Clark (2021) very recently modeled a biomass-producing system that reduces $CO_2$ into formate electrochemically, which is then used aerobically by planktonic cells to grow [18]. They were able to study the dynamics between $CO_2$, $O_2$, and biomass growth as well as the influence of some operational parameters on the general performance of the reactor. $O_2$ and $CO_2$ mass transfer were found to be limiting the formate-mediated reactor. Their study also indicates that gas recycling to increase overall $CO_2$ utilization will be necessary when scaling-up these systems. Salimijazi et al. (2020) also very recently developed a mathematical model to determine the maximum theoretical efficiency of MES processes from electrical power to biofuels [19]. They predicted that by using highly engineered microorganisms, the conversion efficiency to biofuels could increase up to 52%. Their study also shows an interdependence between said efficiency, and biofilm

thickness and resistivity. To maintain a given efficiency, if a biofilm resistivity increases its thickness must decrease, while increasing its area.

The use of computational modeling of MES at reactor scale for process understanding and system optimization has clearly been underexplored. Previous modeling papers mainly focused on studying the effects of operational parameters on the general performance of specific MES processes. Moreover, one of the main knowledge gaps in MES is that microbial growth rates and microbial kinetics have not been experimentally elucidated and are thus unknown to date. To achieve a higher process performance, a deeper understanding on the microbial metabolism and production kinetics is necessary. In addition, the study of how microorganisms adapt to changing operational parameters and to different reactor environments (i.e., changing substrate and/or product concentrations) is of crucial importance when elucidating what is limiting MES performance. A general black-box mathematical model allowing for the dynamic description of attached microbial cells, and their interactions with the cathode can help to study such complex environments and potentially elucidate current process bottlenecks. To this end, the objective of this work was to develop a reactor-scale mathematical modeling framework for the study of biofilm-driven microbial electrosynthesis processes with multiple product spectrum and different operational conditions, i.e., batch or continuous mode, continuous or discontinuous $CO_2$ supply. To achieve this, a dynamic black-box model of a MES reactor for the reduction of $CO_2$ including microbial kinetics with product inhibition and integrated chain elongation, was implemented and solved with the MATLAB software package (MATLAB 2019b).

Since microbial kinetics in MES are not yet available, the biofilm-driven reactor from Jourdin et al. (2019) is used to fit the model and estimate the unknown kinetic parameters [20]. The model is then applied to and validated with experimental data obtained from other studies. First, the capacity of the model to successfully predict different operational conditions is shown by simulating the system from Jourdin et al. (2018) [21]. In this first simulation, the same reactor but operated under different dilution rates and feeding strategies is evaluated. Afterward, since not all reported MES reactors reach chain elongation and more than 75% of all MES studies have reported only acetate production [22], the ability of the model to simulate different product spectrum is also shown. For this purpose, the experimental data from the batch reactor used in Marshall et al. (2013) is used for validation [23].

## 2.2. Model Description

### 2.2.1. System Overview

The model consists of a bioelectrochemical reactor with multiple domains encompassing all subsequent mass balance equations, as well as all electrochemical and biological kinetic reactions. The four domains of the system modeled to simulate reactors from Jourdin et al. are shown in **Figure 2.1B**, namely the gas/liquid mass transfer compartment, the cathode biofilm, and both bulk liquid compartments on either side of the cathode/biofilm. The two domains of the modeled reactor from Marshall et al. can be found in **Figure 2S 1** in the Supplementary Material 2.7.1. All symbols used and their respective units can be found in the main text in **Table 2.1** and in the Supplementary Material 2.7.1. Assumptions for all cases are:

• The biofilm is a continuous phase, thus different microbial species and their distribution are neglected.

• All reactions occur in the biofilm only. Reactions occurring in the bulk liquid are neglected, as the prevalence of the biofilm over suspended cells was demonstrated on their investigation.

• Electrical resistances of the catholyte and the biofilm matrix can be neglected.

• Volumes of all compartments are constant.

• All liquid compartments are well mixed.

• The biofilm domain is also well-mixed (no concentration gradients, see section 2.3.3).

• Microorganisms accumulate in the biofilm domain and do not flow out (detachment from the biofilm is neglected).

• pH, electrical potential, and temperature are strictly controlled.

Simulations were performed with a set of mass balances including the exchange rate (flow in and out) from the continuous operation, the net rate of reactions in the biofilm, and the gas/liquid transfer of $CO_2$ (in detail in Supplementary Material 2.7.1). The gas/liquid mass transfer from the gas to the liquid phase was modeled with the overall gas/liquid mass transfer coefficient ($k_L a$). It is possible to simulate reactors with different geometries, cathode properties or cell cultures modifying the obtained mass balance equations. A general scheme of the microbial catalyst, with

all the relevant biological and electrochemical reactions is depicted in **Figure 2.1A**, and further described in sections 2.2.2 and 2.2.3.
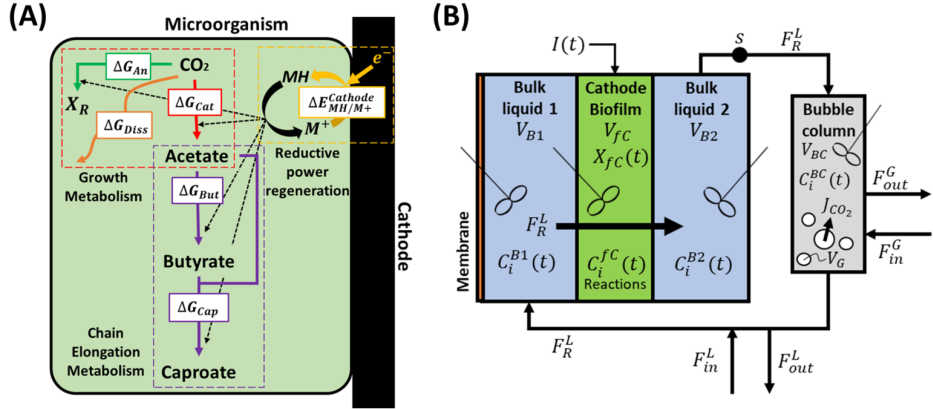


**Figure 2.1. (A)** Biological and electrochemical reactions occurring within a single cell. The energy generated during the reduction of carbon dioxide (catabolism) is used for biomass formation (anabolism), butyrate and caproate formation (chain elongation), and partly dissipated as heat. The reductive power is regenerated in the bioelectrochemical reduction of the oxidized mediator $M^+$ and the excess of reduced mediator is used in the chain elongation metabolism. **(B)** Model domains of the continuous reactor based on Jourdin et al. (2019) [20]. $CO_2$ is supplied in the external bubble column during liquid recirculation and the catholyte is forced through a porous biocathode.

### 2.2.2. Electrochemical Reactions

**Electron Transfer from Cathode to an Intracellular Electron Mediator**

In microbial electrosynthesis, electrons must be transferred from the surface of the cathode to the intracellular space of the microorganism likely via multiple transmembrane redox centers (e.g., cytochromes) [24]. This redox protein chain leads to the reduction of an intracellular redox mediator, which is then used by the microorganism in its metabolism [25]. For simplicity purposes and since intermediate processes are not expected to be limiting the electrochemical rate, the electron transfer between the cathode and the microorganism was assumed to occur by the direct reduction of an oxidized mediator species ($M^+$):

$$M^+ + H^+ + 2e^- \underset{k_e^r}{\overset{k_e^f}{\rightleftharpoons}} MH \tag{1}$$

The electrochemical rate $r_M^{elec}$ ($mol_{M^+} m_{fc}^{-3} s^{-1}$) for Eq. 1 is obtained with the Butler-Volmer equation (Eq. 2). This general model has been successful in the modelling of heterogeneous electron transfer between microorganisms and electrode in microbial fuel cell processes [25,26].

$$r_M^{elec} = k_e^f C_{M^+} C_{H^+} - k_e^r C_{MH} \tag{2}$$

The electrochemical rate coefficients, which account for the electrical potential of the electrode and the mediator, $k_e^f$ (Eq. 3) and $k_e^r$ (Eq. 4) are:

$$k_e^f = k_e^0 exp\left[-\alpha \frac{nF}{RT}(E_C - E_M)\right] \tag{3}$$

$$k_e^r = k_e^0 exp\left[(1 - \alpha)\frac{nF}{RT}(E_C - E_M)\right] \tag{4}$$

To date, the exact mechanism for extracellular electron transfer (EET) is largely unknown. A wide range of different mechanisms has been investigated, from direct electron transfer [27,28] to mediated processes [29,30]. The electron transfer mechanism can be highly dependent on the type of system being studied, hence the aforementioned mathematical expressions were chosen as they allow to mimic different EET mechanisms by adjusting the electrode and the mediator potentials.

## Current Density

The transfer of electrons from cathode to microorganism results in the observed electric current. This current is determined by a balance between the electrochemical reaction rate $r_M^{elec}$ (Eq. 2) and the biological conversion rate. In the present model, the current at the cathode is given by the electrochemical reduction of the redox mediator (Eq. 5). Since the electrochemical rate is defined per biofilm volume, a correction to account for the volume of the biocathode ($V_{fc}$) domain is included.
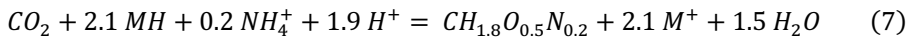
$$I = nF r_M^{elec} V_{fc} \tag{5}$$

### 2.2.3. Biological Reactions

### Microbial Metabolism

Acetate originates from $CO_2$, but the pathways for butyrate and caproate production in MES systems are largely unknown. Acetate elongation can occur via multiple pathways, including or not carbon dioxide utilization [21,31,32]. In addition, ethanol has been hypothesized to act as electron donor for the elongation of acetate into longer carboxylates [32–34]. Owing to the high complexity of mixed microbial communities, simplifications are needed when trying to model such environments. The present study approaches this simplification by encompassing all major metabolisms from different cells into one hypothetical black box organism. However, the addition of solventogenesis and chain elongation to the general growth metabolism would require prior knowledge of the exact ratios at which acetate, butyrate, caproate, and ethanol are produced [35,36]. Since these ratios are

not known, the metabolism of the modeled organism can be separated into four different steps, i.e., 1) the energy-generating catabolic reaction, 2) the energy-consuming anabolic reaction for biomass production, 3) the chain elongation metabolism, and 4) the electrochemical regeneration of the reductive power (**Figure 2.1A**). The use of a thermodynamic approach allows to account only for end products of the metabolism, bypassing intermediates like ethanol. Hence, for modeling purposes and since this information is currently not available for MES processes, a $CO_2$-independent acetate and butyrate elongation pathway not linked to growth is hypothesized. The model includes reaction rates for $CO_2$, acetate, butyrate, and caproate. Including reaction rates for compounds that have not been detected would lead to additional kinetic parameters, and these would be unidentifiable. The studies used in this work for parameter fitting and model validation did not detect ethanol or propionate, for example, so reaction rates for these compounds are not included here. To model studies that did measure concentrations of these compounds, model extension is needed.

The general growth stoichiometry of the proposed bacteria is then calculated following a thermodynamic state analysis [36]. From an energetic point of view, acetate is produced from carbon dioxide to generate energy for all the other reactions occurring within the cell ($\Delta G_{Cat}$). A part of that energy is used for butyrate ($\Delta G_{But}$) and caproate ($\Delta G_{Cap}$) production, as well as for biomass growth and cell maintenance reactions ($\Delta G_{An}$), whereas the rest is dissipated as heat ($\Delta G_{Diss}$). The biomass formula is assumed to be $CH_{1.8}O_{0.5}N_{0.2}$ [37,38]. The catabolic microbial reaction for carbon dioxide reduction to acetate (Eq. 6) and the anabolic reaction for growth (Eq. 7) can be written as follows:

$$2\,CO_2 + 4\,MH + 3\,H^+ = CH_3COO^- + 4\,M^+ + 2\,H_2O \tag{6}$$

$$CO_2 + 2.1\,MH + 0.2\,NH_4^+ + 1.9\,H^+ = CH_{1.8}O_{0.5}N_{0.2} + 2.1\,M^+ + 1.5\,H_2O \tag{7}$$
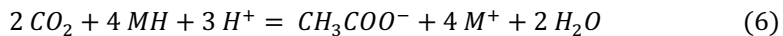
As explained previously, ethanol is not included in the elongation metabolism of the proposed bacteria and the reductive power is assumed to directly come from the redox mediator MH. Then, acetate (Eq. 8) and butyrate (Eq. 9) elongation reactions are described as:

$$2\,CH_3COO^- + 2\,MH + 3\,H^+ = C_3H_7COO^- + 2\,M^+ + 2\,H_2O \tag{8}$$

$$CH_3COO^- + C_3H_7COO^- + 2\,MH + 3\,H^+ = C_5H_{11}COO^- + 2\,M^+ + 2\,H_2O \tag{9}$$
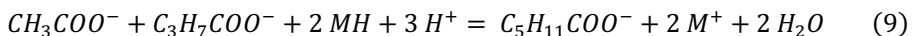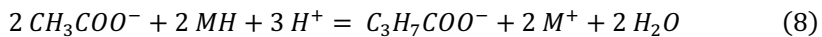
The Gibbs energies of reaction $\Delta G_{Cat}^0$, $\Delta G_{An}^0$, $\Delta G_{But}^0$ and $\Delta G_{Cap}^0$ are calculated using the values for the energy of formation obtained from [36], and adapted to reactor conditions (Supplementary Material 2.7.1). In this model, the mediator couple

MH/M⁺ is the only redox mediator species that limit the rate of the redox reactions of the modelled microorganism. The Gibbs energy of formation for this pair was estimated from the standard redox potential and adapted to reactor conditions, as described by Korth et al. (2015) [39]. In this study, the standard redox potential of NADH/NAD⁺ was chosen (in detail in the Supplementary Material 2.7.1).

The catabolic rate ($\lambda_{cat}$) is a factor representing how many times the catabolic reaction must occur to supply enough energy for the anabolic, elongation, and dissipation reactions. Using a dissipation energy for chemoautotrophic $CO_2$ reducing processes of $\Delta G_{Diss}^{CO_2} = 1076 \: kJ \: mol_X^{-1}$ [35], the catabolic rate (Eq. 10) is calculated:

$$\lambda_{cat} = \frac{\Delta G_{Diss}^{CO_2} + \Delta G_{An}}{-\Delta G_{Cat} + Y_{Ac}^{But}\Delta G_{But} + Y_{Ac}^{Cap}\Delta G_{Cap}} \qquad (10)$$

The thermodynamic yields $Y_{Ac}^{But}$ and $Y_{Ac}^{Cap}$ are calculated as the ratio between the energies of formation of both butyrate and caproate over acetate. The growth stoichiometry ($Y_i^{Met}$) is then obtained by combining both catabolic and anabolic reactions (Eq. 6 and Eq. 7) as $\lambda_{cat}Y_i^{Cat} + Y_i^{An}$, resulting in the following general metabolic reaction (Eq. 11):

$$-Y_{CO_2}^{Met} \: CO_2 - Y_{MH}^{Met} \: MH - Y_{NH_4^+}^{Met} \: NH_4^+ - Y_{H^+}^{Met} \: H^+$$
$$+Y_X^{Met} \: CH_{1.8}O_{0.5}N_{0.2} + Y_{Ac}^{Met} \: C_2H_3O_2^- + Y_{M^+}^{Met} \: M^+ + Y_{H_2O}^{Met} \: H_2O \qquad (11)$$
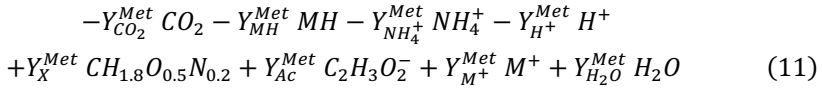
**Microbial Kinetic Equations**

A triple hyperbolic uptake equation accounting for both the carbon and nitrogen sources, as well as for the electron donor is used to describe the carbon dioxide specific uptake rate [40–42] (Eq. 12; Parameters in **Table 2.1**).

$$q_{CO_2} = q_{CO_2}^{max} \frac{C_{CO_2}}{K_{CO_2} + C_{CO_2}} \frac{C_{NH_4^+}}{K_{NH_4^+} + C_{NH_4^+}} \frac{C_{MH}}{K_{MH} + C_{MH}} \qquad (12)$$

The maintenance coefficient on $CO_2$ for anaerobic microorganisms, $m_{CO_2}$ ($mol_{CO_2} \: mol_X^{-1} \: h^{-1}$) is estimated with a temperature dependent Arrhenius-type equation (Eq.13) [43]. The specific biomass growth rate $\mu$ ($h^{-1}$) can then be described as a function of the carbon dioxide uptake and maintenance rates (Eq. 14).

$$m_{CO_2} = \frac{3.3}{\Delta G_{Cat}} exp\left[\frac{-69.4}{R}\left(\frac{1}{T} - \frac{1}{T_0}\right)\right] \qquad (13)$$

$$\mu = \frac{q_{CO_2} + m_{CO_2}}{Y_{CO_2}^{Met}} \qquad (14)$$

The specific elongation rates for butyrate and caproate production are then described using double and triple hyperbolic uptake equations, respectively. Jourdin et al. (2018) described a threshold concentration of acetate necessary for chain elongation to occur [21]. A follow-up study suggested that also a threshold concentration of butyrate for caproate production might exist [20]. To incorporate these threshold values into the model, the method proposed by Ribes et al. (2004) is applied to the hyperbolic specific uptake rates for both acetate (Eq. 15) and butyrate (Eq. 16) [44].

$$q_{But}^{elong} = q_{But}^{max} \frac{C_{Ac} - C_{Ac}^t w_{Ac}}{K_{Ac} + C_{Ac} - C_{Ac}^t w_{Ac}} Z_{Ac} \frac{C_{MH}}{K_{MH} + C_{MH}} \tag{15}$$

$$q_{Cap}^{elong} = q_{Cap}^{max} \frac{C_{Ac} - C_{Ac}^t w_{Ac}}{K_{Ac} + C_{Ac} - C_{Ac}^t w_{Ac}} Z_{Ac} \frac{C_{But} - C_{But}^t w_{But}}{K_{But} + C_{But} - C_{But}^t w_{But}} Z_{But} \frac{C_{MH}}{K_{MH} + C_{MH}} \tag{16}$$

Where $w_i$ and $Z_i$ are empirical sigmoidal functions used to ensure the rates have a smooth increase when the concentration reaches the threshold value $C_i^t$ and to avoid negative values if the threshold is yet to be achieved (Eq. 17 and Eq. 18).

$$w_i = \frac{1}{1 + exp[A_i(C_i^t - C_i)]} \tag{17}$$

$$Z_i = \frac{1}{1 + exp[A_i(T_i - C_i)]} \tag{18}$$

The additional tuning parameters $A_i$ and $T_i$ incorporated into the substrate uptake expressions have no biological meaning and are $10/C_i^t$ and $1.1C_i^t$, respectively. An elaborated discussion on how to determine these terms can be found in the original paper [44].

The overall coupling between substrate uptake, biomass growth, maintenance, and elongation reactions for all the remaining metabolites (excluding CO₂) is achieved by using a Herbert-Pirt relation (Eq. 19) and the general metabolic stoichiometry (Eq. 11).

$$q_i = Y_i^{Met} \mu - m_{CO_2} \frac{Y_i^{Cat}}{Y_{CO_2}^{Cat}} + Y_i^{But} q_{But}^{elong} + Y_i^{Cap} q_{Cap}^{elong} \tag{19}$$

Finally, biological rates for all chemical components are $r_i = q_i C_X$ and $r_X = \mu C_X$ for biomass.

**Carboxylic Acids Inhibition**

Carboxylic acids (CAs) are known for their toxicity, which can be attributed to their acid form. The acid form is able to diffuse across the cell membrane and deprotonate in the cytoplasm, generating a pH gradient. In order to maintain homeostasis, cells typically have to use membrane-bound ATPases to expel the excess of protons to the outside. As more ATP is redirected to keep this gradient under control, growth and production yields are substantially decreased [45,46]. Moreover, the longer the carbon chain, the higher the toxicity of the acid, since long CAs are able to damage the structure of the cell membrane [47].

When modelling microorganisms in MES systems, it is important to account for CAs inhibition. However, product inhibition kinetics in MES remains unknown to date, hence a generalized inhibition model is preferred here. In this study, a linear model is adopted [48]. Product inhibition effect is described by the linear term $(1 - C_i/C_i^*)$, where $C_i^*$ $(mol\ m^{-3})$ refers to the critical concentration at which the whole metabolism is halted due to the toxicity of the produced compound. Acetate, butyrate, and caproate inhibition terms are then added to the carbon dioxide uptake rate Eq. 12 and to the elongation rates Eq. 15 and Eq. 16 as follows:

$$q_{CO_2} = q_{CO_2}^{max} \frac{C_{CO_2}}{K_{CO_2} + C_{CO_2}} \frac{C_{NH_4^+}}{K_{NH_4^+} + C_{NH_4^+}} \frac{C_{MH}}{K_{MH} + C_{MH}} \left(1 - \frac{C_{Ac}}{C_{Ac}^*}\right)\left(1 - \frac{C_{But}}{C_{But}^*}\right)\left(1 - \frac{C_{Cap}}{C_{Cap}^*}\right) \quad (20)$$

$$q_{But}^{elong} = q_{But}^{max} \frac{C_{Ac} - C_{Ac}^t w_{Ac}}{K_{Ac} + C_{Ac} - C_{Ac}^t w_{Ac}} Z_{Ac} \frac{C_{MH}}{K_{MH} + C_{MH}} \left(1 - \frac{C_{Ac}}{C_{Ac}^*}\right)\left(1 - \frac{C_{But}}{C_{But}^*}\right)\left(1 - \frac{C_{Cap}}{C_{Cap}^*}\right) \quad (21)$$

$$q_{Cap}^{elong} = q_{Cap}^{max} \frac{C_{Ac} - C_{Ac}^t w_{Ac}}{K_{Ac} + C_{Ac} - C_{Ac}^t w_{Ac}} Z_{Ac} \frac{C_{But} - C_{But}^t w_{But}}{K_{But} + C_{But} - C_{But}^t w_{But}} Z_{But} \frac{C_{MH}}{K_{MH} + C_{MH}}$$
$$\left(1 - \frac{C_{Ac}}{C_{Ac}^*}\right)\left(1 - \frac{C_{ut}}{C_{But}^*}\right)\left(1 - \frac{C_{Cap}}{C_{Cap}^*}\right) \quad (22)$$

### 2.2.4. Simulation and Model Fitting Procedures

The kinetic maximum specific rates $q_{CO_2}^{max}$, $q_{But}^{max}$ and $q_{Cap}^{max}$ and the concentration thresholds $C_{Ac}^t$ and $C_{But}^t$ have not been experimentally determined in MES to date. Therefore, they were found by minimizing the residual sum of squares when fitting bulk concentrations of acetate, butyrate, and caproate over time. In this work, a residual is the difference between the experimental measurement from Jourdin et al. (2019) FTR2 reactor and the calculated value for that measurement obtained from the model [20]. As the model is a non-linear system of equations, a non- linear least-squares regression was used. The minimization was performed using the Nelder-Mead method as implemented in MATLAB.

**Table 2.1.** Input parameters used in the fitting of the model with their symbols, values, and units.

| Parameter | Symbol | Case value | Units | Source |
|---|---|---|---|---|
| *Thermodynamics and microbial kinetics* | | | | |
| Standard Gibbs energy of dissipation for $CO_2$ | $\Delta G_{Diss}^{CO_2}$ | 1076 | $kJ/mol_x$ | [35] |
| Standard Gibbs energy of M⁺/MH | $\Delta G_{(M^+/MH)}^0$ | -21.85 | $kJ/mol_{(M^+/MH)}$ | Adapted from [39] |
| Half-saturation constant for $CO_2$ | $K_{CO_2}$ | 3.8 | $mol/m^3$ | [49] |
| Half-saturation constant for $NH_4^+$ | $K_{NH_4^+}$ | 0.05 | $mol/m^3$ | [50] |
| Half-saturation constant for MH | $K_{MH}$ | 0.1 | $mol/m^3$ | [39] |
| Half-saturation constant for Acetate | $K_{Ac}$ | 0.27 | $mol/m^3$ | [51] |
| Half-saturation constant for Butyrate | $K_{But}$ | 0.076 | $mol/m^3$ | [52] |
| Critical concentration for Acetate | $C_{Ac}^*$ | 800 | $mol/m^3$ | [53] |
| Critical concentration for Butyrate | $C_{But}^*$ | 285 | $mol/m^3$ | [54] |
| Critical concentration for Caproate | $C_{Cap}^*$ | 170 | $mol/m^3$ | [47] |
| | | | | |
| *Electrochemical kinetics* | | | | |
| Standard heterogeneous electron transfer rate | $k_e^0$ | 0.03 | $1/s$ | [55] |
| Transfer coefficient | $\alpha$ | 0.5 | - | [25] |
| Standard redox potential of M⁺/MH | $E_M$ | -0.32 | V (SHE) | [56] |
| Cathode potential | $E_C$ | -1.2 | V(SHE) | [20] |
| Number of electrons transferred | n | 2 | $mol_{e^-}/mol_{(M^+/MH)}$ | From Eq.1 |
| | | | | |
| *Bulk liquid* | | | | |
| Bulk liquid volume | $V_T^C$ | 370 | mL | [20] |
| Bubble column volume | $V_{BC}$ | 280.9 | mL | [20] |
| Dilution rate | $D_R^L$ | Variable | $1/d$ | [20] |
| H⁺ concentration | $C_{H^+}^B$ | $10^{-5.8}$ | mol/L | [20] |
| Gas-liquid mass transfer coefficient | $k_L a$ | 2.5 | $1/h$ | Calculated from [20] |
| Initial concentrations | | | | |
| Carbon dioxide | $C_{CO_2}^0$ | 0 | $mol/m^3$ | [20] |
| Acetate | $C_{Ac}^0$ | 30 | $mol/m^3$ | [20] |
| Butyrate | $C_{But}^0$ | 0 | $mol/m^3$ | [20] |
| Caproate | $C_{Cap}^0$ | 0 | $mol/m^3$ | [20] |
| | | | | |
| *Biofilm* | | | | |
| Biocathode volume | $V_{fc}$ | 25.5 | mL | Adapted from [20] |
| Initial biomass concentration | $C_X^0$ | 5.2 | $mol/m^3$ | Adapted from [20] |
| Initial concentration of MH + M⁺ | $C_{MH/M^+}^{fc}$ | 20 | $mol/m^3$ | [39] |
| | | | | |
| *Constants* | | | | |
| Faraday constant | $F$ | 96485.34 | C/mol | |
| Universal gas constant | $R$ | 8.31 | J/(mol K) | |
| Standard temperature | $T_0$ | 298 | K | |
| Working temperature | $T$ | 305 | K | [20] |

## 2.3. Results and Discussion

### 2.3.1. Model Fitting

To obtain the necessary parameters for the kinetic equations, the model was fitted with the experimental results obtained by Jourdin et al. (2019) [20]. That system was operated in continuous mode with continuous $CO_2$ sparging. Since the gas-liquid mass transfer coefficient $k_L a$ for $CO_2$ was not reported in the original work, its value was approximated from the reported inorganic carbon concentrations and found to be of the same order of magnitude as those reported on similar sparging mechanisms, i.e. 2.5 $h^{-1}$ [57]. The hydraulic retention time (HRT), used to determine the dilution rate, was first increased from 4 to 8 days and then from 8 to 14 days. The best fitting results are shown in **Figure 2.2A**, together with the organics concentration measured experimentally by Jourdin et al. (2019) [20]. The model is able to follow the main trend of the experimental results. For the data points, the population standard deviation of the model was 31.7 mmol/L for acetate, 14.56 mmol/L for butyrate, and 3.65 mmol/L for caproate. The simulation shows deviations that can be attributed to the previously introduced simplifications on the model, such as exclusion of the dynamics occurring within a mixed culture. No special effect of increasing the HRT can be observed. The kinetic maximum specific rates $q_{CO_2}^{max}$, $q_{But}^{max}$ and $q_{Cap}^{max}$ and the concentration thresholds $C_{Ac}^{t}$ and $C_{But}^{t}$ were found to be -0.307 $mol_{CO2}/(mol_x\ h)$, $2.12 \times 10^{-2}\ mol_{But}/(mol_x\ h)$, $4.64 \times 10^{-3}$ $mol_{Cap}/(mol_x\ h)$, 123 $mmol_{Ac}/L$ and 43 $mmol_{But}/L$, respectively. There is a lack of reported values in MES for these kinetic parameters, hence it is difficult to assess the values obtained here. Nagarajan et al. (2013) used a $CO_2$ specific uptake rate on the same order of magnitude as the one obtained in this study, of -0.2 $mol_{CO2}/(mol_x$ h), when characterizing acetogenic metabolism by using a genome-scale metabolic reconstruction approach; however they failed to confirm the value experimentally [58].

The computed substrate concentrations over time (**Figure 2.2B**) show an initial decrease, with a later stabilization for $CO_2$ and a slight increase for $NH_4^+$. This profile can be related to the developing cell population, with an initial exponential growth phase and a later plateauing when steady-state is reached (**Figure 2.2C**) [40,59]. According to the model, cells use the nitrogen source for growth, whereas the carbon source is used for both growth, maintenance, and elongation reactions. The later ammonium concentration increase can then be attributed to biomass growth slowing down, and the stabilization of the carbon dioxide concentration to its continuous usage in maintenance and elongation reactions.

The maximum growth rate (see Supplementary Material 2.7.2) was calculated to be on average 0.12 d$^{-1}$ and within the range of typical reported growth rates for acetogens (0.1 to 0.4 d$^{-1}$) [52,53].
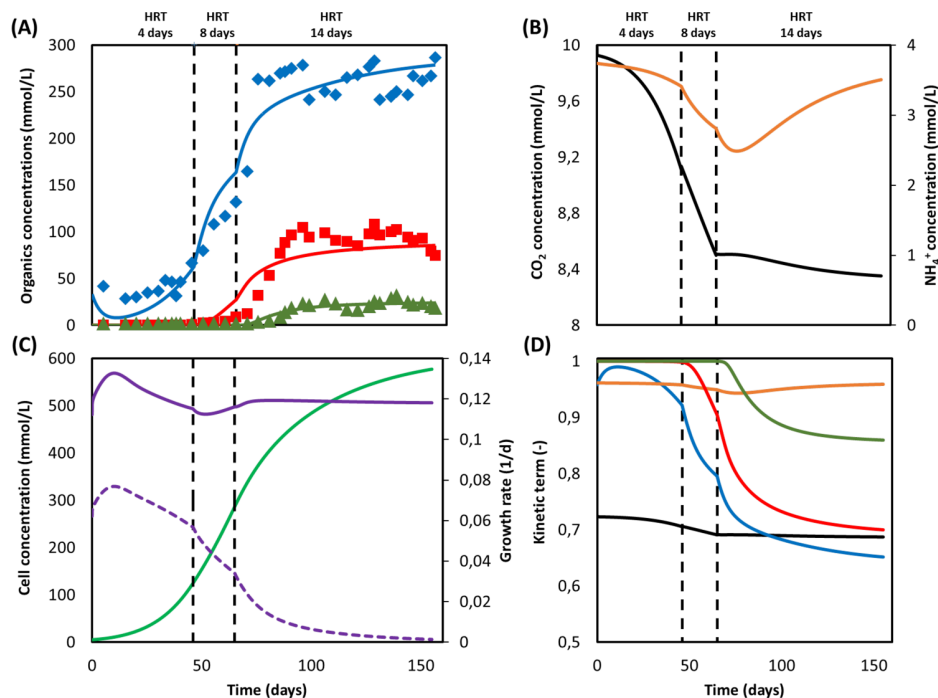


**Figure 2.2.** Model fitting results (lines) and experimental data Jourdin et al. (2019) [20] (markers). **(A)** Concentration of acetate (blue), butyrate (red) and caproate (green); **(B)** Substrate concentration of $CO_2$ (black) and $NH_4^+$ (orange); **(C)** Cell concentration (light green), maximum growth rate (purple), and growth rate (purple dashed line); **(D)** Kinetic uptake terms of $CO_2$ (black) and $NH_4^+$ (orange), and kinetic product inhibition terms of acetate (blue), butyrate (red), and caproate (dark green). The vertical dashed lines represent the time when the hydraulic retention time was increased.

According to the model, none of the substrates was depleted. To study which factor is mainly controlling biological rates, the kinetic hyperbolic uptake and product inhibition terms from Eq. 20, 21, and 22 are graphically depicted over time in **Figure 2.2D**. These terms can be used as indicators for metabolic limitations, being responsible for the deviations between the theoretical maximum rates and the observed ones [60–62]. During the first 100 days of the experiment, carbon dioxide was the main factor limiting microbial kinetics, with a decrease of the maximum rate of about 30%. After day 100, product inhibition became the main limiting step, especially due to high acetate and butyrate concentrations. The initial carbon dioxide limitation can be attributed to its relatively high half-saturation constant of 3.8 mmol/L [63], resulting on a fast drop of its uptake rate even when dissolved $CO_2$ is

still far from being depleted. A combination of poor gas-liquid mass transfer and a low gas inlet $CO_2$ partial pressure were the limiting steps during this first period.
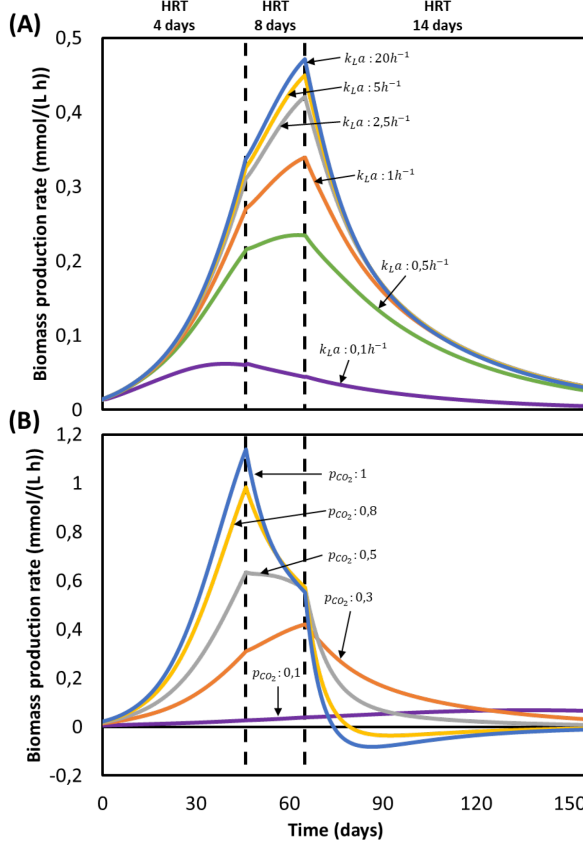


**Figure 2.3.** Computed biomass production rate in time for the reactor from Jourdin et al. (2019) [20]: **(A)** at different gas-liquid mass transfer coefficients ($k_La$) with $p_{CO_2} = 0.3$ and **(B)** at different gas $CO_2$ partial pressures ($p_{CO_2}$) with $k_La = 2.5h^{-1}$. No experimental data available.

The effect of changing these input parameters is depicted in **Figure 2.3**. Increasing the $k_La$ results on a higher biomass production rate, as $CO_2$ is dissolved faster into the liquid (**Figure 2.3A**). This improvement decreases the higher the transfer coefficient. At a certain point, the rate of the gas-liquid mass transfer is sufficient to supply $CO_2$ faster than what the microorganisms consume. Then, the uptake rate starts limiting the system. After an initial growth phase, all rates sharply decrease. This effect is induced by the increasing carboxylates concentrations and the subsequent product inhibition on cell metabolism (**Figure 2S 2A-C** in the Supplementary Material 2.7.3). The $CO_2$ partial pressure ($p_{CO_2}$) of the feed gas determines the saturation concentration at which carbon dioxide can be dissolved

into the liquid [64]. Increasing this partial pressure substantially improves biomass production rate, as shown in **Figure 2.3B**. In this case, the positive effect is because of a higher driving force for gas-liquid mass transfer, i.e. the equilibrium concentration of $CO_2$ with a $p_{CO_2}$ of 1 is of 34 mmol/L, three times higher than with a partial pressure of 0.3. The higher the partial pressure of $CO_2$ used the more pronounced the effect of product inhibition is. This can be attributed to the microbial dynamics during the initial part of the run, reaching the carboxylates' inhibiting concentrations at a faster rate with higher $CO_2$ fraction in the inlet gas (**Figure 2S 2D-E** in the Supplementary Material 2.7.3).

### 2.3.2. Model Validation: Prediction vs. Experimentation

A wide range of biological systems and operational conditions applied to MES are described in literature. In this paper, and in order to study the prediction capabilities of the model, the work of Jourdin et al. (2018) [21] and Marshall et al. (2013) [23] were chosen because of their detailed experimental descriptions and model input parameters availability. The model structure is largely the same as in the fitting case previously discussed. Any model parameters modification done to reflect differences between the studied systems can be found in the Supplementary Material 2.7.4 and 2.7.5.

**CO₂ Supply Strategy Greatly Impacts Reactor Performance**

Simulation results for the system utilized by Jourdin et al. (2018) [21] can be found in **Figure 2.4**. The reactor was operated in fed-batch mode under a discontinuous $CO_2$ sparging regime during periods I and III, in batch mode with continuous sparging of $CO_2$ during period II and in continuous mode with continuous sparging of $CO_2$ during period IV. When comparing the organics concentration obtained from the simulation with the experimental data, although showing a similar trend, the model predictions deviate from the experimental results (**Figure 2.4A**). Calculated acetate and n-butyrate concentrations are substantially higher, especially during periods II and III. For the data points, the population standard deviation of the model was 50.11 mmol/L for acetate, 10.79 mmol/L for butyrate, and 1.13 mmol/L for caproate.

This overshooting contrasts with the good description by the model of the current consumption, as can be seen in **Figure 2.4E**. This good match between simulation and experimental data on the electron consumption, together with the mismatch on organics prediction indicates an overestimation of the coulombic efficiency. These differences could be attributed to hydrogen production, as Jourdin et al. (2018) reported electron recoveries that ranged from 20% to 70% during the first three

periods of the run and from 60% to 100% during the last period [21]. This dynamic behavior between carboxylates production and hydrogen evolution is not included in the present model. During the fitting in section 2.3.1, the biological rates from the model were calculated to match the organics concentration evolution over time from the experimental results. As a consequence, the coulombic efficiency of the system leading to electron losses was not taken into account. When the experimentally reported recoveries are applied to the organics concentration predicted by the model, a better representation of the experimental data is obtained (dashed lines in **Figure 2.4A**). The population standard deviation of the adjusted model was 32.09 mmol/L for acetate, 3.62 mmol/L for butyrate, and 0.68 mmol/L for caproate. This highlights that the model presented in this paper is able to predict the performance of a MES system with a 100% coulombic efficiency, giving for a certain set of conditions an approximation of what the best possible outcome can be.

As can be seen in **Figure 2.4B**, carbon dioxide was periodically depleted in periods I and III as the multiple sparging periods were not able to keep up with its consumption rate. When the feeding strategy was changed to continuous addition in period II, an initial decrease with a later slight increase of $CO_2$ concentration is observed, but no depletion occurred. The later increase of the $CO_2$ concentration can be attributed to the plateauing of the biomass concentration (see **Figure 2.4C**) [59], as the model shows that the ammonium concentration was continuously decreasing and close to being depleted. No nitrogen limitation was observed. Ammonium concentration slightly decreased but stayed high during period I, severely decreased in period II and increased during period III. This later increase can be attributed to the carbon dioxide depletion and the subsequent halt of cell growth, inducing cell death and a decrease of the biomass concentration (**Figure 2.4C**) [65]. During period IV, when the operational mode was switched from batch to continuous, i.e., nutrients and $CO_2$ were continuously added, $CO_2$ concentration shows an initial decrease with a later stabilization when the steady-state is reached. On the other hand, $NH_4^+$ concentration peaks at the beginning and then slowly stabilizes. This sharp increase is attributed to the accumulation produced by the constantly added fresh medium.
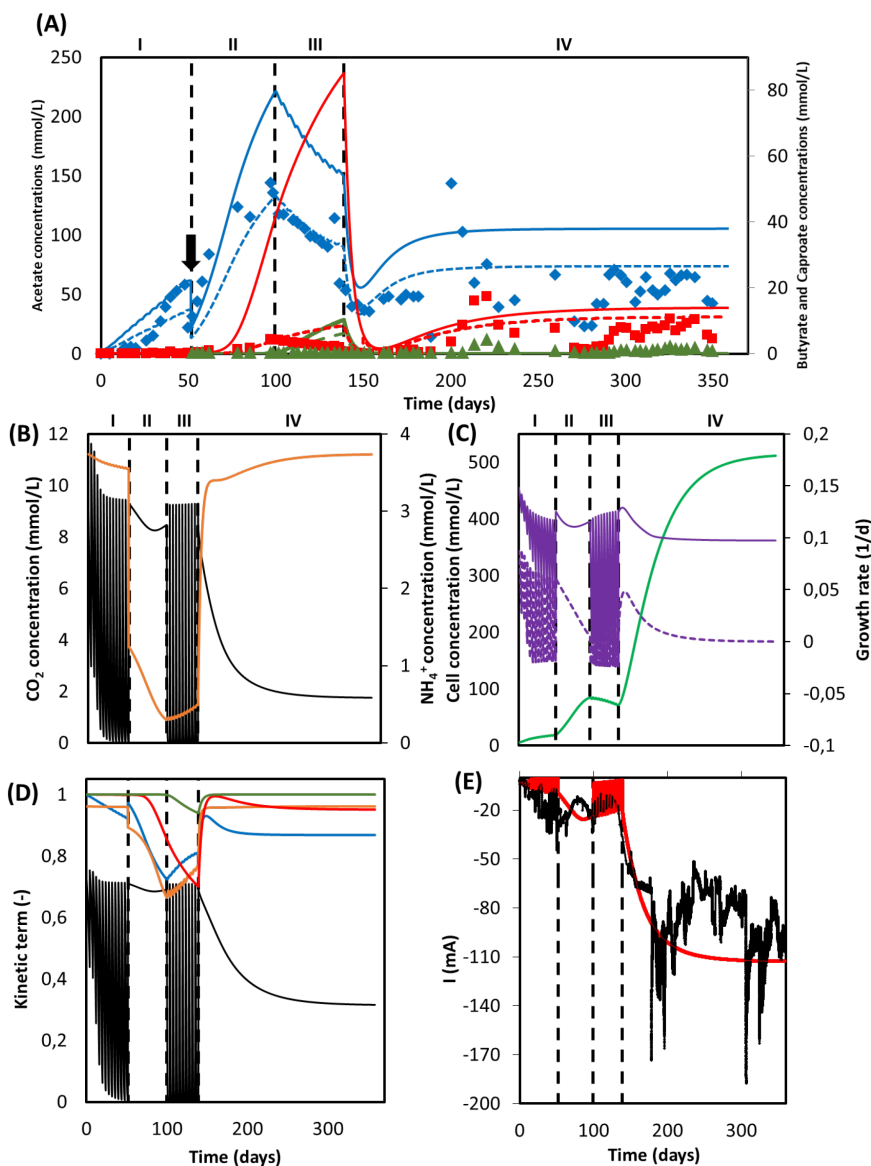
**Figure 2.4.** Simulation results of a MES system with changing feed strategies and operational modes. **(A)** Predicted concentration of acetate (solid blue line), n-butyrate (solid red line) and n-caproate (solid dark green line) and experimental data from Jourdin et al. (2018) [21] of acetate (blue diamonds), n-butyrate (red squares), and n-caproate (dark green triangles). Adjusted concentrations with reported electron recoveries are shown with dashed lines for acetate (blue), n-butyrate (red), and n-caproate (dark green); **(B)** Concentration of $CO_2$ (black) and $NH_4^+$ (orange); **(C)** Microbial cell concentration (light green), calculated maximum growth rate (purple), and growth rate (purple dashed line); **(D)** Kinetic hyperbolic uptake terms of $CO_2$ (black) and $NH_4^+$ (orange), and kinetic product inhibition terms of acetate (blue), n-butyrate (red), and n-caproate (dark green); **(E)** Predicted (red) and experimental (black) current. The vertical dashed lines represent the time when reactor operation was switched from fed-batch to batch and from batch to continuous mode. The black arrow indicates when substantial leakage of the medium occurred.

The depletion of carbon dioxide during fed-batch periods completely stopped the growth metabolism of the cells (**Figure 2.4D**). Even though the nitrogen source could be expected to become the bottleneck of the system during period II, the uptake of $CO_2$ was still the rate limiting microbial kinetics. This can be attributed to the low ammonium half-saturation constant, buffering the effect of a low concentration on the overall kinetics. Again, when the operational mode was switched to continuous in period IV and the steady-state was reached, the $CO_2$ uptake term was the limiting factor, decreasing the maximum rate by about 65%. In summary, it is clear that the limiting step during the entire duration of Jourdin's experiment was the supply of carbon dioxide, pointing out to the importance of not only the amount of $CO_2$ added but also how this addition is carried out.

## Continuous Operation Benefits Biofilm Growth

A second simulation to reproduce the set of data obtained by Marshall et al. (2013) [23] was performed, and the results obtained from the model are showed in **Figure 2.5**. A series of consecutive batches was simulated. After every batch, the catholyte was replaced by fresh medium while the biomass remained attached to the electrode material. The first two batches (periods I and II) operated under a discontinuous $CO_2$ sparging regime, whereas the third batch (period III) was continuously sparged with pure $CO_2$. The model properly predicts the acetate concentration profile obtained experimentally (**Figure 2.5A**). For the data points, the population standard deviation of the model was 1.94 mmol/L for acetate. The elongation thresholds from Eq. 15 and Eq. 16 allowed to properly reproduce a system where only acetate was produced.

Carbon dioxide concentration oscillated during the intermittent sparging phases in periods I and II and showed a subtle decrease during period III, but was far from being depleted (**Figure 2.5B**). However, it should be stressed that the actual $k_L a$ of their sparging method was not reported and thus assumed to be the same as in Jourdin et al. (2019) [20]. Therefore, it is difficult to conclude the system was not $CO_2$ limited. $NH_4^+$ concentration showed a batch-like behavior, decreasing faster in every consecutive batch. This is attributed to the increasing biomass concentration and its exponential behavior, as according to the model nitrogen consumption is strictly bounded to microbial growth (**Figure 2.5C**). Although nitrogen uptake rate was exponentially increasing, $NH_4^+$ was far from depletion.
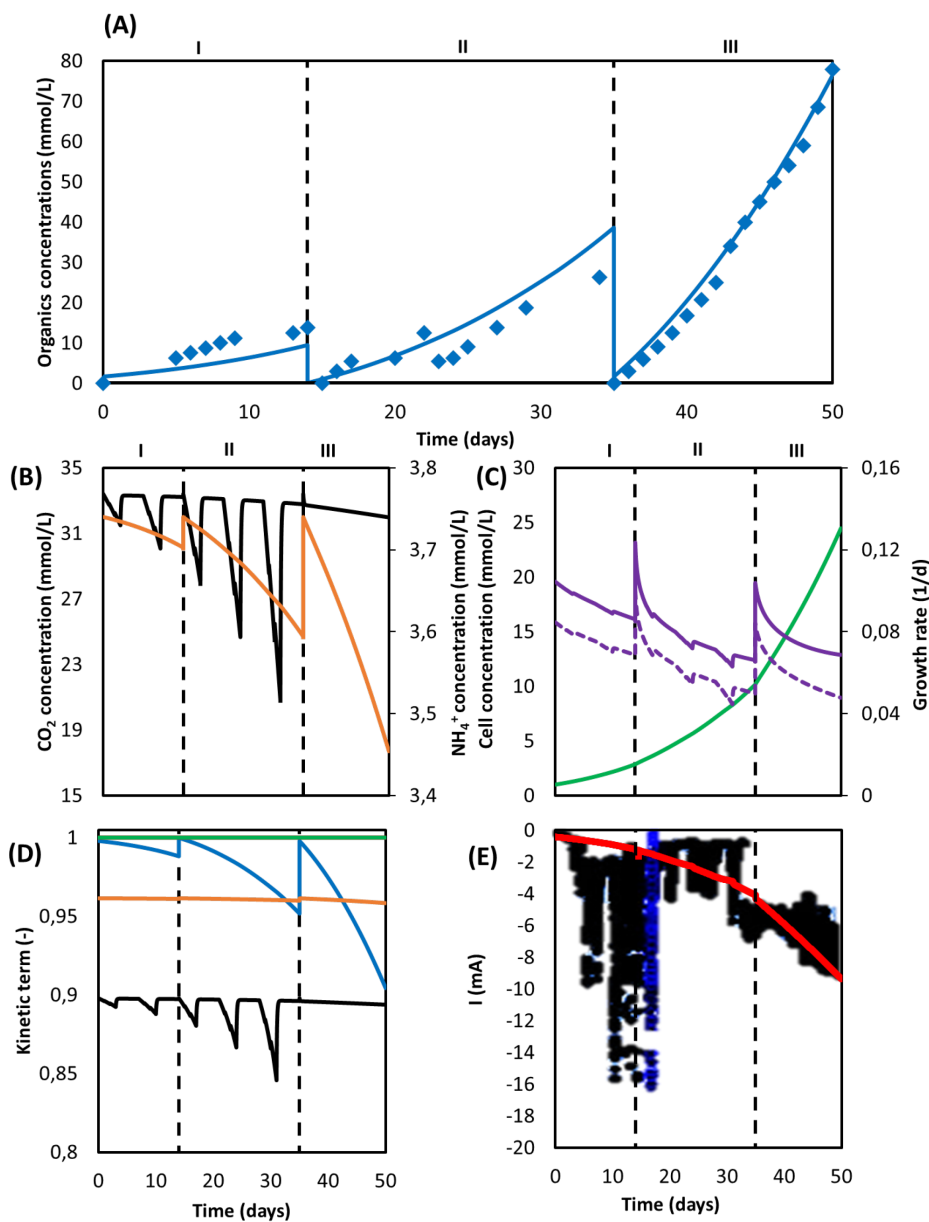
**Figure 2.5.** Computed simulation results of a MES system with three consecutive batches. **(A)** Predicted concentration of acetate (blue line) and experimentally determined acetate concentration from Marshall et al. (2013) [23] (blue diamonds); **(B)** Concentration of $CO_2$ (black) and $NH_4^+$ (orange); **(C)** Microbial cell concentration (light green), calculated maximum growth rate (purple), and growth rate (purple dashed line); **(D)** Kinetic hyperbolic uptake terms of $CO_2$ (black) and $NH_4^+$ (orange), and kinetic product inhibition term of acetate (blue); **(E)** Predicted (red) and experimental (black) current. The vertical dashed lines represent the three different batch operations.

The biomass concentration obtained after 50 days (25 mmol/L) is five times lower than the amount produced in a continuous reactor with constant $CO_2$ sparging (125 mmol/L), as can be seen when comparing **Figure 2.2C** and **Figure 2.5C**. The effect of the dilution rate on the biomass growth is shown in **Figure 2.6**. The higher biomass concentration achieved with biofilm-driven systems operating in continuous mode can be attributed to the exchange flow. Since microorganisms grow attached to the electrode, and are therefore not affected by this dilution rate, the difference in growth rate is caused by the other dilute species concentrations in the system. In continuous operation, nutrients are constantly replenished while products are removed from the reactor, diminishing the effects of low substrate concentrations and product inhibition [66,67]. However, in a batch system like the one used by Marshall et al. (2013) [23], nutrients deplete and products accumulate faster over time.

The kinetic parameters are presented in **Figure 2.5D**. Carbon dioxide uptake was the limiting kinetic rate during all three batches. During the last intermittent sparging phase in period II a total decrease of the maximum uptake rate up to 15% was reached, but stabilized at 10% in period III when continuous gas sparging was applied. Although a 30% decrease on the carbon concentration during period II is observed in **Figure 2.5B**, the use of pure $CO_2$ by Marshall helped to mitigate the effect on the microbial kinetics. The amount of carbon dioxide that can be dissolved in the system increases linearly with the $CO_2$ partial pressure used in the gas [64]. A 3.3 times higher $CO_2$ liquid concentration was obtained by the use of 100% $CO_2$ as feeding gas when compared with the 30% used by Jourdin et al. (2018) [21]. This higher concentration mitigated the decrease of the hyperbolic term for $CO_2$ uptake and avoided a more severe rate inhibition by the carbon source. Since the limiting effect of $CO_2$ and other chemical species in microbial kinetics is low, it is likely that the reactor was limited by the absolute amount of biomass in the system.

The current in periods II and III is correctly described by the model, as can be seen in **Figure 2.5E**. However, during the first period, predictions substantially deviate from the experimental values, with the calculated ones being lower than the ones observed by Marshall. Again, this deviation can be attributed to hydrogen and other by-products formation, as side-reactions are not accounted for in the current model. Microbial attachment and biofilm formation can be a slow process in MES systems, as bacteria do not obtain much energy from $CO_2$ reduction [68]. Hence, it is likely the case that during the first batch, as the biomass was starting to colonize the cathode, electrons were redirected toward hydrogen evolution. When cell concentration further increased, these electrons started being used in microbial

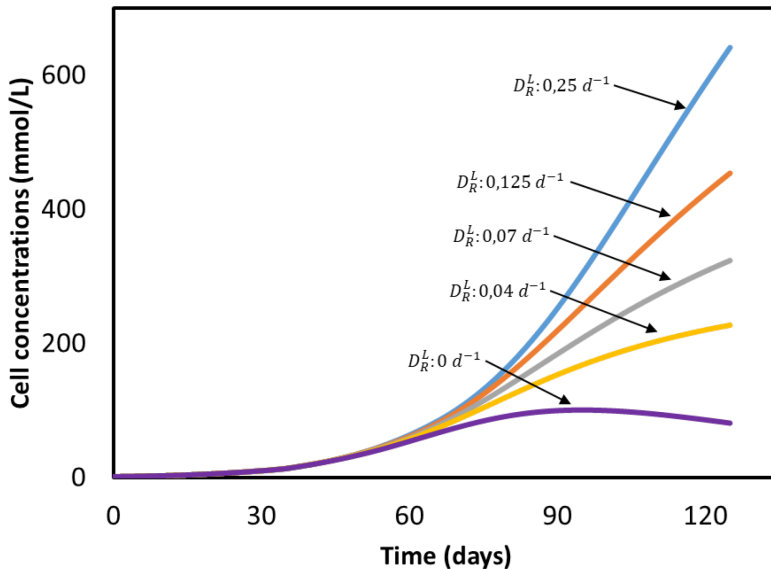reactions instead, giving the initial increase in the cathodic current observed at the beginning of period II.



**Figure 2.6.** Cell concentrations in time at different dilution rates ($D_R^L$) based on the system from Marshall et al. (2013) [23]. All input parameters are the same between simulations, with the exception of the dilution rate. No experimental data available.

### 2.3.3. Model Assumptions Evaluation

#### Concentration Gradients Over the Reactor

The model assumes no concentration gradients in the individual domains. Hence, concentration steps occur only between the domains or at the inflow. To support the assumption that gradients are negligible, the magnitude of the concentration steps will be discussed. Experimental measurements were performed at the sampling port (S in **Figure 2.1B**), thus computed concentrations refer to those leaving the second bulk liquid compartment ($C_i^{B2}$). Individual mass balances over each domain, together with an explanation on how the concentration gradients were calculated can be found in the Supplementary Material 2.7.6. Taking into consideration all compounds present in the system, carbon dioxide and protons are the ones expected to have the highest concentration steps along the reactor.

First, we focus on carbon dioxide. It is consumed by the microorganisms in the biofilm domain and transfers from the gas phase to the bulk liquid in the bubble column. Results obtained for $CO_2$ concentration gradients over the entire duration of Jourdin et al. (2019) [20] experiment are shown in **Figure 2.7**. Positive values

indicate a concentration increase between the previous and the current compartment, whereas a negative value refers to consumption. In no case the concentration difference exceeds $\pm$ 1.5%. This is attributed to the small ratio between the dilution flow rate of 0.018 mL/min and the recirculation rate of 200 mL/min. The characteristic $CO_2$ reaction time is estimated to be 4 min, while the residence time of the convective flow is 0.13 min (Supplementary Material 2.7.7). The ratio between these times causes overall concentration changes in the system to become significant after multiple recirculations rather than after a single pass through the biofilm domain. Therefore, for the purpose of this model $CO_2$ concentration gradients in the reactor domains can be neglected.
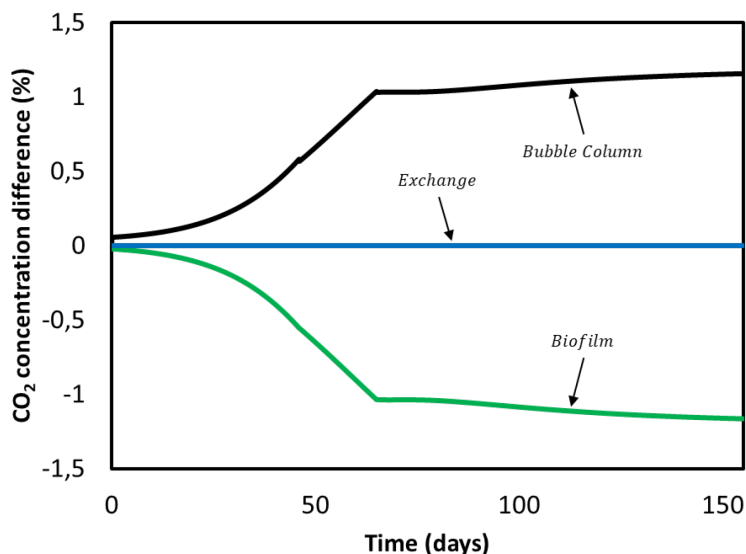


**Figure 2.7.** $CO_2$ concentration difference between domains during Jourdin et al. (2019) [20] experiment.

### pH at the Biofilm

The pH of a biologically active cathodic chamber is highly dependent on the acid-base reaction equilibria. $CO_2$ and all products accounted for in the current model behave as acid. In addition, the presence of a buffer must also be taken into consideration. It is therefore the balance between these production and consumption processes, that determines local pH gradients. In the present study, pH was assumed to be constant but since it has a great influence on both electrochemical and biological reactions, this assumption needs to be further investigated.

Bulk pH is strictly monitored and controlled by acid and base addition, therefore gradients due to protons diffusing from anode to biofilm can be neglected. However, reactions are happening within the biofilm and not in the liquid bulk, therefore a gradient might still be present at the vicinity of the electrode. An estimation of both characteristic reaction and diffusion times for $CO_2$, $H^+$, and the buffer compound was used to determine if large pH gradients would be present in the biofilm. These calculations and respective explanations can be found in the Supplementary Material 2.7.7. Results indicate that although $H^+$ ions are not able to diffuse into the biofilm quick enough, the presence of a buffer allows to compensate for the consumed $H^+$ in the biofilm by a buffering reaction with a reaction time in the same order of magnitude as for $CO_2$. According to the calculated diffusion and reaction times, $CO_2$ diffusion slowed down the biological reaction, which at the same time limited the proton consumption rate by the microorganism. The protonated buffer compound diffusion through the biofilm and buffering reaction would then have to keep up to effectively control pH. By analogy to the case treated by Vander Wielen et al. (1997), the mentioned decrease in the general metabolic rate may have been sufficient to allow the buffer to prevent large pH gradients [69]. A real biofilm is not homogeneous, and large gradients might occur at conditions different from those simulated here. Experimental data on pH values throughout the biofilm are required to validate the calculations.

**Potential Model Improvements**

Only one bacterial population has been included in this model, even though the simulated reactors were systems working with mixed cultures. Therefore, the model could be expanded to include multiple microorganisms with differentiated metabolisms [70,71]. As an example, solventogenesis (i.e., ethanol production from acetate) and chain elongation could be described independently from acetogenesis, allowing a deeper investigation of possible interactions between intermediate compounds, substrates, and microorganisms. It could also lead to a better understanding of which metabolic routes are being used by microorganisms to reduce $CO_2$ into longer chain products such as caproate.

As previously described, pH gradients and other chemicals' gradients should be further investigated for biofilm-driven systems. The addition of acid-base equilibria, hydrogen evolution, and electromigration would allow to better understand gradients at the biofilm level, potentially giving additional insights on rate limiting processes. These gradients could also help to understand biofilm development and biofilm/planktonic cells dynamics. Moreover, mass and ion transport can be expected to become of paramount importance as MES current density and microbial

productivity continue to increase [5]. In this sense, extending the model to a multidimensional model such as the ones developed in Picioreanu et al. (2007), Picioreanu et al. (2010) and Bottero et al. (2013) for microbial fuel cells could be interesting for this purpose [72–74].

The use of a product inhibition model is necessary to account for the inherent toxicity of the produced carboxylates. Even though the model used in this paper gave good results, it should be expanded and validated with experiments in which products have been added to the inflow. This would give a better and more tailored description of product toxicity within these systems, and subsequently a better understanding of chain elongation metabolism and kinetics.

### 2.3.4. Model Implications

Simulations done in this work suggest that $CO_2$ can limit the rate of microbial electrosynthesis. Carbon dioxide is the main substrate and the only carbon source in most MES reactors, hence its concentration has a great impact on cell kinetics. Its relatively high half-saturation constant and low solubility make microorganisms very susceptible to small changes in its dissolved concentration. The model indicates that the use of pure $CO_2$ as feeding gas can mitigate this effect, as shown experimentally in Rojas et al. (2021) [75]. However, it is important to note here that avoiding a kinetic limitation may not be enough to substantially increase productivity, since $CO_2$ diffusion might become the limiting step at some point. Results also indicate not to underestimate the critical effect of the $CO_2$ delivery strategy on reactor performance [76]. In MES studies, mass transfer coefficients are hardly ever reported, therefore it is difficult to conclude that poor $CO_2$ delivery systems are one of the reasons why obtained production rates are still low across the field [6]. Regardless of the supply method used, its mass transfer capability should always be assessed. The model developed in this work can be used to determine the minimum mass transfer capability required to avoid kinetic limitations by the supply method. By ensuring that the used system is able to deliver enough $CO_2$ to sustain a highly active microbial population, a better understanding can be achieved of which steps are intrinsically limiting steps in said MES processes.

To date, most MES studies have been performed under batch conditions and not many researchers used a continuous reactor for reducing $CO_2$ [5,77–81]. The model indicates that the continuous mode enhances cell growth, hence it might be one of the reasons why dense biofilms have been mainly obtained with this type of reactors. This can be attributed to a selective pressure that benefits attached cells since under a continuous operation, planktonic populations are easily washed out the reactor.

However, biofilm development is subject to multiple parameters, and the operational mode is just one of them. It has to be noted that increasing the capacity for growth of a bacterial population does not necessarily mean that the culture will be able to grow that much. As an example, in biofilm-driven systems the electrode surface area available for attachment and its roughness are also key parameters that limit the development of a thick biofilm [82,83]. In that sense, the model can be used to calculate the maximum cell growth that can be obtained with a certain system under a specific set of operational conditions.

## 2.4. Conclusion

The mathematical model presented in this work is able to accurately describe the behavior of different biofilm-driven MES reactors operating in batch, fed-batch, and continuous mode. It was found that under previously reported operational conditions biomass growth was partially limited by the $CO_2$ dissolved concentration. This implies that a more careful assessment of the inorganic carbon supply method is needed to increase production rates. Furthermore, simulations show that operating in continuous mode leads to higher cell densities. Since most current studies are done in batch mode, this might be one of the reasons why cell titers are far below their theoretical maximum [5,6]. These results demonstrate the value of such models in understanding MES systems, and highlight their usefulness when analyzing current process limitations.

## 2.5. Acknowledgements

## 2.6. References

[1]     D.R. Lovley, K.P. Nevin, Electrobiocommodities: powering microbial production of fuels and commodity chemicals from carbon dioxide with electricity, Curr Opin Biotechnol 24 (2013) 385–390. https://doi.org/10.1016/j.copbio.2013.02.012.

[2]     L. Jourdin, D. Strik, Electrodes for Cathodic Microbial Electrosynthesis Processes: Key Developments and Criteria for Effective Research and Implementation, in: Functional Electrodes for Enzymatic and Microbial Electrochemical Systems, WORLD SCIENTIFIC (EUROPE), 2017: pp. 429–473. https://doi.org/10.1142/9781786343543_0012.

[3]     S. Kerzenmacher, Engineering of Microbial Electrodes, in: 2017: pp. 135–180. https://doi.org/10.1007/10_2017_16.

[4]     N.S. Lewis, D.G. Nocera, Powering the planet: Chemical challenges in solar energy utilization, Proceedings of the National Academy of Sciences 103 (2006) 15729–15735. https://doi.org/10.1073/pnas.0603395103.

[5]     L. Jourdin, T. Burdyny, Microbial Electrosynthesis: Where Do We Go from Here?, Trends Biotechnol 39 (2021) 359–369. https://doi.org/10.1016/j.tibtech.2020.10.014.

[6]     A. Prévoteau, J.M. Carvajal-Arroyo, R. Ganigué, K. Rabaey, Microbial electrosynthesis from CO2: forever a promise?, Curr Opin Biotechnol 62 (2020) 48–57. https://doi.org/10.1016/j.copbio.2019.08.014.

[7]     L. Jourdin, J. Sousa, N. van Stralen, D.P.B.T.B. Strik, Techno-economic assessment of microbial electrosynthesis from CO2 and/or organics: An interdisciplinary roadmap towards future research and application, Appl Energy 279 (2020) 115775. https://doi.org/10.1016/j.apenergy.2020.115775.

[8]     C.G.S. Giddings, K.P. Nevin, T. Woodward, Simplifying microbial electrosynthesis reactor design, Front Microbiol 6 (2015). https://doi.org/10.3389/fmicb.2015.00468.

[9]     M.F. Alqahtani, K.P. Katuri, S. Bajracharya, Y. Yu, Z. Lai, P.E. Saikaly, Porous Hollow Fiber Nickel Electrodes for Effective Supply and Reduction of Carbon Dioxide to Methane through Microbial Electrosynthesis, Adv Funct Mater 28 (2018). https://doi.org/10.1002/adfm.201804860.

[10]    F. Enzmann, F. Mayer, M. Stöckl, K.-M. Mangold, R. Hommel, D. Holtmann, Transferring bioelectrochemical processes from H-cells to a scalable bubble column reactor, Chem Eng Sci 193 (2019) 133–143. https://doi.org/10.1016/j.ces.2018.08.056.

[11]    L.F.M. Rosa, S. Hunger, T. Zschernitz, B. Strehlitz, F. Harnisch, Integrating Electrochemistry Into Bioreactors: Effect of the Upgrade Kit on Mass Transfer, Mixing Time and Sterilizability, Front Energy Res 7 (2019). https://doi.org/10.3389/fenrg.2019.00098.

[12]    B. Korth, F. Harnisch, Modeling Microbial Electrosynthesis, in: 2017: pp. 273–325. https://doi.org/10.1007/10_2017_35.

[13]    A. V Pandit, R. Mahadevan, In silico characterization of microbial electrosynthesis for metabolic engineering of biochemicals, Microb Cell Fact 10 (2011) 76. https://doi.org/10.1186/1475-2859-10-76.

[14]    F. Kracke, J.O. Krömer, Identifying target processes for microbial electrosynthesis by elementary mode analysis, BMC Bioinformatics 15 (2014) 410. https://doi.org/10.1186/s12859-014-0410-2.

[15]    C.W. Marshall, D.E. Ross, K.M. Handley, P.B. Weisenhorn, J.N. Edirisinghe, C.S. Henry, J.A. Gilbert, H.D. May, R.S. Norman, Metabolic Reconstruction and Modeling Microbial Electrosynthesis, Sci Rep 7 (2017) 8391. https://doi.org/10.1038/s41598-017-08877-z.

[16]    M. Kazemi, D. Biria, H. Rismani-Yazdi, Modelling bio-electrosynthesis in a reverse microbial fuel cell to produce acetate from $CO_2$ and $H_2O$, Physical Chemistry Chemical Physics 17 (2015) 12561–12574. https://doi.org/10.1039/C5CP00904A.

[17]    S. Gadkari, M. Shemfe, J.A. Modestra, S.V. Mohan, J. Sadhukhan, Understanding the interdependence of operating parameters in microbial electrosynthesis: a numerical investigation, Physical Chemistry Chemical Physics 21 (2019) 10761–10772. https://doi.org/10.1039/C9CP01288E.

[18]    A.J. Abel, D.S. Clark, A Comprehensive Modeling Analysis of Formate-Mediated Microbial Electrosynthesis**, ChemSusChem 14 (2021) 344–355. https://doi.org/10.1002/cssc.202002079.

[19]    F. Salimijazi, J. Kim, A.M. Schmitz, R. Grenville, A. Bocarsly, B. Barstow, Constraints on the Efficiency of Engineered Electromicrobial Production, Joule 4 (2020) 2101–2130. https://doi.org/10.1016/j.joule.2020.08.010.

[20]    L. Jourdin, M. Winkelhorst, B. Rawls, C.J.N. Buisman, D.P.B.T.B. Strik, Enhanced selectivity to butyrate and caproate above acetate in continuous bioelectrochemical chain elongation from CO2: Steering with CO2 loading rate and hydraulic retention time, Bioresour Technol Rep 7 (2019) 100284. https://doi.org/10.1016/j.biteb.2019.100284.

[21]    L. Jourdin, S.M.T. Raes, C.J.N. Buisman, D.P.B.T.B. Strik, Critical Biofilm Growth throughout Unmodified Carbon Felts Allows Continuous Bioelectrochemical Chain Elongation from CO2 up to Caproate at High Current Density, Front Energy Res 6 (2018). https://doi.org/10.3389/fenrg.2018.00007.

[22]    V. Flexer, L. Jourdin, Purposely Designed Hierarchical Porous Electrodes for High Rate Microbial Electrosynthesis of Acetate from Carbon Dioxide, Acc Chem Res 53 (2020) 311–321. https://doi.org/10.1021/acs.accounts.9b00523.

[23]    C.W. Marshall, D.E. Ross, E.B. Fichot, R.S. Norman, H.D. May, Long-term Operation of Microbial Electrosynthesis Systems Improves Acetate Production by Autotrophic Microbiomes, Environ Sci Technol 47 (2013) 6023–6029. https://doi.org/10.1021/es400341b.

[24]    L. Morgado, V.B. Paixão, M. Schiffer, P.R. Pokkuluri, M. Bruix, C.A. Salgueiro, Revealing the structural origin of the redox-Bohr effect: the first solution structure of a cytochrome from *Geobacter sulfurreducens*, Biochemical Journal 441 (2012) 179–187. https://doi.org/10.1042/BJ20111103.

[25]    H.V.M. Hamelers, A. ter Heijne, N. Stein, R.A. Rozendal, C.J.N. Buisman, Butler–Volmer–Monod model for describing bio-anode polarization curves, Bioresour Technol 102 (2011) 381–387. https://doi.org/10.1016/j.biortech.2010.06.156.

[26]    Y. Zeng, Y.F. Choo, B.-H. Kim, P. Wu, Modelling and simulation of two-chamber microbial fuel cell, J Power Sources 195 (2010) 79–89. https://doi.org/10.1016/j.jpowsour.2009.06.101.

[27]    K.P. Nevin, T.L. Woodard, A.E. Franks, Z.M. Summers, D.R. Lovley, Microbial Electrosynthesis: Feeding Microbes Electricity To Convert Carbon Dioxide and Water to Multicarbon Extracellular Organic Compounds, MBio 1 (2010). https://doi.org/10.1128/mBio.00103-10.

[28]    K.P. Nevin, S.A. Hensley, A.E. Franks, Z.M. Summers, J. Ou, T.L. Woodard, O.L. Snoeyenbos-West, D.R. Lovley, Electrosynthesis of Organic Compounds from Carbon Dioxide Is Catalyzed by a Diversity of Acetogenic Microorganisms, Appl Environ Microbiol 77 (2011) 2882–2886. https://doi.org/10.1128/AEM.02642-10.

[29]    E. Blanchet, F. Duquenne, Y. Rafrafi, L. Etcheverry, B. Erable, A. Bergel, Importance of the hydrogen route in up-scaling electrosynthesis for microbial CO₂ reduction, Energy Environ Sci 8 (2015) 3731–3744. https://doi.org/10.1039/C5EE03088A.

[30]    L. Jourdin, Y. Lu, V. Flexer, J. Keller, S. Freguia, Biologically Induced Hydrogen Production Drives High Rate/High Efficiency Microbial Electrosynthesis of Acetate from Carbon Dioxide, ChemElectroChem 3 (2016) 581–591. https://doi.org/10.1002/celc.201500530.

**2**

[31]    S.M.T. Raes, L. Jourdin, C.J.N. Buisman, D.P.B.T.B. Strik, Continuous Long-Term Bioelectrochemical Chain Elongation to Butyrate, ChemElectroChem 4 (2017) 386–395. https://doi.org/10.1002/celc.201600587.

[32]    I. Vassilev, P.A. Hernandez, P. Batlle-Vilanova, S. Freguia, J.O. Krömer, J. Keller, P. Ledezma, B. Virdis, Microbial Electrosynthesis of Isobutyric, Butyric, Caproic Acids, and Corresponding Alcohols from Carbon Dioxide, ACS Sustain Chem Eng 6 (2018) 8485–8493. https://doi.org/10.1021/acssuschemeng.8b00739.

[33]    R. Ganigué, S. Puig, P. Batlle-Vilanova, M.D. Balaguer, J. Colprim, Microbial electrosynthesis of butyrate from carbon dioxide, Chemical Communications 51 (2015) 3235–3238. https://doi.org/10.1039/C4CC10121A.

[34]    P. Batlle-Vilanova, R. Ganigué, S. Ramió-Pujol, L. Bañeras, G. Jiménez, M. Hidalgo, M.D. Balaguer, J. Colprim, S. Puig, Microbial electrosynthesis of butyrate from carbon dioxide: Production and extraction, Bioelectrochemistry 117 (2017) 57–64. https://doi.org/10.1016/j.bioelechem.2017.06.004.

[35]    J.J. Heijnen, J.P. Van Dijken, In search of a thermodynamic description of biomass yields for the chemotrophic growth of microorganisms, Biotechnol Bioeng 39 (1992) 833–858. https://doi.org/10.1002/bit.260390806.

[36]    R. KLEEREBEZEM, M.C.M. VAN LOOSDRECHT, A Generalized Method for Thermodynamic State Analysis of Environmental Systems, Crit Rev Environ Sci Technol 40 (2010) 1–54. https://doi.org/10.1080/10643380802000974.

[37]    J.A. Roels, Energetics and kinetics in biotechnology., Elsevier Biomedical Press, 1983.

[38]    E.H. Battley, Energetics of microbial growth, New York: Wiley, 1987.

[39]    B. Korth, L.F.M. Rosa, F. Harnisch, C. Picioreanu, A framework for modeling electroactive microbial biofilms performing direct electron transfer, Bioelectrochemistry 106 (2015) 194–206. https://doi.org/10.1016/j.bioelechem.2015.03.010.

[40]    J. Monod, The growth of bacterial cultures., Selected Papers in Molecular Biology by Jacques Monod 139 (2012) 606.

[41]    F.G. Bader, Analysis of double-substrate limited growth, Biotechnol Bioeng 20 (1978) 183–202. https://doi.org/10.1002/bit.260200203.

[42]    W. Bae, B.E. Rittmann, A structured model of dual-limitation kinetics., Biotechnol Bioeng 49 (1996) 683–689.

[43]    L. Tijhuis, M.C.M. Van Loosdrecht, J.J. Heijnen, A thermodynamically based correlation for maintenance gibbs energy requirements in aerobic and anaerobic chemotrophic growth, Biotechnol Bioeng 42 (1993) 509–519. https://doi.org/10.1002/bit.260420415.

[44]    J. Ribes, K. Keesman, H. Spanjers, Modelling anaerobic biomass growth kinetics with a substrate threshold concentration, Water Res 38 (2004) 4502–4510. https://doi.org/10.1016/j.watres.2004.08.017.

[45]    J.B. Russell, Another explanation for the toxicity of fermentation acids at low pH: anion accumulation versus uncoupling, Journal of Applied Bacteriology 73 (1992) 363–370. https://doi.org/10.1111/j.1365-2672.1992.tb04990.x.

[46] J.B. Russell, The Energy Spilling Reactions of Bacteria and Other Organisms, Microb Physiol 13 (2007) 1–11. https://doi.org/10.1159/000103591.

[47] M. Roghair, Y. Liu, J.C. Adiatma, R.A. Weusthuis, M.E. Bruins, C.J.N. Buisman, D.P.B.T.B. Strik, Effect of n-Caproate Concentration on Chain Elongation and Competing Processes, ACS Sustain Chem Eng 6 (2018) 7499–7506. https://doi.org/10.1021/acssuschemeng.8b00200.

[48] T.K. Ghose, R.D. Tyagi, Rapid ethanol fermentation of cellulose hydrolysate. II. Product and substrate inhibition and optimization of fermentor design, Biotechnol Bioeng 21 (1979) 1401–1420. https://doi.org/10.1002/bit.260210808.

[49] C.F. Nielsen, L. Lange, A.S. Meyer, Classification and enzyme kinetics of formate dehydrogenases for biomanufacturing via CO2 utilization, Biotechnol Adv 37 (2019) 107408. https://doi.org/10.1016/j.biotechadv.2019.06.007.

[50] J. Pérez, C. Picioreanu, M. van Loosdrecht, Modeling biofilm and floc diffusion processes based on analytical solution of reaction-diffusion equations, Water Res 39 (2005) 1311–1323. https://doi.org/10.1016/j.watres.2004.12.020.

[51] D.P. Wiesenborn, F.B. Rudolph, E.T. Papoutsakis, Thiolase from *Clostridium acetobutylicum* ATCC 824 and Its Role in the Synthesis of Acids and Solvents, Appl Environ Microbiol 54 (1988) 2717–2722. https://doi.org/10.1128/aem.54.11.2717-2722.1988.

[52] B.K. Ahring, P. Westermann, Kinetics of Butyrate, Acetate, and Hydrogen Metabolism in a Thermophilic, Anaerobic, Butyrate-Degrading Triculture, Appl Environ Microbiol 53 (1987) 434–439. https://doi.org/10.1128/aem.53.2.434-439.1987.

[53] R. Klemps, SiegfriedM. Schoberth, H. Sahm, Production of acetic acid by Acetogenium kivui, Appl Microbiol Biotechnol 27 (1987). https://doi.org/10.1007/BF00252923.

[54] X.-J. Zheng, H.-Q. Yu, Inhibitory effects of butyrate on biological hydrogen production with mixed anaerobic cultures, J Environ Manage 74 (2005) 65–70. https://doi.org/10.1016/j.jenvman.2004.08.015.

[55] H.K. Ly, F. Harnisch, S. Hong, U. Schröder, P. Hildebrandt, D. Millo, Unraveling the Interfacial Electron Transfer Dynamics of Electroactive Microbial Biofilms Using Surface-Enhanced Raman Spectroscopy, ChemSusChem 6 (2013) 487–492. https://doi.org/10.1002/cssc.201200626.

[56] H. Dubouchaud, L. Walter, M. Rigoulet, C. Batandier, Mitochondrial NADH redox potential impacts the reactive oxygen species production of reverse Electron transfer through complex I, J Bioenerg Biomembr 50 (2018) 367–377. https://doi.org/10.1007/s10863-018-9767-7.

[57] S. Bajracharya, K. Vanbroekhoven, C.J.N. Buisman, D. Pant, D.P.B.T.B. Strik, Application of gas diffusion biocathode in microbial electrosynthesis from carbon dioxide, Environmental Science and Pollution Research 23 (2016) 22292–22308. https://doi.org/10.1007/s11356-016-7196-x.

[58] H. Nagarajan, M. Sahin, J. Nogales, H. Latif, D.R. Lovley, A. Ebrahim, K. Zengler, Characterizing acetogenic metabolism using a genome-scale metabolic reconstruction of Clostridium ljungdahlii, Microb Cell Fact 12 (2013) 118. https://doi.org/10.1186/1475-2859-12-118.

[59] J. Hwang, A. Hari, R. Cheng, J.G. Gardner, D. Lobo, Kinetic modeling of microbial growth, enzyme activity, and gene deletions: An integrated model of β-glucosidase function in *Cellvibrio japonicus*, Biotechnol Bioeng 117 (2020) 3876–3890. https://doi.org/10.1002/bit.27544.

**2**

[60]     Y.R. Chen, A.G. Hashimoto, Substrate utilization kinetic model for biological treatment process, Biotechnol Bioeng 22 (1980) 2081–2095. https://doi.org/10.1002/bit.260221008.

[61]     S.G. Pavlostathis, E. Giraldo-Gomez, Kinetics of Anaerobic Treatment, Water Science and Technology 24 (1991) 35–59. https://doi.org/10.2166/wst.1991.0217.

[62]     A. -P. Zeng, W. -D. Deckwer, A Kinetic Model for Substrate and Energy Consumption of Microbial Growth under Substrate-Sufficient Conditions, Biotechnol Prog 11 (1995) 71–79. https://doi.org/10.1021/bp00031a010.

[63]     K. Schuchmann, V. Müller, Direct and Reversible Hydrogenation of $CO_2$ to Formate by a Bacterial Carbon Dioxide Reductase, Science (1979) 342 (2013) 1382–1385. https://doi.org/10.1126/science.1244758.

[64]     R.F. Weiss, Carbon dioxide in water and seawater: the solubility of a non-ideal gas, Mar Chem 2 (1974) 203–215. https://doi.org/10.1016/0304-4203(74)90015-2.

[65]     L. Váchová, Z. Palková, Physiological regulation of yeast cell death in multicellular colonies is triggered by ammonia, J Cell Biol 169 (2005) 711–717. https://doi.org/10.1083/jcb.200410064.

[66]     D. Michel-Savin, R. Marchal, J.P. Vandecasteele, Butyrate production in continuous culture of Clostridium tyrobutyricum: effect of end-product inhibition, Appl Microbiol Biotechnol 33 (1990). https://doi.org/10.1007/BF00176512.

[67]     P. Andrić, A.S. Meyer, P.A. Jensen, K. Dam-Johansen, Reactor design for minimizing product inhibition during enzymatic lignocellulose hydrolysis, Biotechnol Adv 28 (2010) 407–425. https://doi.org/10.1016/j.biotechadv.2010.02.005.

[68]     K. Schuchmann, V. Müller, Autotrophy at the thermodynamic limit of life: a model for energy conservation in acetogenic bacteria, Nat Rev Microbiol 12 (2014) 809–821. https://doi.org/10.1038/nrmicro3365.

[69]     L.A.M. Vander Wielen, M.J. Van Buel, A.J.J. Straathof, K.Ch.A.M. Luyben, Modelling the Enzymatic Deacylation of Penicillin G: Equilibrium and Kinetic Considerations, Biocatal Biotransformation 15 (1997) 121–146. https://doi.org/10.3109/10242429709003614.

[70]     W. Rauch, H. Vanhooren, P.A. Vanrolleghem, A simplified mixed-culture biofilm model, Water Res 33 (1999) 2148–2162. https://doi.org/10.1016/S0043-1354(98)00415-1.

[71]     J.B. Xavier, C. Picioreanu, M.C.M. Van Loosdrecht, A framework for multidimensional modelling of activity and structure of multispecies biofilms, Environ Microbiol 7 (2005) 1085–1103. https://doi.org/10.1111/j.1462-2920.2005.00787.x.

[72]     C. Picioreanu, M.C.M. van Loosdrecht, T.P. Curtis, K. Scott, Model based evaluation of the effect of pH and electrode geometry on microbial fuel cell performance, Bioelectrochemistry 78 (2010) 8–24. https://doi.org/10.1016/j.bioelechem.2009.04.009.

[73]     C. Picioreanu, I.M. Head, K.P. Katuri, M.C.M. van Loosdrecht, K. Scott, A computational model for biofilm-based microbial fuel cells, Water Res 41 (2007) 2921–2940. https://doi.org/10.1016/j.watres.2007.04.009.

[74]    S. Bottero, T. Storck, T.J. Heimovaara, M.C.M. van Loosdrecht, M. V. Enzien, C. Picioreanu, Biofilm development and the dynamics of preferential flow paths in porous media, Biofouling 29 (2013) 1069–1086. https://doi.org/10.1080/08927014.2013.828284.

[75]    M. del P.A. Rojas, M. Zaiat, E.R. González, H. De Wever, D. Pant, Enhancing the gas–liquid mass transfer during microbial electrosynthesis by the variation of CO2 flow rate, Process Biochemistry 101 (2021) 50–58. https://doi.org/10.1016/j.procbio.2020.11.005.

[76]    P. Izadi, J.-M. Fontmorin, A. Godain, E.H. Yu, I.M. Head, Parameters influencing the development of highly conductive and efficient biofilm during microbial electrosynthesis: the importance of applied potential and inorganic carbon source, NPJ Biofilms Microbiomes 6 (2020) 40. https://doi.org/10.1038/s41522-020-00151-x.

[77]    P. Batlle-Vilanova, S. Puig, R. Gonzalez-Olmos, M.D. Balaguer, J. Colprim, Continuous acetate production through microbial electrosynthesis from <scp> CO 2 </scp> with microbial mixed culture, Journal of Chemical Technology & Biotechnology 91 (2016) 921–927. https://doi.org/10.1002/jctb.4657.

[78]    J.B.A. Arends, S.A. Patil, H. Roume, K. Rabaey, Continuous long-term electricity-driven bioproduction of carboxylates and isopropanol from CO 2 with a mixed microbial community, Journal of CO2 Utilization 20 (2017) 141–149. https://doi.org/10.1016/j.jcou.2017.04.014.

[79]    S. Bajracharya, K. Vanbroekhoven, C.J.N. Buisman, D.P.B.T.B. Strik, D. Pant, Bioelectrochemical conversion of CO 2 to chemicals: CO 2 as a next generation feedstock for electricity-driven bioproduction in batch and continuous modes, Faraday Discuss 202 (2017) 433–449. https://doi.org/10.1039/C7FD00050B.

[80]    E. V. LaBelle, H.D. May, Energy Efficiency and Productivity Enhancement of Microbial Electrosynthesis of Acetate, Front Microbiol 8 (2017). https://doi.org/10.3389/fmicb.2017.00756.

[81]    S. Molenaar, P. Saha, A. Mol, T. Sleutels, A. Ter Heijne, C. Buisman, Competition between Methanogens and Acetogens in Biocathodes: A Comparison between Potentiostatic and Galvanostatic Control, Int J Mol Sci 18 (2017) 204. https://doi.org/10.3390/ijms18010204.

[82]    A.A. Myint, W. Lee, S. Mun, C.H. Ahn, S. Lee, J. Yoon, Influence of membrane surface properties on the behavior of initial bacterial adhesion and biofilm development onto nanofiltration membranes, Biofouling 26 (2010) 313–321. https://doi.org/10.1080/08927010903576389.

[83]    Y. Ammar, D. Swailes, B. Bridgens, J. Chen, Influence of surface roughness on the initial formation of biofilm, Surf Coat Technol 284 (2015) 410–416. https://doi.org/10.1016/j.surfcoat.2015.07.062.

**2**

## 2.7. Supplementary Material

### 2.7.1. Model Description

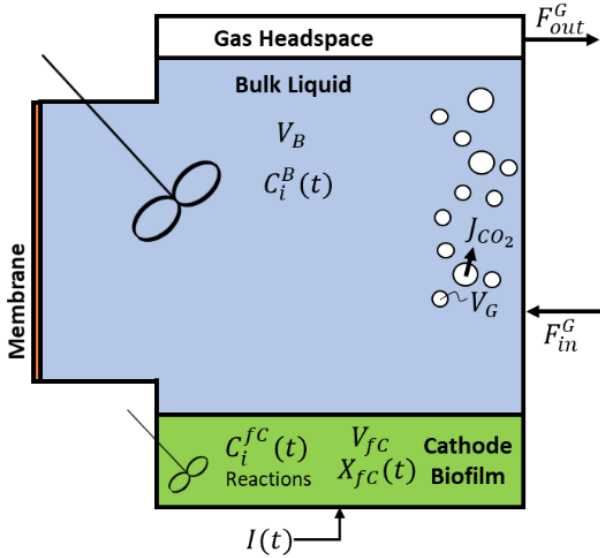**Batch H-cell reactor from Marshall et al. (2013)**



**Figure 2S 1.** Model domains of the batch reactor based on Marshall et al. (2013) [1].

**Mass balances of the dissolved chemical species**

    i.   <u>Continuous reactor from Jourdin et al. (2019) [2] and Jourdin et al. (2018) [3]</u>

Overall concentration changes in time of all dissolved species ($i$) are caused by biological reactions, electrochemical reactions, gas/liquid $CO_2$ transfer and the exchange of medium (e.g. continuous operation). The total volume of the reactor ($V_T^C$), including the bioelectrochemical cells and the bubble column, is described in Eq. S1. In a continuous operating system, a dilution rate term ($D_T^L$) can be defined as shown in Eq. S2. This rate describes the relation between the exchange flow of fresh medium into the system ($F_{in}^L$) and the volume of said system. It can also be expressed as the inverse of the retention time ($HRT$).

$$V_T^C = V_{B1} + V_{B2} + V_{fc} + V_{BC} \qquad (S1)$$

$$D_T^L = \frac{F_{in}^L}{V_T} = \frac{1}{HRT} \qquad (S2)$$

The mass balance equations over the entirety of the reactor volume can be described as:

$$\frac{dC_i}{dt} = D_T^L\left(C_i^{in} - C_i\right) + \frac{V_{fc}}{V_T^C}r_i^{fc} \pm \frac{V_{fc}}{V_T^C}r_M^{elec} + \frac{V_{BC}}{V_T^C}k_L a\left(C^*_{CO_2} - C^{BC}_{CO_2}\right) \qquad (S3)$$

The set of equations obtained from Eq. S3 includes changes produced by the continuous operation mode $(D_T^L)$, reactions within the biofilm $(r_i^{fc})$, the electrochemical reaction of the mediator pair $(r_M^{elec})$ and the gas/liquid $CO_2$ mass transfer $(k_L a)$. Volume corrections to account for the difference in volume between compartments are also included. The initial conditions are $C_i(0) = C_i^0$.

ii.    Batch reactor from Marshall et al. (2013) [1]

The main difference between the H-cell reactor and the reactor from Jourdin et al. consists on the operating mode and the different liquid compartments. The total volume of the reactor $(V_T^H)$ is now the sum of the bulk and the cathode/biofilm volumes. Marshall et al. (2013) operated their reactor in batch mode, meaning no exchange flow was applied, hence $D_T^L = 0$.

$$V_T^H = V_B + V_{fc} \qquad (S4)$$

$$\frac{dC_i}{dt} = \frac{V_{fc}}{V_T^H}r_i^{fc} \pm \frac{V_{fc}}{V_T^H}r_M^{elec} + \frac{V_B}{V_T^H}k_L a\left(C^*_{CO_2} - C^B_{CO_2}\right) \qquad (S5)$$

**Gibbs energies correction**

The Gibbs energies of reaction $\Delta G^0_{Cat}$, $\Delta G^0_{An}$, $\Delta G^0_{But}$ and $\Delta G^0_{Cap}$ were first corrected for temperature using the Gibbs-Helmholtz equation:

$$\Delta G_i^{0T} = \Delta G_i^0 \frac{T}{T_0} + \Delta H_i^0 \frac{T_0 - T}{T_0} \qquad (S6)$$

Then, the concentration-dependent free energy change was calculated for every reaction. The effect of non-ideality was neglected, hence the activity coefficients of all compounds were assumed to be equal to 1. Proton concentrations $(C_{H^+} = 10^{-5.8}\ mol\ L^{-1})$ were assumed constant during all simulations.

$$\Delta G_i^{01} = \Delta G_i^{0T} + RT\sum_{j=1}^{n}\left(ln(C_j)\cdot Y_j^i\right) \qquad (S7)$$

**Redox mediator pair**

Microbial metabolism is a complex network of interlinked biochemical reactions. Different redox mediator couples are used for multiple reactions, e.g., NADH/NAD⁺, H₂/H⁺, or Fd(red)/Fd(ox). It is known that some intermediate

reactions within the anaerobic reduction of $CO_2$ to acetate require electrons at low potential, likely at that of ferredoxin [4,5]. However, NADH is also known to be involved in the energy conservation mechanisms of acetogenic bacteria [6]. Moreover, the anaerobic chain elongation of acetate to carboxylates has been seen to be highly dependent on NADH [7]. Therefore, it is not straightforward which mediator pair limits microbial metabolism in MES.

In this work, a black box organism is assumed and therefore, intermediate reactions are not accounted for during the thermodynamic state analysis calculations [8]. For modelling purposes, the energy gain by the microorganism was simplified into one reaction, i.e. oxidation of the electrochemically reduced mediator pair (Eq. 11 in the main text). Hence, from a pure energetic point of view, any of the previously introduced mediators could be used. The proposed model only allows the use of one mediator pair, and since a mixed microbial biofilm is simulated it is not possible to know what redox couple would be limiting biological rates. In this study, as the NADH/NAD$^+$ pair is one of the most common redox couples in microbial metabolisms [9], all simulations are performed with the standard redox potential of NADH/NAD$^+$ of -320 mV vs SHE [10].

### 2.7.2. Calculation of the Maximum Growth Rate

In this paper, the maximum growth rate is approximated by neglecting the effect of substrate concentrations and products inhibition. It is therefore calculated as follows:

$$\mu^{max} = \frac{q_{CO_2}^{max} + m_{CO_2}}{Y_{CO_2}^{Met}} \qquad (S8)$$

### 2.7.3. Simulated Product Inhibition at different $k_L a$ and $p_{CO_2}$ in the System from Jourdin et al. (2019)
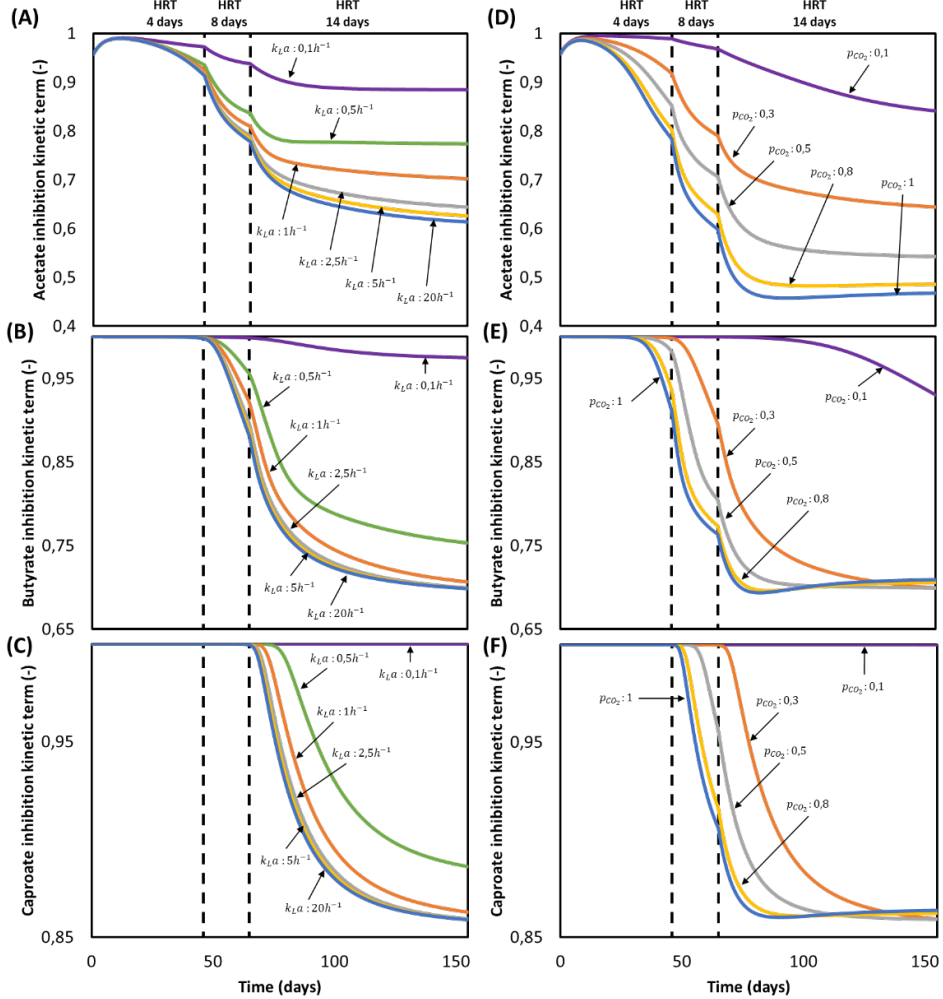


**Figure 2S 2** Simulated kinetic product inhibition terms of acetate, butyrate, and caproate in time for the reactor from Jourdin et al. (2019) [2]: **(A-C)** at different gas-liquid mass transfer coefficients ($k_L a$) with $p_{CO_2} = 0.3$ and **(D-E)** at different gas $CO_2$ partial pressures ($p_{CO_2}$) with $k_L a = 2.5 h^{-1}$.

### 2.7.4. Model Validation Jourdin et al. (2018)

All parameters used in simulations were taken from **Table 2.1** found in the main text, with the exception of the values presented in **Table 2S 1**.

**Table 2S 1.** Parameters used to represent the reactor from Jourdin et al. (2018) [3].

| Parameter | Symbol | Value | Units | Source |
|---|---|---|---|---|
| *Bulk liquid* | | | | |
| Dilution rate | $D_R^L$ | Variable | 1/d | [3] |
| Gas-liquid mass transfer coefficient | $k_L a$ | 0.45 | 1/h | Calculated from [3] |
| Acetate initial concentration | $C_{Ac}^0$ | 0 | mol/m³ | [3] |

## 2.7.5. Model Validation Marshall et al. (2013)

All parameters used in simulations were taken from **Table 2.1** found in the main text, with the exception of the values presented in **Table 2S 2**.

**Table 2S 2.** Parameters used to represent the rector from Marshall et al. (2013) [1].

| Parameter | Symbol | Value | Units | Source |
|---|---|---|---|---|
| *Bulk liquid* | | | | |
| Bulk liquid volume | $V_B$ | 135 | mL | [1] |
| Dilution rate | $D_R^L$ | 0 | 1/d | [1] |
| H⁺ concentration | $C_{H+}^B$ | Variable per batch | mol/L | [1] |
| Gas-liquid mass transfer coefficient | $k_L a$ | 0.45 | 1/h | Chosen |
| Acetate initial concentration | $C_{Ac}^0$ | 0 | mol/m³ | [1] |
| | | | | |
| *Biofilm* | | | | |
| Biocathode volume | $V_{fc}$ | 15 | mL | [1] |
| Initial biomass concentration | $C_X^0$ | 1 | mol/m³ | Chosen |

## 2.7.6. Gradients Over the Reactor

Concentration changes in time of all dissolved species (*i*) for all four compartments are:

$$\frac{dC_i^{B1}}{dt} = \frac{F_R^L}{V_{B1}}\left(C_i^{B1,in} - C_i^{B1}\right) \quad (S9) \qquad \frac{dC_i^{B2}}{dt} = \frac{F_R^L}{V_{B2}}\left(C_i^{fc} - C_i^{B2}\right) \quad (S11)$$

$$\frac{dC_i^{fc}}{dt} = \frac{F_R^L}{V_{fc}}\left(C_i^{B1} - C_i^{fc}\right) + r_i^{fc} \quad (S10) \qquad \frac{dC_i^{BC}}{dt} = \frac{F_R^L}{V_{BC}}\left(C_i^{B2} - C_i^{BC}\right) + k_L a\left(C_{CO_2}^* - C_{CO_2}^{BC}\right) \quad (S12)$$

Reactions in the bulk liquid are negligible, hence any change occurring in the bulk compartment 2 has to come from the biological reactions occurring in the cathode/biofilm compartment. Combining Eq. S10 and S11, an expression can be derived for the concentration in the first bulk domain.

$$\frac{dC_i^{B2}}{dt} = \frac{dC_i^{fc}}{dt} \tag{S13}$$

Since no reaction occurs in the bulk liquid, $C_i^{B2} = C_i^{fc}$ hence Eq. S13 becomes zero and the following equation is obtained:

$$C_i^{B1} = C_i^{B2} - \frac{V_{fc}}{F_R^L} r_i^{fc} \tag{S14}$$

A similar balancing can be done to obtain the concentration after the bubble column. By combining Eq. S11 and S12, and taking into consideration that $C_i^{B2} = C_i^{fc}$, the expression for $C_i^{BC}$ can be obtained. As expected, this expression is only valid for CO₂ since the other dissolved species concentrations remain constant.

$$C_i^{BC} = C_i^{B2} + \frac{V_{BC}}{F_R^L} k_L a \left( C_{CO_2}^* - C_{CO_2}^{BC} \right) \tag{S15}$$

The concentration change due to the exchange flow is:

$$\frac{dM_i^{B1,in}}{dt} = F_R^L C_i^{BC} + F_{in}^L C_i^{L,in} - F_{out}^L C_i^{BC} - F_R^L C_i^{B1,in} \tag{S16}$$

Following previous reasoning, the change in the bulk liquid 1 compartment is equal to the change due to the addition of fresh medium meaning $C_i^{B1,in} = C_i^{B1}$. Thus, combining Eq. S9 and S16:

$$C_i^{B1,in} = C_i^{BC} \left( 1 - \frac{F_{out}^L}{F_R^L} \right) + C_i^{L,in} \frac{F_{in}^L}{F_R^L} \tag{S17}$$

The concentration difference between two consecutive compartments can then be calculated as follows:

$$\%_i^{Difference} = \frac{C_i^{Compartment\ 2} - C_i^{Compartment\ 1}}{C_i^{Compartment\ 2}} \cdot 100 \tag{S18}$$

### 2.7.7. pH at the Biofilm

The characteristic reaction time and diffusion time can be calculated with Eq. S19 and Eq. S20, respectively [11]. Concentrations and volumetric rates were taken from the steady state of Jourdin et al. (2019) reactor [2]. Results can be found in **Table 2S 3** and the parameters used in **Table 2S 4**.

$$Reaction\ time = \frac{C_i^{liquid}}{r_i^b} \tag{S19}$$

$$Diffusion\ time = \frac{L_b{}^2}{D_i} \qquad (S20)$$

**Table 2S 3.** Characteristic times calculated for the steady state in Jourdin et al. (2019) [2].

| Chemical species | Reaction time | Diffusion time | Units |
|---|---|---|---|
| *CO₂* | 4.2 | 2.2 | min |
| *H+* | 1.1x10⁻³ | 0.45 | min |
| *Buffer* | 45.2 | 11.6 | min |

**Table 2S 4.** Parameters used for calculating characteristic times with their symbols, values, and units.

| Parameter | Symbol | Value | Units | Source |
|---|---|---|---|---|
| Biofilm thickness | $L_b$ | 5x10⁻⁴ | m | Chosen |
| *Diffusion coefficients in water* | | | | |
| Carbon dioxide | $D_{CO_2}$ | 1.9x10⁻⁹ | m²/s | [12] |
| Protons | $D_{H^+}$ | 9.3x10⁻⁹ | m²/s | [13] |
| Buffer | $D_{Phosphate}$ | 3.6x10⁻¹⁰ | m²/s | [14] |
| *Concentrations in the bulk liquid* | | | | |
| Carbon dioxide | $C_{CO_2}^{liquid}$ | 8.35 | mol/m³ | From simulations |
| Protons | $C_{H^+}^{liquid}$ | 10⁻⁵·⁸ | mol/L | [2] |
| Buffer | $C_{Phosphate}^{liquid}$ | 6.4x10⁻² | mol/L | [2] |
| *Reaction rates at steady state* | | | | |
| Carbon dioxide | $r_{CO_2}^b$ | 120 | mol/(m³ h) | From simulations |
| Protons | $r_{H^+}^b$ | 85 | mol/(m³ h) | From simulations |
| Buffer | $r_{Phosphate}^b$ | 85 | mol/(m³ h) | Same as H⁺ consumed |

$CO_2$ characteristic reaction and diffusion times are in the same order of magnitude, hence it is likely that $CO_2$ diffusion in the biofilm limited its uptake rate. For H⁺ it is clear that the diffusion time is much larger than the time of reaction, therefore it is safe to say that protons were not able to diffuse into the biofilm fast enough. However, the presence of a buffer has to be assessed (**Figure 2S 3**). The diffusion time of the protonated compound is of the same order of magnitude to that of $CO_2$, hence it is the reaction rate that limited its deprotonation. Since the microbial reaction cannot be faster than the substrate diffusion rate, $CO_2$ diffusion limitation slowed down biological rates, subsequently limiting proton consumption. This

decrease in the uptake of protons might have been enough to give enough time to the buffering reaction and prevent a large pH gradient, as seen by Vander Wielen et al. (1997) [11].
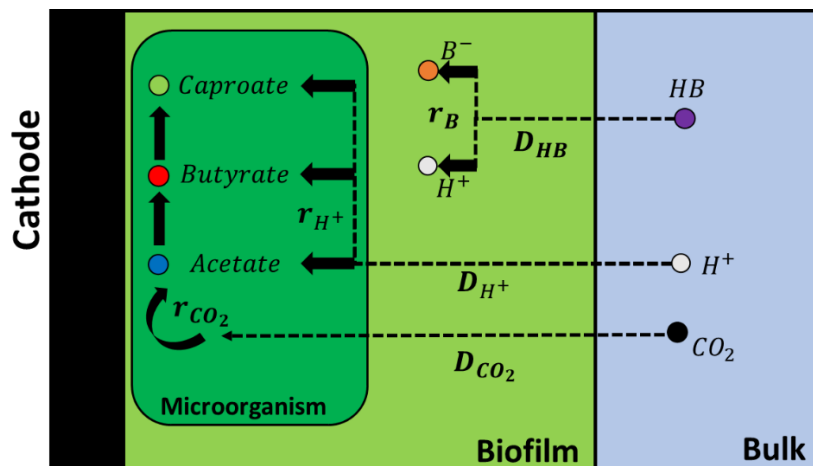


**Figure 2S 3.** Buffering mechanism within the biofilm. Dashed arrows indicate diffusion mechanisms, solid arrows indicate reactions. B⁻ refers to the buffer compound and HB to its protonated form.

### 2.7.8. Supplementary Material Reference List

[1]. Marshall, C. W., D. E. Ross, E. B. Fichot, R. S. Norman and H. D. May (2013). "Long-term operation of microbial electrosynthesis systems improves acetate production by autotrophic microbiomes." Environmental science & technology **47**(11): 6023-6029.

[2]. Jourdin, L., M. Winkelhorst, B. Rawls, C. J. N. Buisman and D. P. B. T. B. Strik (2019). "Enhanced selectivity to butyrate and caproate above acetate in continuous bioelectrochemical chain elongation from CO2: Steering with CO2 loading rate and hydraulic retention time." Bioresource Technology Reports: 100284.

[3]. Jourdin, L., S. M. Raes, C. J. Buisman and D. P. Strik (2018). "Critical biofilm growth throughout unmodified carbon felts allows continuous bioelectrochemical chain elongation from CO2 up to caproate at high current density." Frontiers in Energy Research **6**: 7.

[4]. Furdui, C. and S. W. Ragsdale (2000). "The role of pyruvate ferredoxin oxidoreductase in pyruvate synthesis during autotrophic growth by the Wood-Ljungdahl pathway." Journal of Biological Chemistry **275**(37): 28494-28499.

[5]. Kracke, F., B. Virdis, P. V. Bernhardt, K. Rabaey and J. O. Krömer (2016). "Redox dependent metabolic shift in Clostridium autoethanogenum by extracellular electron supply." Biotechnology for biofuels **9**(1): 1-12.

[6].    Bertsch, J., C. Öppinger, V. Hess, J. D. Langer and V. Müller (2015). "Heterotrimeric NADH-oxidizing methylenetetrahydrofolate reductase from the acetogenic bacterium Acetobacterium woodii." Journal of bacteriology **197**(9): 1681-1689.

[7].    Spirito, C. M., H. Richter, K. Rabaey, A. J. Stams and L. T. Angenent (2014). "Chain elongation in anaerobic reactor microbiomes to recover resources from waste." Current opinion in biotechnology **27**: 115-122.

[8].    Kleerebezem, R. and M. C. Van Loosdrecht (2010). "A generalized method for thermodynamic state analysis of environmental systems." Critical Reviews in Environmental Science and Technology **40**(1): 1-54.

[9].    Madigan, M. T., J. M. Martinko and J. Parker (1997). Brock biology of microorganisms, Prentice hall Upper Saddle River, NJ.

[10].   Schuchmann, K. and V. Müller (2014). "Autotrophy at the thermodynamic limit of life: a model for energy conservation in acetogenic bacteria." Nature Reviews Microbiology **12**(12): 809.

[11].   Vander Wielen, L., M. Van Buel, A. Straathof and K. C. A. Luyben (1997). "Modelling the enzymatic deacylation of penicillin G: Equilibrium and kinetic considerations." Biocatalysis and Biotransformation **15**(2): 121-146.

[12].   Newman, J. and K. E. Thomas-Alyea (2012). Electrochemical systems, John Wiley & Sons.

[13].   McCall, D. W. and D. C. Douglass (1965). "The effect of ions on the self-diffusion of water. I. Concentration dependence." The Journal of Physical Chemistry **69**(6): 2001-2011.

[14].   Krom, M. D. and R. A. Berner (1980). "The diffusion coefficients of sulfate, ammonium, and phosphate ions in anoxic marine sediments 1." Limnology and Oceanography **25**(2): 327-337.
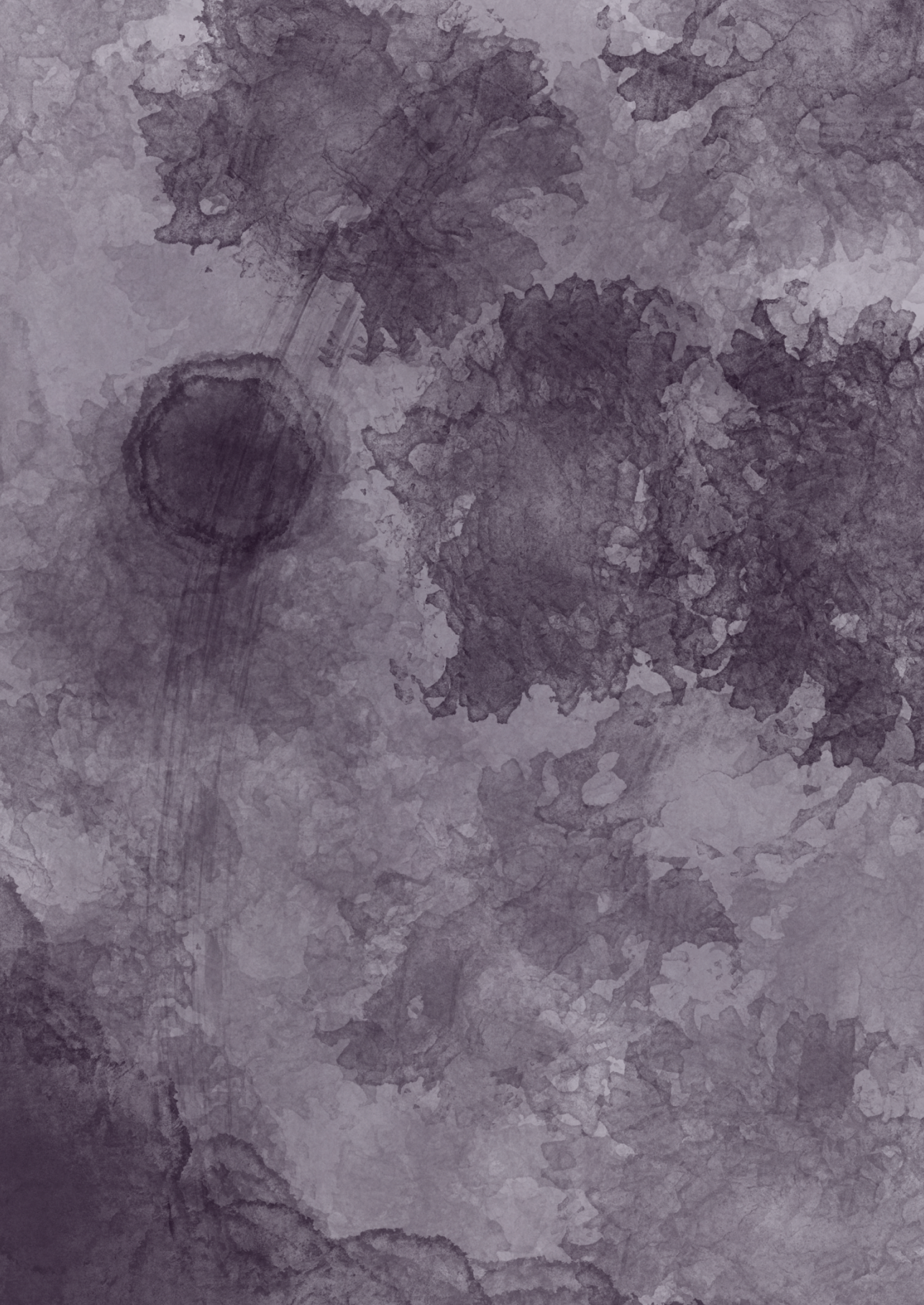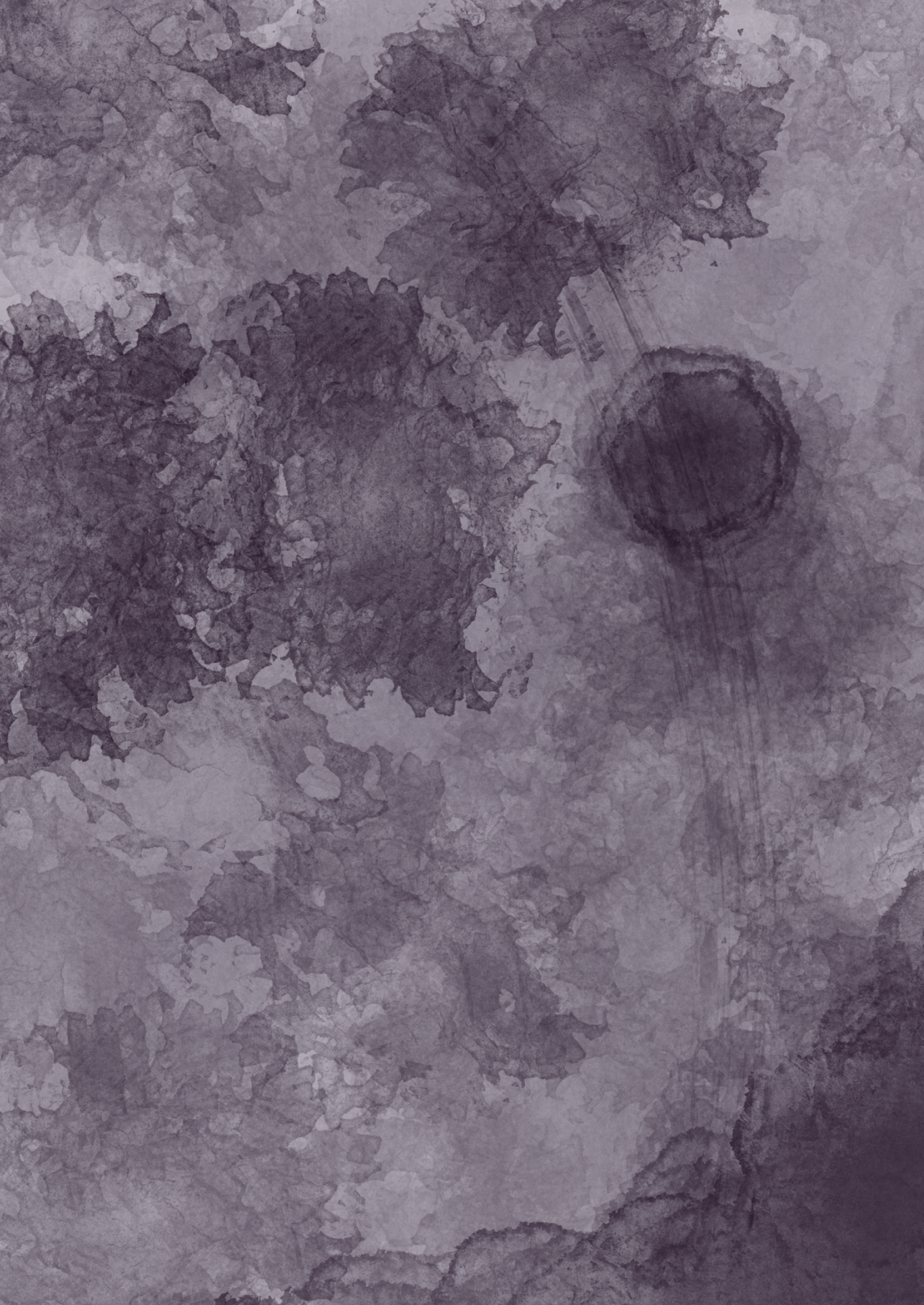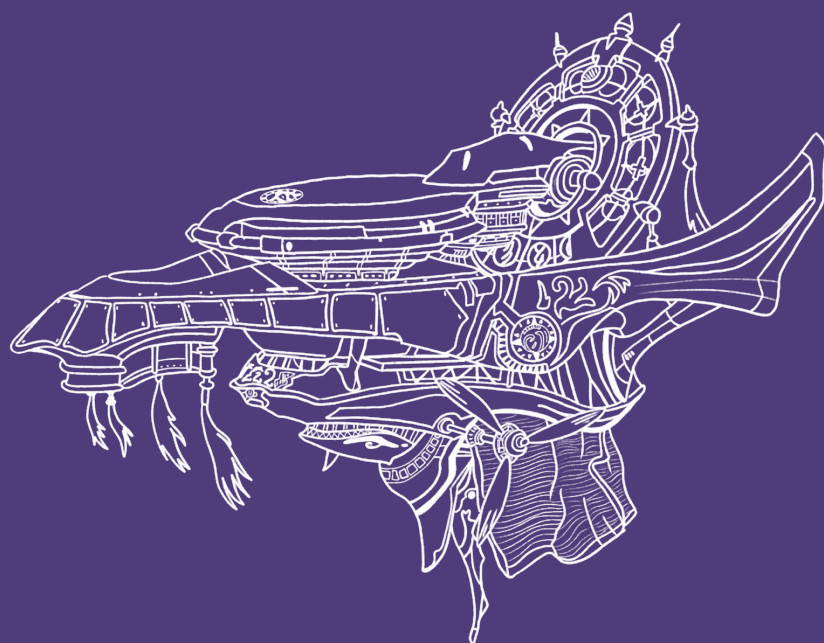
# Chapter 3

Biomass-specific rates as key performance indicators: A nitrogen balancing method for biofilm-based electrochemical conversion

## Abstract

Microbial electrochemical technologies (METs) employ microorganisms utilizing solid-state electrodes as either electron sink or electron source, such as in microbial electrosynthesis (MES). METs reaction rate is traditionally normalized to the electrode dimensions or to the electrolyte volume, but should also be normalized to biomass amount present in the system at any given time. In biofilm-based systems, a major challenge is to determine the biomass amount in a non-destructive manner, especially in systems operated in continuous mode and using 3D electrodes. We developed a simple method using a nitrogen balance and optical density to determine the amount of microorganisms in biofilm and in suspension at any given time. For four MES reactors converting $CO_2$ to carboxylates, >99% of the biomass was present as biofilm after 69 days of reactor operation. After a lag phase, the biomass-specific growth rate had increased to $0.12 - 0.16$ days$^{-1}$. After 100 days of operation, growth became insignificant. Biomass-specific production rates of carboxylates varied between $0.08 - 0.37$ mol$_C$ mol$_X^{-1}$ d$^{-1}$. Using biomass-specific rates, one can more effectively assess the performance of MES, identify its limitations, and compare it to other fermentation technologies.

## 3.1. Introduction

In recent years, Microbial Electrochemical Technologies (METs) gained substantial interest as innovative methods to replace fossil fuel based technologies and processes such as energy and chemicals production [1]. METs exploit microorganisms by utilizing solid-state electrodes as either electron sink or electron source. To date, most studies on METs determine their performance by determining titers, current density or production rates normalized to volume (catholyte, cathode chamber or electrode volume) or electrode surface area [2–4]. While these performance indicators are important from an engineering perspective and to determine the technologies' readiness level, they provide limited information on the actual metabolic activity. While the microorganisms perform the reaction(s) of interest, replicate, die, and wash-out, their amount changes over time. Traditional fermentation studies report performance and rates normalized to the amount of microbial biomass (X) in the reactor at any given time, i.e., biomass-specific rates of production or consumption (e.g., $q_i$ in $mol_i\ mol_X^{-1}\ h^{-1}$ or $g_i\ g_x^{-1}\ h^{-1}$) [5–7]. This allows to assess the performance of the microbial catalyst under any condition. Similarly, chemo-catalytic electrochemical systems or other catalytic processes typically report the amount of catalyst used. The same approach should be followed for METs.

One MET of interest is microbial electrosynthesis (MES). In MES, microorganisms capable of reducing $CO_2$ into valuable organic compounds such as carboxylic acids and alcohols are grown in a bioreactor in the presence of a cathode [8]. This cathode supplies electrons for the $CO_2$ reduction by the microorganisms. To date, the only experimental study reporting a biomass-specific growth rate in MES is from Sydow et al. (2017), who derived a biomass-specific growth rate $\mu = 2.16$ days$^{-1}$ for *Cupriavidus necator* [9]. They measured the amount of planktonic biomass (i.e., microorganisms in suspension) by calibrating cell dry mass with optical density at 600nm. However, this method is only applicable to systems using planktonic cells. Cabau-Peinado et al. (2021) constructed a generalized model for biofilm-driven MES of carboxylates from $CO_2$ and derived $\mu = 0.12$ days$^{-1}$ based on the open culture system of Jourdin et al. (2019a) [10,11]. The model showed that the microbial rates were probably kinetically limited by $CO_2$ availability even though dissolved $CO_2$ was far from being depleted during the first 100 days. After 100 days, the system became limited by product toxicity, mainly from acetate and butyrate. These findings show that invaluable fundamental insights on the performance of the microorganisms can be derived from biomass-specific rates, also referred to as *q*-values. The real impact of variables such as operating conditions, electrode

**3**

composition, and reactor design can be assessed from *q*-values. Consequently, there is a need for a low-cost *operando* method for quantifying biomass amount retained in the system to determine *q*-values at any given time in biofilm-based METs. *Operando* methods refer to methods used to describe systems over time in a non-destructive manner [12].

Several methods exist to quantify biomass amount, including in biofilm studies, such as dry weight measurements [9], qPCR [13], optical density measurements [9], protein content [14], flow cytometry [15], optical coherence tomography (OCT) [16,17], magnetic resonance imaging [18,19], cell counting using microscopy [20–22] or by cryo-sectioning thin biofilm slices [23–25]. However, these techniques suffer from key limitations to determine time-dependent *q*-values in biofilm-based systems. Most prominently, several of these techniques are destructive, allowing only one data point for biofilm biomass quantification at the end of operation. Tracking optical density of the fermentation broth allows non-destructive cell density determination over time, but only of microorganisms in suspension. OCT does allow tracking of the amount of biofilm over time, but only on 2D surfaces and the equipment is costly and requires a specific experimental design as well as specialized skills and expertise of the operator [26].

Several of the aforementioned techniques to determine biomass amount are compromised in reactors fitted with 3D electrodes. Biofilm coverage might not be equally thick throughout the cathode due to regional differences in porosity (especially in fibrous 3D electrodes such as carbon felt), preferred flow patterns, and sheer stress. These can significantly alter the biofilm density and thickness, and become dynamic due to biofilm growth and its intrinsic effect on porosity [27,28]. For example, Jourdin et al. (2018), who forced their catholyte to flow through a carbon felt cathode to overcome mass transfer limitations in their MES system, visually observed that a thick biofilm developed on the membrane-side of the electrode and a less thick biofilm on the outflow side of the electrode [29]. Moreover, they described full biofilm coverage of the carbon felt fibers inside the electrode. To the best of our knowledge, biomass-specific rates have not been experimentally determined in biofilm- based METs.

The purpose of this study was to develop a simple method to experimentally derive biomass-specific rates in biofilm-based METs and to show its usefulness. A biofilm-based microbial electrosynthesis system (bMES) was used as case study here. The developed method consists of determining the amount of biomass present in the system, as biofilm and in suspension, at any given time, using total nitrogen and optical density ($OD_{600nm}$) measurements. To demonstrate the need for biomass-

specific rates in bMES, biomass-specific production rate ($q_p$) and biomass specific growth rate ($\mu$) were experimentally determined and used to assess the microorganisms' performance during bMES by comparing with other relevant technologies, i.e., syngas fermentation and chain elongation fermentation.

## 3.2. Material and Methods

### 3.2.1. Microbial Electrosynthesis Reactor Operation

Four identical bioelectrochemical reactors were used (R1 to R4), each with a 7.35 cm³ piece of unmodified carbon felt (CGT Carbon, Germany) as cathode (7.35 cm² projected surface area, 1 cm thickness as supplied by the manufacturer). The carbon felt volume of 7.35 cm³ was chosen to allow fast full biofilm colonization. An overview of the reactor and cathode dimensions can be found in the Supplementary Material 3.6.1. Prior to use, carbon felt was cleaned by submerging it in 1 mol L⁻¹ HCl and 1 mol L⁻¹ NaOH for 24 h and subsequently treated with UV/ozone (Novascan, United States) for 45 min. A titanium wire (Advent Research Materials, United Kingdom) of $7 \pm 0.5$ cm was weaved through the carbon felt as current collector. To improve the conductivity between carbon felt and wire, a conductive coating was applied where the wire entered and exited the carbon felt, and was left to dry in an oscillator for 2 days.

Each reactor was operated continuously for 194 days with a hydraulic retention time (HRT) of 8 days ($F_{in}$ = 0.625 mL h⁻¹) and a total catholyte volume of VCT = 0.12 L. The medium was continuously circulated at a flow rate of 4.1 L h⁻¹ (derived from [11]). The catholyte medium consisted of 0.4 g L⁻¹ $NH_4Cl$, 0.12 g L⁻¹ $MgCl_2 \cdot 6H_2O$, 0.06 g L⁻¹ $CaCl_2 \cdot 2H_2O$, 0.9 g L⁻¹ $Na_2HPO_4$, 8.1 g L⁻¹ $KH_2PO_4$, 4.5 g L⁻¹ $BrCH_2CH_2SO_3Na$ and 2 mL L⁻¹ trace nutrient medium. $BrCH_2CH_2SO_3Na$ was used as methane inhibitor. The trace nutrient medium consisted of: 10 g L⁻¹ EDTA, 1.5 g L⁻¹ $FeCl_3 \cdot 6H_2O$, 0.15 g L⁻¹ $H_3BO_4$, 0.03 g L⁻¹ $CuSO_4 \cdot 5H_2O$, 0.18 g L⁻¹ KI, 0.12 g L⁻¹ $MnCl_2 \cdot 4H_2O$, 0.06 g L⁻¹ $Na_2MoO_4 \cdot 2H_2O$, 0.12 g L⁻¹ $ZnSO_4 \cdot 7H_2O$, 0.15 g L⁻¹ $CoCl_2 \cdot 6H_2O$ and 0.023 g L⁻¹ $NiCl_2 \cdot 6H_2O$. At day 62, the catholyte solutes, except the phosphates and methane inhibitor, were doubled in concentration to avoid possible nutrient limitations. Moreover, a gas mixture of $CO_2/N_2$ 50:50 was continuously bubbled at a rate of 100 mL min⁻¹ through the catholyte in a bubble column.

A titanium plate with a platinum-iridium coating (Ti Pt/Ir MMO, Magneto, Netherlands) was used as anode. The anolyte composition was similar to the catholyte composition, but excluded trace nutrients and methane inhibitor.

Furthermore, the anolyte pH was corrected to pH ~ 1.8 using 87% $H_3PO_4$ (approximately 10 mL per L anolyte) in order to favor protons crossing over the membrane over other cations. The cathode and anode compartments were separated by a cation exchange membrane (CEM, Membrane International, United States). pH was controlled at 5.80 ± 0.03 using either 1 mol $L^{-1}$ NaOH or 1 mol $L^{-1}$ HCl titration, with a pH probe (Prosense, Netherlands) attached to a PID system (JUMO, Germany). The reactors were operated inside a temperature-controlled cabinet at 31 ± 1°C and kept in the dark to avoid potential phototrophic growth. At day 0 all reactors were inoculated with ± 460 mg $L^{-1}$ biomass, obtained from cryogenic stocks of previously long-term operated MES reactors by Jourdin et al. (2019a) [11]. The inoculum was derived from biofilm as well as from planktonic cells. The electrochemical studies were controlled by a VMP3 Multichannel potentiostat (BioLogic, France) using an Ag/AgCl 3 mol $L^{-1}$ KCl reference electrode (Prosense, Netherlands). During long- term operation, the cathodes were polarized in potentiostatic mode at −0.85 V vs. SHE (standard hydrogen electrode). Unless otherwise mentioned, all potentials are reported versus SHE in this manuscript.

### 3.2.2. Maintenance Events

On day 42 and on day 52 of the experiment, electricity was switched off for 3 h (no gas feed, heat control, pH control, liquid recirculation or potential control by the potentiostat) due to maintenance (events I and II, respectively). To prevent acidification of the cathode chamber due to proton crossover, the anolyte was drained and refilled with the same composition, except for phosphoric acid, which was not added in order to maintain a pH of 5.8. After the power restart, the anolyte was changed again to its normal composition described earlier.

### 3.2.3. Analytical Methods

A catholyte sample of 5 mL was taken twice a week from all reactors after inoculation. 100 µL was used to measure alcohols and carboxylic acids by GC-FID (Thermofisher, United States) with a Stabil-waxTM column of 25 m × 0.2 µm ID. The column was kept at 50°C for 7 min, ramped to 180°C in 8 min and kept at this temperature for 9 min. Helium was carrier gas at 1 mL $min^{-1}$. Flame ionization detection was used at 250°C.

To investigate microbial growth, 2 mL catholyte was diluted ~7.5x, filtered (0.2 µm), and the filtrate was analyzed for total nitrogen using a TOC analyzer coupled with a TN unit and auto sampler (TOC-L Series Total Organic Carbon Analyzer, Shimadzu, Japan). The oven temperature was set at 720°C. Optical density of the

original undiluted sample was recorded at 600 nm ($OD_{600nm}$) to account for planktonic cells in the outflow of the system using a UV-VIS spectrophotometer (UV- 1800 series, Shimadzu, Japan). The OD was calibrated to the nitrogen concentration in suspended biomass (planktonic cells, $c_{N-pX}$ in mol $L^{-1}$) in the catholyte. The calibration was obtained by the aforementioned total nitrogen analysis on a series of biomass (obtained from filtration of catholyte outflow on day 75) dilutions in catholyte without a nitrogen source. The derived calibration curve for concentration of nitrogen in planktonic biomass (mol $L^{-1}$) was:

$$c_{N-pX} = 0.0052 * [OD_{600nm}] - 0.00002 \tag{1}$$

The obtained $R^2$ value for the calibration curve was 0.9989. The calibration data can be found in Supplementary Material 3.6.2.

### 3.2.4. Imaging

After terminating the reactors, three samples were taken from each biocathode using a sterile stainless-steel knife under anaerobic conditions for viability analysis. For live/dead staining a FilmTracer™ LIVE/DEAD Biofilm Viability kit (Invitrogen™) was used. The biofilm viability checker tool developed by Mountcastle et al. (2021) was used to quantify biofilm viability at the end of the experiments [30]. For imaging the stained samples a confocal laser scanning microscope system, LSM 710 (Zeiss Observer Z.1, Carl Zeiss), equipped with an AxioCam MRm camera was used. This LSM 710 system uses a Zeiss Observer Z.1 inverted microscope stand with transmitted light (HAL 100), UV (HBO 50), and laser illumination sources. The microscope is completely motorized with a motorized stage, z-drive (for focusing), objective turret. The samples were irradiated at excitation wavelengths at 488 nm and 543 nm for SYTO 9 and propidium iodine respectively, whereas the detection wavelengths were set to 493–578 nm and 566–797 nm respectively. The pinhole was set at 1 AU, and the detector gain at 500 and 700 for SYTO 9 and propidium iodine, respectively. For most images a Plan-Apochromat 20x/ 0.8 M27 objective was used, with the exception of the image for the R4 outflow sample where a Fluar 2.5x/0.12 M27 objective was used with a pinhole set at 0.68 AU.

### 3.2.5. Reactor Performance Determination

The mass balance for each reactor's cathode compartment was defined as:

$$\frac{dn_i}{dt} = F_{in}c_{i,in} - F_{out}c_{i,out} + r_i V_T^C \tag{2}$$

Where $n_i$ is the mole amount of compound $i$, $t$ is time (d), $F$ is the flow rate (L $d^{-1}$), $c_{i,in}$ is the ingoing concentration (0 $mol_i$ $L^{-1}$ for products in this study), $c_{i,out}$ is the

outgoing concentration , $r_i$ is the volume-specific production rate of $i$ (mol$_i$ L$^{-1}$ d$^{-1}$) and $V_T^C$ is the total catholyte volume (L). The titrant flow, $F_{pH}$ was much smaller than $F_{in}$. Therefore, we disregarded it in this study, and we assumed $F_{in} = F_{out} = F$. Faradaic efficiency (*FE%*), or electron recovery, is defined as the total amount of electric charge retrieved in the products of interest (organics and biomass), $Q_{products}$ (coulomb), divided by the total electric charge $Q_T$ (coulomb) provided to the cathodic reaction:

$$FE\% = \frac{Q_{products}}{Q_T} * 100\% \tag{3}$$

### 3.2.6. Biomass-specific Rates Determination

One method that does not suffer from being destructive and/or costly is using the elemental balances to quantify biomass amount and differentiate between planktonic and biofilm-based microorganisms. de Rink et al. (2022) used a nitrogen balance in their desulfurization process [31]. They measured organic nitrogen using Hach kits to account for planktonic cells. Here, we measure total nitrogen to account for nitrogen assimilation into biomass, and calibrate optical density to nitrogen in planktonic cells to measure the planktonic cells amount at any given time as described in the analytical methods section. This prevents the needs for expensive testing kits for nitrogen species present in the medium. Biomass production was estimated based on a total nitrogen mass balance, assuming that nitrogen assimilation into biomass was the only relevant reaction involving elemental nitrogen. A schematic overview of the parameters used as well as a list of all parameters and subscripts used in the following equations can be found in Supplementary Material 3.6.2. Elemental nitrogen balances are used because the carbon balances include large terms for $CO_2$ inflow and outflow, which will obscure carbon accumulation in biomass.

For total elemental nitrogen (N), balance Eq. 1 becomes:

$$\frac{dn_N}{dt} = Fc_{N-aq,in} - Fc_{N-aq,out} - Fc_{N-pX,out} \tag{4}$$

Where $n_N$ is the amount of total nitrogen in the cathode compartment, $c_{N-aq,in}$ is the incoming dissolved nitrogen concentration (mol L$^{-1}$), $c_{N-aq,out}$ is the dissolved nitrogen concentration in the outflow (mol L$^{-1}$), and $c_{N-pX,out}$ is the nitrogen content in planktonic cells in the outflow (mol L$^{-1}$). No reaction rate $r$ occurs in this equation as elemental nitrogen cannot be created nor destroyed. Integrating Eq. (4) for short time intervals $\Delta t$ between two sampling moments led to an equation for the amount of nitrogen accumulating in that interval:

$$\Delta n_N = (Fc_{N-aq,in} - Fc_{N-aq,out} - Fc_{N-pX,out})\Delta t \tag{4a}$$

Overall nitrogen amount in the reactor over time was described by:

$$n_N = n_{N,0} + \sum \Delta n_N \tag{5}$$

Where $n_{N,0}$ is the initial mol amount of nitrogen, and $\sum \Delta n_N$ is the sum of the amounts of nitrogen accumulated between sampling moments. Assuming that the catholyte composition was similar to the measured outflow composition, the change in amount of dissolved N in the catholyte, obtained from multiplying $c_{N-aq,out}$ by $V_T^C$ was negligible relative to the change in $n_N$. Therefore, the change in nitrogen amount in the cathodic compartment was assumed to be due to uptake by biomass growth. Consequently, assuming $v_{N,X} = 0.2$ mol$_N$ mol$_X^{-1}$ as coefficient of nitrogen in the elemental formula of dry biomass [32], the total amount of biomass in the reactor was obtained from:

$$n_{X,T} = \frac{-n_N}{v_{N,X}} \tag{5a}$$

The concentration of planktonic cells biomass $c_{pX}$ (mol L$^{-1}$) in the catholyte due to planktonic cell growth and detachment of cells from the biofilm was obtained from:

$$c_{pX} = \frac{c_{N-pX}}{v_{N,X}} \tag{6}$$

Biomass-specific rates ($q_i$ in mol$_i$ mol$_X$ d$^{-1}$, including $\mu$) were calculated using:

$$q_i = \frac{r_i V_T^C}{n_{X,T}} \tag{7}$$

Moreover, after multiplying $c_{pX}$ by $V_T^C$ to obtain the amount $n_{pX}$ of planktonic cells in the system, the amount $n_{bX}$ of biofilm-based biomass in the system was obtained from:

$$n_{bX} = n_{X,T} - n_{pX} \tag{8}$$

## 3.3. Results and Discussion

Four reactors were operated under identical conditions as described in the materials and methods in order to derive $q$-values in biofilm-based microbial electrosynthesis. These reactors were used as benchmark reactors based on previous work [11,29]. For the purpose of benchmarking, the performance of these reactors is shown in **Table 3.1** normalized to conventionally used key performance indicators in MES at pseudo steady states. As these pseudo steady states occurred at different times, the selected days vary among reactors. The time-dependent performance of all reactors

is shown in Supplementary Material 3.6.3. An extended version of **Table 3.1** can be found in Supplementary Material 3.6.4.

### 3.3.1. Operational Conditions and the Inoculation of an Enriched Culture Allowed Hexanoate Production after 30 Days

Throughout the experiment acetate, butyrate and hexanoate were the only products measured in relevant amounts. Small peaks for propionate and valerate were observed irregularly, but always below the measurement limit. No alcohol peaks were observed. The first acetate production was recorded in R1 and R3 after 13 days, immediately reaching 1.08 g $L^{-1}$ and 0.46 g $L^{-1}$ respectively. In this study a 50:50 $CO_2/N_2$ ratio was used *versus* 30:70 in previous work. R2 started producing organics on day 19. However, R4 only started producing organics on day 82. The reason behind this observed lag phase is not fully clear, but could be explained by contamination of the reactor by competing microorganisms, as biomass growth as well as current consumption were still observed during the first 82 days. On the same day as acetate was first measured, 230 mg $L^{-1}$ and 210 mg $L^{-1}$ butyrate was recorded in R1 and R3 respectively. This was surprising as according to previous work the threshold $C_2$ concentration triggering butyrate production was 2.5 – 4 g $L^{-1}$ [29]. The start of hexanoate production did match with the threshold of 0.5 – 2.5 $g_{C4}$ $L^{-1}$ observed in said study. It was first measured after 29 days in R1, 77 days in R2, and 131 days in R4. In R3 hexanoate was only recorded in 2 data points (day 103 and day 106). When comparing the data from **Table 3.1** with literature, it can be deduced that all reactors performed in accordance with commonly derived numbers for biofilm-based MES using 3D cathodes [33,34]. The methane inhibitor $BrCH_2CH_2SO_3Na$ (2-BES) was used in this study, which was postulated to function as electron acceptor to oxidize ethanol to $CO_2$ by *Azospira Oryzae* by Steinbusch et al. (2011) [35]. Future research should address if 2-BES affects performance in biofilm- based MES systems. The results show that the reactors were able to produce relevant concentrations of carboxylates up to hexanoate, making them suitable as benchmark systems to determine biomass- specific rates for biofilm-based MES reactors.

**Table 3.1. Conventional key performance indicators in MES: concentration, production rates and current densities.** Selected time periods for R1: days 71-101, for R2: days 75-118, for R3 days 54-92, and for R4 days 141-198. Reactors were operated for 194 days with a HRT of 8 days. $C_2$, $C_4$, and $C_6$ refer to acetate, butyrate, and hexanoate respectively. PSA: projected surface area.

| | | Concentration | Production rates | | | Current densities | |
|---|---|---|---|---|---|---|---|
| | | $g\ L^{-1}$ | Catholyte volume ($g\ L^{-1}\ d^{-1}$) | Electrode volume ($g\ L_{cathode}^{-1}\ d^{-1}$) | Projected surface area ($g\ m^{-2}_{PSA}\ d^{-1}$) | Projected surface area ($A\ m^{-2}_{PSA}$) | Cathode volume ($kA\ m^{-3}$) |
| **R1** | $C_2$ | 5.71±0.32 | 0.74±0.13 | 12.1±2.1 | 121±21 | | |
| | $C_4$ | 3.62±0.36 | 0.48±0.11 | 7.78±1.85 | 77.7±18.5 | -75.17±10.50 | -7.52±1.05 |
| | $C_6$ | 0.08±0.01 | 0.09±0.02 | 1.52±0.28 | 15.2±2.8 | | |
| **R2** | $C_2$ | 4.25±0.32 | 0.54±0.11 | 8.8±1.9 | 88±19 | | |
| | $C_4$ | 0.87±0.21 | 0.11±0.05 | 1.76±0.78 | 17.6±7.8 | -22.19±2.64 | -2.22±0.26 |
| | $C_6$ | 0.09±0.08 | 0.01±0.03 | 0.18±0.44 | 1.8±4.4 | | |
| **R3** | $C_2$ | 4.96±0.16 | 0.64±0.12 | 10.4±2.0 | 104±20 | | |
| | $C_4$ | 0.90±0.18 | 0.11±0.04 | 1.78±0.67 | 17.8±6.8 | -25.55±2.08 | -2.55±0.21 |
| | $C_6$ | n.a. | n.a. | n.a. | n.a. | | |
| **R4** | $C_2$ | 9.37±0.60 | 1.17±0.17 | 19.1±2.8 | 191±28 | | |
| | $C_4$ | 7.99±0.92 | 1.04±0.24 | 17.0±4.0 | 170±40 | -58.56±13.39 | -5.86±1.34 |
| | $C_6$ | 0.72±0.11 | 0.010±0.03 | 1.55±0.43 | 15.5±4.3 | | |

**3**

### 3.3.2. The amount of Biomass Retained in the Reactors Deviated by a Factor of 2 After Full Colonization of the Cathode was Achieved

In **Figure 3.1**, the total nitrogen concentration (A), calculated planktonic cell amount (PCA) (B), calculated total biomass amount (C) and derived $\mu$-values (D) are shown for all four reactors.
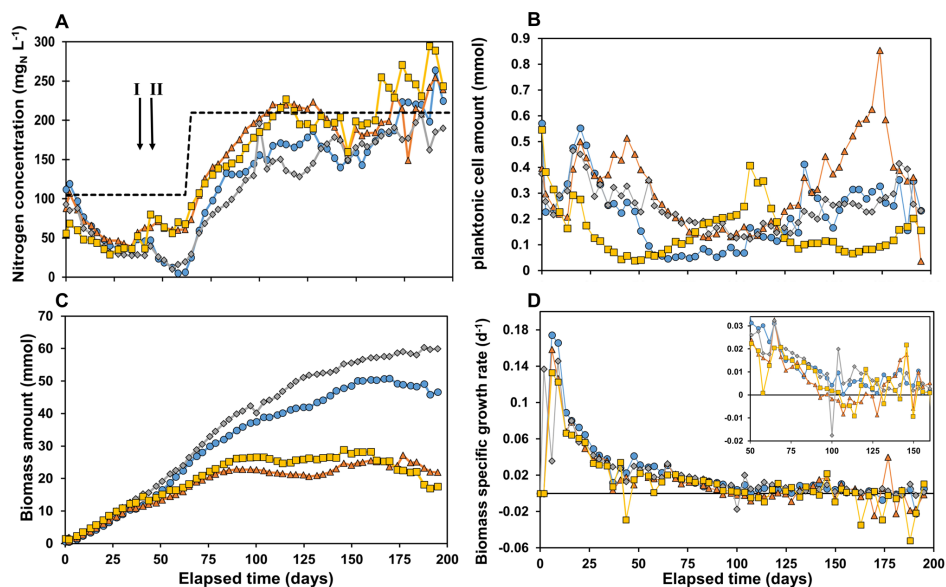
**Figure 3.1. (A)** nitrogen concentration in the reactors, with the total nitrogen inflow concentration as dashed line **(B)** planktonic cell amount in the reactor, **(C)** total biomass amount in the reactor and **(D)** specific growth rate $\mu$. R1 is in blue circles, R2 in orange triangles, R3 in grey diamonds, and R4 in yellow squares. The arrows in figure 1A indicate event I and II as discussed in the materials & methods section.

A decrease in nitrogen concentration was measured in all reactors, indicating nitrogen consumption (**Figure 3.1A**). On day 62 the soluble total nitrogen in R1 and R3 was almost depleted. Hence, it was decided to double the nutrient concentration to prevent limitation. This was implemented in all reactors to maintain similar conditions. After ~100 days the ammonium concentration was close to its feed concentration, indicating limited growth. After 160 days the nitrogen concentration measured was higher than the influent $NH_4^+$-N concentration in R4, with R2 and R1 following on day 167 and 170 respectively. The reason for this was most likely cell lysis of non-viable cells and/or extracellular polymeric substances (EPS) releasing soluble nitrogen compounds (proteins, amino acids and $NH_4^+$). **Figure 3.1B** shows an initially decreasing concentration of planktonic cell amount (PCA) in the reactor. This can be caused by: 1) washout via the effluent and/or 2) biomass attachment to the electrode and consequently biofilm formation. An increasing PCA can be caused by 1) more planktonic cells growth and/or 2) cell detachment from the biofilm. The effect of these phenomena caused significant different trends in PCA in all reactors. After 110 days the PCA started to gradually increase in R2 and performance was deteriorating (see Supplementary Material 3.6.3). After 173 days the reactor PCA sharply decreased and performance spiked.

The reason for this observation is not clear, but it was suspected that something in the system caused substantial resistance which was suddenly reduced as cathodic current significantly increased on day 173. The amount of biomass in all reactors (**Figure 3.1C**) was very similar until reaching $10.9 \pm 1.2$ mmol$_X$ around day 30. From this point onwards, the amount of biomass started to deviate between R1 + R3 and R2 + R4. R1 and R3 reached significantly higher values, plateauing at $50.0 \pm 1.0$ mmol$_X$ and $59.2 \pm 0.8$ mmol$_X$, respectively, both after ~150 days. R2 and R4 plateaued much earlier and at lower values, after about 85 days at $23.1 \pm 1.6$ and $26.5 \pm 1.1$ mmol$_X$, respectively. However, as these trends are not observed in the PCA in **Figure 3.1B**, the plateauing can be attributed to full colonization of the cathode by biofilm. The biomass specific growth rates ($\mu$-values) are shown in **Figure 3.1D**. A lag phase of 3 days was observed in all reactors, after which the $\mu$-value increased to $0.12 - 0.17$ days$^{-1}$. The $\mu$-value steadily decreased for all reactors to $0.026 \pm 0.004$ days$^{-1}$ after 50 days, and below $0.01$ days$^{-1}$ after 100 days. Yet, even after 100 days the difference in biomass amount in the reactors was increasing. This was caused by: 1) the $\mu$-value being routinely higher in R1 and R3 than R2 and R4 over long periods as can be observed in the zoom in window in **Figure 3.1D**, and 2) The $\mu$-value reaching negative values in R2 and R4 especially after 160 days as biofilm- based biomass decays and/or detaches. The results show that the reactors did not behave as replicates even though they were controlled at the same conditions. Due to the complexity of the systems and use of mixed culture the reactor performances are likely extremely sensitive to slight variations in operational conditions (e.g., exact applied potential, temperature, retention time, pH control, electrode packing and placement). The difference in performances between the four reactors deserves further investigation.

### 3.3.3. Biofilm Accounted for >99% of Biomass Present in the Reactors

The most plausible hypothesis for the total amount of biomass in the reactors reaching a plateau as shown in **Figure 3.1C** is biofilm saturation, in which space restriction prevents more biofilm growth. Subtracting the planktonic cells amount (**Figure 3.1B**) from the total amount of biomass (**Figure 3.1C**) gives the biomass retained in the system as biofilm at any time. In Supplementary Material 3.6.5 the ratio between biomass as planktonic cells and biofilm is shown, which shows that after 69 days > 99% of the biomass is in biofilm in all reactors. Photos of the cathodes (membrane side and outflow side) can be found in the Supplementary Material 3.6.6. These images show full coverage of the carbon felt, but the thickness of the biofilm varies. The variation in biomass amount per reactor may be due to the heterogeneity of the structural composition of the carbon felt. Moreover, the

way the carbon felt electrode is placed and packed inside its chamber can unintentionally vary, affecting its porosity and thus the space available for biofilm formation. Consequently, the liquid flow through the carbon felt is also affected by its packing and placement, also impacting local mass transport and biofilm formation. The values of the concentrations of biomass when normalizing to electrode volume at the end of the experiments are 6.7, 3.7, 8.1, and 3.9 $mmol_x$ $cm^{-3}_{cathode}$ for R1, R2, R3, and R4 respectively. These values are in a similar order of magnitude as predicted by Cabau-Peinado et al. (2021), who described microbial kinetics and reactor performance of a comparable MES system by computational modelling [10]. In their model, the biomass concentration in the reactor plateaus after approximately 150 days, with a biomass concentration of 8.2 mmol $cm^{-3}_{cathode}$. In comparison, the theoretical biomass concentration is approximately 13 mmol $cm^{-3}$ (based on a cell density of 1.09 g $cm^{-3}$ and dry weight ratio of 30%) [36]. This would mean that 29 – 63% of the physical space is occupied by biomass in the cathodes.

### 3.3.4. The Biofilm Colonization may be Improved by Growth Medium Engineering and Enhancement of Mass Transport

As also found in this experimental study, μ-values reaching below 0.01 $days^{-1}$ after 100 days of reactor operation resulted from model calculations by Cabau-Peinado et al. (2021) [10]. This indicates that all reactors used in the present study reached a mature biofilm and organics production was most likely maintenance dictated. The derived biomass growth rates in this study are relatively low compared to growth rates found in related anaerobic fermentation technologies such as syngas fermentation and chain elongation. As a consequence, reaching a mature biofilm was relatively time consuming and requires improvement from an application point of view. Reported *μ*-values can widely vary due to suboptimal conditions for biomass growth. For acetogens grown on $H_2/CO_2$ *μ*-values are generally in the region of 1.2 – 2.9 $days^{-1}$ [5,37–40]. The highest reported growth rate is by Groher and Weuster-Botz (2016), who reported a maximum biomass-specific growth rate of 5.77 $days^{-1}$ for the acetogen *Terrisporobacter mayombei* grown on a $H_2/CO_2$ mixture using their developed growth medium specific to acetogens [37]. Candry et al. (2018), obtained a maximum specific growth rate for *Clostridium kluyveri* of 2.9 $days^{-1}$, a model organism frequently studied in carboxylate chain elongation using soluble electron donors [41]. Allaart et al. (2021) found an average growth rate of 1.39 $days^{-1}$ for an open culture when studying the effect of product inhibition in chain elongation using sequencing batch bioreactors [42]. In open cultures, generally lower growth rates are found, ranging between 0.12 $days^{-1}$ to 2.9 $days^{-1}$ [43–45]. The

relatively low growth rates observed in our study may be attributed to absence of vitamins and/or yeast extract supplementation. Species dependent on these supplements must rely on interspecies supplementation of minerals and vitamins, potentially limiting their growth. Growth medium engineering could be performed in follow-up work in order to improve the start-up time and full colonization of the electrode [37,46]. Moreover, the electron transfer mechanisms and mass transport of protons, hydroxide ions, nutrients, substrates, and products in cathodic biofilms should be studied more extensively as these may be contributing factors to growth limitations [47].

### 3.3.5. Biofilms Are Key in this System, But More Does Not Necessarily Result in Higher Volume-Specific Productivity

To study the performance of the reactor's biofilms more extensively, biomass-specific production rates ($q_p$) were determined over time on basis of moles of carbon in the three organic products jointly. The results are shown in **Figure 3.2**.

**3**
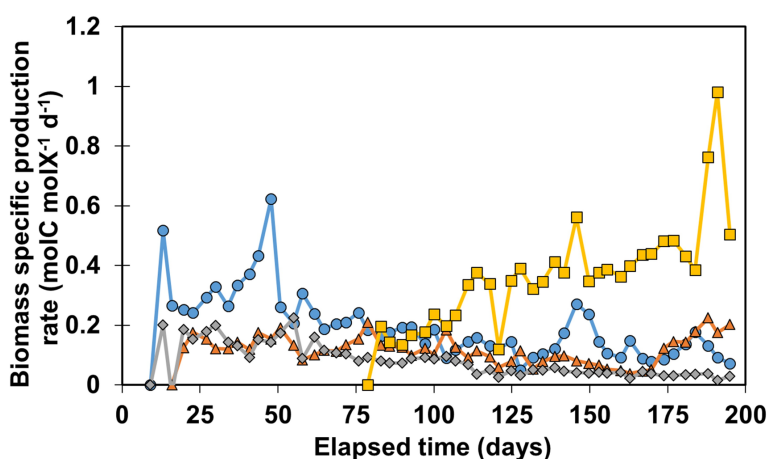


**Figure 3.2. Calculated $q_p$ values for all reactors.** R1 is in blue circles, R2 in orange triangles, R3 in grey diamonds, and R4 in yellow squares.

The general trend for R1-R3 shows a gradual decrease of $q_p$ over time as the biofilm matures. Biomass-specific production rates in R1 increased until day 50, reaching 0.62 mol$_C$ mol$_X$ $^{-1}$ d$^{-1}$, and decreased rapidly to 0.24 mol$_C$ mol$_X$ $^{-1}$ d$^{-1}$. After 55 days the performance of R1 and R3 gradually decreased from 0.2 mol$_C$ mol$_X$ $^{-1}$ d$^{-1}$ to 0.12 mol$_C$ mol$_X$ $^{-1}$ d$^{-1}$ and 0.06 mol$_C$ mol$_X$ $^{-1}$ d$^{-1}$ respectively on day 128. R2 stayed relatively stable around 0.17 mol$_C$ mol$_X$ $^{-1}$ d$^{-1}$, until day 100, after which $q_p$ decreased to 0.06 mol$_C$ mol$_X$ $^{-1}$ d$^{-1}$ on day 160. As production rates increased again, R2 reached 0.2 mol$_C$ mol$_X$ $^{-1}$ d$^{-1}$ at the end of the experiment. Remarkably, organics production was only recorded after 80 days of operation in R4. Contrary to the declining trend

of $q_p$ observed in the other reactors, $q_p$ in R4 increased over time from 0.2 to 0.48 $mol_C$ $mol_X^{-1}$ $d^{-1}$ on day 175. This increase of $q_p$ can be explained by both an increase in volumetric performance during this time as well as a slight decrease in biomass amount retained in the system. It is also possible that this microbial community shifted towards enrichment of acetogens and chain elongators after 80 days. The highest $q_p$ value was recorded in R4 on day 196 at 0.96 $mol_C$ $mol_X^{-1}$ $d^{-1}$, after which it decreased again to 0.49 $mol_C$ $mol_X^{-1}$ $d^{-1}$. No clogging of influent or effluent tubing was observed between day 183 – 195 which could have explained the two outliers. The results of **Figure 3.2** illustrate that $q_p$ is a variable that can fluctuate over time, showing a decreasing trend when biomass amount increased while production rates at reactor scale are relatively stable. More biomass present in the system does not necessarily mean higher volumetric productivity, especially in systems with active cell retention. For example, R4 retained three times less biomass than R3 (**Figure 3.1C**), however the biomass in R4 is 11.6 ± 3.2 times more active in terms of biomass-specific production rate than the biomass in R3 between day 150 and 183 (**Figure 3.2**).

### 3.3.6. Biomass-Specific Production Rates in MES Can Be Enhanced

In **Table 3.2** the average $q_p$ of the MES reactors are compared to several syngas fermentation and chain elongation studies in order to assess whether the derived values for $q_p$ are relevant or insignificant quantities. These studies were selected based on whether $q_p$ was reported and/or sufficient data was provided to calculate it. Moreover, the studies are compared based on whether they utilize open or single cultures, on the substrate(s) used, and whether a biofilm was formed or only suspended cells were considered.

The table illustrates that in general, the performance of the MES reactors normalized to biomass amount was relatively low. The study most closely related to the current study is by Zhang et al. (2013), as they formed an open culture biofilm in a hollow fiber membrane bioreactor producing medium chained carboxylates up to caprylate (C8) from a $CO_2/H_2$ mixture [48]. Their $q_p$ is lower than the average $q_p$ measured in R4, but higher than the average found in the other reactors. The highest $q_p$ values were found in more recent single culture syngas fermentation studies, with the exception of the chain elongation study [43]. In their study, they managed to form chain elongating granular sludge, allowing cell retention and applying relatively short hydraulic retention time, increasing steady-state soluble substrate concentrations, decreasing product inhibition, and therefore increasing production rates. This comparative analysis highlights that there is room to significantly improve metabolic rates in MES.

**Table 3.2. Comparison of reactor performance with Syngas fermentation and Chain elongation fermentation.** For studies normalizing biomass to dry cell weight (DCW), a molecular weight of 25.25 g mol⁻¹ was used for biomass. For studies normalizing biomass to volatile suspended solids (VSS) it was assumed that 1 gVSS equals 1 gDCW. $C_5$, $C_7$, and $C_8$ refer to pentanoate, heptanoate, and octanoate respectively.

| Technique | Culture | Biofilm/ Planktonic | Input composition | Main Products | $q_p$ (molC molx⁻¹ d⁻¹) | Reference |
|---|---|---|---|---|---|---|
| **Microbial electrosynthesis** | Open | Biofilm | $e^-/CO_2$ | Carboxylates $C_2, C_4, C_6$ | 0.08 - 0.37 | Average between reactors in this study |
| **Gas fermentation** | Open | Biofilm | $H_2/CO_2$ | Carboxylates $C_2, C_4, C_6, C_8$ | 0.31 | [49] |
| **Gas fermentation** | Pure | Planktonic | $H_2/CO_2$ | Acetate, Ethanol | 0.23 | [50] |
| **Syngas fermentation** | Pure | Planktonic | $H_2/CO/CO_2$ | Acetate, Ethanol | 0.81 | [51] |
| **Syngas fermentation** | Pure | Planktonic | $H_2/CO/CO_2$ | Acetate, Ethanol | 9.49 | [52] |
| **Syngas fermentation** | Pure | Planktonic | $H_2/CO/CO_2$ | Acetate, Ethanol | 2.94 | [53] |

(See continuation on next page)

**3**

Continuation of **Table 3.2.**

| Technique | Culture | Biofilm/ Planktonic | Input composition | Main Products | $q_p$ (molC molx$^{-1}$d$^{-1}$) | Reference |
|---|---|---|---|---|---|---|
| **Syngas fermentation** | Pure | Planktonic | $H_2/CO/CO_2$ | Acetate, Ethanol | 7.58 | [54] |
| **Syngas fermentation** | Pure | Planktonic | $H_2/CO/CO_2$ | Acetate, Ethanol | 12.4 | [55] |
| **Syngas fermentation** | Pure | Planktonic | $H_2/CO/CO_2$ | Acetate, Ethanol | 0.73 | [56] |
| **Syngas fermentation** | Pure | Planktonic | $H_2/CO/CO_2$ | Acetate, Ethanol | 0.12 | [57] |
| **Chain elongation** | Pure | Planktonic | Acetate + Ethanol | Carboxylates $C_4,C_6,C_8$ | 0.26 | [58] |
| **Chain elongation** | Open | Biofilm + Planktonic | Acetate + Ethanol | Carboxylates $C_4,C_5,C_6,C_7$ | 10.0 | [59] |

### 3.3.7. Limitations of this Study

Even though the method used in this study circumvents several disadvantages of more commonly used techniques, there are still some limitations. Most evident, the method relies on the assumption that the gap in the nitrogen balance when accounting for outflow of medium and suspended cells can be assigned to biofilm-based biomass. Several phenomena can potentially complicate this method. The identified complications relevant for the current study are nitrogen accumulation in extracellular polymer substances, nitrogen-containing salt precipitation and retained non-viable cells accumulating in biofilm. To determine if accumulation of non-viable cells in the biofilm may have caused an underestimation of $q_p$, live/dead staining was performed at three different locations of the cathode for every reactor. Confocal images can be found in the Supplementary Material 3.6.7 and were analyzed for viable/non-viable ratio using biofilm viability checker tool developed by Mountcastle et al. (2021) [30] for ImageJ [60]. The results of the analysis are illustrated in **Figure 3.3**.
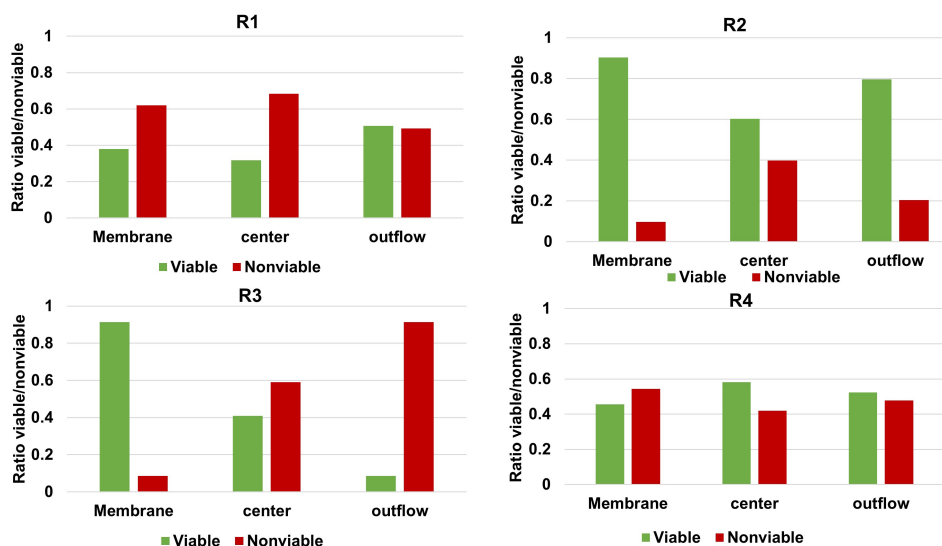


**Figure 3.3. Relative abundance of live and dead microorganisms in the cathodic biofilm of each MES reactor at three different locations of the carbon felt.**

**Figure 3.3** shows that in all reactors a significant percentage of the biofilm stained as non-viable, but the extent varies greatly per reactor and per location. Izadi et al. (2020) found >90% of viable cells in their biofilm-based MES reactor when applying −1 V vs. Ag/ AgCl and feeding $CO_2$, after 104 days while refreshing 40% of the medium every 14–21 days [61]. The higher non-viable cell ratio in our study may be explained by the longer operation of 194 days and diminished biomass growth rates

as illustrated in **Figure 3.1D**. Based on the significant ratio of non-viable cells shown in **Figure 3.3** it should therefore be noted that the biomass-specific rates ($q_p$ and $\mu$-values) of the reactors were indeed underestimated due to retained non-viable biomass in the biofilm. The main advantages of the method are that it allows *operando* monitoring of biomass amount present in the system in a non-destructive manner. Techniques to improve the accuracy, e.g., EPS and live/dead determination, can be considered as complementary. When applying this method to other METs, other limitations may be important as well. In this study, reducing conditions were used, but if ammonium can get oxidized to NOx and/or elemental nitrogen, off-gas analysis may be required to close the nitrogen balance. In other cases, low biomass quantity or low nitrogen content may compromise using the nitrogen balance. Moreover, in this study $OD_{600nm}$ was used to calibrate nitrogen content in suspended cells, which is known to fluctuate over time even in pure cultures [41]. This can be circumvented by updating the calibration over time. The impact of any change in the slope of the calibration curve presented for the systems used in this study is very low. This is due to the low optical density recorded, and thus low planktonic cell concentration, in comparison to total biomass amount retained in the reactors. However, other continuous systems with a higher ratio of planktonic biomass could be impacted to a larger extent as a higher or lower ratio of the biomass retained in the system would wash out. Moreover, in systems with much higher suspended cell densities versus biofilm cells or larger reactor volumes, other methods such as routine dry weight measurements of reactor broth may become viable methods as well.

### 3.3.8. Biomass Specific Rates Are the True Microbial Performance Indicators

When normalizing the production rate to projected surface area of the electrode (PSA), an average production rate of $214 \pm 43$ g m$^{-2}$ PSA d$^{-1}$ and current density of $-75 \pm 10$ A m$^{-2}$ PSA in R1 were found, which is within the top 5% of MES studies, as reported in the review by Flexer and Jourdin (2020) [34]. Even though current densities, production rates and titers reported in this study are reasonable compared to previous studies in MES, biomass specific production rates show that the microbial community is most likely facing limitations and is not performing to its full potential. This information is key in order to assess the true impact of changes such as in operational conditions, reactor configuration or electrode modifications on the microbial performance. Studying the biofilm as described in this study allows differentiating improvements in performance thanks to increased biomass quantity or to higher metabolic activity. Moreover, it allows comparing performance to other biotechnological processes such as syngas fermentation or chain elongation. Further

research should focus on investigating what is limiting biofilm-based MES. As demonstrated in the results section, significant differences in performance were observed for all reactors. The reasons for these differences are currently unknown and should be studied more extensively. Proposed research areas are cathode design (especially porosity) and interactions within the microbial community, using biomass specific rates as key performance indicators (growth, uptake and production rates).

## 3.4. Acknowledgements

## 3.5. References

[1]     H. Wang, Z.J. Ren, A comprehensive review of microbial electrochemical systems as a platform technology, Biotechnol Adv 31 (2013) 1796–1807. https://doi.org/10.1016/j.biotechadv.2013.10.001.

[2]     S.A. Patil, S. Gildemyn, D. Pant, K. Zengler, B.E. Logan, K. Rabaey, A logical data representation framework for electricity-driven bioproduction processes, Biotechnol Adv 33 (2015) 736–744. https://doi.org/10.1016/j.biotechadv.2015.03.002.

[3]     H.M. Fruehauf, F. Enzmann, F. Harnisch, R. Ulber, D. Holtmann, Microbial Electrosynthesis—An Inventory on Technology Readiness Level and Performance of Different Process Variants, Biotechnol J 15 (2020). https://doi.org/10.1002/biot.202000066.

[4]     L. Jourdin, T. Burdyny, Microbial Electrosynthesis: Where Do We Go from Here?, Trends Biotechnol 39 (2021) 359–369. https://doi.org/10.1016/j.tibtech.2020.10.014.

[5]     J.J. Heijnen, J.A. Roels, A.H. Stouthamer, Application of balancing methods in modeling the penicillin fermentation, Biotechnol Bioeng 21 (1979) 2175–2201. https://doi.org/10.1002/bit.260211204.

[6]     D.L. Rice, A Simple mass transport model for metal uptake by marine macroalgae growing at different rates, J Exp Mar Biol Ecol 82 (1984) 175–182. https://doi.org/10.1016/0022-0981(84)90102-3.

[7]     P. Wechselberger, P. Sagmeister, C. Herwig, Real-time estimation of biomass and specific growth rate in physiologically variable recombinant fed-batch processes, Bioprocess Biosyst Eng 36 (2013) 1205–1218. https://doi.org/10.1007/s00449-012-0848-4.

[8]     K. Rabaey, R.A. Rozendal, Microbial electrosynthesis — revisiting the electrical route for microbial production, Nat Rev Microbiol 8 (2010) 706–716. https://doi.org/10.1038/nrmicro2422.

[9]     A. Sydow, T. Krieg, R. Ulber, D. Holtmann, Growth medium and electrolyte—How to combine the different requirements on the reaction solution in bioelectrochemical systems using *Cupriavidus necator*, Eng Life Sci 17 (2017) 781–791. https://doi.org/10.1002/elsc.201600252.

[10]    O. Cabau-Peinado, A.J.J. Straathof, L. Jourdin, A General Model for Biofilm-Driven Microbial Electrosynthesis of Carboxylates From CO2, Front Microbiol 12 (2021). https://doi.org/10.3389/fmicb.2021.669218.

[11]    L. Jourdin, M. Winkelhorst, B. Rawls, C.J.N. Buisman, D.P.B.T.B. Strik, Enhanced selectivity to butyrate and caproate above acetate in continuous bioelectrochemical chain elongation from CO2:

**3**

Steering with CO2 loading rate and hydraulic retention time, Bioresour Technol Rep 7 (2019) 100284. https://doi.org/10.1016/j.biteb.2019.100284.

[12]    B.M. Weckhuysen, Snapshots of a working catalyst: possibilities and limitations of in situ spectroscopy in the field of heterogeneous catalysis, Chemical Communications (2002) 97–110. https://doi.org/10.1039/b107686h.

[13]    A.P. Magalhães, Â. França, M.O. Pereira, N. Cerca, RNA-based qPCR as a tool to quantify and to characterize dual-species biofilms, Sci Rep 9 (2019) 13639. https://doi.org/10.1038/s41598-019-50094-3.

[14]    S. Babanova, K. Carpenter, S. Phadke, S. Suzuki, S. Ishii, T. Phan, E. Grossi-Soyster, M. Flynn, J. Hogan, O. Bretschger, The Effect of Membrane Type on the Performance of Microbial Electrosynthesis Cells for Methane Production, J Electrochem Soc 164 (2017) H3015–H3023. https://doi.org/10.1149/2.0051703jes.

[15]    M. Vignola, D. Werner, F. Hammes, L.C. King, R.J. Davenport, Flow-cytometric quantification of microbial cells on sand from water biofilters, Water Res 143 (2018) 66–76. https://doi.org/10.1016/j.watres.2018.05.053.

[16]    S.D. Molenaar, T. Sleutels, J. Pereira, M. Iorio, C. Borsje, J.A. Zamudio, F. Fabregat-Santiago, C.J.N. Buisman, A. ter Heijne, In situ Biofilm Quantification in Bioelectrochemical Systems by using Optical Coherence Tomography, ChemSusChem 11 (2018) 2171–2178. https://doi.org/10.1002/cssc.201800589.

[17]    J. Hou, C. Wang, R.T. Rozenbaum, N. Gusnaniar, E.D. de Jong, W. Woudstra, G.I. Geertsema-Doornbusch, J. Atema-Smit, J. Sjollema, Y. Ren, H.J. Busscher, H.C. van der Mei, Bacterial Density and Biofilm Structure Determined by Optical Coherence Tomography, Sci Rep 9 (2019) 9794. https://doi.org/10.1038/s41598-019-46196-7.

[18]    G. Wolf, J.G. Crespo, M.A.M. Reis, Optical and spectroscopic methods for biofilm examination and monitoring, Rev Environ Sci Biotechnol 1 (2002) 227–251. https://doi.org/10.1023/A:1021238630092.

[19]    L. Häuser, J. Erben, G. Pillot, S. Kerzenmacher, W. Dreher, E. Küstermann, *In vivo* characterization of electroactive biofilms inside porous electrodes with MR Imaging, RSC Adv 12 (2022) 17784–17793. https://doi.org/10.1039/D2RA01162J.

[20]    B.J. Eddie, Z. Wang, A.P. Malanoski, R.J. Hall, S.D. Oh, C. Heiner, B. Lin, S.M. Strycharz-Glaven, 'Candidatus Tenderia electrophaga", an uncultivated electroautotroph from a biocathode enrichment,' Int J Syst Evol Microbiol 66 (2016) 2178–2185. https://doi.org/10.1099/ijsem.0.001006.

[21]    D.A. Phillips, L.J. Bird, B.J. Eddie, M.D. Yates, L.M. Tender, C.A. Voigt, S.M. Glaven, Activation of Protein Expression in Electroactive Biofilms, ACS Synth Biol 9 (2020) 1958–1967. https://doi.org/10.1021/acssynbio.0c00278.

[22]    M. Relucenti, G. Familiari, O. Donfrancesco, M. Taurino, X. Li, R. Chen, M. Artini, R. Papa, L. Selan, Microscopy Methods for Biofilm Imaging: Focus on SEM and VP-SEM Pros and Cons, Biology (Basel) 10 (2021) 51. https://doi.org/10.3390/biology10010051.

[23]    C. Huang, G.A. Mcfeters, P.S. Stewart, Evaluation of physiological staining, cryoembedding and autofluorescence quenching techniques on fouling biofilms, Biofouling 9 (1996) 269–277. https://doi.org/10.1080/08927019609378309.

[24]    M.J. Franklin, C. Chang, T. Akiyama, B. Bothner, New Technologies for Studying Biofilms, Microbiol Spectr 3 (2015). https://doi.org/10.1128/microbiolspec.MB-0016-2014.

[25]    F. Persson, C. Suarez, M. Hermansson, E. Plaza, R. Sultana, B. Wilén, Community structure of partial nitritation-anammox biofilms at decreasing substrate concentrations and low temperature, Microb Biotechnol 10 (2017) 761–772. https://doi.org/10.1111/1751-7915.12435.

[26]    M. Hackbarth, T. Jung, J.E. Reiner, J. Gescher, H. Horn, A. Hille-Reichel, M. Wagner, Monitoring and quantification of bioelectrochemical Kyrpidia spormannii biofilm development in a novel flow cell setup, Chemical Engineering Journal 390 (2020) 124604. https://doi.org/10.1016/j.cej.2020.124604.

[27]    P.S. Stewart, Mini-review: Convection around biofilms, Biofouling 28 (2012) 187–198. https://doi.org/10.1080/08927014.2012.662641.

[28]    S. Bottero, T. Storck, T.J. Heimovaara, M.C.M. van Loosdrecht, M. V. Enzien, C. Picioreanu, Biofilm development and the dynamics of preferential flow paths in porous media, Biofouling 29 (2013) 1069–1086. https://doi.org/10.1080/08927014.2013.828284.

[29]    L. Jourdin, S.M.T. Raes, C.J.N. Buisman, D.P.B.T.B. Strik, Critical Biofilm Growth throughout Unmodified Carbon Felts Allows Continuous Bioelectrochemical Chain Elongation from CO2 up to Caproate at High Current Density, Front Energy Res 6 (2018). https://doi.org/10.3389/fenrg.2018.00007.

[30]    S.E. Mountcastle, N. Vyas, V.M. Villapun, S.C. Cox, S. Jabbari, R.L. Sammons, R.M. Shelton, A.D. Walmsley, S.A. Kuehne, Biofilm viability checker: An open-source tool for automated biofilm viability analysis from confocal microscopy images, NPJ Biofilms Microbiomes 7 (2021) 44. https://doi.org/10.1038/s41522-021-00214-7.

[31]    R. de Rink, M. B. Lavender, D. Liu, J.B.M. Klok, D.Y. Sorokin, A. ter Heijne, C.J.N. Buisman, Continuous electron shuttling by sulfide oxidizing bacteria as a novel strategy to produce electric current, J Hazard Mater 424 (2022) 127358. https://doi.org/10.1016/j.jhazmat.2021.127358.

[32]    M. Popovic, Thermodynamic properties of microorganisms: determination and analysis of enthalpy, entropy, and Gibbs free energy of biomass, cells and colonies of 32 microorganism species, Heliyon 5 (2019) e01950. https://doi.org/10.1016/j.heliyon.2019.e01950.

[33]    A. Prévoteau, J.M. Carvajal-Arroyo, R. Ganigué, K. Rabaey, Microbial electrosynthesis from CO2: forever a promise?, Curr Opin Biotechnol 62 (2020) 48–57. https://doi.org/10.1016/j.copbio.2019.08.014.

[34]    V. Flexer, L. Jourdin, Purposely Designed Hierarchical Porous Electrodes for High Rate Microbial Electrosynthesis of Acetate from Carbon Dioxide, Acc Chem Res 53 (2020) 311–321. https://doi.org/10.1021/acs.accounts.9b00523.

[35]    K.J.J. Steinbusch, H.V.M. Hamelers, C.M. Plugge, C.J.N. Buisman, Biological formation of caproate and caprylate from acetate: fuel and chemical production from low grade biomass, Energy Environ. Sci. 4 (2011) 216–224. https://doi.org/10.1039/C0EE00282H.

**3**

[36]     L.R. Bakken, R.A. Olsen, Buoyant Densities and Dry-Matter Contents of Microorganisms: Conversion of a Measured Biovolume into Biomass, Appl Environ Microbiol 45 (1983) 1188–1195. https://doi.org/10.1128/aem.45.4.1188-1195.1983.

[37]     A. Groher, D. Weuster-Botz, General medium for the autotrophic cultivation of acetogens, Bioprocess Biosyst Eng 39 (2016) 1645–1650. https://doi.org/10.1007/s00449-016-1634-5.

[38]     F.R. Bengelsdorf, M.H. Beck, C. Erz, S. Hoffmeister, M.M. Karl, P. Riegler, S. Wirth, A. Poehlein, D. Weuster-Botz, P. Dürre, Bacterial Anaerobic Synthesis Gas (Syngas) and CO 2 + H 2 Fermentation, in: Adv. Appl. Microbiol. 2018: pp. 143–221. https://doi.org/10.1016/bs.aambs.2018.01.002.

[39]     B. Acharya, A. Dutta, P. Basu, Ethanol production by syngas fermentation in a continuous stirred tank bioreactor using *Clostridium ljungdahlii*, Biofuels 10 (2019) 221–237. https://doi.org/10.1080/17597269.2017.1316143.

[40]     J. Philips, Extracellular Electron Uptake by Acetogenic Bacteria: Does H2 Consumption Favor the H2 Evolution Reaction on a Cathode or Metallic Iron?, Front Microbiol 10 (2020). https://doi.org/10.3389/fmicb.2019.02997.

[41]     P. Candry, T. Van Daele, K. Denis, Y. Amerlinck, S.J. Andersen, R. Ganigué, J.B.A. Arends, I. Nopens, K. Rabaey, A novel high-throughput method for kinetic characterisation of anaerobic bioproduction strains, applied to Clostridium kluyveri, Sci Rep 8 (2018) 9724. https://doi.org/10.1038/s41598-018-27594-9.

[42]     M.T. Allaart, G.R. Stouten, D.Z. Sousa, R. Kleerebezem, Product Inhibition and pH Affect Stoichiometry and Kinetics of Chain Elongating Microbial Communities in Sequencing Batch Bioreactors, Front Bioeng Biotechnol 9 (2021). https://doi.org/10.3389/fbioe.2021.693030.

[43]     M. Roghair, D.P.B.T.B. Strik, K.J.J. Steinbusch, R.A. Weusthuis, M.E. Bruins, C.J.N. Buisman, Granular sludge formation and characterization in a chain elongation process, Process Biochemistry 51 (2016) 1594–1598. https://doi.org/10.1016/j.procbio.2016.06.012.

[44]     P. Candry, S. Huang, J.M. Carvajal-Arroyo, K. Rabaey, R. Ganigue, Enrichment and characterisation of ethanol chain elongating communities from natural and engineered environments, Sci Rep 10 (2020) 3682. https://doi.org/10.1038/s41598-020-60052-z.

[45]     S. Shrestha, B. Colcord, X. Fonoll, L. Raskin, Fate of influent microbial populations during medium chain carboxylic acid recovery from brewery and pre-fermented food waste streams, Environ Sci (Camb) 8 (2022) 257–269. https://doi.org/10.1039/D1EW00656H.

[46]     F. Ammam, P.-L. Tremblay, D.M. Lizak, T. Zhang, Effect of tungstate on acetate and ethanol production by the electrosynthetic bacterium Sporomusa ovata, Biotechnol Biofuels 9 (2016) 163. https://doi.org/10.1186/s13068-016-0576-0.

[47]     L. Jourdin, T. Burdyny, Microbial Electrosynthesis: Where Do We Go from Here?, Trends Biotechnol 39 (2021) 359–369. https://doi.org/10.1016/j.tibtech.2020.10.014.

[48]     F. Zhang, J. Ding, Y. Zhang, M. Chen, Z.-W. Ding, M.C.M. van Loosdrecht, R.J. Zeng, Fatty acids production from hydrogen and carbon dioxide by mixed culture in the membrane biofilm reactor, Water Res 47 (2013) 6122–6129. https://doi.org/10.1016/j.watres.2013.07.033.

[49]    F. Zhang, J. Ding, Y. Zhang, M. Chen, Z.W. Ding, M.C.M. van Loosdrecht, R.J. Zeng, Fatty acids production from hydrogen and carbon dioxide by mixed culture in the membrane biofilm reactor, Water Research 47 (2013) 6122–6129. https://doi.org/10.1016/j.watres.2013.07.033.

[50]    F. Ammam, P.L. Tremblay, D.M. Lizak, T. Zhang, Effect of tungstate on acetate and ethanol production by the electrosynthetic bacterium Sporomusa ovata, Biotechnology for Biofuels 9 (2016) 163. https://doi.org/10.1186/s13068-016-0576-0.

[51]    Y. Shen, R. Brown, Z. Wen, Syngas fermentation of Clostridium carboxidivoran P7 in a hollow fiber membrane biofilm reactor: Evaluating the mass transfer coefficient and ethanol production performance, Biochemical Engineering Journal 85 (2014) 21–29. https://doi.org/10.1016/j.bej.2014.01.010.

[52]    J. Lee, J.W. Lee, C.G. Chae, S.J. Kwon, Y.J. Kim, J.H. Lee, H.S. Lee, Domestication of the novel alcohologenic acetogen Clostridium sp. AWRP: From isolation to characterization for syngas fermentation, Biotechnology for Biofuels 12 (2019) 228. https://doi.org/10.1186/s13068-019-1570-0.

[53]    S. Shen, G. Wang, M. Zhang, Y. Tang, Y. Gu, W. Jiang, Y. Wang, Y. Zhuang, Effect of temperature and surfactant on biomass growth and higher-alcohol production during syngas fermentation by Clostridium carboxidivorans P7, Bioresources and Bioprocessing 7 (2020) 56. https://doi.org/10.1186/s40643-020-00344-4.

[54]    K. Valgepea, R. de Souza Pinto Lemgruber, K. Meaghan, R.W. Palfreyman, T. Abdalla, B.D. Heijstra, J.B. Behrendorff, R. Tappel, M. Köpke, S.D. Simpson, L.K. Nielsen, E. Marcellin, Maintenance of ATP Homeostasis Triggers Metabolic Shifts in Gas-Fermenting Acetogens, Cell Systems 4 (2017) 505-515.e5. https://doi.org/10.1016/j.cels.2017.04.008.

[55]    J.K. Heffernan, K. Valgepea, R. de Souza Pinto Lemgruber, I. Casini, M. Plan, R. Tappel, S.D. Simpson, M. Köpke, L.K. Nielsen, E. Marcellin, Enhancing CO2-Valorization Using Clostridium autoethanogenum for Sustainable Fuel and Chemicals Production, Frontiers in Bioengineering and Biotechnology 8 (2020) 204. https://doi.org/10.3389/fbioe.2020.00204.

[56]    A. Ahmed, B.G. Cateni, R.L. Huhnke, R.S. Lewis, Effects of biomass-generated producer gas constituents on cell growth, product distribution and hydrogenase activity of Clostridium carboxidivorans P7T, Biomass and Bioenergy 30 (2006) 665–672. https://doi.org/10.1016/j.biombioe.2006.01.007.

[57]    J.R. Phillips, K.T. Klasson, E.C. Clausen, J.L. Gaddy, Biological production of ethanol from coal synthesis gas - Medium development studies, Applied Biochemistry and Biotechnology 39–40 (1993) 559–571. https://doi.org/10.1007/BF02919018.

[58]    K.J.J. Steinbusch, H.V.M. Hamelers, C.M. Plugge, C.J.N. Buisman, Biological formation of caproate and caprylate from acetate: Fuel and chemical production from low grade biomass, Energy and Environmental Science 4 (2011) 216–224. https://doi.org/10.1039/c0ee00282h.

[59]    M. Roghair, D.P.B.T.B. Strik, K.J.J. Steinbusch, R.A. Weusthuis, M.E. Bruins, C.J.N. Buisman, Granular sludge formation and characterization in a chain elongation process, Process Biochemistry 51 (2016) 1594–1598. https://doi.org/10.1016/j.procbio.2016.06.012.

**3**

[60]     D. Legland, I. Arganda-Carreras, P. Andrey, MorphoLibJ: integrated library and plugins for mathematical morphology with ImageJ, Bioinformatics 32 (2016) 3532–3534. https://doi.org/10.1093/bioinformatics/btw413.

[61]     P. Izadi, J.-M. Fontmorin, A. Godain, E.H. Yu, I.M. Head, Parameters influencing the development of highly conductive and efficient biofilm during microbial electrosynthesis: the importance of applied potential and inorganic carbon source, NPJ Biofilms Microbiomes 6 (2020) 40. https://doi.org/10.1038/s41522-020-00151-x.

## 3.6. Supplementary Material

### 3.6.1. Schematic Overview Reactor Set Up
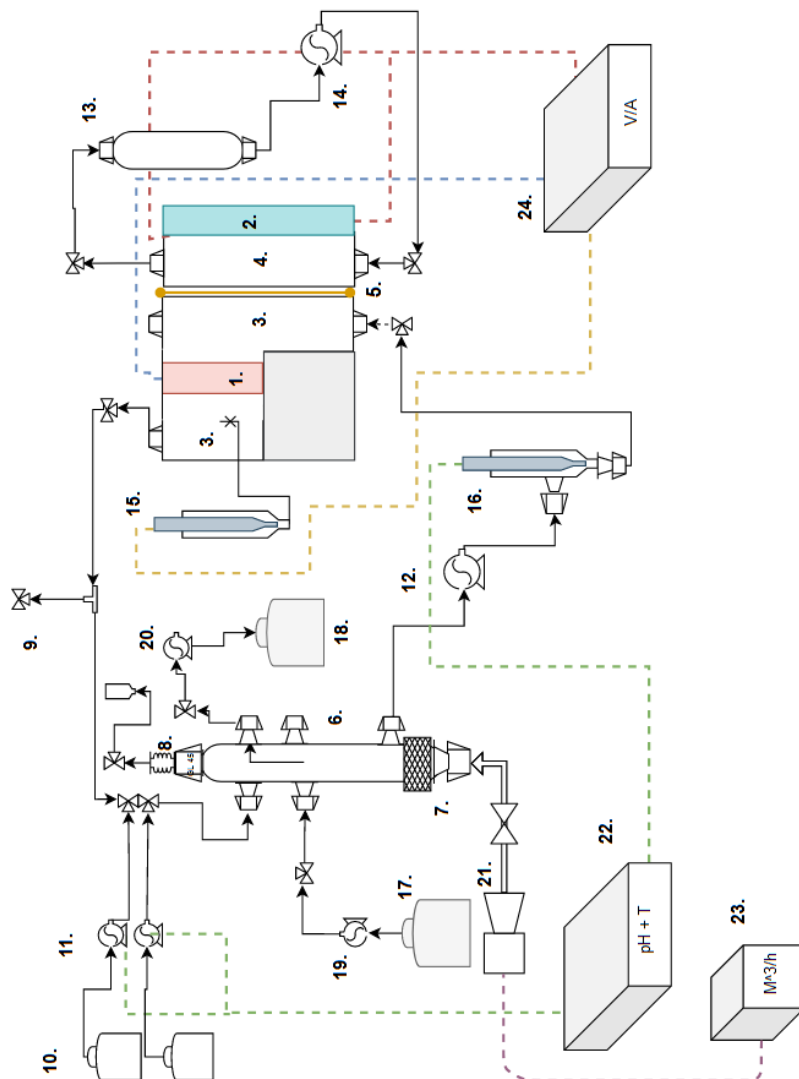


**Figure 3S 1. Schematic overview of the reactor set up.** The numbers represent: 1. Cathode, 2. Anode, 3. Cathode chamber, 4. Anode chamber, 5. (Cation exchange) membrane 6. Cathode medium recirculation column 7. Gas sparger, 8. Condenser, 9. Sampling point, 10. pH control flasks (1M HCl and 1M NaOH), 11. pH control pumps, 12. Cathode recirculation pump 13. Anode medium recirculation bottle, 14. Anode recirculation pump, 15. Reference electrode (Ag/AgCl 3M KCl), 16. pH meter + flask, 17. Influent bottle, 18. Effluent bottle, 19. Influent pump, 20. Effluent pump, 21. Mass flow controller, 22. pH and temperature controller, 23. Mass flow controller operator, 24. Potentiostat. The black arrows represent tubing, the black dotted arrow represents the potential "safety" tubing to bypass the cathode, the yellow dotted, blue dotted and red dotted lines represent the reference, cathodic and anodic cables respectively, the green dotted line represents the pH control cables and the purple dotted line represents the mass flow control cable.
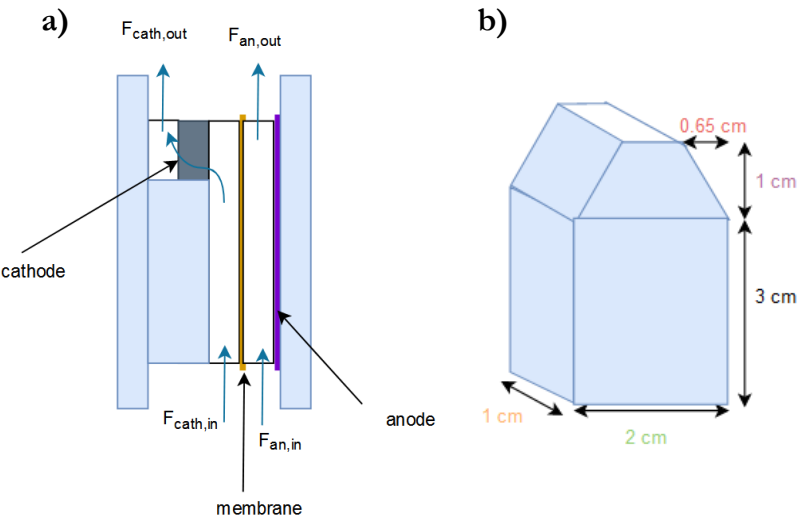
**Figure 3S 2. Schematic overview of a)** reactor cell with catholyte flow path; **b)** cathode with its dimensions. The cathode's projected surface area equals 7.35 cm², the volume equals 7.35 cm³.

### 3.6.2. Nitrogen Balance

i. <u>Schematic overview parameters</u>
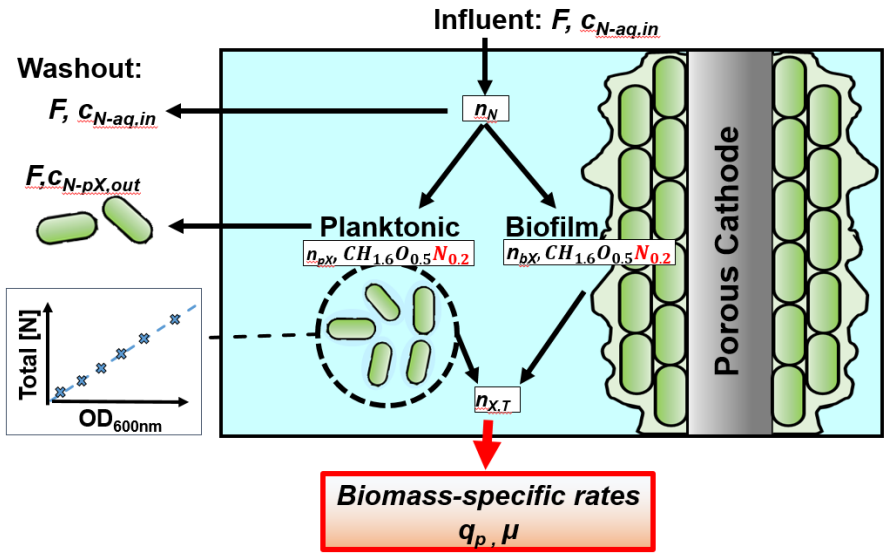


**Figure 3S 3. Schematic overview parameters.**

ii.    Parameter list & abbreviations

**Table 3S 1. List of parameters.**

| Symbol | Description parameter | Unit |
|--------|----------------------|------|
| $n_i$ | mole amount of compound $i$ | $Mol_i$ |
| $t$ | Time | d |
| $F$ | Flow rate | L d$^{-1}$ |
| $V_T{}^f$ | Total catholyte volume | L |
| $r_i$ | Reaction rate of compound i | $Mol_i$ d$^{-1}$ |
| $c_{i,in}$ | Inflow concentration compound i | $Mol_i$ L$^{-1}$ |
| $c_{i,out}$ | Outflow concentration compound i | $Mol_i$ L$^{-1}$ |
| $FE\%$ | Faradaic efficiency | % |
| $Q_{products}$ | Amount of electric charge retrieved in the products of interest | Coulomb |
| $Q_T$ | Total electric charge provided | Coulomb |
| $v_{i,y}$ | Stoichiometric coefficient of i in y | Dimensionless |
| $q_i$ | Biomass-specific production/consumption rate of compound i | mol$_i$ mol$_X$ d$^{-1}$ |

**Table 3S 2. List of subscripts used to discriminate parameters.**

| Subscript | Description subscript |
|-----------|---------------------|
| $N$ | Nitrogen |
| $N$-*aq,in* | Soluble nitrogen in inflow |
| $N$-*aq,out* | Soluble nitrogen in outflow |
| $N$-*pX,out* | Nitrogen content of planktonic biomass in outflow |
| $N,0$ | Starting nitrogen content |
| $N,X$ | Nitrogen content in biomass |
| $X,T$ | Total biomass |
| $bX$ | Biofilm biomass |
| $pX$ | Planktonic biomass |

### iii.   Nitrogen versus optical density calibration curve
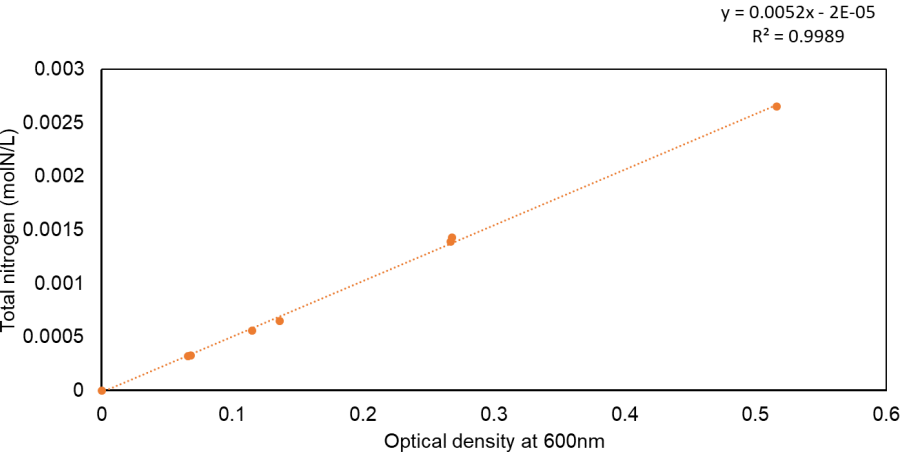


**Figure 3S 4. Calibration total nitrogen with optical density.**

## 3.6.3. Reactor Performance

### i.   Measured optical density for all reactors
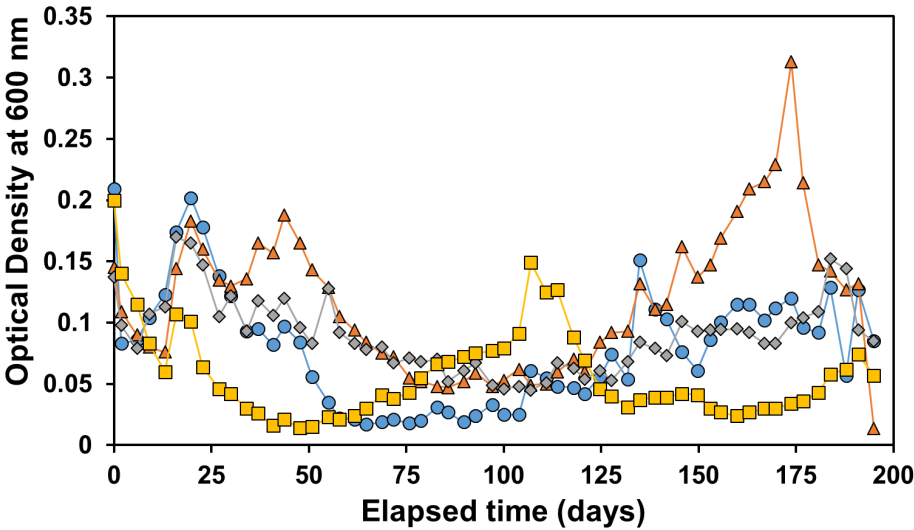


**Figure 3S 5. Measured optical density at 600 nm for all reactors.** R1 is in blue circles, R2 in orange triangles, R3 in grey diamonds, and R4 in yellow squares.

ii.    Performance of R1
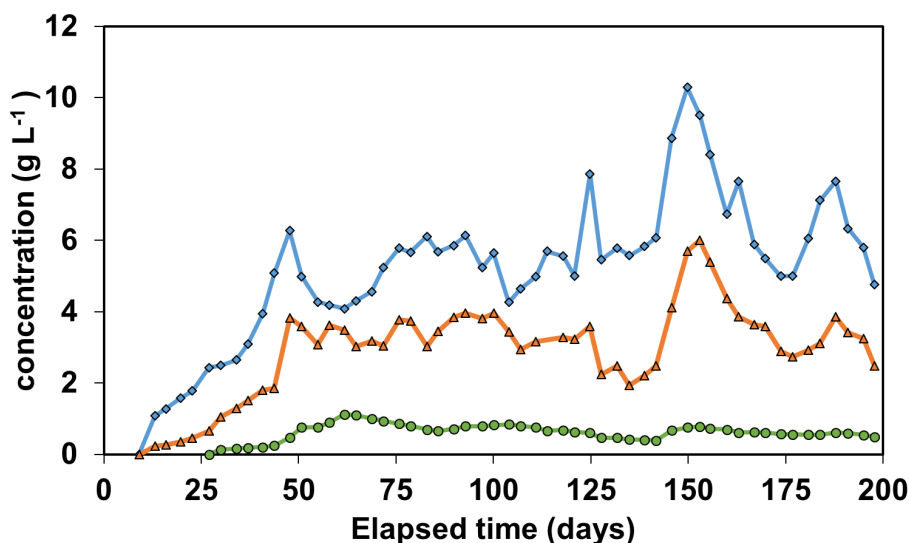


**Figure 3S 6. Concentration of organics R1.** Color code: blue diamonds is acetate, orange squares is butyrate, and green circles is hexanoate.
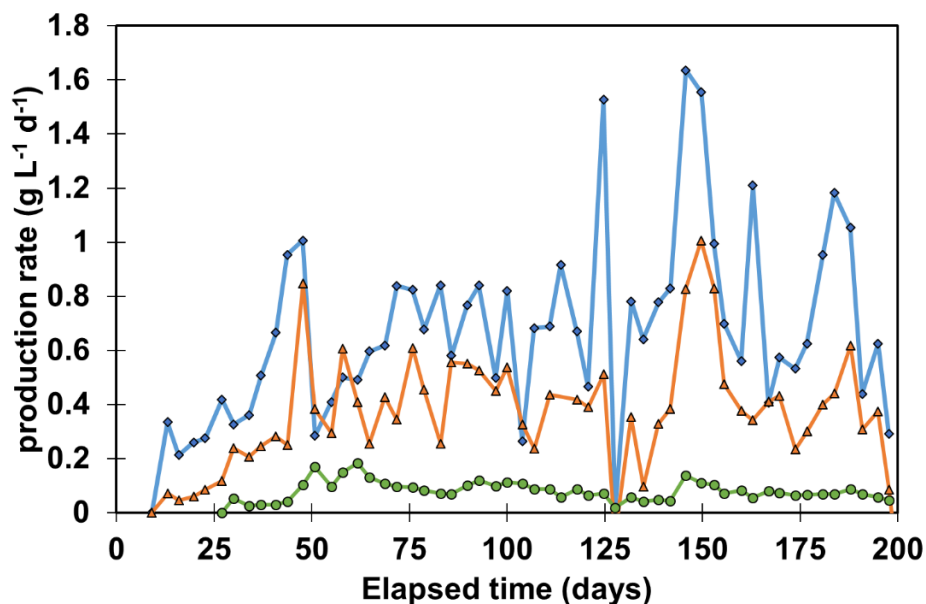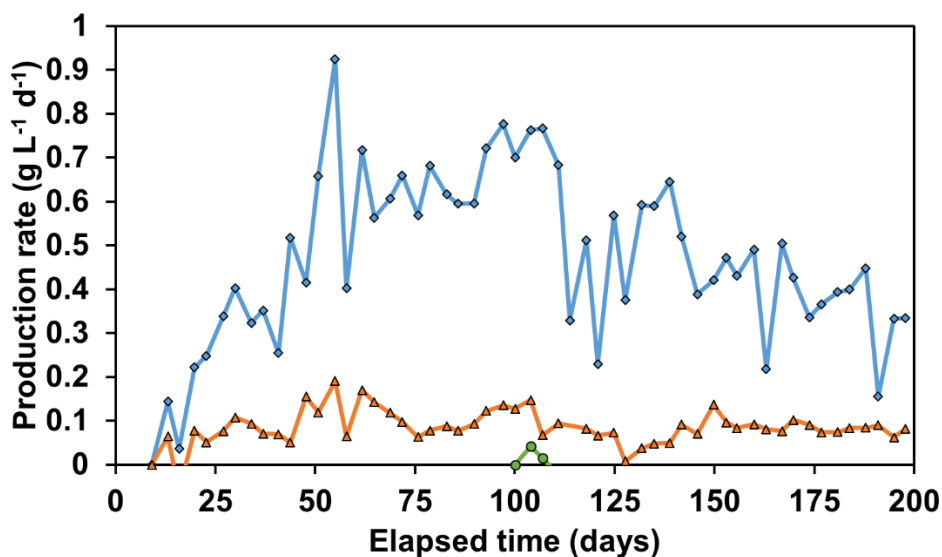


**Figure 3S 7. Volume-specific production rate normalized to total catholyte volume in R1.** Color code: blue diamonds is acetate, orange squares is butyrate, and green circles is hexanoate.
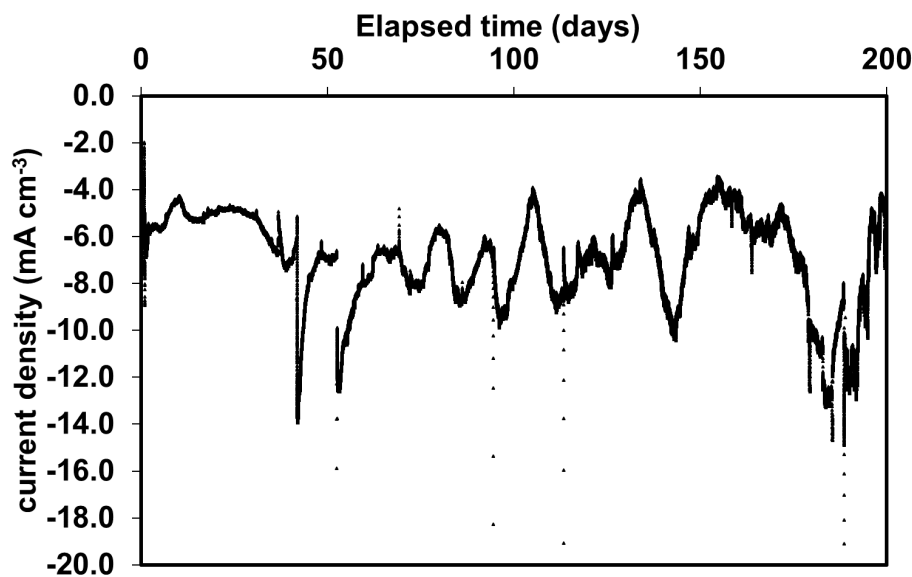
**Figure 3S 8. Volume-specific current density of R1.**
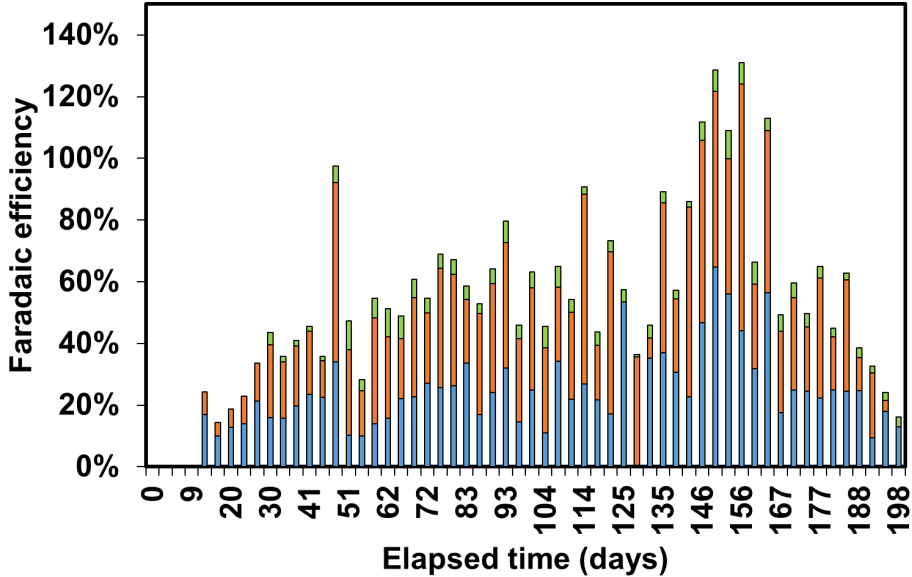


**Figure 3S 9. Faradaic efficiency R1.** Color code: blue is acetate, oranges is butyrate, and green is hexanoate.

iii.    Performance of R2
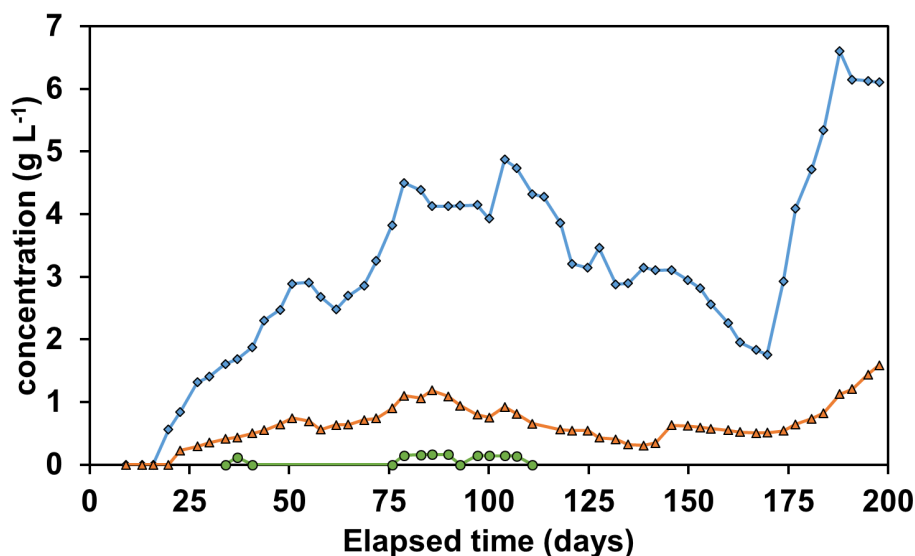


**Figure 3S 10. Concentration of organics R2.** Color code: blue diamonds is acetate, orange squares is butyrate, and green circles is hexanoate.
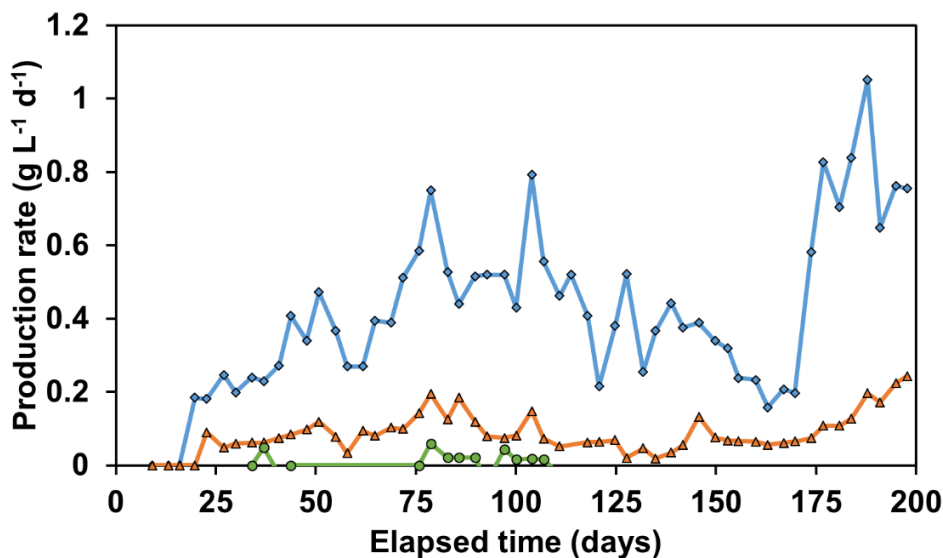


**Figure 3S 11. Volume-specific production rate normalized to total catholyte volume in R2.** Color code: blue diamonds is acetate, orange squares is butyrate, and green circles is hexanoate.
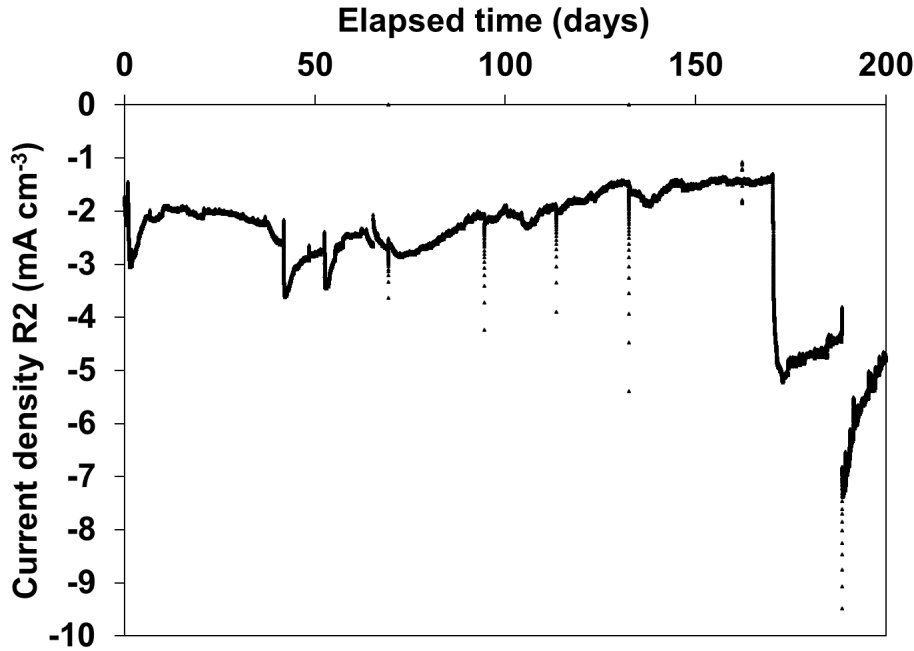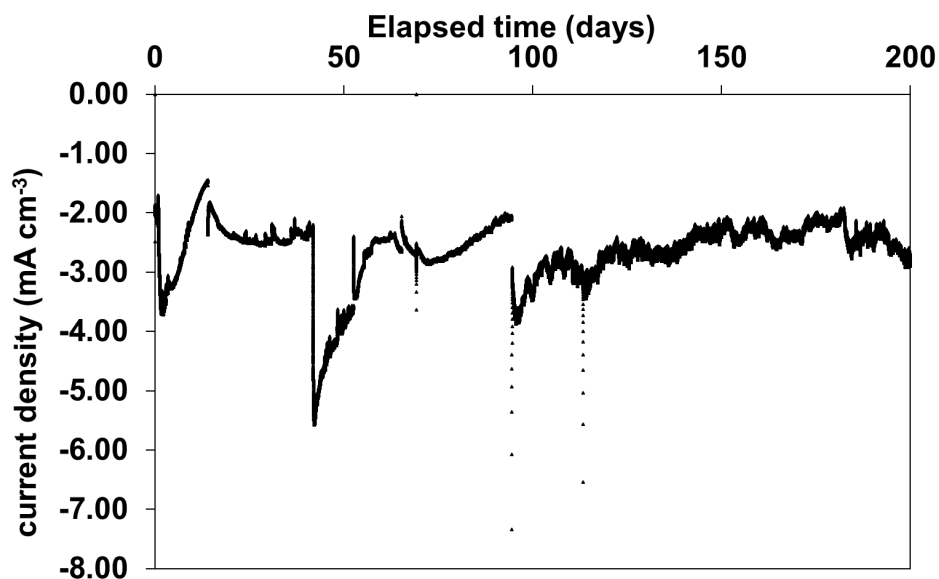
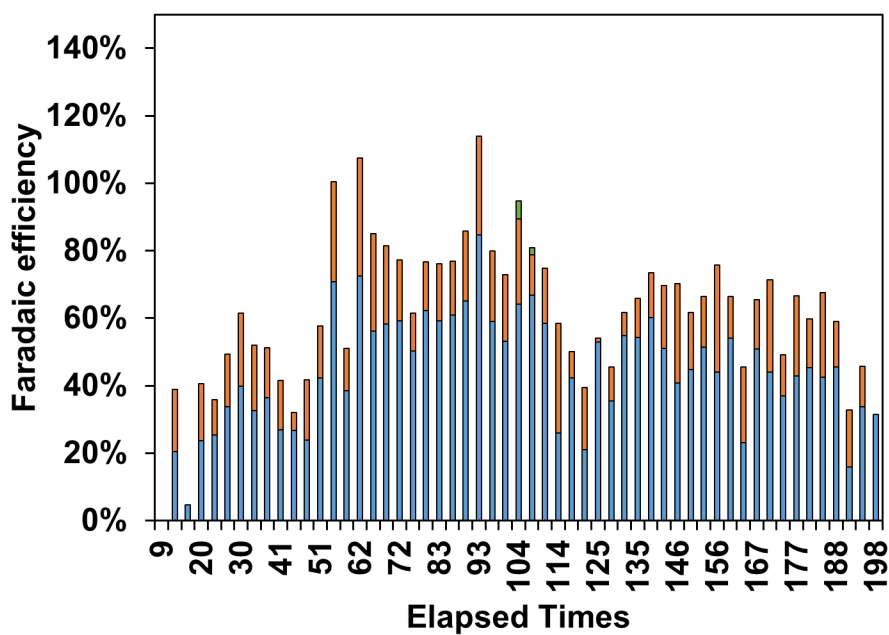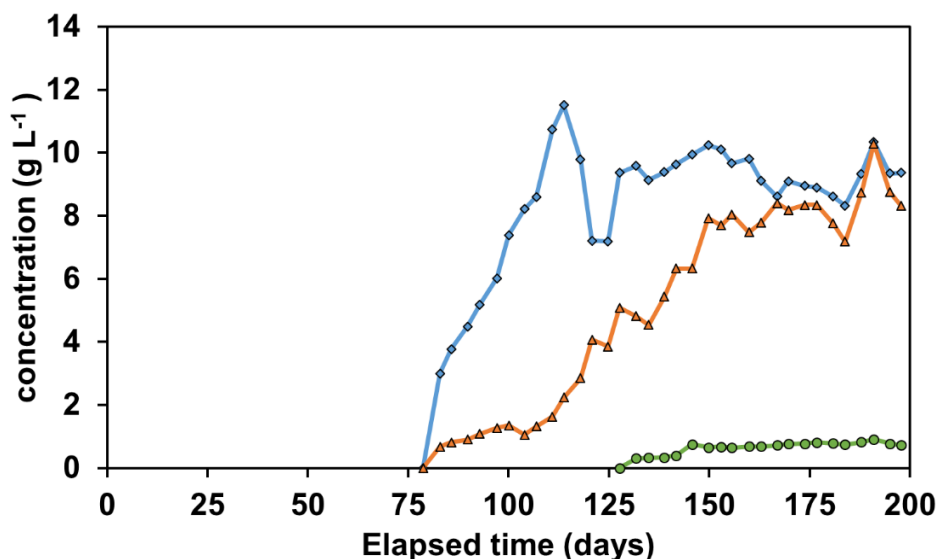**Figure 3S 12. Volume-specific current density of R2.**
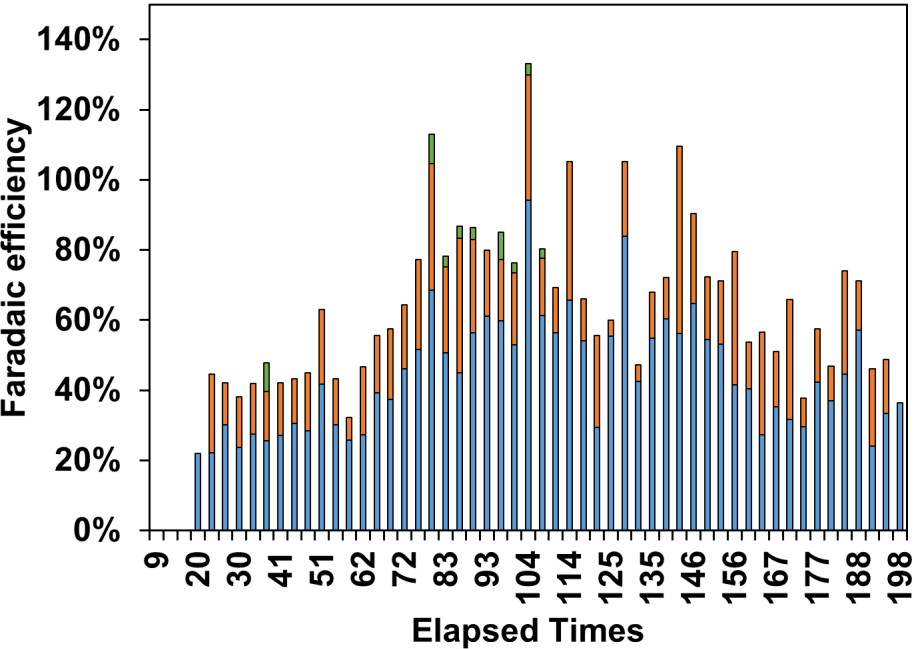
**Figure 3S 13. Faradaic efficiency R2.** Color code: blue is acetate, orange is butyrate, and green is hexanoate.

iv.    Performance of R3
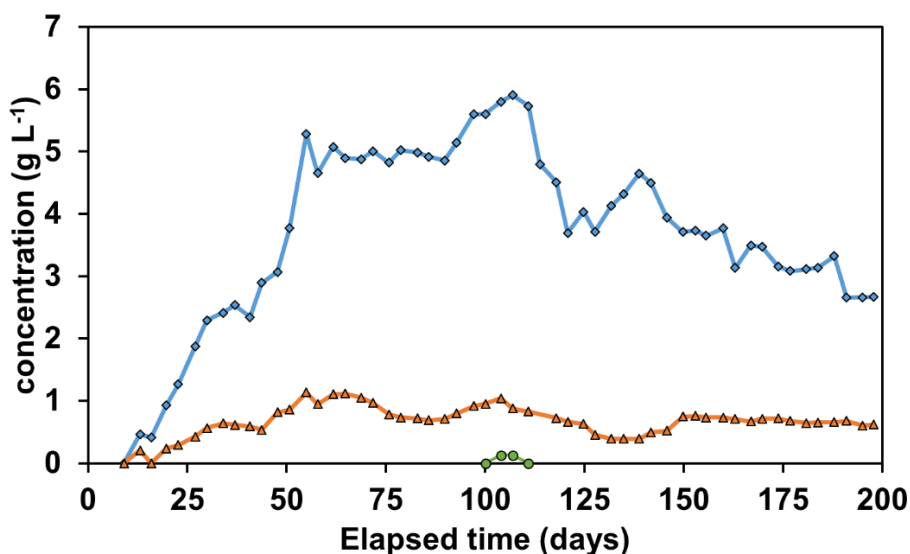


**Figure 3S 14. Concentration of organics R3.** Color code: blue is acetate, orange is butyrate, and green is hexanoate.
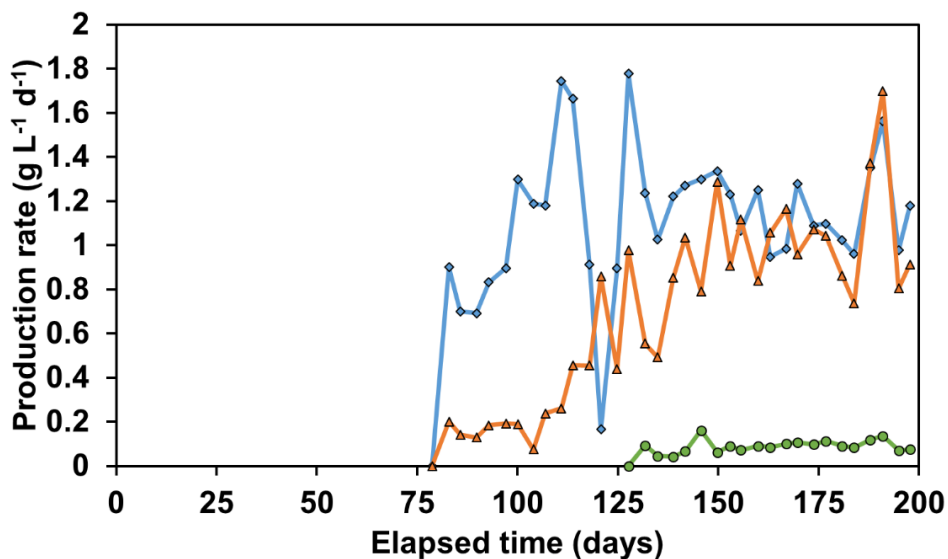


**Figure 3S 15. Volume-specific production rate normalized to total catholyte volume in R3.** Color code: blue diamonds is acetate, orange squares is butyrate, and green circles is hexanoate.

**Figure 3S 16. Volume-specific current density R3.**



**Figure 3S 17. Faradaic efficiency R3.** Color code: blue is acetate, orange is butyrate, and green is hexanoate.

v.    Performance of R4



**Figure 3S 18. Concentration of organics R4.** Color code: blue diamonds is acetate, orange squares is butyrate, and green circles is hexanoate.



**Figure 3S 19. Volume-specific production rate normalized to total catholyte volume in R4.** Color code: blue diamonds is acetate, orange squares is butyrate, and green circles is hexanoate.
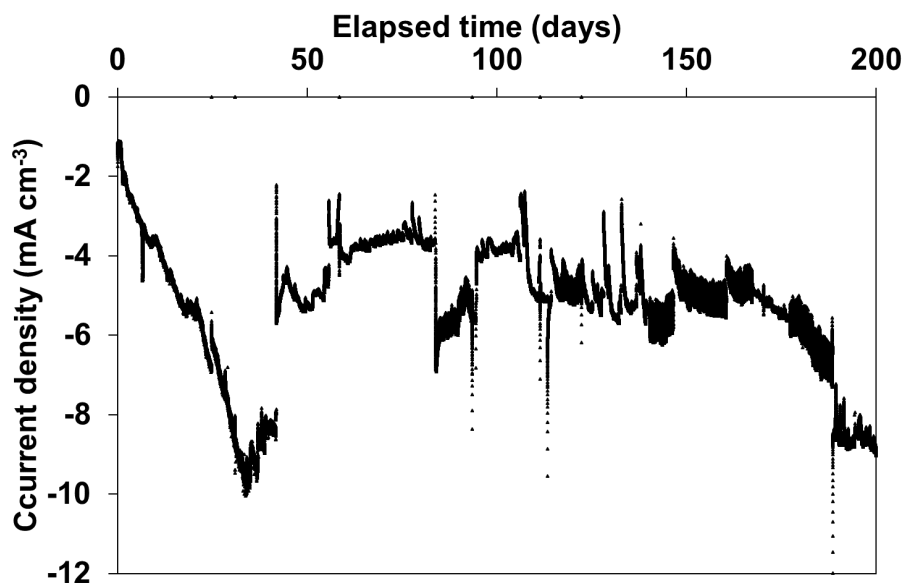
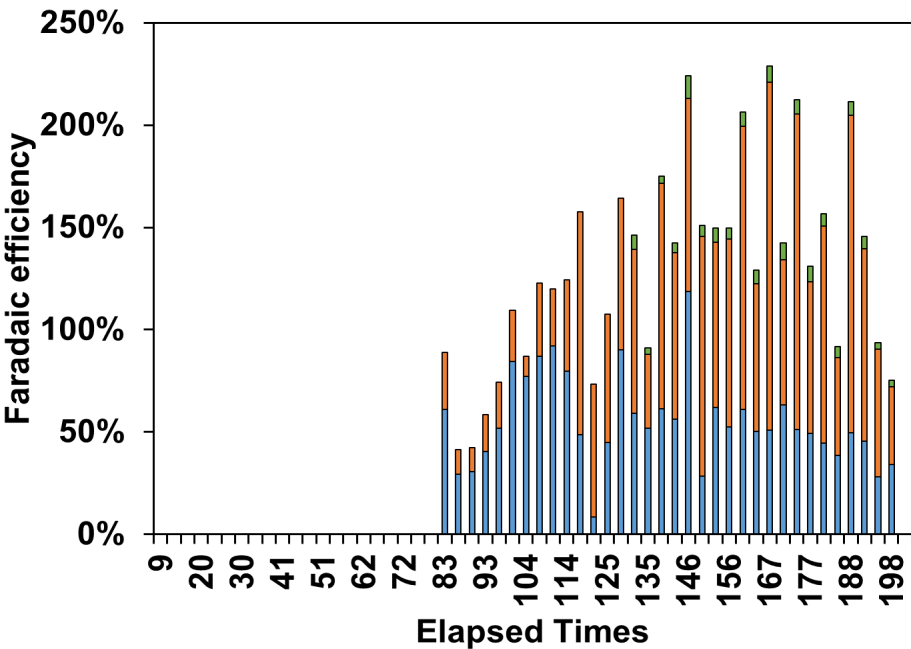**Figure 3S 20. Volume-specific current density R4.**



**Figure 3S 21. Faradaic efficiency R4.** Color code: blue is acetate, orange is butyrate, and green is hexanoate [1].

[1]The authors recognize the high improbability of the faradaic efficiencies of >100% obtained from day 100 onwards in R4. However, no flaws were discovered in the calculations, GC analysis, potentiostat channel or reference electrode. No additional electron donor was introduced to the reactor. One could speculate electron retention in the form of biomass and/or an unknown product between day 0 and day 83 which is then metabolized to organics between day 83-198. The faradaic efficiency over the whole experiment in R4 is 57%. 2-BES cannot be the responsible carbon and electron donor. Rago et al. (2015) showed degradation of 2-BES in their aerobic microbial fuel cell system, but no degradation occurred in their anaerobic microbial electrolysis system. Moreover, hypothetical full consumption of 2-BES (4.5 g/L at 15 mL/d inflow) would result in an additional current of 3.2 mA, which is insufficient to explain the coulombic efficiency excess."

### 3.6.4. Concentration, Production Rates and Current Densities with Conventional Normalizations

**Table 3S 3. Current density normalizations and cell voltages.** Selected time periods for R1: days 71-101, for R2: days 75-118, for R3 days 54-92, and for R4 days 141-198. The total surface area is calculated using carbon felt characteristics provided by the supplier: a specific area of 0.7 $m^2 g^{-1}$ and a density of 0.09 g $cm^{-3}$.

| | Current Density Normalizations | | | | |
|---|---|---|---|---|---|
| | Projected surface area (A $m^{-2}_{PSA}$) | Total surface area (A $m^{-2}_{TSA}$) | Cathode volume (kA $m^{-3}$) | Biomass-specific current (A $mol_X^{-1}$) | Cell voltage (V) |
| **R1** | -75.17±10.50 | -0.12±0.02 | -7.52±1.05 | 3.08±0.69 | -4.03±0.17 |
| **R2** | -22.19±2.64 | -0.035±0.004 | -2.22±0.26 | 0.83±0.44 | -3.12±0.06 |
| **R3** | -25.55±2.08 | -0.041±0.003 | -2.55±0.21 | 1.34±0.56 | -3.12±0.05 |
| **R4** | -58.56±13.39 | -0.094±0.021 | -5.86±1.34 | 1.62±0.47 | -3.64±0.17 |

**Table 3S 4. Concentration and production rate normalizations.** Selected time periods for R1: days 71-101, for R2: days 75-118, for R3 days 54-92, and for R4 days 141-198. The total surface area is calculated using carbon felt characteristics provided by the supplier: a specific area of 0.7 m² g⁻¹ and a density of 0.09 g cm⁻³.

| | | Concentration | | Production rates | | | | | |
| --- | --- | --- | --- | --- | --- | --- | --- | --- | --- |
| | | $g\ L^{-1}$ | $mmol\ L^{-1}$ | Catholyte volume $(g\ L^{-1}\ d^{-1})$ | Catholyte volume $(mmol\ L^{-1}\ d^{-1})$ | Electrode volume $(g\ L_{cathode}^{-1}\ d^{-1})$ | Projected surface area $(g\ m^{-2}_{PSA}\ d^{-1})$ | Total surface area $(g\ m^{-2}_{TSA}\ d^{-1})$ | Biomass specific $(mol\ mol_x^{-1}\ d^{-1})$ |
| **R1** | $C_2$ | 5.71±0.32 | 96.7±5.4 | 0.74±0.13 | 12.6±2.2 | 12.1±2.1 | 121±21 | 0.193±0.033 | 0.046±0.010 |
| | $C_4$ | 3.62±0.36 | 41.6±4.2 | 0.48±0.11 | 5.47±1.30 | 7.78±1.85 | 77.7±18.5 | 0.123±0.029 | 0.020±0.005 |
| | $C_6$ | 0.078±0.008 | 6.81±0.74 | 0.094±0.017 | 0.81±0.15 | 1.52±0.28 | 15.2±2.8 | 0.024±0.004 | 0.0029±0.0005 |
| **R2** | $C_2$ | 4.25±0.32 | 72.0±5.4 | 0.54±0.11 | 9.2±1.9 | 8.8±1.9 | 88±19 | 0.140±0.030 | 0.031±0.008 |
| | $C_4$ | 0.87±0.21 | 10.0±2.4 | 0.11±0.05 | 1.24±0.55 | 1.76±0.78 | 17.6±7.8 | 0.028±0.012 | 0.004±0.002 |
| | $C_6$ | 0.09±0.08 | 0.80±0.66 | 0.011±0.027 | 0.10±0.23 | 0.18±0.44 | 1.8±4.4 | 0.003±0.007 | 0.0004±0.0008 |
| **R3** | $C_2$ | 4.96±0.16 | 84.1±2.8 | 0.64±0.12 | 10.8±2.1 | 10.4±2.0 | 104±20 | 0.165±0.032 | 0.048±0.018 |
| | $C_4$ | 0.90±0.18 | 10.3±2.0 | 0.11±0.04 | 1.25±0.47 | 1.78±0.67 | 17.8±6.8 | 0.028±0.011 | 0.006±0.003 |
| | $C_6$ | n.a. | n.a. | n.a. | n.a. | n.a. | n.a. | n.a. | n.a. |
| **R4** | $C_2$ | 9.37±0.60 | 159±10 | 1.17±0.17 | 19.8±2.9 | 19.1±2.8 | 191±28 | 0.303±0.045 | 0.048±0.008 |
| | $C_4$ | 7.99±0.92 | 91.9±10.6 | 1.04±0.24 | 11.9±2.8 | 17.0±4.0 | 170±40 | 0.269±0.063 | 0.029±0.008 |
| | $C_6$ | 0.72±0.11 | 6.29±0.95 | 0.095±0.026 | 0.83±0.23 | 1.55±0.43 | 15.5±4.3 | 0.025±0.007 | 0.0020±0.0006 |

### 3.6.5. Biofilm Versus Planktonic Cells Retained in the Systems Over Time

**Figures 3S 22-25** show the ratio of biofilm versus planktonic cells in the reactors until day 70, with the exception of R2 (**Figure 3S 23**) which shows the ratio until day 197. Reactor 2 showed an increase in the planktonic cells ratio with a peak of 3.6% on day 174, whereas the other reactors remained <1% in planktonic cells ratio until the end of the experiment. Day 70 was chosen for reactor R1, R3 and R4 for visualization purposes of the start-up phase.
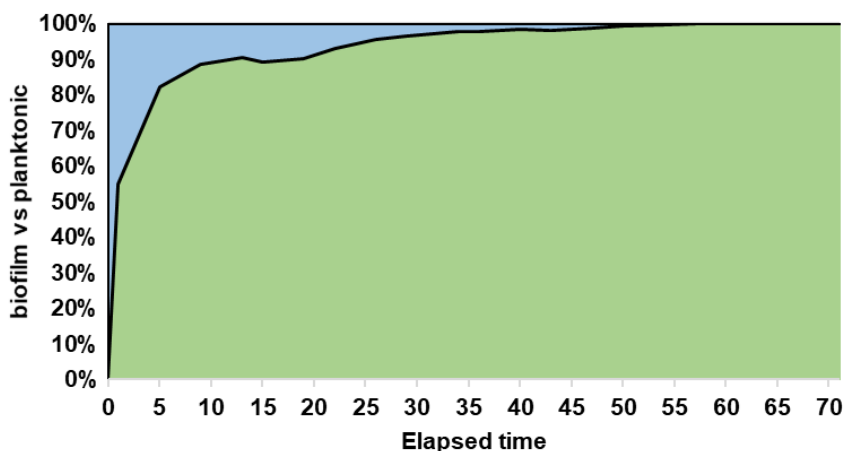


**Figure 3S 22. R1 biofilm versus planktonic cells until day 70.** The planktonic biomass is shown in blue and biofilm-based biomass is shown in green.
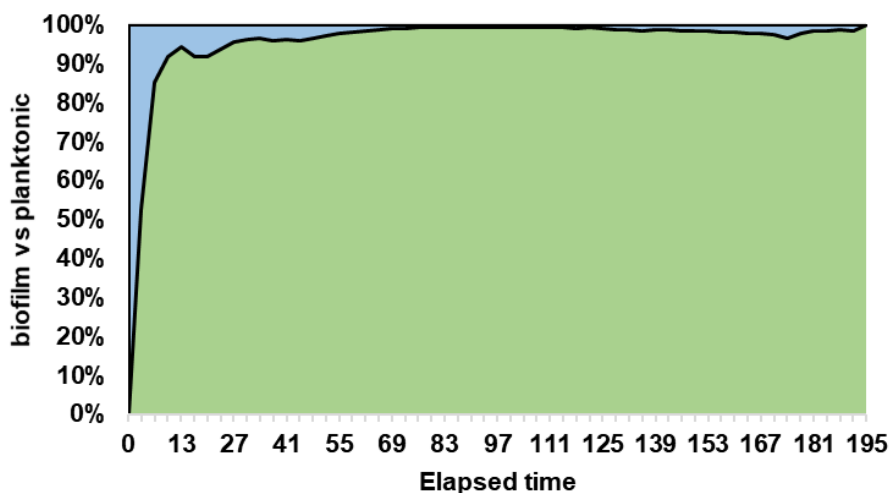


**Figure 3S 23. R2 biofilm versus planktonic cells until day 197.** The planktonic biomass is shown in blue and biofilm-based biomass is shown in green.
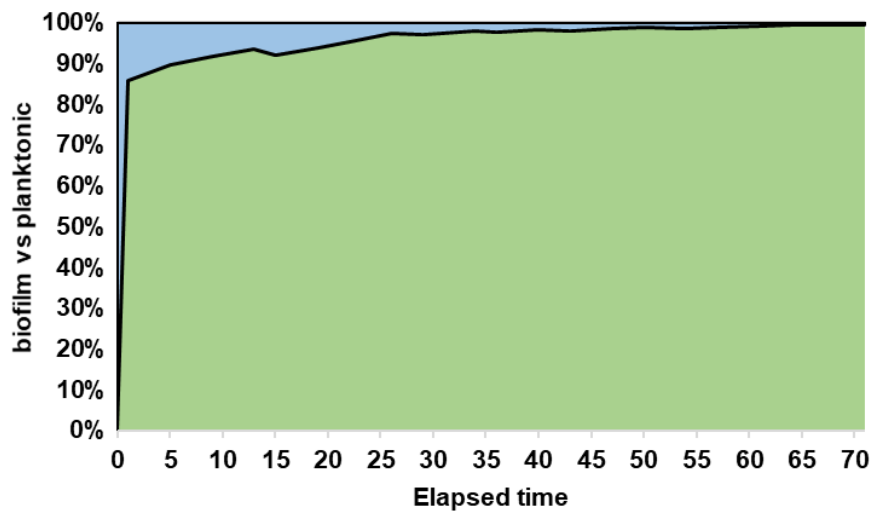
**Figure 3S 24. R3 biofilm versus planktonic cells.** The planktonic biomass is shown in blue and biofilm-based biomass is shown in green.
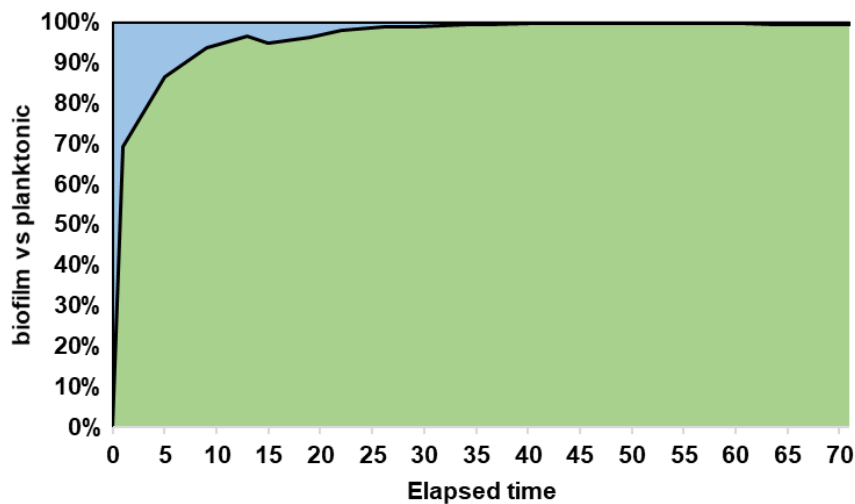


**Figure 3S 25. R4 biofilm versus planktonic cells.** The planktonic biomass is shown in blue and biofilm-based biomass is shown in green.
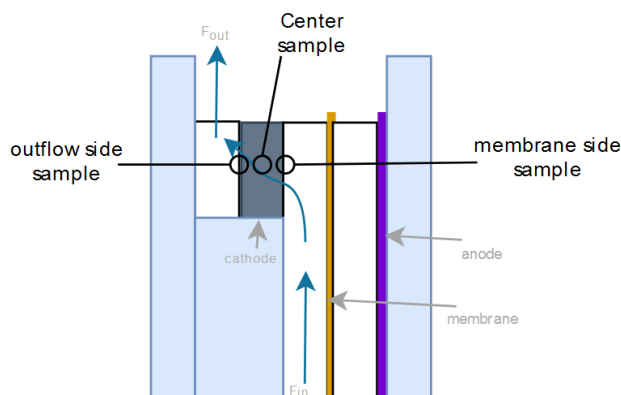
### 3.6.6. Biofilm Pictures



**Figure 3S 26. Schematic overview of biofilm sampling locations for imaging.**
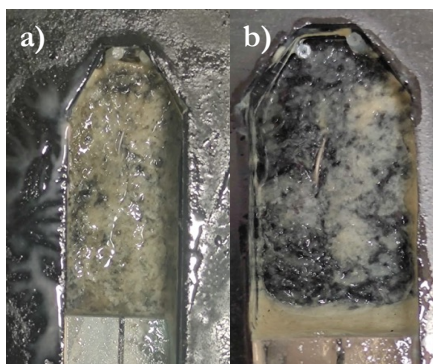
    i.    <u>Biofilm images R1</u>



**Figure 3S 27. Biofilm R1 a)** membrane side; **b)** outflow side.
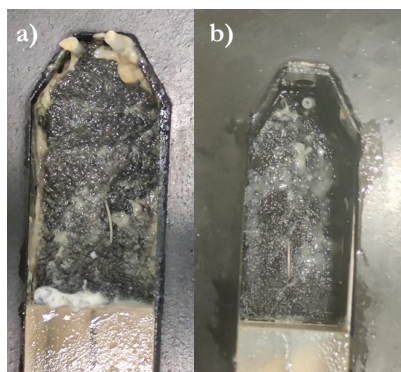
    ii.    <u>Biofilm images R2</u>



**Figure 3S 28. Biofilm R2 a)** membrane side; **b)** outflow side.

iii.     <u>Biofilm images R3</u>



**Figure 3S 29. Biofilm R3 membrane side.** Picture of outflow side of R3 was not taken.
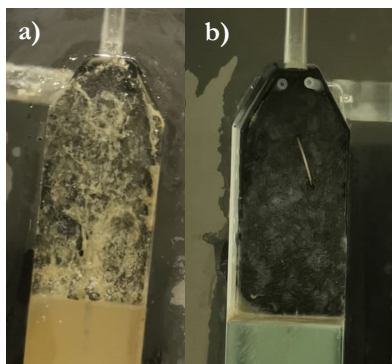
iv.     <u>Biofilm images R4</u>



**Figure 3S 30. Biofilm R4 a)** membrane side; **b)** outflow side.

## 3.6.7. Live/Dead Staining Images
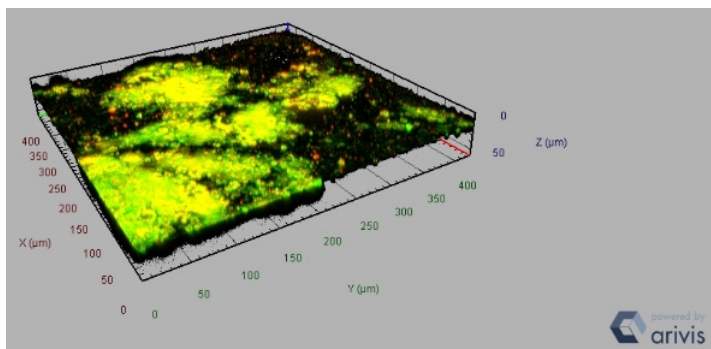
i.     <u>Live/dead R1</u>



**Figure 3S 31. R1 membrane side image.** Z-stack: 42 slices (57.4 µm). 20x magnification.
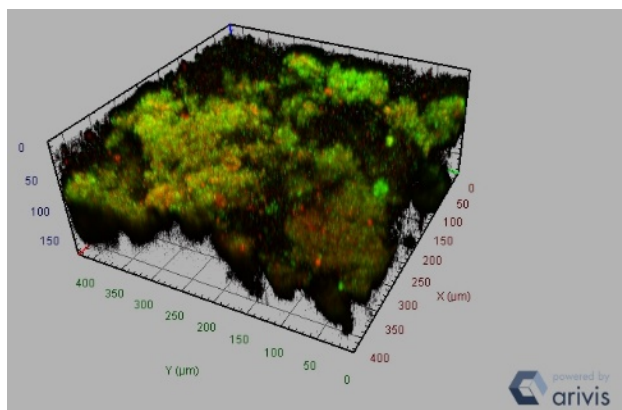
**Figure 3S 32. R1 center sample image.** Z-stack: 31 slices (180 µm). 20x magnification.



**Figure 3S 33. R1 outflow side image.** Z-stack: 41 slices (120 µm). 20x magnification.

ii.    <u>Live/dead R2</u>



**Figure 3S 34. R2 Membrane side image.** Z-stack:29 slices (84 µm). 20x magnification.

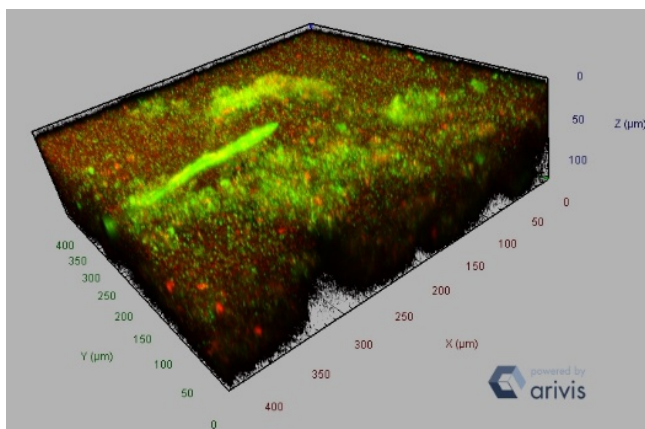**Figure 3S 35. R2 center sample image.** Z-stack: 36 slices (105 μm). 20x magnification.
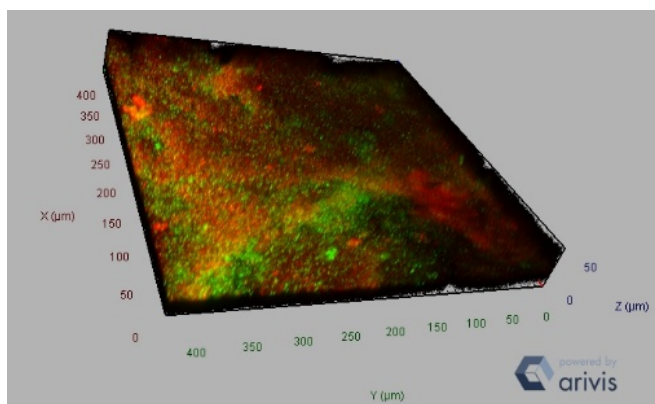


**Figure 3S 36. R2 outflow side image.** Z-stack: 19 slices (54 μm). 20x magnification.

iii. Live/dead R3
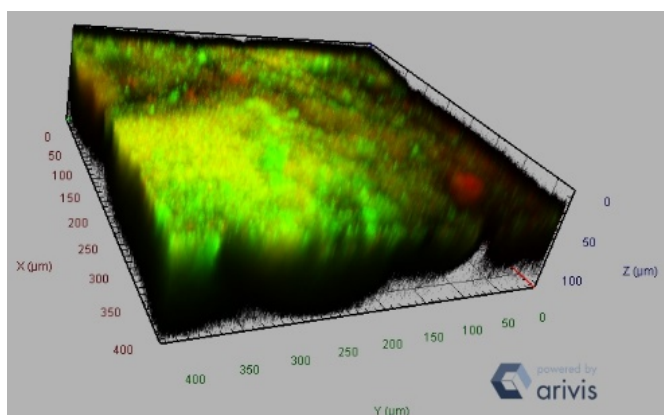


**Figure 3S 37. R3 membrane side.** Z-stack: 25 slices (120 μm). 20x magnification.
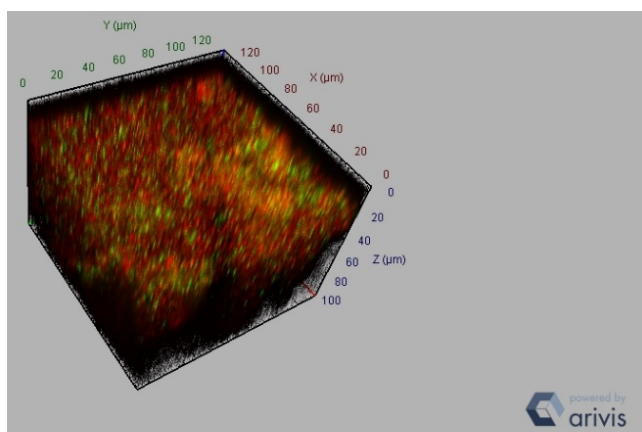
**Figure 3S 38. R3 center sample.** Z-stack: 20 slices (95 µm). 20x magnification.
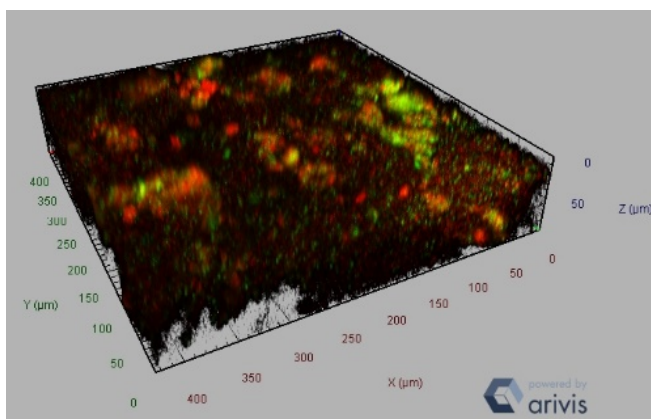


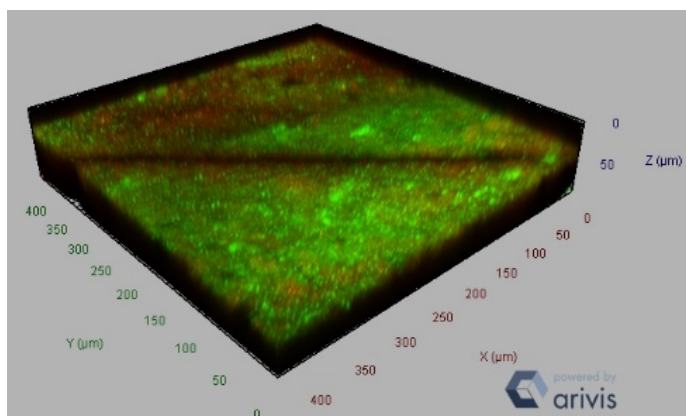**Figure 3S 39. R3 outflow side.** Z-stack:18 slices (85 µm). 20x magnification.

iv.   Live/dead R4



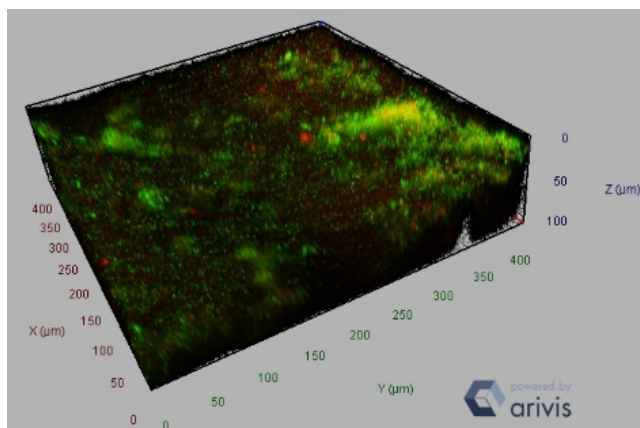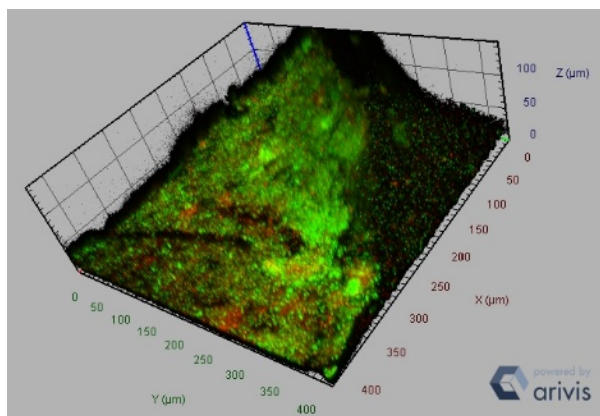**Figure 3S 40. R4 Membrane side.** Z-stack: 49 slices 144 µm). 20x magnification.
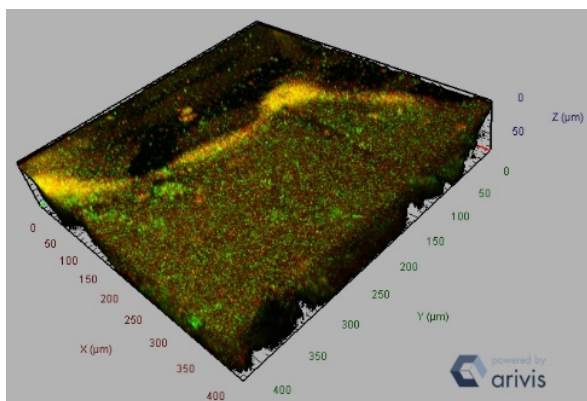
**Figure 3S 41. R4 center sample.** Z-stack: 51 slices (75 µm). 20x magnification.
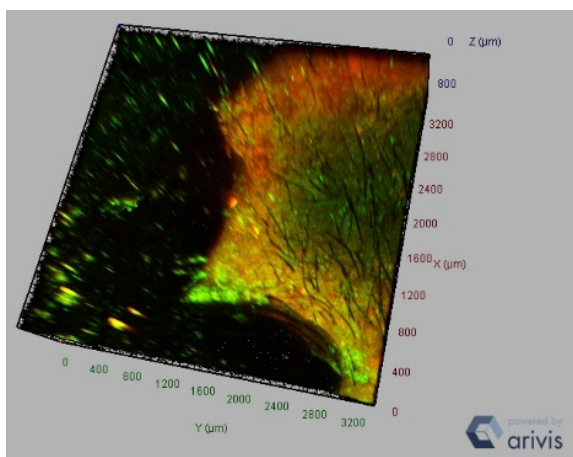


**Figure 3S 42. R4 outflow side.** Z-stack: 29 slices (840 µm). 2.5x magnification.

### 3.6.8. Supplementary Material Reference List

[1].    L. Rago, J. Guerrero, J.A. Baeza, A. Guisasola, 2-Bromoethanesulfonate degradation in bioelectrochemical systems, Bioelectrochemistry 105 (2015) 44–49. https://doi.org/10.1016/j.bioelechem.2015.05.001.
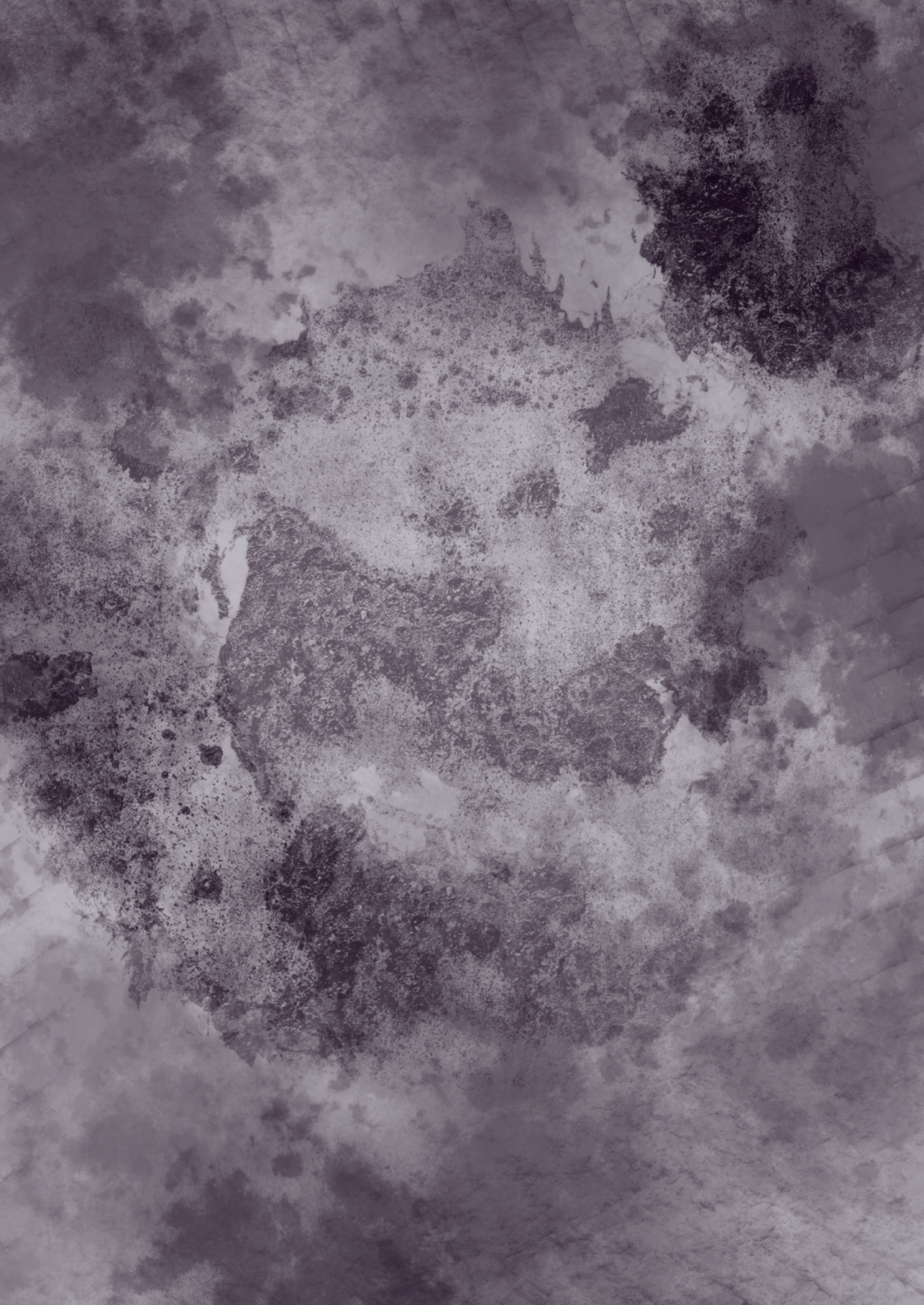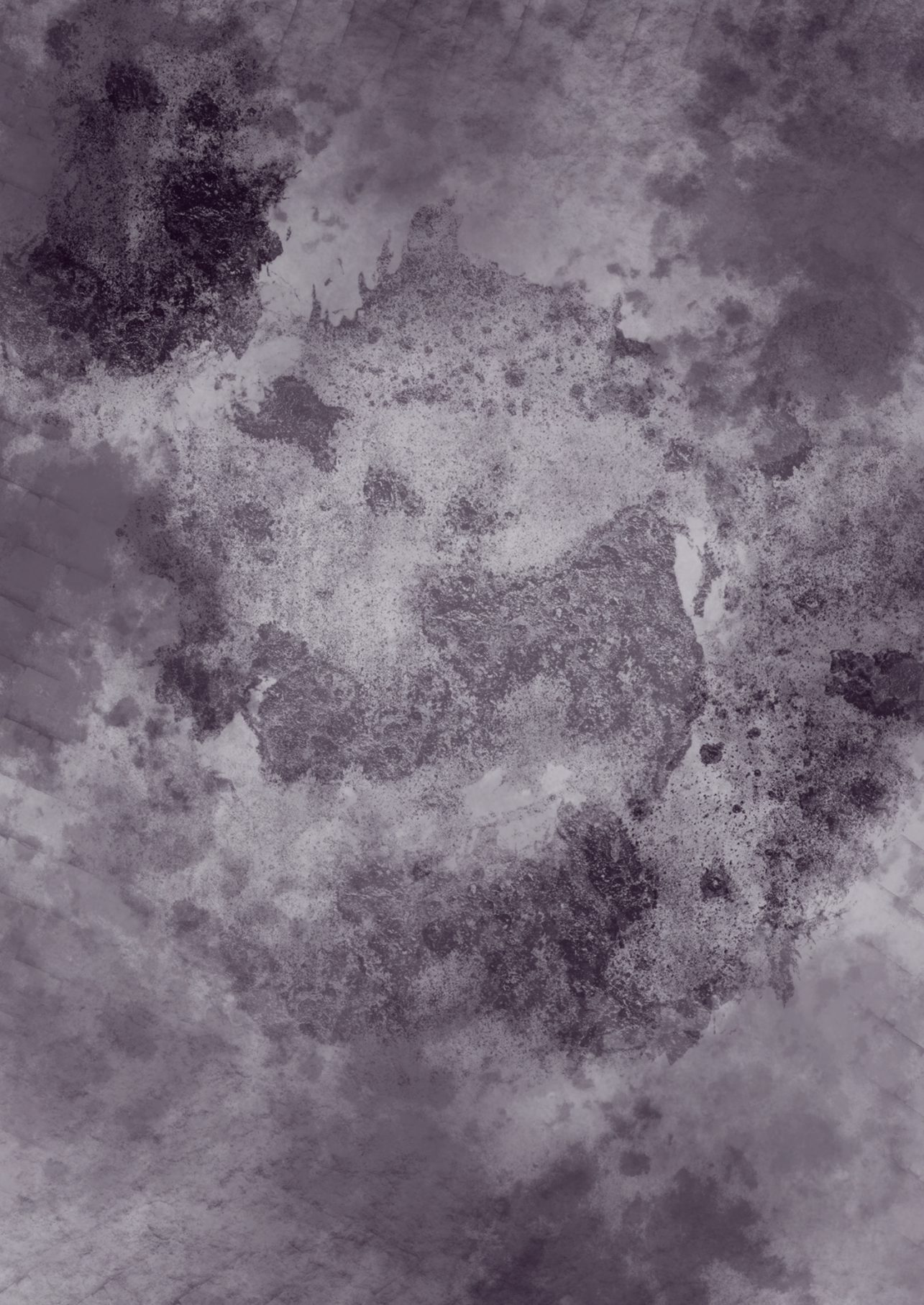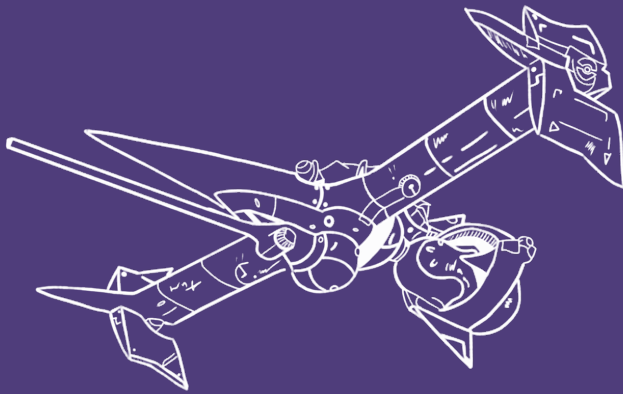
# Chapter 4

Microbial electrosynthesis from CO$_2$ reaches productivity of syngas and chain elongation fermentations

## Abstract

Carbon-based products are essential to society, yet producing them from fossil fuels is unsustainable. Microorganisms have the ability to take up electrons from solid electrodes and convert $CO_2$ to valuable carbon-based chemicals. However, higher productivities and energy efficiencies are needed to reach a viability that can make the technology transformative. Here we show how a biofilm-based microbial porous cathode in a directed flow-through electrochemical system can continuously reduce $CO_2$ to even-chain C2-C6 carboxylic acids over 248 days. We demonstrate a 3-fold higher biofilm concentration, volumetric current density, and productivity than the state of the art. Most notably, the volumetric productivity resembles those achieved in lab-scale and industrial syngas ($CO-H_2-CO_2$) fermentation and chain elongation fermentation. This work highlights key design parameters for efficient electricity-driven microbial $CO_2$ reduction. There is need and room to improve the rates of electrode colonization and microbe-specific kinetics to scale-up the technology.

## 4.1. Introduction

By exploiting the ability of microorganisms to reduce carbon dioxide, microbial electrosynthesis (MES) has become a candidate technology to satisfy the growing demand for fossil-free chemicals synthesis, by harnessing the increasing amount of electrical energy obtained from renewable sources [1]. Microbiomes are living systems with the ability to self-repair and regenerate, offering a major advantage for resilient industrial applications over abiotic $CO_2$ electrolysis. Unlike heterogeneous catalysts, which exhibit stability for limited durations (hours/days), microbial electrochemical reactors demonstrate remarkable operational continuity lasting for several years [2]. Beyond their robustness, biocatalysts in MES systems exhibit the capacity to generate multi-carbon products with notable selectivity and faradaic efficiency [3]. The bioelectrochemical reduction of $CO_2$ to produce medium-chain carboxylic acids (MCCAs), such as butyric (4 carbons, C4) and caproic (6 carbons, C6) acids, presents a promising avenue for generating low $CO_2$ footprint precursors crucial for applications in the fuel, chemical, feed, and food industries [4,5]. Nonetheless, it is noteworthy that existing studies elucidating microbial $CO_2$ reduction to MCCAs report production rates lower than those achieved in alternative fermentation technologies for organics production, including syngas fermentation and chain elongation fermentation [6–9].

Following the initial proof-of-concept demonstrating the production of soluble organics from $CO_2$ in microbial electrosynthesis [10], the primary focus within the MES research community has centered on enhancing microbial catalysts, improving cathode materials, and elucidating fundamental mechanisms and microbial functionalities [2,11]. These endeavors have been pivotal in achieving noteworthy key performance indicators (KPIs), including productivities and faradaic efficiencies. Nevertheless, these KPIs have not yet reached a level that ensures the economic viability of the technology [4,11]. In the context of transitioning to industrial implementation of MES and its potential role in the electrification of the chemical industry, reactor design emerges as a crucial aspect requiring attention [2,11]. State-of-the-art MES reactors capable of producing acids longer than C2 are predominantly biofilm-driven systems, exploiting the proximity to the electron source for $CO_2$ reduction [2,6,12]. Biofilm-driven MESs have so far outperformed MES driven by microorganisms in suspension by several orders of magnitude [3]. Nevertheless, biofilms growing in other environments have demonstrated susceptibility to mass transfer limitations, impacting microbial activities due to the necessity for substrates and products to diffuse in and out of biofilms [13–16]. Despite these limitations, relatively few efforts have been dedicated to researching

and developing biofilm-driven MES reactor design concepts that ameliorate mass transport [6,17,18].

The predominant focus in devising innovative reactor designs has been directed towards MES systems employing microorganisms in suspension [19]. Notably, Cui and colleagues recently presented an electrolytic bubble column featuring an external hollow fiber membrane gas–liquid contactor for the production of acetate from $CO_2$, achieving an acetate titer and production rate of up to 34.5 g $L^{-1}$ and 1.15 g $L^{-1}$ $d^{-1}$ at an average faradaic efficiency of 64% into acetate [20]. In a different approach, Rosa and coworkers retrofitted a conventional stirred bioreactor with electrodes, showcasing adaptability to MES applications [21,22]. Enzmann and colleagues introduced a bioelectrochemical bubble-column reactor, serving the dual function of a microbial fuel cell and microbial electrosynthesis system [23]. They tested MES of methane and obtained a mean methane production rate of 36.7 ± 7.8 mmol $m^{-2}$ $d^{-1}$ at a faradaic efficiency of 49.9 ± 4.1%. Puig and coworkers explored a tubular MES reactor for the production of 34.7 mMC of acetate and 87.5 mMC of butyrate at a current density of -2.74 ± 0.09 A $m^{-2}$ and faradaic efficiency of about 60% [24]. In another study they used the same tubular MES for the production of 35 to 47 mMC of acetate and ethanol at a 1-to-1 ratio, at a current density of -0.33-0.55 A $m^{-2}$ and faradaic efficiency of 12-14% [25]. Additionally, a 4.3 L scaled-up version of a flat-plate double-chamber reactor design demonstrated the production of 3.6 ± 0.6 g $L^{-1}$ acetate at a rate of 0.23 g $L^{-1}$ $d^{-1}$ by microorganisms in suspension, at -6.6 A $m^{-2}$ and faradaic efficiency of 82% [26].

Configurations for biofilm-driven microbial electrosynthesis employing flow-through designs, where convective flow is intensified near the biofilm-cathode interface, have resulted in elevated production rates, enhanced biofilm growth, and increased carbon selectivity towards longer MCCAs compared to other tested designs [6,13]. However, the flat-plate design employed by Jourdin and colleagues presents scalability challenges [6]. In this design, the cathode compartment featured a 1.2 cm-thick free-flowing catholyte volume positioned between the membrane and the 3D-filamentous cathode. The catholyte was directed to flow through the cathode material and exit the compartment on the opposite side, where an additional 1.2 cm-thick free-flowing liquid volume was located. The incorporation of such free-flowing liquid dead-volumes substantially increases both the footprint and capital cost of the reactor upon scale-up. Moreover, these dead-volumes contribute to issues related to hydrogen accumulation, negatively impacting system performance [27]. The fluid dynamics within this reactor design exhibit suboptimal characteristics, leading to dead zones within the cathode material where mass transport and

microbial activity are constrained. Furthermore, the 2.4 cm separation between the anode and the cathode proves to be excessively large, resulting in considerable ohmic and mass transfer resistances, consequently leading to high energy losses [11].

Here we introduce a directed-flow-through bioelectrochemical reactor (DFBR) featuring a serpentine flow-pattern architecture, as illustrated in **Figure 4.1A-B**. In this innovative design, $CO_2$-saturated catholyte is directed through a continuous serpentine channel entirely filled with a porous 3D carbon-based electrode, where $CO_2$ undergoes biological reduction to form medium-chain carboxylic acids (**Figure 4.1C**). Unlike previously used systems, the DFBR design eliminates free-flowing liquid in the cathode chamber, thereby facilitating substrate and product turnover at the biofilm-cathode surface. Additionally, the serpentine flow-pattern enables an extended residence time, potentially enhancing carbon and electron/hydrogen utilization efficiency, which are key performance indicators upon scale-up. While not explored in this study, the ability to manipulate this residence time theoretically positions this reactor design for further carbon elongation towards carboxylic acids longer than C6. Notably, the design is characterized by its scalability and stackability, enhancing its versatility and applicability.

It must be noted that serpentine flow channels have been used in many electrochemical systems (e.g. fuel cell, $CO_2$ electrolysis, etc.) yet in a different way. In those systems, 2D electrodes, 2D gas diffusion electrodes or 2D membrane electrode assemblies are used adjacent to the serpentine channel, where the channel is used to distribute a gas or a liquid. Here the main novelty lies in filling the flow channel with a 3D electrode and promoting biofilm growth. Recently, Chu and coworkers (2023) used a flow-electrode-based MES reactors, which was constructed using a liquid-type flow-electrode that is separated from the electrochemical cells [28]. Practically, they used powder activated carbon as cathode materials which was suspended in the catholyte and recirculated through the cathode compartment. The cathode compartment was a hollow serpentine channel carved into a conductive graphite sheet. This reactor differs from the concept studied here, which uses a fixed carbon felt electrode in a serpentine flow channel, with the catholyte being forced to flow through the electrode. Chu and colleagues operated their reactors in batch mode with passive $CO_2$ supply from a gas bag and reported an acetate production rate of $16 \pm 1$ g m$^{-2}$ d$^{-1}$ at -5 A m$^{-2}$, and an acetate concentration of about 1.5 g L$^{-1}$ both in the catholyte and extraction compartment. Other by-products were detected below 0.1 g L$^{-1}$. Baek and coworkers (2022) designed a zero-gap MES reactor configuration with a vapor-fed anode and a liquid catholyte, which they tested for methane and acetate production from $CO_2$ [29]. Similarly to our design, the cathode

4

chamber was filled with carbon felt and the catholyte pushed through it, yet a flow channel was not implemented to avoid zones with low fluid velocities. Baek and colleagues operated their reactors in batch with both bicarbonate and sporadically sparged $CO_2$ as C-source and achieved methane and acetate production rates up to 12 and 55 g m$^{-2}$ d$^{-1}$, respectively, at 17.4 A m$^{-2}$. Quantification of biofilm growth and biomass-specific microbial rates were lacking in those studies.
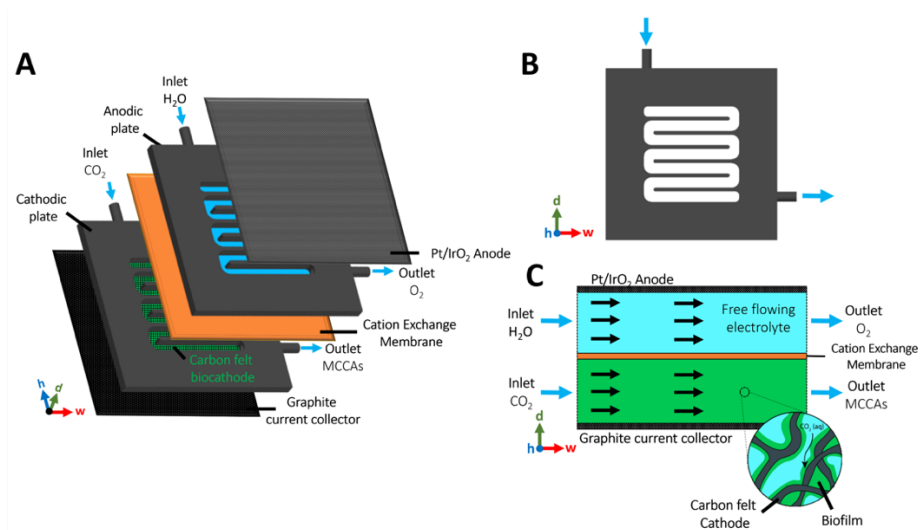


**Figure 4.1. Schematic of a directed-flowthrough serpentine bioelectrochemical reactor. (A)** Reactor cell diagram. Each unit consists of a serpentine plate filled with a carbon-based 3D-biocathode on a graphite current collector, an empty serpentine plate (free flowing electrolyte) on a Pt/IrO$_2$ coated 2D-titanium anode, and a cation exchange membrane. **(B)** Schematic of the serpentine plate design. **(C)** Top-view schematic of both flow-channels on a reactor cell unit.

The key performance indicators of the DFBR design for the production of MCCAs directly from $CO_2$ were investigated. We comprehensively examine the microbial growth, electrode colonization, metabolic activity, organics production, and energy efficiency over an operational period spanning 248 days. 16S rRNA-sequencing allowed to identify the dominant microbial species responsible for the elongation of $CO_2$ to MCCAs. Our findings highlight the remarkable capability of microbial electrosynthesis to attain reactor-scale performances comparable to established technologies, establishing the viability of the novel directed-flow-through reactor as a potentially scalable system.

## 4.2. Materials and Methods

### 4.2.1. MES Reactor Setup

Two bioelectrochemical reactors were assembled. Each reactor comprised two identical cathodic and anodic compartments, as well as two supporting plates used to press and close the reactor cell. A scheme of the reactor setup and a picture of the assembled reactor can be seen in **Figure 4.1**. Exact reactor dimensions are also given (**Figure 4S 9**). A biocompatible resin (BioMed Clear Resin V1, Formlabs) and the Form 2 printer (Formlabs) were used to 3D-print all the plates that formed the reactor.

The anode used in this work was a $Pt/IrO_2$ coated titanium plate (Magneto Special Anodes, Schiedam, The Netherlands). Unmodified carbon felt was used as the cathode electrode material (CTG Carbon GmbH, Germany). Before being used, all felt pieces underwent a cleaning step with 1 mol $L^{-1}$ HCl, 1 mol $L^{-1}$ NaOH, and an UV/ozone treatment as described in Winkelhorst and colleagues [30]. Once in the reactor, the total volume of carbon felt was 9.5 cm³, with a thickness of 0.5 cm and a total projected surface area of 19 cm². In one of the reactors, a titanium wire (Salomon's Metalen, The Netherlands) was placed between two layers of tightly pressed carbon felt (0.25 cm thick each) and used as current collector. The other reactor used an iso-molded graphite plate (GP) (3.2 mm thick, Fuel Cell Store, USA) as current collector, placed parallel to the cathodic plate. Conductive coating (Graphite Conductive Adhesive, Electron Microscopy Sciences, USA) was applied at the surface between current collector and carbon felt in order to enhance the electric connection between both materials [30]. A cation exchange membrane (CEM) (CMI-7000s, Membrane International Inc.) was used to separate the cathodic and anodic compartment.

A pH probe (QP108X, ProSense) was installed in the catholyte recirculation loop outside the reactor and a pH controller (AQUIS touch S, Jumo) was used to control the pH of the catholyte at pH 5.8. pH titrant addition was negligible, likely as a combination of a fairly high phosphate buffer concentration, $CO_2$ continuous sparging, and proton electrochemical reduction. A bubble column was also installed in the recirculation loop, and used to sparge a $CO_2$-$N_2$ mixture into the catholyte. The total volume of the catholyte in the setup was 135 mL. This volume includes the cathodic chamber, recirculation bottle, and all tubing comprising the recirculation loop.

4

### 4.2.2. MES Reactor Operation

The catholyte medium composition was based on the one described in Winkelhorst and coworkers [30], and contained 0.2 g L$^{-1}$ NH$_4$Cl, 0.015 g L$^{-1}$ CaCl$_2$·2H$_2$O, 0.04 g L$^{-1}$ MgCl$_2$·6H$_2$O, 8.1 g L$^{-1}$ KH$_2$PO$_4$, 0.9 g L$^{-1}$ Na$_2$HPO$_4$, 1 mL L$^{-1}$ of a trace elements solution, and 4.5 g L$^{-1}$ 2-bromoethanesulfonic acid as methanogenic activity inhibitor. The trace elements solution contained 1.5 g L$^{-1}$ FeCl$_3$·6H$_2$O, 0.15 g L$^{-1}$ H$_3$BO$_3$, 0.03 g L$^{-1}$ CuSO$_4$·5H$_2$O, 0.18 g L$^{-1}$ KI, 0.12 g L$^{-1}$ MnCl$_2$·4H$_2$O, 0.06 g L$^{-1}$ Na$_2$MoO$_4$·2H$_2$O, 0.12 g L$^{-1}$ ZnSO$_4$·7H$_2$O, 0.15 g L$^{-1}$ CoCl$_2$·6H$_2$O, 0.023 g L$^{-1}$ NiCl$_2$·6H$_2$O, and 10 g L$^{-1}$ EDTA. To avoid possible limitations caused by nutrients depletion, a second catholyte medium composition was used from day 18 containing 0.6 g L$^{-1}$ NH$_4$Cl, 0.045 g L$^{-1}$ CaCl$_2$·2H$_2$O, 0.12 g L$^{-1}$ MgCl$_2$·6H$_2$O, 8.1 g L$^{-1}$ KH$_2$PO$_4$, 0.9 g L$^{-1}$ Na$_2$HPO$_4$, 3 mL L$^{-1}$ of a trace elements solution, and 13.5 g L$^{-1}$ 2-bromoethanesulfonic acid. The anolyte composition was identical to the catholyte medium used at that specific moment, without the trace elements solution and the methanogenic inhibitor. The pH of the anolyte was also decreased to 2 with phosphoric acid to facilitate proton crossing over the membrane.

The reactors were operated in continuous mode with a hydraulic retention time (HRT) of 4 days. Both catholyte and anolyte were continuously circulated between the reactor cell and the recirculation bottles at a flow rate of 1.8 L h$^{-1}$. Dissolved CO$_2$ was supplied by continuously sparging a gas mixture of CO$_2$:N$_2$ 50:50 at a rate of 0.1 L min$^{-1}$ in the cathodic bubble column. The volumetric CO$_2$ mass transfer coefficient (k$_L$a) of the bubble column was determined with the dynamic gassing-out method and found to be 70 h$^{-1}$ (data not shown). The entire setup was placed inside a cabinet, keeping the reactors in the dark to avoid any phototrophic growth. Temperature was kept at 31 °C.

The reactors were connected in a three-electrode configuration to a multichannel potentiostat (BioLogic) to control either the cathode potential (chronoamperometry, CA) or the applied current (chronopotentiometry, CP). A 3M Ag/AgCl reference electrode (QM710X, ProSense) was installed in both reactors. The CP reactor was first controlled in potentiostatic mode at -0.85 V vs. SHE (standard hydrogen electrode) from day 0 to 28, and then switched to galvanostatic mode for the rest of the experiment (day 248). From day 28 to 68 a current of -26 A m$_2^{-1}$ $_{psa}$ was applied, from day 68 to 114 it was increased to -53 A m$_2^{-1}$ $_{psa}$, and from day 114 to the end of the experiment -105 A m$_2^{-1}$ $_{psa}$ were applied. The CA reactor was controlled at -0.85 V vs. SHE throughout the course of the experiment (221 days).

Each reactor was inoculated on day 0 with 1.2 g $COD_x$ $L^{-1}$. The inoculum was taken from running laboratory MES reactors producing acetate, *n*-butyrate, and *n*-caproate from $CO_2$ [30].

### 4.2.3. Analytical Methods

Twice a week, liquid samples were taken from each reactor. Concentration of C2 to C6 carboxylic acids and alcohols were analyzed by gas chromatography (Thermofisher, USA) using a Stabil-wax™ column with a length of 25 m and internal diameter of 0.2 μm. Colum temperature was kept at 50 °C for 7 min, increased to 180 °C during 8 min and kept at that temperature for 9 minutes. Helium was used as carrier gas at a flow rate of 1 mL $min^{-1}$ and the ionization detector was kept at 250 °C. Production of organics and faradaic efficiency were calculated as described by Raes and colleagues [31]. Biomass-specific growth rates and production rates were calculated as described by Winkelhorst and coworkers [30]. Here, carbon selectivity represents the fraction of carbon going into a specific product over the total amount of carbon assimilated in all identified products, i.e. acetate, butyrate, caproate, and biomass.

Samples were filtered with a 0.2 μm microporous filter and their total nitrogen content was analysed using a TOC analyser coupled with a TN unit (TOC-L Series Total Organic Carbon Analyzers, Shimadzu, Japan). Oven temperature was kept at 720 °C. The optical density of the unfiltered samples was measured at 600 nm with a UV-VIS spectrophotometer (UV-1800 series, Shimadzu, Japan) to account for planktonic cells. To study microbial activity, the method described by Winkelhorst and colleagues [30]. was utilized to estimate microbial growth in both biofilm and suspension separately as well as biomass concentration and biomass-specific productivity.

### 4.2.4. Scanning Electron Microscopy

Carbon felt pieces were carefully cut at different places along the length of the flow channel (**Figure 4.6**). Samples were immediately fixed with 2.5% glutaraldehyde in PBS buffer for 24 h at 4 °C, rinsed with PBS buffer and dehydrated with a graded series of ethanol.

### 4.2.5. DNA Extraction and 16S Sequence Analysis

To extract DNA from the biofilm both on and within the 3D porous cathode, the samples were ground with a pestle in a mortar, periodically incorporating liquid nitrogen to prevent DNA degradation. The resulting powder comprised a mixture of biomass and carbon felt fibers. Subsequently, DNA extraction was carried out

using a Qiagen DNeasy PowerBiofilm Kit (Qiagen, Hilden, Germany), employing a detergent lysis method in conjunction with bead beating using an MPTM FastPrep-24 homogenizer (MP Biomedicals, Irvine, CA), following the manufacturer's instructions. The purified DNA underwent quality assessment by measuring the A260/280 and A260/230 ratios (Nanodrop 2000 spectrophotometer (ThermoFischer Scientific, Waltham, MA) and quantification using a Qubit broad-range assay (Qubit 2.0 Fluorometer and Qubit dsDNA BR Assay Kit (Thermo Fischer Scientific)).

### 4.2.6. Microbial Community Analysis

Microbial community analysis was conducted through 16S rRNA sequencing. For this purpose, extracted DNA samples were sent to Novogene (UK) (Cambridge, United Kingdom). The 16S rRNA amplicon was sequenced using barcoded primers 341F (CCTAYGGGRBGCASCAG) and 806R (GGACTACNNGGGTATCTAAT) to amplify regions V3 + V4 of both bacterial and archaeal microorganisms. All polymerase chain reactions (PCR) were carried out in 30 µL reaction volumes, comprising 15 µL of Phusion® High-Fidelity PCR Master Mix (New England Biolabs, Ipswich, MA), 0.2 µM of forward and reverse primers, and approximately 10 ng of template DNA. Thermal cycling involved initial denaturation at 98 °C for 10 s, annealing at 50 °C for 30 s, elongation at 72 °C for 30 s, and a final extension at 72 °C for 5 min. PCR products underwent purification through gel electrophoresis using a 2% agarose gel and subsequent extraction using a Qiagen Gel Extraction Kit. Sequencing libraries were generated using the NEBNext® UltraTM DNA Library Prep Kit for Illumina (Illumina, San Diego, CA), following the manufacturer's recommendations, with index codes added. The library quality was evaluated using a Qubit 2.0 Fluorometer (Thermo Scientific) and Agilent Bioanalyzer 2100 system (Agilent, Santa Clara, CA), and the sequencing was performed on an Illumina HiSeq platform to generate 250 bp paired-end reads. Data analysis was performed as described in Supplemental Material 4.6.2.

## 4.3. Results and Discussion

In the current investigation, we devised an innovative microbial electrosynthesis reactor, termed a directed-flow-through bioelectrochemical reactor (DFBR). This DFBR introduces a serpentine flow-pattern architecture in both the cathode and anode compartments. At the cathode, the serpentine channel is filled with a carbon felt electrode through which the catholyte is forced to flow through. Two reactors were continuously operated, either potentiostatically (CA) or galvanostatically (CP),

for more than 220 days. Nutrients were replenished using a hydraulic retention time of 4 days, complementing the continuous sparging of $CO_2$.

### 4.3.1. Biomass Growth Rate and Microbial Kinetics of Electrode Colonization Similar in Potentiostatic and Galvanostatic-Controlled Reactors

The time-dependent biomass-specific growth rate ($\mu$) was experimentally determined for both reactors (**Figure 4.2A**), using a recently published method [30]. This method differentiates microbial growth in biofilm and in suspension. The progression of biofilm quantity per electrode volume over time and the associated percentage of electrode colonization under our experimental conditions were assessed (**Figure 4.2B**). The percentage was calculated on basis of the total biofilm amount, which reached a plateau after 225 days, representing biofilm saturation. This saturation point likely indicates a restriction in space that impeded further biofilm growth.

In both reactors, growth rates ranging from 0.03 to 0.11 $d^{-1}$ were recorded during the initial 50 days, followed by a decline in growth rates to approximately 0.01 $d^{-1}$ until the conclusion of the experiments. Comparable growth rates and trends were previously observed in non-optimized flow-through MES reactors [30]. Consequently, the present DFBR did not speed-up biofilm growth and electrode colonization. These growth rates remain modest compared to those observed in analogous anaerobic fermentation technologies like syngas fermentation and chain elongation (up to 2.9-5.7 $d^{-1}$) [32,33]. Consequently, achieving a fully grown and colonized electrode proved time-consuming in this context (225 days), underscoring the need for improvements from an application perspective. Furthermore, our observations indicated that keeping either current or potential at the used static value did not influence the growth of biofilms and electrode colonization. This suggests that electron uptake from the electrode may not be the limiting process, indicating the presence of other limiting factors influencing growth. This underscores the significant challenge of rapidly colonizing a large electrode, representing a key limitation in the scale-up of microbial electrosynthesis technology.

**4**
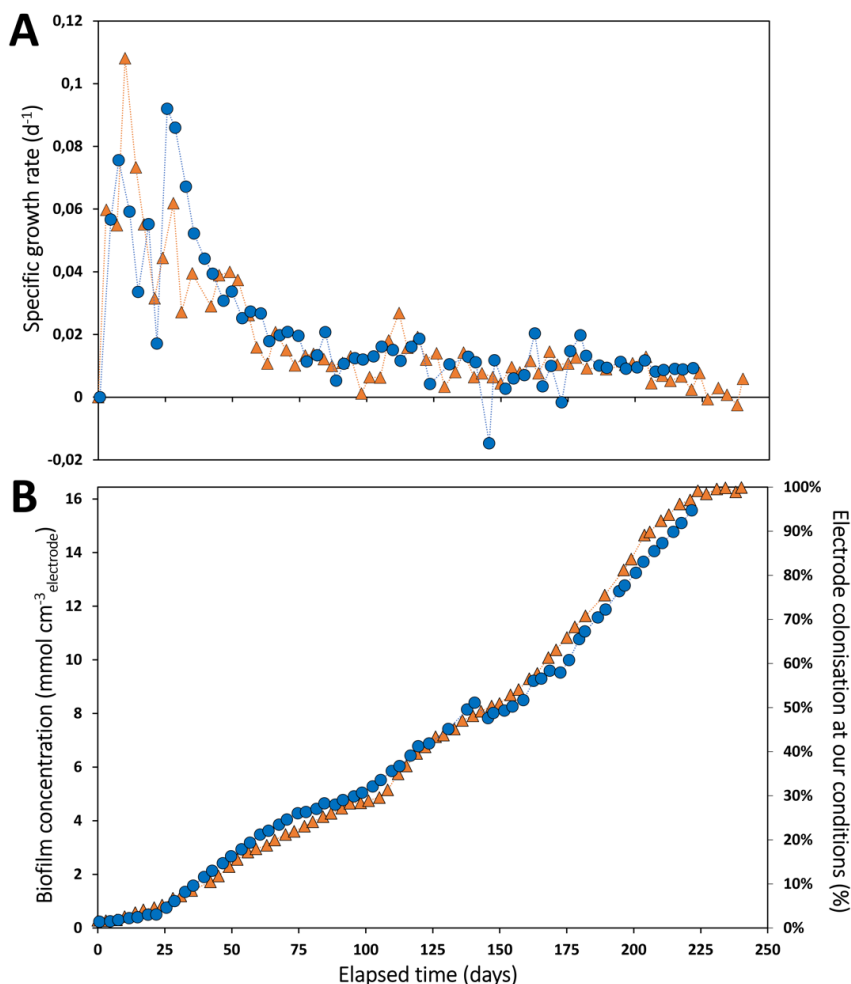
**Figure 4.2. Biomass-specific growth rate (A)**, biofilm concentration and electrode colonization **(B)** measured over time in the CP (orange triangles) and CA (blue circles) reactors.

### 4.3.2. Directed-Flow-Through Bioelectrochemical Reactor Allows Three Times Denser Biofilm than Previous State-of-the-Art

The preceding state-of-the-art in MES [30] achieved a biofilm apparent density, or amount of biofilm per electrode volume, of $5.0 \pm 2.7$ mmol$_x$ cm$^{-3}$$_{cathode}$ (**Figure 4S 1** in Supplementary Material). In contrast, the novel serpentine design of the directed-flow-through bioelectrochemical reactor remarkably increased the biofilm apparent density (dry cell mass concentration) by over three-fold, reaching 16.4 mmol$_x$ cm$^{-3}$$_{cathode}$. Notably, biofilm constituted >99% of the biomass in the reactors (**Figure 4S 2**), underscoring the DFBR's efficacy for biofilm-driven bioelectrochemical processes. Attempts to promote biofilm growth in other reactor

concepts faced challenges, with microorganisms being washed out during the transition from fed-batch to continuous mode [34,35]. A higher biofilm apparent density translates into a larger number of microbes available for the target reaction. As inoculum and electrode material were consistent between our study and Winkelhorst and colleagues (2023) [30], this suggests that the reactor architecture and flow pattern/fluid dynamics played a pivotal role in the increased apparent biofilm density. The DFBR design mitigates dead zones, ensuring the entire carbon felt is accessible for biofilm growth. Additionally, the DFBR design eliminates free-flowing liquid in the cathode chamber, facilitating transport of CO$_2$, nutrients, H$_2$, and products at the biofilm-cathode interface and throughout the channel. It is noteworthy that the catholyte superficial fluid velocity through the electrode in the DFBR was 12 times higher than in Winkelhorst and coworkers (20.0 vs. 1.7 mm s$^{-1}$), which may have contributed to the observed biofilm density as well. Further investigation is warranted to elucidate the impact of fluid velocity on biofilm in MES.
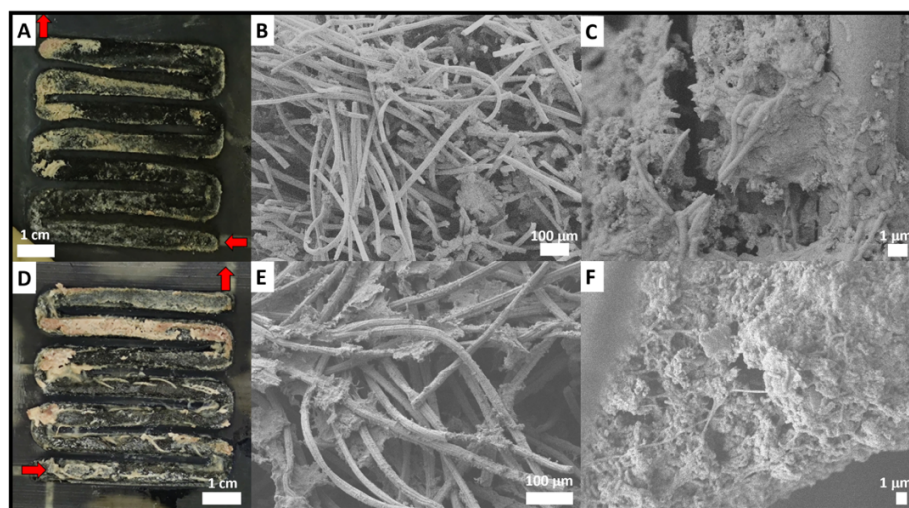


**Figure 4.3.** Photograph and scanning electron microscopy images of the biofilm grown on the carbon felt electrode of the CP **(A-C)** and CA **(D-F)** reactors, at the end of the experiment.

Photographic evidence of the cathodes and SEM images from both reactors at the experiment's conclusion (**Figure 4.3** and **Figure 4S 3**) confirmed the development of a thick and dense biofilm, visible to the naked eye, on both sides of the carbon felt, spanning its entire thickness and along the entire serpentine channel. Well-formed biofilm on individual carbon fibres, comprising morphologically diverse microorganisms encapsulated in an extracellular matrix, is observable throughout the entirety of the carbon felt.

### 4.3.3. Directed-Flow-Through Bioelectrochemical Reactor Results in 5-Fold Higher Volumetric Current Density and Productivity than the State-of-the-Art

The evolution over time of the current density, cathode potential, organics concentration, and faradaic efficiency in both reactors were evaluated (**Figure 4.4**). The trends in organics production rates and current normalized to electrode volume are depicted in **Figure 4S 4** and **Figure 4S 5**. Notably, no alcohols such as ethanol were detected at any point during the experiments.

In the CP reactor, the cathode potential consistently ranged between -0.8 V and -1.0 V vs. SHE throughout successive applied current steps, reaching up to -105 A $m^{-2}_{PSA}$ (projected surface area). In the CA reactor (-0.85 V vs. SHE), the cathodic current initially remained low at around -5 A $m^{-2}_{PSA}$ for the first 25 days, gradually increasing to -15 A $m^{-2}_{PSA}$ by day 35. Subsequently, the current remained relatively stable until day 85, coinciding with approximately 30% biofilm colonization of the carbon felt (**Figure 4.2B**). Between day 85 and day 139, the current exhibited exponential growth, reaching -100 A $m^{-2}_{PSA}$, corresponding to 50% biofilm coverage on the carbon felt. The reactor experienced a crash on day 139, inducing biofilm stress, resuspension, and rapid re-attachment, evident by a sudden increase and subsequent decrease in optical density (**Figure 4S 6**). Following a lag phase, the electron uptake rate recovered from day 170 and remarkably surged further to a cathodic current of approximately -200 A $m^{-2}_{PSA}$ (-40 mA $cm^{-3}_{cathode}$) at the experiment's conclusion, with peaks reaching -300 A $m^{-2}_{PSA}$ (-60 mA $cm^{-3}_{cathode}$) over a 7-day period between days 200 and 207. The prior state-of-the-art MES reactor, producing soluble organics, reported a current of -101 A $m^{-2}_{PSA}$, equivalent to -7.8 mA $cm^{-3}_{cathode}$, at the same cathode potential [6]. The DFBR demonstrated a notable enhancement, achieving a two-fold increase in current normalized to projected surface area and a five-fold increase in volume of the electrode. Normalizing performance to electrode volume is particularly relevant when employing 3D electrodes [36,37], accounting for the electrode thickness. The previous state of the art current of -101 A $m^{-2}_{PSA}$ was attained with a 1.2 cm thick carbon felt, whereas our study employed a 0.5 cm thick carbon felt. A thinner cathode is advantageous, promoting lower ohmic resistances and consequently higher energy efficiencies [2,11]. In the last 10 days of the experiment, a faradaic efficiency of 40% (and increasing) was achieved, corresponding to volumetric productivities of 43 $kg_{C2}$ $m^{-3}_{cathode}$ $d^{-1}$, 30 $kg_{C4}$ $m^{-3}_{cathode}$ $d^{-1}$, and 5 $kg_{C6}$ $m^{-3}_{cathode}$ $d^{-1}$ (equivalent to a total C production of 37.3 $kg_C$ $m^{-3}_{cathode}$ $d^{-1}$).
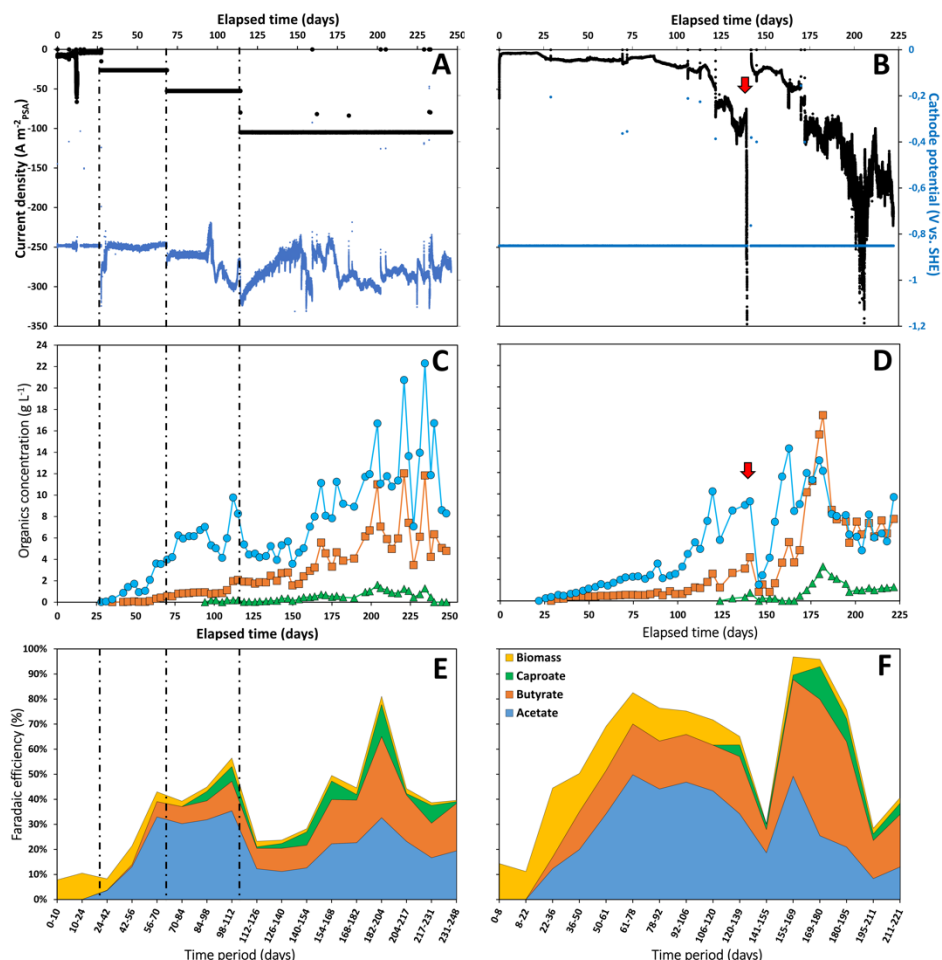
**Figure 4.4.** Current density and cathode potential **(A-B)**, concentration of acetate (blue circles), butyrate (orange squares) and caproate (green triangles) **(C-D)**, and faradaic efficiency **(E-F)** evolution over time in the CP (left) and CA (right) reactors. The red arrow (day 139) indicates a leakage event that emptied the cathode compartment almost entirely, which stopped the potentiostat and the liquid recirculation, and the reactor remained in this state for 3 days (long weekend).

### 4.3.4. Biofilm Suspension and Re-Attachment Leads to Higher Carbon Selectivity and Faradaic Efficiency into C4 and C6

Within the initial 25 days, only biomass growth occurred, representing approximately $11.3 \pm 2.9\%$ of electron recovery into biomass in both reactors, at comparable current densities. Consequently, both reactors exhibited a lag phase of approximately 25 days before measurable amounts of soluble organics were produced, a phenomenon previously observed in microbial electrosynthesis (MES) [30,38]. Acetate (C2) was the initial product in both reactors, closely followed by n-butyrate (C4). During the initial 100 days, under CP, C2 and C4 concentrations

increased more rapidly than under CA (7.0 vs. 2.5 $g_{C2}$ $L^{-1}$ and 0.9 vs. 0.6 $g_{C4}$ $L^{-1}$), albeit at the expense of faradaic efficiency (45% vs. 75%), likely due to higher currents, i.e. higher availability of $H_2$. A lower faradaic efficiency corresponds to reduced energy efficiency (**Figure 4S 7**), indicating higher energy wastage. Despite the application of a higher current (CP) than that measured under CA, it did not result in increased growth rates or higher biofilm amounts (28% electrode colonization in both reactors at day 100, **Figure 4.2**). It did however lead to higher acetate production rates in the first 100 days, 26 vs 10 $kg_{C2}$ $m^{-3}_{cathode}$ $d^{-1}$ (**Figure 4S 4**), likely due to a higher $H_2$ availability, suggesting a decoupling of growth and production metabolisms. As observed previously, once a mature biofilm was established, carboxylate production became maintenance-driven [30]. This pattern persisted here, with acetate concentration reaching up to 10 g $L^{-1}$ and productivity 34 $kg_{C2}$ $m^{-3}_{cathode}$ $d^{-1}$ when the current density increased to similar, and subsequently higher, levels under CA from day 125 to 139 (up to -100 A $m^{-2}$). Simultaneously, butyrate concentration reached 4 g $L^{-1}$ and productivity 18 $kg_{C4}$ $m^{-3}_{cathode}$ $d^{-1}$. A higher faradaic efficiency of 65% was achieved at -100 A $m^{-2}$ under CA compared to -52 A $m^{-2}$ under CP (50%). Caproate (C6) production commenced earlier under CP than CA (98 vs. 130 days), likely attributable to the earlier attainment of higher concentrations of C2 and C4 [6,18].

Following the lag phase subsequent to the CA reactor crash on day 139, a notable faradaic efficiency of 90% was achieved from day 155 to 169 at a current density of approximately -47 A $m^{-2}$. An even higher faradaic efficiency of 93% was reached at -102 A $m^{-2}_{PSA}$ (-20 mA $cm^{-3}_{cathode}$) from day 169 to 180, coinciding with elevated concomitant volumetric productivities of 50 $kg_{C2}$ $m^{-3}_{cathode}$ $d^{-1}$, 71 $kg_{C4}$ $m^{-3}_{cathode}$ $d^{-1}$, and 15 $kg_{C6}$ $m^{-3}_{cathode}$ $d^{-1}$ (equivalent to 69 $kg_C$ $m^{-3}_{cathode}$ $d^{-1}$). This represents a remarkable 3.1-fold increase in soluble organics productivity compared to the state-of-the-art (22 $kg_C$ $m^{-3}_{cathode}$ $d^{-1}$) [6]. Notably, a high carbon selectivity of 57%$_{C4}$ and 14%$_{C6}$ (**Figure 4S 8**) and a faradaic efficiency of 55% and 13% into C4 and C6, respectively, were achieved. Higher selectivity towards C4 and C6 is advantageous given their higher value compared to acetate [4]. Lower carbon selectivity (29%$_{C4}$ and 4%$_{C6}$) and faradaic efficiency (23%$_{C4}$ and 5%$_{C6}$) into C4 and C6 were recorded before the reactor crash at the same current density of -102 A $m^{-2}_{PSA}$ from day 120 to 139. Similarly, a lower carbon selectivity (36 ± 6%$_{C4}$ and 8 ± 5%$_{C6}$) and faradaic efficiency (16 ± 7%$_{C4}$ and 4 ± 4%$_{C6}$) into C4 and C6 were achieved in the CP reactor at -105 A $m^{-2}$, which did not experience significant biofilm disturbance. A previous study also demonstrated that rapid detachment and reattachment, leading to biofilm reorganization, significantly improved carbon selectivity and faradaic efficiency

towards C4 and C6 over acetate [18]. The mechanism responsible for this phenomenon is yet to be fully elucidated. It is noteworthy that a lower total faradaic efficiency was recorded from day 120 to 139 (62%) compared to day 169 to 180 (93%) at the same current density in the CA reactor. This discrepancy may be attributed to a lower biofilm amount (7.4 vs. 10.8 $mmol_x$ $cm^{-3}_{cathode}$) and electrode coverage (43 vs. 68%) (**Figure 4.2B**) and/or to the biofilm reorganization.

The faradaic efficiency declined notably after the escalation of current density to -200 A $m^{-2}_{PSA}$ (-40 mA $cm^{-3}_{cathode}$) from day 195 to 221. The cause of this surge in cathodic current remains unclear at this stage, but it might be attributed to the increase in electrode coverage by biofilm to over 90% during that period (**Figure 4.2B**). A higher biofilm amount correlates with an increased demand for electrons. On day 180, the highest concentrations ever reported in continuously-operated MES reactors of C4 (17.4 g $L^{-1}$) and C6 (3.2 g $L^{-1}$) were reached. Subsequently, a decline in organics concentration and production rates was observed. A plausible explanation could be the inhibition of the biofilm by C4 and C6 acids, known for their toxicity, as previously modeled in MES [13], though further investigation is required for confirmation. Nonetheless, a 2-fold higher volumetric productivity compared to the previous state-of-the-art was maintained from day 195 until the experiment's conclusion. Additionally, carbon selectivity remained favorable, with 57% and 11% directed into C4 and C6, respectively.

When comparing with Chu and Baek and colleagues, who studied a flow-electrode-based MES reactor and a zero-gap MES reactor, respectively, an order of magnitude higher current density, productivity, and products concentration were obtained with our directed-flow-through bioelectrochemical reactor, while producing significant amounts of butyrate and caproate in addition to acetate (and no methane). Combining a vapor-fed anode as tested by Baek and coworkers with our cathode configuration could be a promising avenue to further increase the energy efficiency of MES while achieving high productivity.

### 4.3.5. Potentiostatic Control Results in Higher Faradaic and Energy Efficiencies

Under galvanostatic control (CP), an increment in cathodic current density from -26 to -53 or -105 A $m^{-2}$ did not significantly elevate the organics concentration until day 150 (**Figure 4.4C**). This observation could be attributed to the fact that by day 150, only half of the electrode was colonized (**Figure 4.2B**). The limited biofilm coverage hampers the microbial uptake of electrons (and $CO_2$). This is evident in the relatively low faradaic efficiency during this period. Subsequently, from day 150

until the end of the experiment, concentrations and production rates gradually increased as biofilm coverage expanded. High acetate and butyrate concentrations of 22.3 g $L^{-1}$ and 12 g $L^{-1}$ were attained in this reactor. Simultaneous volumetric productivities of 64 $kg_{C2}$ $m^{-3}_{cathode}$ $d^{-1}$, 42 $kg_{C4}$ $m^{-3}_{cathode}$ $d^{-1}$, and 17 $kg_{C6}$ $m^{-3}_{cathode}$ $d^{-1}$ (equivalent to 60 $kg_C$ $m^{-3}_{cathode}$ $d^{-1}$) were achieved (**Figure 4S 4**), marking a 2.7-fold increase compared to the previous state-of-the-art and similar to the CA reactor. Relative to the CA reactor, lower faradaic and energy efficiencies were observed under galvanostatic control, despite similar current density and biofilm amount/coverage. The reasons for these differences warrant further investigation. In the CA reactor, energy efficiencies averaged 34 ± 17% at -102 A $m^{-2}$, with a peak at 64% (**Figure 4S 7**). It is important to note that optimizing the energy efficiency of the directed-flow-through bioelectrochemical reactor (DFBR) was beyond the scope of this work; for instance, a thick membrane was employed, leading to high ohmic overpotentials. Overall, CP did not accelerate biofilm growth or result in higher organics productivity and faradaic efficiency in this study.

### 4.3.6. Biomass-Specific Production Rates Maintained Over a Long Period of Time

Employing a recently established methodology [30], biomass-specific production rates ($q_p$) can now be determined over time in MES (**Figure 4.5**). Biomass-specific production rate represents a microbial kinetic parameter that normalizes the production rate to the quantity of biomass within the reactor at a specific moment. Utilizing biomass-specific rates, one can more effectively assess the specific performance of the biocatalysts in MES, facilitating meaningful comparisons with other technologies.

In both reactors, $q_p$ exhibited an initial increase before stabilizing at comparable values of 0.19 ± 0.06 $mol_C$ $mol_x^{-1}$ $d^{-1}$ until the conclusion of the experiments. A preceding study, which reported $q_p$ in microbial electrosynthesis, documented biomass-specific production rates of C2-C6 carboxylates around 0.25 ± 0.05 $mol_C$ $mol_x^{-1}$ $d^{-1}$ in the initial 50 days, followed by a gradual decline to 0.05 ± 0.03 $mol_C$ $mol_x^{-1}$ $d^{-1}$ by day 200 [30]. It was suggested that this rate, like the specific growth rate, declined as the biofilm quantity increased and matured to fully colonize the electrode. The aforementioned study utilized non-optimized flow-through reactors with the same electrode material and inoculum. In contrast, our findings demonstrate that the novel directed-flow-through bioelectrochemical reactor concept allows for the preservation of biomass-specific production rates over an extended period, even with biofilm apparent density three times higher and

elevated product concentrations compared to the study by Winkelhorst and colleagues [30]. These results can be attributed to improved mass transport of $CO_2$, nutrients, $H_2$, and/or products throughout the entire cathode, facilitated by the specific reactor architecture and fluid dynamics.
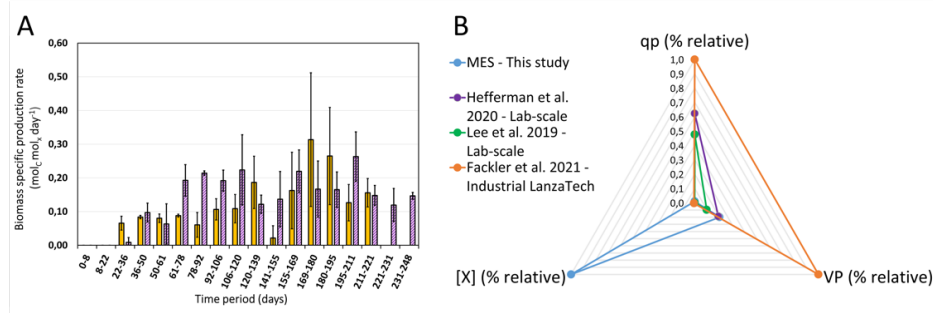


**Figure 4.5. A)** Biomass-specific production rates measured over time in the CP (purple bars) and CA (yellow bars) reactors. **B)** Comparison of three key performance indicators between our MES reactor and two of the best-performing lab-scale syngas fermentation reported in literature [8,9] as well as the industrial LanzaTech syngas fermentation process [7]. Instead of absolute values for each KPIs, relative percentages calculated from the max value are represented. Biomass specific production rates $qp$ vary from 0,2 to 20 $mol_C$ $molx^{-1}$ $d^{-1}$, biomass concentrations [X] from 0.5 to 390 $g_x$ $L^{-1}$, and volumetric productivities (VP) from 0.1 to 1 $g_C$ $L^{-1}$ $h^{-1}$. VP is here normalized to the total medium volume, and not to the cathode volume in MES. Refer to **Table 4S 1** in the Supplementary Material to see the values extracted from literature and used here.

### 4.3.7. Volumetric Productivity in MES Now Comparable to Syngas Fermentation

Syngas fermentation serves as a pertinent benchmark for assessing microbial electrosynthesis. Syngas fermentation, employing acetogens to convert gas mixtures of $H_2$, CO, and $CO_2$ into a mixture of acetate and ethanol, has been successfully scaled up to an industrial level, exemplified by the LanzaTech process [7]. When comparing these technologies, three technical key performance indicators— biomass-specific production rates ($q_p$), the amount of biomass per reactor volume, and the product of both i.e. the volumetric productivity—should be considered. A comparison was drawn using data from two lab-scale syngas fermentation studies reporting the highest performance to the best of our knowledge [8,9], and the industrial-scale LanzaTech process [7] (**Figure 4.5B**). The achieved biomass-specific production rates in MES were notably lower than those reported in syngas fermentation, reaching up to 20 $mol_C$ $mol_x^{-1}$ $d^{-1}$. This observation presents an opportunity for MES, indicating the potential for higher microbial rates. Conversely, the amount of microbial biomass per unit of reactor volume in MES (390 $g_x$ $L^{-1}$ $_{cathode}$) significantly surpassed that in syngas fermentation (2.5 $g_x$ $L^{-1}$). MES relies on a dense biofilm, while the highest syngas fermentation performances were attained

with microorganisms in suspension. Consequently, our MES process demonstrated a comparable volumetric productivity of approximately 0.2 $g_C$ $L^{-1}$ $h^{-1}$ to lab-scale syngas fermentation and was five times lower than the LanzaTech process. It is important to note that volumetric productivity calculations in MES here utilized the total volume of catholyte, including the catholyte in the tubing and in the bubble column. Comparing volumetric production rates between biofilm-based and planktonic-based systems makes sense because the product is soluble in the medium. Normalizing to the volume of catholyte in the cathode chamber yielded productivity values 14 times higher, surpassing the LanzaTech process by 2.5 times. Optimization of the catholyte to electrode volume ratio requires further investigation. Additionally, considering market prices, it is noteworthy that C4 and C6 carboxylic acids, produced in MES, have higher prices than ethanol, although their market volumes are lower [4]. Actual scale-up of MES and in-depth techno-economic assessment of both technologies must then be performed to compare them fairly. Both technologies may also be complementary. This study represents a milestone in developing MES as a competitive technology, marking a promising outcome that warrants further scaling-up of MES technology.

Furthermore, microbial rates in microbial electrosynthesis are within the same order of magnitude as rates achieved in gas fermentation converting $H_2$ + $CO_2$ to carboxylates [8,39,40]. In a study by Zhang and colleagues [39], biofilms were cultivated on hollow-fibre membranes to convert an $H_2/CO_2$ mixture, yielding volumetric production rates considerably lower at 0.003 $g_C$ $L^{-1}$ $h^{-1}$ compared to the rates reported in our study. Another study by Kantzow and coworkers (2015) reported the use of a standard stirred-tank bioreactor equipped with a customized submerged microfiltration unit for biomass retention [41]. Continuously supplying $CO_2$-$H_2$ gas mixture and yeast extract, 14 g $L^{-1}$ of cell dry weight and 2.5 $g_C$ $L^{-1}$ $h^{-1}$ of acetate were produced. A systematic comparison of these two technologies is essential to delineate the advantages and disadvantages of each approach, especially in the context of scale-up considerations. Notably, Roghair and colleagues reported higher biomass-specific rates of 10 $mol_C$ $mol_x^{-1}$ $d^{-1}$ in their fermentation process, converting acetate and ethanol to a mixture of C2-C6 carboxylates, accompanied by a volumetric productivity of 2.7 $g_C$ $L^{-1}$ $h^{-1}$ [42]. Such comparative analyses can contribute valuable insights into optimizing and advancing these microbial processes.

It is important to note that the calculated biomass-specific production rates ($q_p$) in MES presented in this study are underestimated, as they do not consider the accumulation of dead biomass within the biofilm. Winkelhorst and coworkers [30]

demonstrated that after 200 days, up to 50% of the microbes within the biofilms were found to be dead. Consequently, the estimated $q_p$ values were approximately half of the actual values, emphasizing the need to account for dead biomass to obtain a more accurate assessment of microbial kinetics in MES. Moreover, the maximum theoretical amount of dry biomass per electrode volume should not exceed 12 mmol cm$^{-3}$, (based on a cell density of 1.09 g cm$^{-3}$, a dry weight ratio of 30%, and a carbon felt porosity of 90%; see calculations in the Supplementary Material). However, we calculated a maximum of 16.4 mmol$_x$ cm$^{-3}_{cathode}$, i.e. 37% higher than the theoretical maximum. This may be due to approximations in the N-balance method used for biomass quantification [30]. Therefore, the estimated $\mu$ and $q_p$ values may be at least 37% higher than reported above. Nevertheless, the volumetric productivities (VP) remain true and comparable with VP achieved in syngas fermentation. Even if the actual biomass-specific production rates were two to three times higher than reported above, i.e. up to 0.6 mol$_C$ mol$_x^{-1}$ d$^{-1}$, it would still be more than 30 times lower than microbial kinetics reported in syngas fermentation (20 mol$_C$ mol$_x^{-1}$ d$^{-1}$), which means that microbial kinetics in MES can be improved further.

### 4.3.8. *Clostridium luticellarii* and *Eubacterium limosum* are Dominant Species

To gain a deeper understanding of the notable performance distinctions between potentiostatically (CA) operated bioreactors and their galvanostatically (CP) controlled counterparts, we employed high-throughput 16S rRNA gene sequencing to investigate microbial community structures. Following an experimental period exceeding 220 days, microbial samples were collected from cathode-attached cells at three locations along the serpentine flow channel (**Figure 4.6A**). Each sample exhibited a dominant amplicon sequence variant (ASV) representation of more than 65%, encompassing no more than seven ASVs. Across the six samples, only 13 dominant species were identified (**Figure 4.6B**). Four species—*Eubacterium limosum, E. callanderi*, *Fermentimonas caenicola*, and *Clostridium luticellari*—were consistently present in all samples, regardless of the operational mode.

Among the remaining nine species, eight were specific to a single process. The CP reactor consistently featured ASVs belonging to the *Methanobrevibacter* and *Pseudoclavibacter* genera. In contrast, microbial communities from the CA reactor consistently shared six species, including *Oscillibacter* and *Phocaeicola* ASVs, in addition to the four species systematically found. Strikingly, none of these 13 ASVs have been associated to MES microbial communities before [43–45].
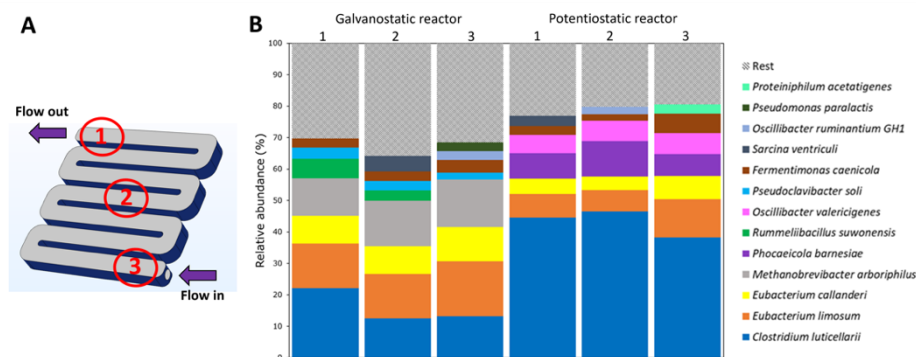
**Figure 4.6. A)** Sampling location along the serpentine electrode. **B)** Relative abundance of 16S rRNA of biofilm samples taken from three locations in both the CP and CA reactors, at the end of the experiment.

Three of the four systematically identified dominant species—*E. limosum*, *E. callanderi*, and *Clostridium luticellari* belong to the Clostridia class. These are known acetogens typically found in microbial communities associated with syngas fermentation. In this process, they grow autotrophically by utilizing a mixture of $H_2$, CO and $CO_2$ as carbon and energy sources, converting them into the central intermediate acetyl-CoA which is converted to acetate by most acetogens [46]. Interestingly, *Eubacterium limosum* and *Clostridium luticellari* were also found to perform chain elongation and produce C4 and C6 carboxylic acids [46,47], a characteristic dependent on environmental conditions. The presence of the three anaerobic species *Phocaeicola barnesiae* [48], *Oscilibacter valericigenes and Fermentimonas caenicola* remains unclear. Only *Oscilibacter valericigenes* (*Clostridia* class) was linked to C5 carboxylic acid biosynthesis [49]. The presence of these ancillary species could be necessary to meet specific nutritional requirements and contribute to the stable establishment of the biofilm.

On basis of these initial taxonomic findings, it is inferred that the serpentine design, which establishes a flow pattern in the forced-flow-through reactor, enabling an extended residence time for nutrients, $CO_2$, $H_2$, and products within the 3D-electrode, did not yield a pronounced gradient in community composition along the flow channel in each reactor. The microbial composition was found to be comparable at all three locations. It is essential to underscore that relative abundance does not necessarily align with activity levels. To understand the microbial function and physiology of these highly active biofilms, further analyses involving metagenomics, metatranscriptomics, and metaproteomics are imperative.

The source of the biofilm inoculum plays a pivotal role in shaping the composition of the ultimate microbial community, and the considerable diversity in inoculum origins documented in scientific literature poses challenges for meaningful comparisons. Nonetheless, our results conclusively demonstrate that novel microbial communities capable of driving highly efficient processes can be assembled in MES bioreactors.

### 4.3.9. Towards Scale-up and Practical Applications: Remaining Challenges

We established that forcing an electron flow through the application of current does not accelerate the growth of biofilms. This investigation underscores that the primary constraint on the applicability of microbial electrosynthesis lies in the rate at which a large electrode can be colonized. Mass transport of nutrients, $CO_2$, and products, fluid dynamic through the electrode, and the medium compositions could help alleviate growth limitations. Once colonization occurred, we demonstrated a 3-fold higher volumetric current density and productivity than the state of the art, up to a new record of $-28 \pm 7$ mA $cm^{-3}_{cathode}$ ($-142 \pm 39$ A $m^{-2}$) and $43 \pm 24$ $kg_C$ $m^{-3}_{cathode}$ $day^{-1}$, sustained over 50 days. Maximum production of 69 $kg_C$ $m^{-3}_{cathode}$ $day^{-1}$ were recorded over periods of more than 15 days. Faradaic and energy efficiencies of 60-97% and 30-35% were achieved, respectively. The designed directed-flow-through bioelectrochemical reactor (DFBR) showcased in this work enables the achievement of elevated biofilm concentrations per electrode volume, sustained microbial activity over a period exceeding 225 days, and notable volumetric productivity, now comparable to rates observed in syngas fermentation.

This study emphasizes the feasibility of enhancing microbe-specific rates to further increase volumetric productivity and product selectivity. Uncovering the exact electron transfer mechanisms from $CO_2$ to C6 will help gain control over the process. A compromise must be found between having enough electrode surface area for sufficient biofilm coverage, i.e. for high organics production rates, and efficient mass transport and fluid dynamics through the 3D/filamentous electrode. Another aspect to improve is the stability of production. Where syngas fermentations are generally stable in terms of production rates, MES shows instability over time, up to now. Moreover, high $CO_2$ conversion efficiencies should be aimed at upon scaling up to larger reactor size, which could be promoted with long flow channels as proposed here. Another aspect to optimize is the catholyte to electrode volume ratio which can be tuned to increase volumetric productivity, while avoiding product inhibition and allowing sufficient mass transport. In addition, the volume of the anolyte / the design of the anode compartment should be considered and optimized upon scale-up. Volumetric production rate accounting for the whole

reactor volume must be considered when comparing with other technologies. Here, we disregarded the anolyte volume because optimizing the anode compartment was out-of-scope. Given that the anode compartment was identical to the cathode compartment, one can apply a factor 2 to calculate the reactor-scale volumetric production rate from the reported values.

A practical challenge to the proposed design approach is the energy needed to force the catholyte through the carbon felt. Here, an overpressure of 0.4 to 0.7 bar was measured over a 40cm-long flow channel at the end of the experiments (**Figure 4S 6**). The overpressure increased over time as the biofilm grew, which led to more fluid channels within the carbon felt to clog (**Figure 4.3** and **Figure 4S 3**). Upon scale-up, a high overpressure would require more pumping energy, ultimately decreasing the overall energy efficiency. Further research should look at ways to minimize the pressure drop, such as using electrodes with a more open structure.

Inhibiting methanogenesis in a cost-effective way when using a mixed microbial culture remains a pressing challenge. Continuously feeding an expensive compound such as sodium-bromoethanesulfonate is not a solution.

Society needs sustainable carbon-based chemicals. Several feedstock and technologies will be needed to satisfy the demand. Carbon dioxide is an attractive feedstock, as it is widely available and must be taken out of the atmosphere. Beyond lab-scale research, microbial electrosynthesis has the potential to be one of those technologies that transform the chemical industry and provide sustainable products to the society. MES distinguishes itself from other $CO_2$-conversion technologies such as $CO_2$ electrolysis (using heterogeneous catalysts) or plasma technology, as it can produce more complex molecules, with more than two carbons. Therefore, MES does not compete with these technologies, as different markets and applications are targeted. MES also does not heavily rely on metals for which availability and supply chain challenges may arise in the future, and instead uses cheap carbon electrodes and microorganisms. Another advantage is that microbial biofilms in MES are self-repairing and robust, which has been demonstrated with reactors operated for more than 2 years. Our here-presented findings represent a milestone in developing MES as a competitive technology for efficient $CO_2$ valorization.

## 4.4. Acknowledgements

## 4.5. References

[1]     K. Rabaey, R.A. Rozendal, Microbial electrosynthesis — revisiting the electrical route for microbial production, Nat Rev Microbiol 8 (2010) 706–716. https://doi.org/10.1038/nrmicro2422.

[2]     L. Jourdin, T. Burdyny, Microbial Electrosynthesis: Where Do We Go from Here?, Trends Biotechnol 39 (2021) 359–369. https://doi.org/10.1016/j.tibtech.2020.10.014.

[3]     V. Flexer, L. Jourdin, Purposely Designed Hierarchical Porous Electrodes for High Rate Microbial Electrosynthesis of Acetate from Carbon Dioxide, Acc Chem Res 53 (2020) 311–321. https://doi.org/10.1021/acs.accounts.9b00523.

[4]     L. Jourdin, J. Sousa, N. van Stralen, D.P.B.T.B. Strik, Techno-economic assessment of microbial electrosynthesis from CO2 and/or organics: An interdisciplinary roadmap towards future research and application, Appl Energy 279 (2020) 115775. https://doi.org/10.1016/j.apenergy.2020.115775.

[5]     I. Vassilev, P.A. Hernandez, P. Batlle-Vilanova, S. Freguia, J.O. Krömer, J. Keller, P. Ledezma, B. Virdis, Microbial Electrosynthesis of Isobutyric, Butyric, Caproic Acids, and Corresponding Alcohols from Carbon Dioxide, ACS Sustain Chem Eng 6 (2018) 8485–8493. https://doi.org/10.1021/acssuschemeng.8b00739.

[6]     L. Jourdin, S.M.T. Raes, C.J.N. Buisman, D.P.B.T.B. Strik, Critical Biofilm Growth throughout Unmodified Carbon Felts Allows Continuous Bioelectrochemical Chain Elongation from CO2 up to Caproate at High Current Density, Front Energy Res 6 (2018). https://doi.org/10.3389/fenrg.2018.00007.

[7]     N. Fackler, B.D. Heijstra, B.J. Rasor, H. Brown, J. Martin, Z. Ni, K.M. Shebek, R.R. Rosin, S.D. Simpson, K.E. Tyo, R.J. Giannone, R.L. Hettich, T.J. Tschaplinski, C. Leang, S.D. Brown, M.C. Jewett, M. Köpke, Stepping on the Gas to a Circular Economy: Accelerating Development of Carbon-Negative Chemical Production from Gas Fermentation, Annu Rev Chem Biomol Eng 12 (2021) 439–470. https://doi.org/10.1146/annurev-chembioeng-120120-021122.

[8]     J.K. Heffernan, K. Valgepea, R. de Souza Pinto Lemgruber, I. Casini, M. Plan, R. Tappel, S.D. Simpson, M. Köpke, L.K. Nielsen, E. Marcellin, Enhancing CO2-Valorization Using Clostridium autoethanogenum for Sustainable Fuel and Chemicals Production, Front Bioeng Biotechnol 8 (2020). https://doi.org/10.3389/fbioe.2020.00204.

[9]     J. Lee, J.W. Lee, C.G. Chae, S.J. Kwon, Y.J. Kim, J.-H. Lee, H.S. Lee, Domestication of the novel alcohologenic acetogen Clostridium sp. AWRP: from isolation to characterization for syngas fermentation, Biotechnol Biofuels 12 (2019) 228. https://doi.org/10.1186/s13068-019-1570-0.

[10] K.P. Nevin, T.L. Woodard, A.E. Franks, Z.M. Summers, D.R. Lovley, Microbial Electrosynthesis: Feeding Microbes Electricity To Convert Carbon Dioxide and Water to Multicarbon Extracellular Organic Compounds, MBio 1 (2010). https://doi.org/10.1128/mBio.00103-10.

[11] A. Prévoteau, J.M. Carvajal-Arroyo, R. Ganigué, K. Rabaey, Microbial electrosynthesis from CO2: forever a promise?, Curr Opin Biotechnol 62 (2020) 48–57. https://doi.org/10.1016/j.copbio.2019.08.014.

[12] I. Vassilev, P. Dessì, S. Puig, M. Kokko, Cathodic biofilms – A prerequisite for microbial electrosynthesis, Bioresour Technol 348 (2022) 126788. https://doi.org/10.1016/j.biortech.2022.126788.

[13] O. Cabau-Peinado, A.J.J. Straathof, L. Jourdin, A General Model for Biofilm-Driven Microbial Electrosynthesis of Carboxylates From CO2, Front Microbiol 12 (2021). https://doi.org/10.3389/fmicb.2021.669218.

[14] M. Kühl, B.B. Jørgensen, Microsensor Measurements of Sulfate Reduction and Sulfide Oxidation in Compact Microbial Communities of Aerobic Biofilms, Appl Environ Microbiol 58 (1992) 1164–1174. https://doi.org/10.1128/aem.58.4.1164-1174.1992.

[15] C. Picioreanu, M.C. Van Loosdrecht, J.J. Heijnen, A theoretical study on the effect of surface roughness on mass transport and transformation in biofilms., Biotechnol Bioeng 68 (2000) 355–369.

[16] C. Picioreanu, I.M. Head, K.P. Katuri, M.C.M. van Loosdrecht, K. Scott, A computational model for biofilm-based microbial fuel cells, Water Res 41 (2007) 2921–2940. https://doi.org/10.1016/j.watres.2007.04.009.

[17] M.F. Alqahtani, K.P. Katuri, S. Bajracharya, Y. Yu, Z. Lai, P.E. Saikaly, Porous Hollow Fiber Nickel Electrodes for Effective Supply and Reduction of Carbon Dioxide to Methane through Microbial Electrosynthesis, Adv Funct Mater 28 (2018). https://doi.org/10.1002/adfm.201804860.

[18] L. Jourdin, M. Winkelhorst, B. Rawls, C.J.N. Buisman, D.P.B.T.B. Strik, Enhanced selectivity to butyrate and caproate above acetate in continuous bioelectrochemical chain elongation from CO2: Steering with CO2 loading rate and hydraulic retention time, Bioresour Technol Rep 7 (2019) 100284. https://doi.org/10.1016/j.biteb.2019.100284.

[19] T. Krieg, J. Madjarov, L.F.M. Rosa, F. Enzmann, F. Harnisch, D. Holtmann, K. Rabaey, Reactors for Microbial Electrobiotechnology, in: 2018: pp. 231–271. https://doi.org/10.1007/10_2017_40.

[20] K. Cui, K. Guo, J.M. Carvajal-Arroyo, J. Arends, K. Rabaey, An electrolytic bubble column with an external hollow fiber membrane gas–liquid contactor for effective microbial electrosynthesis of acetate from CO2, Chemical Engineering Journal 471 (2023) 144296. https://doi.org/10.1016/j.cej.2023.144296.

[21] L.F.M. Rosa, S. Hunger, C. Gimkiewicz, A. Zehnsdorf, F. Harnisch, Paving the way for bioelectrotechnology: Integrating electrochemistry into bioreactors, Eng Life Sci 17 (2017) 77–85. https://doi.org/10.1002/elsc.201600105.

[22] L.F.M. Rosa, S. Hunger, T. Zschernitz, B. Strehlitz, F. Harnisch, Integrating Electrochemistry Into Bioreactors: Effect of the Upgrade Kit on Mass Transfer, Mixing Time and Sterilizability, Front Energy Res 7 (2019). https://doi.org/10.3389/fenrg.2019.00098.

[23] F. Enzmann, F. Mayer, M. Stöckl, K.-M. Mangold, R. Hommel, D. Holtmann, Transferring bioelectrochemical processes from H-cells to a scalable bubble column reactor, Chem Eng Sci 193 (2019) 133–143. https://doi.org/10.1016/j.ces.2018.08.056.

[24] P. Batlle-Vilanova, R. Ganigué, S. Ramió-Pujol, L. Bañeras, G. Jiménez, M. Hidalgo, M.D. Balaguer, J. Colprim, S. Puig, Microbial electrosynthesis of butyrate from carbon dioxide: Production and extraction, Bioelectrochemistry 117 (2017) 57–64. https://doi.org/10.1016/j.bioelechem.2017.06.004.

[25] M. Romans-Casas, R. Blasco-Gómez, J. Colprim, M.D. Balaguer, S. Puig, Bio-electro CO2 recycling platform based on two separated steps, J Environ Chem Eng 9 (2021) 105909. https://doi.org/10.1016/j.jece.2021.105909.

[26] M. Roy, M. Saich, S.A. Patil, Scalability of the Microbial Electro-acetogenesis Process for Biogas Upgradation: Performance and Technoeconomic Assessment of a Liter-Scale System, Energy & Fuels 37 (2023) 15822–15831. https://doi.org/10.1021/acs.energyfuels.3c02312.

[27] S.M. de Smit, J.J.H. Langedijk, J.H. Bitter, D.P.B.T.B. Strik, Alternating direction of catholyte forced flow-through 3D-electrodes improves start-up time in microbial electrosynthesis at applied high current density, Chemical Engineering Journal 464 (2023) 142599. https://doi.org/10.1016/j.cej.2023.142599.

[28] N. Chu, D. Wang, H. Wang, Q. Liang, J. Chang, Y. Gao, Y. Jiang, R.J. Zeng, Flow-Electrode Microbial Electrosynthesis for Increasing Production Rates and Lowering Energy Consumption, Engineering 25 (2023) 157–167. https://doi.org/10.1016/j.eng.2021.09.015.

[29] G. Baek, R. Rossi, P.E. Saikaly, B.E. Logan, High-rate microbial electrosynthesis using a zero-gap flow cell and vapor-fed anode design, Water Res 219 (2022) 118597. https://doi.org/10.1016/j.watres.2022.118597.

[30] M. Winkelhorst, O. Cabau-Peinado, A.J.J. Straathof, L. Jourdin, Biomass-specific rates as key performance indicators: A nitrogen balancing method for biofilm-based electrochemical conversion, Front Bioeng Biotechnol 11 (2023). https://doi.org/10.3389/fbioe.2023.1096086.

[31] S.M.T. Raes, L. Jourdin, C.J.N. Buisman, D.P.B.T.B. Strik, Continuous Long-Term Bioelectrochemical Chain Elongation to Butyrate, ChemElectroChem 4 (2017) 386–395. https://doi.org/10.1002/celc.201600587.

[32] A. Groher, D. Weuster-Botz, General medium for the autotrophic cultivation of acetogens, Bioprocess Biosyst Eng 39 (2016) 1645–1650. https://doi.org/10.1007/s00449-016-1634-5.

[33] P. Candry, T. Van Daele, K. Denis, Y. Amerlinck, S.J. Andersen, R. Ganigué, J.B.A. Arends, I. Nopens, K. Rabaey, A novel high-throughput method for kinetic characterisation of anaerobic bioproduction strains, applied to Clostridium kluyveri, Sci Rep 8 (2018) 9724. https://doi.org/10.1038/s41598-018-27594-9.

[34] J.B.A. Arends, S.A. Patil, H. Roume, K. Rabaey, Continuous long-term electricity-driven bioproduction of carboxylates and isopropanol from CO 2 with a mixed microbial community, Journal of CO2 Utilization 20 (2017) 141–149. https://doi.org/10.1016/j.jcou.2017.04.014.

[35] S. Bajracharya, K. Vanbroekhoven, C.J.N. Buisman, D.P.B.T.B. Strik, D. Pant, Bioelectrochemical conversion of CO 2 to chemicals: CO 2 as a next generation feedstock for electricity-driven

4

bioproduction in batch and continuous modes, Faraday Discuss 202 (2017) 433–449. https://doi.org/10.1039/C7FD00050B.

[36]   L. Jourdin, D. Strik, Electrodes for Cathodic Microbial Electrosynthesis Processes: Key Developments and Criteria for Effective Research and Implementation, in: Functional Electrodes for Enzymatic and Microbial Electrochemical Systems, WORLD SCIENTIFIC (EUROPE), 2017: pp. 429–473. https://doi.org/10.1142/9781786343543_0012.

[37]   S.A. Patil, S. Gildemyn, D. Pant, K. Zengler, B.E. Logan, K. Rabaey, A logical data representation framework for electricity-driven bioproduction processes, Biotechnol Adv 33 (2015) 736–744. https://doi.org/10.1016/j.biotechadv.2015.03.002.

[38]   M. Romans-Casas, L. Feliu-Paradeda, M. Tedesco, H.V.M. Hamelers, L. Bañeras, M.D. Balaguer, S. Puig, P. Dessì, Selective butyric acid production from CO2 and its upgrade to butanol in microbial electrosynthesis cells, Environmental Science and Ecotechnology 17 (2024) 100303. https://doi.org/10.1016/j.ese.2023.100303.

[39]   F. Zhang, J. Ding, Y. Zhang, M. Chen, Z.-W. Ding, M.C.M. van Loosdrecht, R.J. Zeng, Fatty acids production from hydrogen and carbon dioxide by mixed culture in the membrane biofilm reactor, Water Res 47 (2013) 6122–6129. https://doi.org/10.1016/j.watres.2013.07.033.

[40]   F. Ammam, P.-L. Tremblay, D.M. Lizak, T. Zhang, Effect of tungstate on acetate and ethanol production by the electrosynthetic bacterium Sporomusa ovata, Biotechnol Biofuels 9 (2016) 163. https://doi.org/10.1186/s13068-016-0576-0.

[41]   C. Kantzow, A. Mayer, D. Weuster-Botz, Continuous gas fermentation by Acetobacterium woodii in a submerged membrane reactor with full cell retention, J Biotechnol 212 (2015) 11–18. https://doi.org/10.1016/j.jbiotec.2015.07.020.

[42]   M. Roghair, D.P.B.T.B. Strik, K.J.J. Steinbusch, R.A. Weusthuis, M.E. Bruins, C.J.N. Buisman, Granular sludge formation and characterization in a chain elongation process, Process Biochemistry 51 (2016) 1594–1598. https://doi.org/10.1016/j.procbio.2016.06.012.

[43]   D. Wang, Q. Liang, N. Chu, R.J. Zeng, Y. Jiang, Deciphering mixotrophic microbial electrosynthesis with shifting product spectrum by genome-centric metagenomics, Chemical Engineering Journal 451 (2023) 139010. https://doi.org/10.1016/j.cej.2022.139010.

[44]   C.W. Marshall, D.E. Ross, K.M. Handley, P.B. Weisenhorn, J.N. Edirisinghe, C.S. Henry, J.A. Gilbert, H.D. May, R.S. Norman, Metabolic Reconstruction and Modeling Microbial Electrosynthesis, Sci Rep 7 (2017) 8391. https://doi.org/10.1038/s41598-017-08877-z.

[45]   D.E. Ross, C.W. Marshall, H.D. May, R.S. Norman, Metagenome-Assembled Genome Sequences of *Acetobacterium* sp. Strain MES1 and *Desulfovibrio* sp. Strain MES5 from a Cathode-Associated Acetogenic Microbial Community, Genome Announc 5 (2017). https://doi.org/10.1128/genomeA.00938-17.

[46]   F.R. Bengelsdorf, M.H. Beck, C. Erz, S. Hoffmeister, M.M. Karl, P. Riegler, S. Wirth, A. Poehlein, D. Weuster-Botz, P. Dürre, Bacterial Anaerobic Synthesis Gas (Syngas) and CO 2 + H 2 Fermentation, in: Adv. Appl. Microbiol. 2018: pp. 143–221. https://doi.org/10.1016/bs.aambs.2018.01.002.

[47]   D. Litty, V. Müller, Butyrate production in the acetogen *Eubacterium limosum* is dependent on the carbon and energy source, Microb Biotechnol 14 (2021) 2686–2692. https://doi.org/10.1111/1751-7915.13779.

[48]    P.T.N. Lan, M. Sakamoto, S. Sakata, Y. Benno, Bacteroides barnesiae sp. nov., Bacteroides salanitronis sp. nov. and Bacteroides gallinarum sp. nov., isolated from chicken caecum, Int J Syst Evol Microbiol 56 (2006) 2853–2859. https://doi.org/10.1099/ijs.0.64517-0.

[49]    T. Iino, K. Mori, K. Tanaka, K. Suzuki, S. Harayama, Oscillibacter valericigenes gen. nov., sp. nov., a valerate-producing anaerobic bacterium isolated from the alimentary canal of a Japanese corbicula clam, Int J Syst Evol Microbiol 57 (2007) 1840–1845. https://doi.org/10.1099/ijs.0.64717-0.

4

## 4.6. Supplementary Material
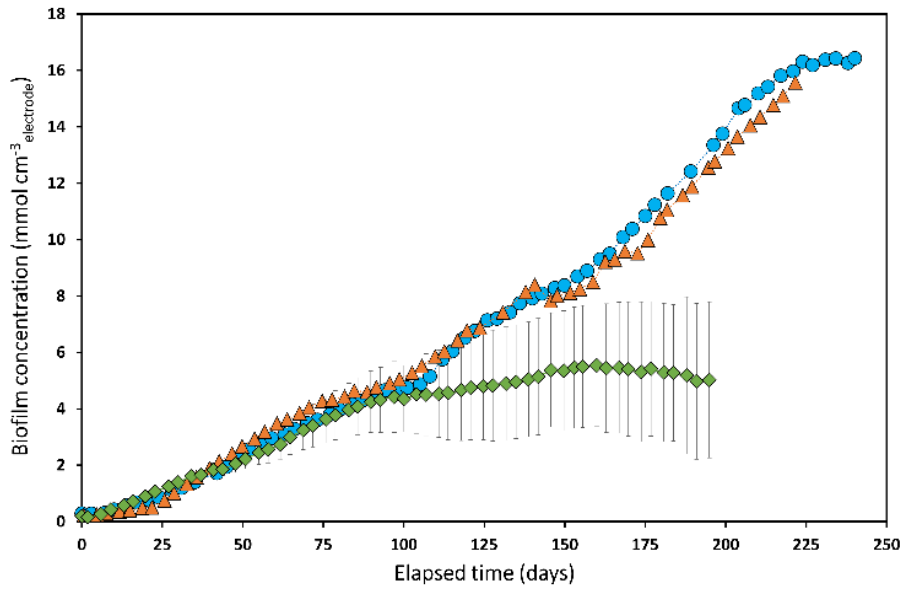


**Figure 4S 1.** Biofilm concentration measured over time in the CP (orange triangles) and CA (blue circles) reactors, compared with the state-of-the-art from Winkelhorst et al. 2023 [1] (green diamonds).
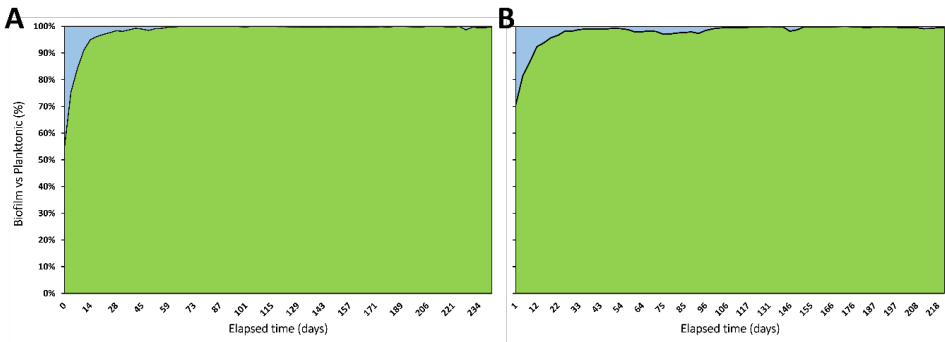


**Figure 4S 2.** Relative abundance of biomass in biofilm (green) and in suspension (blue) in the CP **(A)** and CA **(B)** reactors.
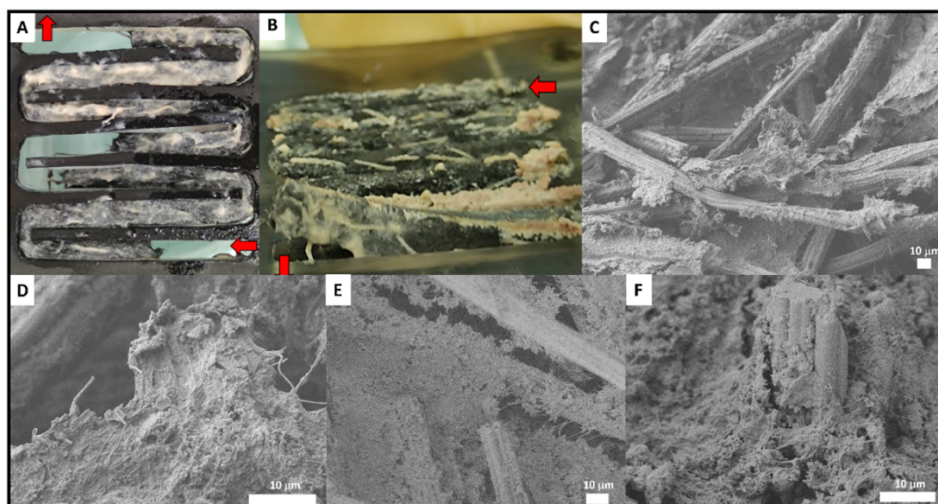
**Figure 4S 3.** Photograph of the biofilm on the side of the carbon felt facing the current collector **(A)** and throughout its thickness **(B)**. SEM images of the biofilm grown on the carbon felt electrode of the CA **(C-D)** and CP **(E-F)** reactors, at the end of the experiment.

4
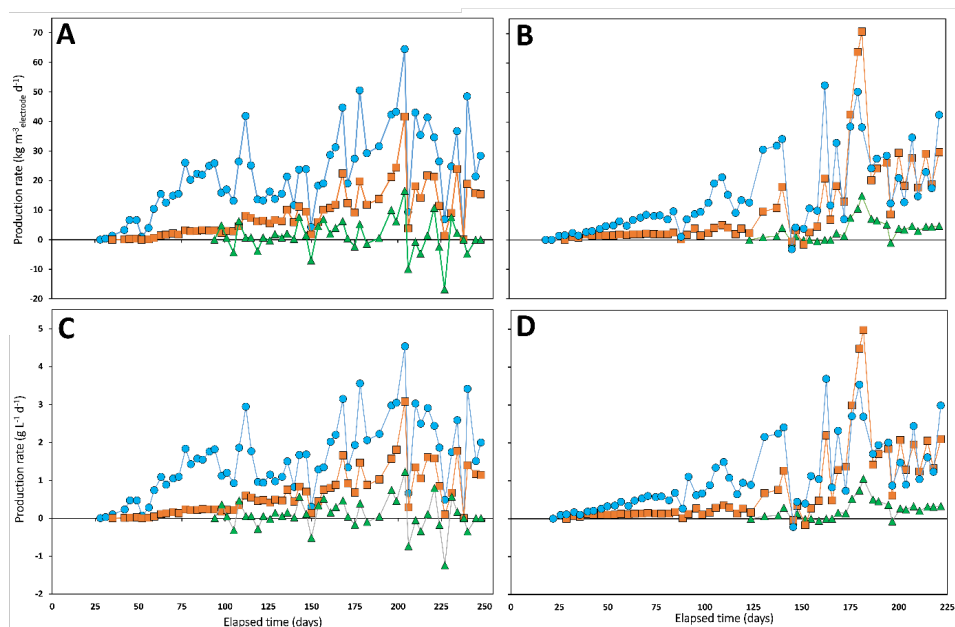


**Figure 4S 4.** Production rates, normalized to electrode volume **(A-B)** and total catholyte volume **(C-D)**, of acetate (blue circles), butyrate (orange squares) and caproate (green triangles) measured over time in the CP **(A, C)** and CA **(B, D)** reactors.
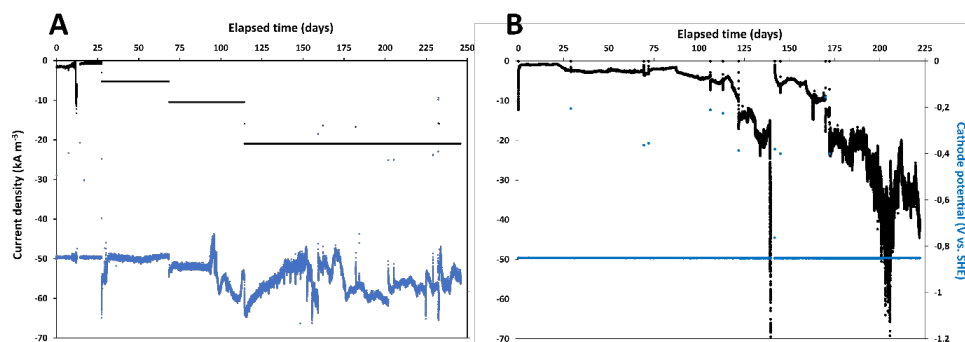
**Figure 4S 5.** Current profile in mA cm$^{-3}_{cathode}$ in the CP **(A)** and CA **(B)** reactors.
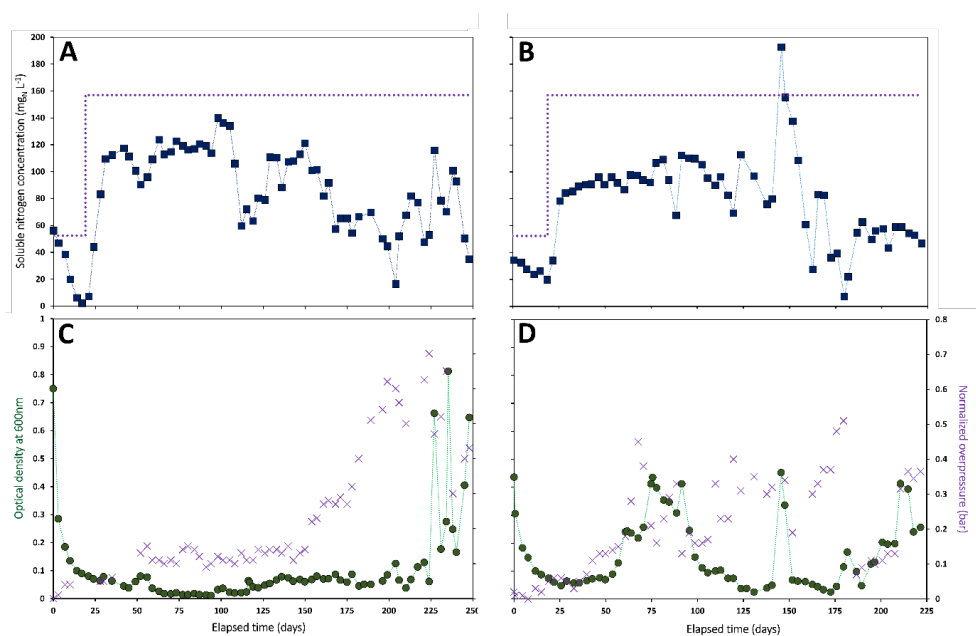


**Figure 4S 6.** Soluble nitrogen concentration **(A-B)**, optical density and normalized overpressure **(C-D)** measured over time in the CP **(A & C)** and CA **(B & D)** reactors.
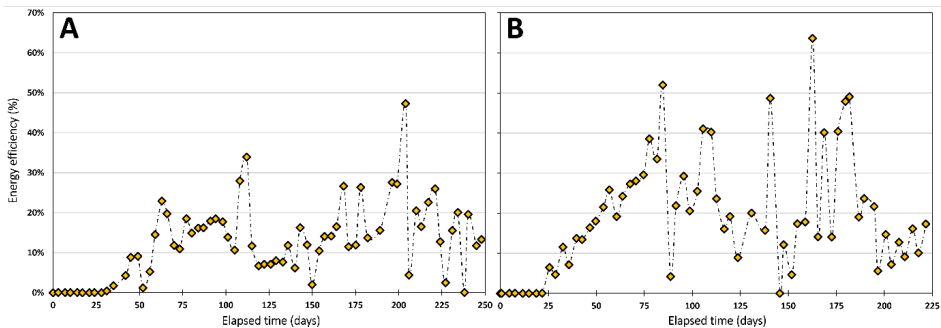
**Figure 4S 7.** Energy efficiency and cell voltage over time in the CP **(A, C)** and CA **(B, D)** reactors.
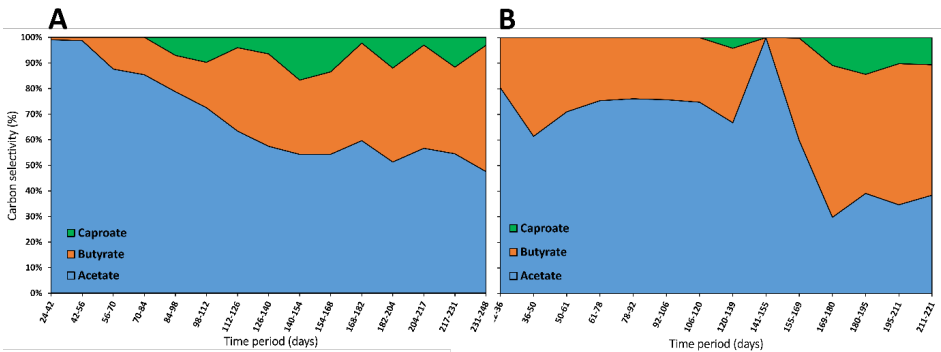


**Figure 4S 8.** Carbon selectivity over time in the CP **(A)** and CA **(B)** reactors.
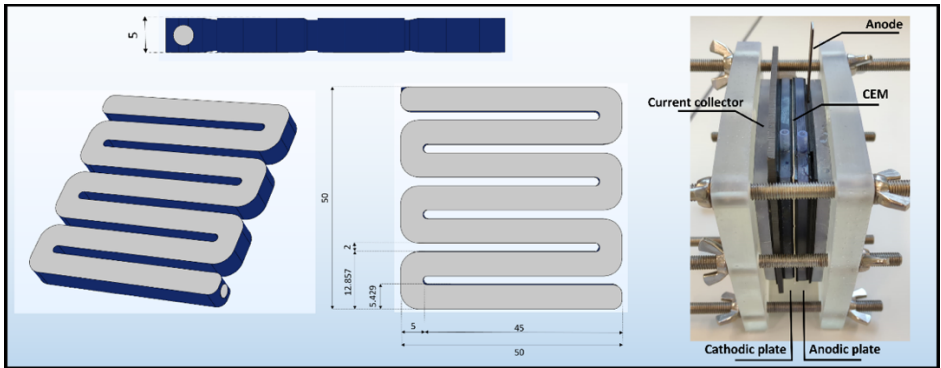


**Figure 4S 9.** Reactor scheme with dimensions **(left and middle)** and photo of the CA reactor **(right)**.

**Table 4S 1.** Literature data used to make **Figure 4.5B**.

| | | CO$_2$ + H$_2$O + electricity | Syngas (CO, CO$_2$, H$_2$) fermentation producing a mixture of ethanol + acetate | | |
|---|---|---|---|---|---|
| | | (MES) This study | Lab-scale [2] | Lab-scale [3] | LanzaTech [4] |
| **$q_p$** | mol$_C$ mol$^{-1}$ d$^{-1}$ | 0.2 | 9.5 | 12.4 | 19.9 |
| | % relative | 0.0 | 0.5 | 0.6 | 1.0 |
| **Biomass concentration** | g$_x$ L$^{-1}$ | 390 | 0.5 | 0.5 | 2.5 |
| | % relative | 1 | 0.001 | 0.001 | 0.006 |
| **Volumetric productivity** | g$_C$ L$^{-1}$ h$^{-1}$ | 0.2 | 0.1 | 0.2 | 1.0 |
| | % relative | 0.2 | 0.1 | 0.2 | 1.0 |

**Table 4S 2.** Other syngas fermentation studies **(N.A. not available)**.

| | | Syngas (CO, CO$_2$, H$_2$) fermentation producing a mixture of ethanol + acetate | | |
|---|---|---|---|---|
| | | [5] | [6] | [7] |
| **$q_p$** | mol$_C$ mol$^{-1}$ d$^{-1}$ | 0.8 | 7.6 | 0.7 |
| **Biomass concentration** | g$_x$ L$^{-1}$ | N.A. | 1.4 | 0.4 |
| **Volumetric productivity** | g$_C$ L$^{-1}$ h$^{-1}$ | 0.13 | N.A. | N.A. |

## 4.6.1. Theoretical Amount of Dry Biomass per Electrode Volume

Biomass formula: $CH_{1.8}O_{0.5}N_{0.2}$

Molar mass = 24.6 g mol$^{-1}$

Biomass density (hydrated) = 1.09 g$_x$ cm$^{-3}_x$

Biomass density (hydrated) = 1.09 / 24.6 = 44.3 mmol$_x$ cm$^{-3}_x$

Dry weight ratio = 30%

Dry biomass density = 44.3 * 0.3 = 13.3 mmol$_x$ cm$^{-3}_x$

Carbon felt porosity = 90%

Theoretical max dry biomass concentration = 13.3 * 0.9 = 12 mmol$_x$ cm$^{-3}_{cathode}$

## 4.6.2. Sequencing Data Analysis

### Paired-End Reads Assembly and Quality Control

    i.    <u>Data split</u>

Paired-end reads was assigned to samples based on their unique barcode and truncated by cutting off the barcode and primer sequence.

    ii.    <u>Sequence assembly</u>

Paired-end reads were merged using FLASH

(V1.2.7,http://ccb.jhu.edu/software/FLASH/) [8], a very fast and accurate analysis tool, which was designed to merge paired-end reads when at least some of the reads overlap the read generated from the opposite end of the same DNA fragment, and the splicing sequences were called raw tags.

    iii.    <u>Data Filtration</u>

Quality filtering on the raw tags were performed under specific filtering conditions to obtain the high-quality clean tags [9] according to the QIIME (V1.7.0, http://qiime.org/index.html) [10] quality controlled process.

    iv.    <u>Chimera removal</u>

The tags were compared with the reference database (Gold database, http://drive5.com/uchime/uchime_download.html)using UCHIME algorithm (UCHIME Algorithm, http://www.drive5.com/usearch/manual/uchime_algo.html) [11] to detect chimera sequences, and then the chimera sequences were removed [12]. Then the Effective Tags finally obtained.

### ASV Denoise and Species Annotation

    i.    <u>ASVs Denoise</u>

For the Effective Tags obtained previously, denoise was performed with DADA2 or deblur module in the QIIME2 software (Version QIIME2-202006) to obtain initial ASVs (Amplicon Sequence Variants) (default: DADA2), and then ASVs with abundance less than 5 were filtered out [13].

    ii.    <u>Species annotation</u>

Species annotation was performed using QIIME2 software. For 16S/18S, the annotation database is Silva Database, while for ITS, it is Unite Database.

### iii.    Phylogenetic relationship Construction

In order to study phylogenetic relationship of each ASV and the differences of the dominant species among different samples(groups), multiple sequence alignment was performed using QIIME2 software.

### iv.    Data Normalization

The absolute abundance of ASVs was normalized using a standard of sequence number corresponding to the sample with the least sequences. Subsequent analysis of alpha diversity and beta diversity were all performed based on the output normalized data.

## Alpha Diversity

In order to analyze the diversity, richness and uniformity of the communities in the sample, alpha diversity was calculated from 7 indices in QIIME2, including Observed_otus, Chao1, Shannon, Simpson, Dominance, Good's coverage and Pielou_e.

Three indices were selected to identify community richness:

Observed_otus – the number of observed species (http://scikit-bio.org/docs/latest/generate d/skbio.diversity.alpha.observed_otus.html);

Chao – the Chao1 estimator (http://scikit-bio.org/docs/latest/generated/skbio.diversity.alpha. chao1.html);

Dominance – the Dominance index (http://scikit-bio.org/docs/latest/generated/skbio.diversity. alpha.dominance.html);

Two indices were used to identify community diversity:

Shannon – the Shannon index (http://scikit-bio.org/docs/latest/generated/skbio.diversity.alp ha.shannon.html);

Simpson – the Simpson index (http://scikit-bio.org/docs/latest/generated/skbio.diversity.alph a.simpson.html);

One indice was used to calculate sequencing depth:

Coverage – the Good's coverage (http://scikit-bio.org/docs/latest/generated/skbio.diversity.a lpha.goods_coverage.html);

One indice was used to calculate species evenness:

Pielou_e – Pielou's evenness index (http://scikit-bio.org/docs/latest/generated/skbio.diversit y.alpha.pielou_e.html).

**Beta Diversity**

In order to evaluate the complexity of the community composition and compare the differences between samples(groups), beta diversity was calculated based on weighted and unweighted unifrac distances in QIIME2.

Cluster analysis was performed with principal component analysis (PCA), which was applied to reduce the dimension of the original variables using the ade4 package and ggplot2 package in R software (Version 3.5.3).

Principal Coordinate Analysis (PCoA) was performed to obtain principal coordinates and visualize differences of samples in complex multi-dimensional data. A matrix of weighted or unweighted unifrac distances among samples obtained previously was transformed into a new set of orthogonal axes, where the maximum variation factor was demonstrated by the first principal coordinate, and the second maximum variation factor was demonstrated by the second principal coordinate, and so on. The three-dimensional PCoA results were displayed using QIIME2 package,

while the two-dimensional PCoA results were displayed using ade4 package and ggplot2 package in R software (Version 2.15.3).

To study the significance of the differences in community structure between groups, the adonis and anosim functions in the QIIME2 software were used to do analysis. To find out the significantly different species at each taxonomic level (Phylum, Class, Order, Family, Genus, Species), the R software (Version 3.5.3) was used to do MetaStat and T-test analysis. The LEfSe software (Version 1.0) was used to do LEfSe analysis (LDA score threshold: 4) so as to find out the biomarkers. Further, to study the functions of the communities in the samples and find out the different functions of the communities in the different groups, the PICRUSt2 software (Version 2.1.2-b) was used for function annotation analysis.

**4**

### 4.6.3. Supplementary Material Reference List

[1]. M. Winkelhorst, O. Cabau-Peinado, A.J.J. Straathof, L. Jourdin, Biomass-specific rates as key performance indicators: A nitrogen balancing method for biofilm-based electrochemical conversion, Front Bioeng Biotechnol 11 (2023). https://doi.org/10.3389/fbioe.2023.1096086.

[2]. J. Lee, J.W. Lee, C.G. Chae, S.J. Kwon, Y.J. Kim, J.-H. Lee, H.S. Lee, Domestication of the novel alcohologenic acetogen Clostridium sp. AWRP: from isolation to characterization for syngas fermentation, Biotechnol Biofuels 12 (2019) 228. https://doi.org/10.1186/s13068-019-1570-0.

[3]. J.K. Heffernan, K. Valgepea, R. de Souza Pinto Lemgruber, I. Casini, M. Plan, R. Tappel, S.D. Simpson, M. Köpke, L.K. Nielsen, E. Marcellin, Enhancing CO2-Valorization Using Clostridium autoethanogenum for Sustainable Fuel and Chemicals Production, Front Bioeng Biotechnol 8 (2020). https://doi.org/10.3389/fbioe.2020.00204.

[4]. N. Fackler, B.D. Heijstra, B.J. Rasor, H. Brown, J. Martin, Z. Ni, K.M. Shebek, R.R. Rosin, S.D. Simpson, K.E. Tyo, R.J. Giannone, R.L. Hettich, T.J. Tschaplinski, C. Leang, S.D. Brown, M.C. Jewett, M. Köpke, Stepping on the Gas to a Circular Economy: Accelerating Development of Carbon-Negative Chemical Production from Gas Fermentation, Annu Rev Chem Biomol Eng 12 (2021) 439–470. https://doi.org/10.1146/annurev-chembioeng-120120-021122.

[5]. S. Shen, G. Wang, M. Zhang, Y. Tang, Y. Gu, W. Jiang, Y. Wang, Y. Zhuang, Effect of temperature and surfactant on biomass growth and higher-alcohol production during syngas fermentation by Clostridium carboxidivorans P7, Bioresour Bioprocess 7 (2020) 56. https://doi.org/10.1186/s40643-020-00344-4.

[6]. K. Valgepea, R. de Souza Pinto Lemgruber, K. Meaghan, R.W. Palfreyman, T. Abdalla, B.D. Heijstra, J.B. Behrendorff, R. Tappel, M. Köpke, S.D. Simpson, L.K. Nielsen, E. Marcellin, Maintenance of ATP Homeostasis Triggers Metabolic Shifts in Gas-Fermenting Acetogens, Cell Syst 4 (2017) 505-515.e5.

[7]. A. Ahmed, B.G. Cateni, R.L. Huhnke, R.S. Lewis, Effects of biomass-generated producer gas constituents on cell growth, product distribution and hydrogenase activity of Clostridium carboxidivorans P7T, Biomass Bioenergy 30 (2006) 665–672. https://doi.org/10.1016/j.biombioe.2006.01.007.

[8]. T. Magoč, S.L. Salzberg, FLASH: fast length adjustment of short reads to improve genome assemblies, Bioinformatics 27 (2011) 2957–2963. https://doi.org/10.1093/bioinformatics/btr507.

[9]. N.A. Bokulich, S. Subramanian, J.J. Faith, D. Gevers, J.I. Gordon, R. Knight, D.A. Mills, J.G. Caporaso, Quality-filtering vastly improves diversity estimates from Illumina amplicon sequencing, Nat Methods 10 (2013) 57–59. https://doi.org/10.1038/nmeth.2276.

[10].   J.G. Caporaso, J. Kuczynski, J. Stombaugh, K. Bittinger, F.D. Bushman, E.K. Costello, N. Fierer, A.G. Peña, J.K. Goodrich, J.I. Gordon, G.A. Huttley, S.T. Kelley, D. Knights, J.E. Koenig, R.E. Ley, C.A. Lozupone, D. McDonald, B.D. Muegge, M. Pirrung, J. Reeder, J.R. Sevinsky, P.J. Turnbaugh, W.A. Walters, J. Widmann, T. Yatsunenko, J. Zaneveld, R. Knight, QIIME allows analysis of high-throughput community sequencing data, Nat Methods 7 (2010) 335–336. https://doi.org/10.1038/nmeth.f.303.

[11].   R.C. Edgar, B.J. Haas, J.C. Clemente, C. Quince, R. Knight, UCHIME improves sensitivity and speed of chimera detection, Bioinformatics 27 (2011) 2194–2200. https://doi.org/10.1093/bioinformatics/btr381.

[12].   B.J. Haas, D. Gevers, A.M. Earl, M. Feldgarden, D. V. Ward, G. Giannoukos, D. Ciulla, D. Tabbaa, S.K. Highlander, E. Sodergren, B. Methé, T.Z. DeSantis, J.F. Petrosino, R. Knight, B.W. Birren, Chimeric 16S rRNA sequence formation and detection in Sanger and 454-pyrosequenced PCR amplicons, Genome Res 21 (2011) 494–504. https://doi.org/10.1101/gr.112730.110.

[13].   Q. Wang, G.M. Garrity, J.M. Tiedje, J.R. Cole, Naïve Bayesian Classifier for Rapid Assignment of rRNA Sequences into the New Bacterial Taxonomy, Appl Environ Microbiol 73 (2007) 5261–5267. https://doi.org/10.1128/AEM.00062-07.

4
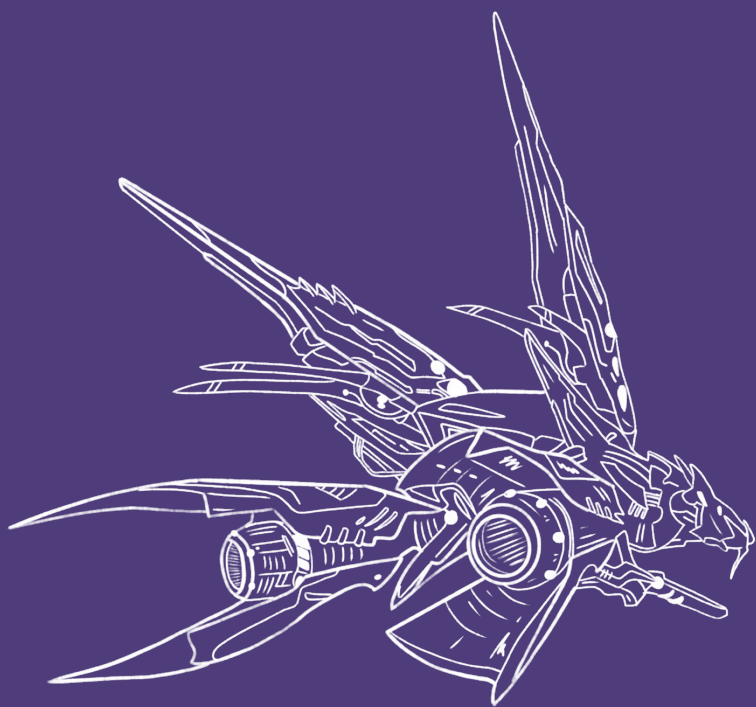
# Chapter 5

General discussion

The research presented in this thesis covers the development and testing of a scalable bioreactor for microbial electrosynthesis from $CO_2$, combining mathematical modelling and experimental work. In order to obtain the necessary information on critical process parameters, and to understand prevailing limitations on currently used reactors, a dynamic computational model was developed (**Chapter 2**). Simulation results unraveled mass transfer limited biomass growth within state-of-the-art systems. Such simulations had not yet been reported for biofilm-based MES reactors. To complement the model, a method to measure biomass concentration in said reactors was developed and used to investigate biofilm growth dynamics (**Chapter 3**). Lastly, with the newly acquired insight on limiting parameters and their link with operational process conditions, a rational design strategy was employed to develop a novel bioreactor for the production of carboxylates from $CO_2$ (**Chapter 4**). Results demonstrated the ability of a step-by-step approach to design MES reactors to attain performances closer to those required in industry. Future challenges for the comprehensive upscaling of MES that were identified during this thesis are discussed in the following sections.

## 5.1. Effective $CO_2$ Delivery is the Main Bottleneck for Present and Foreseeable Future MES Development

In a typical MES operation, $CO_2$ is the main substrate and the sole carbon source available to the microorganisms. Even though its solubility exceeds that of carbon monoxide, for example, it remains relatively low as compared to the desired product concentrations. Hence, to avoid limitations it still needs to be dissolved and supplied to the organisms at a rate that can keep up with the $CO_2$ conversion rate. **Chapter 2** showed that dissolved $CO_2$ concentrations have been partially limiting MES investigations to date. Even when pure $CO_2$ is used, diffusion can still become the rate-limiting step making it unavailable to part of the biofilm, resulting in decreased performances. Because of this, the critical effect of the employed delivery strategy should be properly assessed [1,2]. Understanding what is the most efficient way to dissolve and deliver $CO_2$ is of crucial importance when trying to scale up MES. The most straightforward approaches are to simply use a gas bag or to directly supply it as bicarbonate salt, but these two methods are highly impractical outside laboratory research [3–5]. A possible alternative strategy could be the utilization of membrane-based technologies, such as gas diffusion electrodes (GDE) and hollow fibers (HF). Membranes provide large interfacial areas that facilitate mass transfer between gas and liquid phases [6,7]. MES studies utilizing membrane-based $CO_2$ delivery strategies have shown modest performance results so far, albeit most of these investigations were performed with non-optimized bioreactors [8–12]. Whether

GDEs and HFs can reach mass transfer rates allowing for production rates similar to those observed in this thesis remains unknown.

In theory, the biofilm can grow attached on the liquid side of the membrane surface, supplying $CO_2$ right next to the biocatalyst and thus lowering mass transfer overpotentials (**Figure 5.1a-b**). Furthermore, the membrane itself provides support for biofilm attachment, enabling cell retention [13]. However, $CO_2$ still needs to be dissolved into water before becoming available for the microorganisms. It is precisely this reason that renders null the major benefit of utilizing membrane-based electrodes on pure electrochemical systems in the first place. When utilizing a GDE on for example a $CO_2$ electrolysis reactor, mass transfer overpotentials are greatly diminished because gaseous $CO_2$ can react at the electrode [14,15]. Avoiding the need to dissolve $CO_2$ into water where its solubility is low allows for increased mass transfer, improved production rates, and lower potential losses.
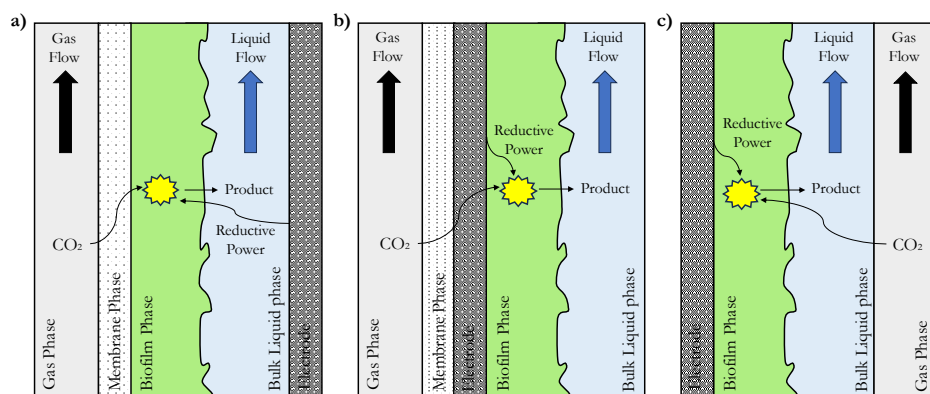


**Figure 5.1. Schematic of strategies to supply $CO_2$ in a biofilm-based MES system.** Yellow star polygon represents microbial reactions. **a)** Hollow fiber membrane; **b)** gas diffusion electrode; **c)** direct sparging.

By similarity with the GDE case, HFs suffer from the same technical limitation when applied to MES systems. Nonetheless, it is also true that the use of a large amount of small tubular fibers solves one of the critical downsides of GDEs, namely their low interfacial surface area. This allows for improved mass transfer, even if the issue of dissolving $CO_2$ is still present. Apart from the complications derived from operating with membranes, these technologies are less likely to be commercially competitive at large production volumes. The main costs related to them are linked to membrane area per volume, therefore benefiting very little from economy of scale.

Supplementary bubble columns (BC) have been used by some research groups to supply the reactor with an external recirculation loop (**Figure 5.1c**) [16–18]. In this thesis, such a column was used (**Chapters 3** and **4**), and even though remarkable performances were obtained it is important to properly assess if such a gas delivery method is the most suited one for upscaling. It is therefore of great interest to know how a BC and the previously presented membrane strategies would perform when used in the bioreactor developed in this thesis at larger scales. Preliminary results obtained with computational modeling give us some insight on their theoretical performance and scalability potential (**Figure 5.2**). Both membrane strategies suffer from mass transfer limitations to some extent, especially the GDE system. The HF strategy is not expected to reach saturation unless pure $CO_2$ is used, mostly due to large concentration drops within the gas phase along the fiber. At the rates obtained in this thesis, only the BC is able to provide a fully $CO_2$ saturated liquid. However, at current densities needed for industrial viability (e.g., $10^3$ A m$^{-2}$ PSA [19]) all strategies show mass transfer limitations, indicating the need for further optimization of the $CO_2$ supply method in the future. This data shows that even though at the moment $CO_2$ supply is not the main issue when using a BC, it might eventually limit reactor performance. Therefore, more research is required on what the most efficient way to upscale the gas supply method is for a hypothetical MES industrial production plant.

An example on how to approach BC scalability could be to look at tubular photobioreactors for microalgae production, where a single column is shared between multiple reactor units [20,21]. Such an approach allows to scale-up the BC by volume, while potentially allowing for a different upscaling approach for the reactor. Researchers have also tackled the need to work with multiple phases by utilizing airlift or fluidized bed type MES reactors. Such configurations allow to incorporate the $CO_2$ supply inside the reactor cell while still using the benefits of a BC [22,23]. It is also possible to couple a BC and HFs in one single reactor setup by combining an airlift with an external recirculation loop HF module, as shown by Cui et al. (2023) [24]. Regardless of the chosen strategy, MES development will run into $CO_2$ limitations in the future and it is therefore necessary to start investigations in the present.

**5**
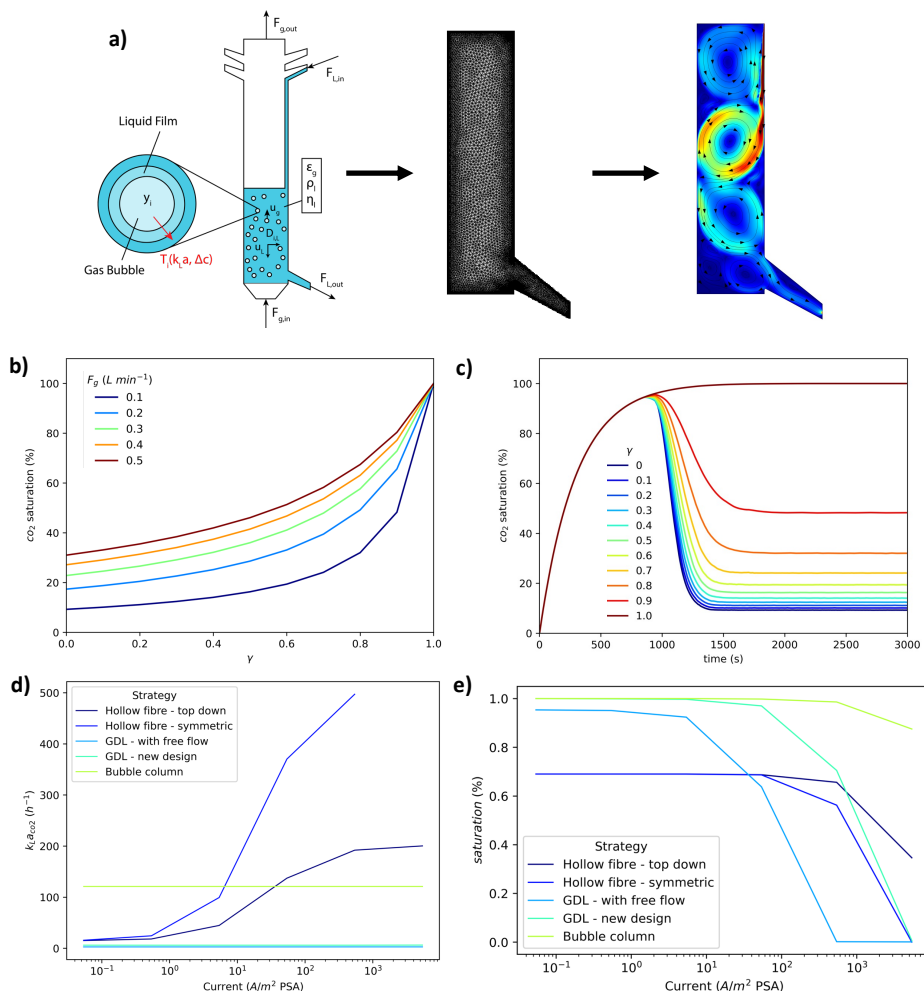
**Figure 5.2. Parametric sweep study on mass transfer capabilities of different strategies on a MES reactor**. **a)** Computational approach used to compare all strategies (bubble column shown as example). COMSOL Multiphysics was used to compute and solve multiple parametric sweeps on the different strategies used, namely the bubble column, two different GDE configurations ("GDL – with free flow" refers to the configuration modelled in **Chapter 2** and "GDL – new design" to the design used in **Chapter 4**), and two different HF configurations ("symmetric" refers to an axis symmetric model along the length of the fibers, while "top down" is a top view involving flow around the fibers). The $CO_2$ gas phase fraction was set to 0.3 for the bubble column in **b** and **c**, and to 0.9 for all strategies in **d** and **e**. Required model parameters were either derived from reported work on similar setups or obtained experimentally (see [25] for a more in-depth description); **b)** steady state concentrations obtained in the bubble column for different gas flow rates at different values of $CO_2$ consumption within the reactor. $CO_2$ consumption is represented by the fraction out/in within the reactor cell ($\gamma$). A consumption factor of 0.5 equals 25 kA m$^{-2}$ PSA; **c)** $CO_2$ saturation development over liquid residence time in the bubble column at different values of $CO_2$ consumption ($\gamma$) within the reactor (consumption was introduced after reaching 90% saturation); **d)** mass transfer coefficient of each strategy at different current densities; **e)** saturation reached at steady state at different current densities. Saturation concentration is based on gas composition at the inlet of each system.

## 5.2. Unraveling Biofilm Fundamentals for Process Optimization

Microbial fundamentals were out of the scope of this thesis. However, understanding how microorganisms operate within a MES reactor is key to successfully identify what the limiting steps are when attempting to scale up and optimize a MES production platform. Even after the main limitation of a given system is addressed, a different part will become the main limiting factor holding back reactor performance. At some point in the future, microbial factors will become limiting. Therefore, successful scaling up will require a deeper knowledge on these fundamentals as well. It should become clear how microorganisms react to a changing local environment and sometimes harsher operational conditions.

### 5.2.1. Addressing Low Biofilm Growth Rates

Start-up times in MES studies are long, usually necessitating weeks for achieving decent biofilm coverage and for chain elongation to start. Reported growth rates for biofilm-based MES reactors are low when compared to typical values of acetogens growing on $H_2/CO_2$, in the region of 1.2 to 2.9 $d^{-1}$ [26–29]. Experiments performed in this thesis suffered from this issue, with relatively low observed specific growth rates around 0.12 $d^{-1}$ (**Chapters 3** and **4**). For MES to reach industrial scale, low growth rates will have to be addressed. These not only imply longer operational times, but many other challenges that could make industrial application impractical. Assuming the time scale needed for an industrial reactor remains fairly similar to the values currently observed, large scale carboxylate production would require reactors to operate for months before reaching steady state. On top of the operational costs such long start-up times imply, genetic instability and microbial community shifts become a reality to consider [30–34]. Similar to the strategy applied in this thesis, focusing solely on macroscale parameters (e.g., flow rate, electrode porosity) can yield improved growth rates and potentially faster start-up times [35]. However, even when alternative reactor-level strategies are employed to try and speed up biofilm growth and development, timescales obtained remain significantly higher than in other gas fermentations [18,36,37]. Some researchers have claimed that operating at fixed high current densities during the first stages of a MES operation stimulates microbial activity [38]. However, **Chapter 4** showed no relation between a galvanostatic operational mode and a faster start-up.

To date, it is unclear how to actively improve biofilm attachment and maturation in a MES reactor. Because biofilm formation occurs as a natural response to stress, microorganisms could be pushed by applying different type of stresses. For instance, Phillips et al. (2017) showed how monoculture biofilm formation could be induced

**5**

by the addition of NaCl, achieving a 20 times higher attached biomass volume [39]. However, it is hard to assess if such an approach would work the same way on mixed cultures like the one used in this thesis. Microbial syntrophic interactions are crucial in mixed cultures, hence subjecting the developing biofilm to harsh conditions might alter its community composition in unpredictable ways [40,41]. An interesting alternative could be to minimize the first attachment phase by mimicking the production of extracellular polymeric substances (EPS) needed to sustain biofilm formation. By either supplying an electrode with a synthetic scaffold or by supplementing the nascent biofilm with additional EPS, the time needed for microorganisms to settle and start growing could be significantly reduced [42]. Growth media engineering could also be a way to solve metabolic related limitations on biofilm formation, such as cell attachment and low growth rates. Such studies are usually done on processes with a higher technological readiness level, since extensive fundamental understanding on the metabolism of each different microorganism and their syntrophic interactions is needed. Albeit this level of knowledge on MES biofilm communities is mostly unavailable, initial studies could already be performed to try and improve the start-up time and full colonization of the cathode [29,43].

### 5.2.2. Local Gradients Could be Limiting MES Performance

Another aspect that has to be taken into consideration is the presence of local gradients. The model developed in **Chapter 2** focused on reactor scale black-box simulations, excluding multi-dimensional dynamics at the biofilm level. Dense biofilms like the ones obtained in this thesis facilitate high rates, but will inevitably lead to mass transfer limitations [44]. Therefore, in biofilm-based reactors concentration gradients will be present at the biofilm's local vicinity, and therefore need to be accounted for. On top of biological reactions and diffusion, acid-base equilibria, hydrogen evolution, and electromigration all contribute to their formation. Significant local gradients of pH, $CO_2$, nutrients, products, and hydrogen are likely to occur [45–49]. Understanding these would give additional insights on rate limiting processes, as well as help understand biofilm development and electrode/microbial dynamics. The pH gradients are the most relevant, since they affect microbial growth and community selection, substrate availability, as well as most local thermodynamic limitations that might occur [50–53].

To increase current densities and microbial rates, mass transport in the biofilm is expected to become even more relevant [54]. The local concentrations are difficult to measure, and require specialized equipment not easily available to most research groups [55,56]. However, one can utilize mathematical modeling to simulate local

gradients at the conditions seen experimentally. Preliminary results obtained from computational simulations showed that small changes on electrode porosity and conductivity, convective flow rate, or electrolyte composition might yield significant changes on local gradients within the biofilm (data not shown). It is expected that the ability to easily obtain such data will give researchers insight on how biofilm dynamics change at different operational conditions, easing future scale-up efforts.

### 5.2.3. Operational Conditions and Their Effect on Biofilm Dynamics

Operational parameters are key when trying to understand a bioreactor's performance. These can critically affect all aspects of a MES system, from the biological and electrochemical reactions to the stability of the process, as well as how to scale up the reactor itself. In this thesis, most operational parameters were based on previous research with similar microbial communities. Although all operational conditions and parameters are relevant, some are more critical than others when assessing reactor performance at bigger scales.

Most microorganisms utilized in research of MES are mesophilic, and temperature sensitivity on biochemical performance has been observed [54,57]. Temperature control and heat integration are well-known topics at industrial scale. Instead of bulk temperature, a more relevant and critical parameter in larger reactors will be the local temperature gradients at the electrode/biofilm vicinity. With ever increasing current and biofilm densities, heat generation and dissipation might become problematic, as seen in $CO_2$ electrolyzers [58–60]. Even though the operational temperature affects not only microbial reactions but the electrochemical ones as well, such data is hardly ever reported. Another effect of increased temperatures is a change on solubility, for instance $CO_2$ solubility in water will decrease. This can generate even more extreme concentration gradients on the electrode vicinity. Therefore, when possible, researchers should monitor and report local temperature profiles of all future experiments to help elucidate changes on process performance and to better understand microbial and electrochemical dynamics within MES reactors.

The hydraulic retention time (HRT) is a highly relevant operational parameter, influencing biochemical rates, microbial growth and biofilm formation, as well as being used as a scale-up metric [61–63]. Hence, its optimization is critical for the long-term stability of MES reactors, as well as their economic feasibility [64]. Using computational modeling, the effect on biological reactions of different HRTs was investigated (**Figure 5.3**). Preliminary results indicate that achievable product concentrations and $CO_2$ conversion rates are strongly dependent on the HRT. Data similar to the one obtained here is expected to help identify limiting steps and

**5**

processes within MES reactors, and to pinpoint future design and operational flaws. Further development, upscaling, and intensification of MES systems will therefore require researchers to heavily rely on mathematical tools.
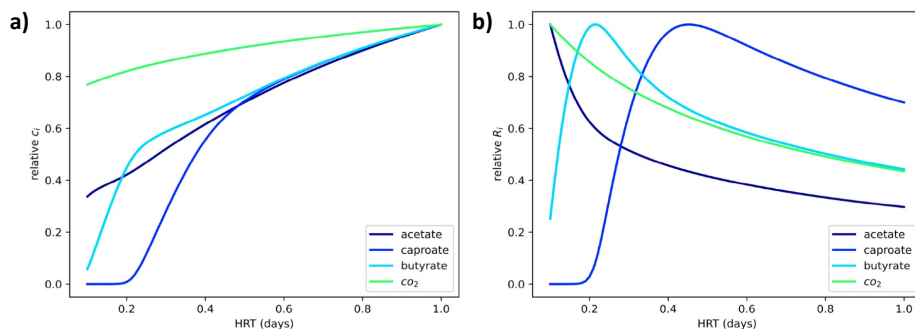


**Figure 5.3. Sweep on the vicinity of a fully developed biofilm in a MES reactor utilizing HFs as CO$_2$ supply method**. An axis symmetric model was developed to study gradients along the axial direction and evaluate results in two dimensions (average values are shown here). Sweeping over the local HRT, not accounting for liquid recirculation outside the reactor cell. The microbial model equations derived in **Chapter 2** were used to simulate biological rates (more details available at [25]). **a)** Relative CO$_2$ and product concentrations, normalized to the maximum concentration in the sweep; **b)** relative conversion rates, normalized to the maximum rate in the sweep.

## 5.3. Towards Industrial Application

MES processes are still far from being industrially viable, both economically and performance wise. In this thesis, a rational design approach was utilized to develop a better performing reactor. Industrial application will require further design, optimization, and intensification. At the moment, knowledge gaps exist regarding what strategy to follow when upscaling and how to ensure long-term stability of the developed process. Assessing these issues is a necessity to unravel how to successfully upscale MES reactors.

### 5.3.1. Upscaling by Stacking

To move towards industrial application, understanding how to scale up the newly designed reactor is crucial. Even though progress has been made when trying to elucidate the main limiting step within the reactor, it is currently largely unknown what this step is. In addition, a wide variety of processes (e.g., ion transport, mass transfer within the biofilm, electrochemistry) could be limiting at different scales. It is therefore difficult to properly assess how to immediately scale the reactor described in **Chapter 4**. Directly scaling up by volume (e.g., increasing distance between electrodes) would significantly increase overpotentials within the reactor and potentially lead to complications, necessitating further extensive research [65]. On the other hand, scaling up by means of creating stacks of manageable sized

reactors might be the most cost and time effective approach when wanting to push MES to industrial applicability [66–68]. A small, compact, and stackable design is thus preferred. However, it is necessary to find the appropriate size of the stackable unit reactor, understand how to stack and connect said units, and to optimize liquid flow within the stack.

Flat-plate reactors are examples of scalable configurations, which subsequently increase the electrode surface to volume ratio [69]. The same concept used when scaling commercially available designs of electrochemical cells can be applied to MES reactors [70–72]. The shape and geometry of the flow field directly affects microbial reactions and the overall reactor performance. For example, dissolved $CO_2/H_2$ concentrations and retention time are of great importance when moving towards bigger scales, while being greatly impacted by the utilized flow field [73]. If scale-up efforts on a similar design as the one presented in this thesis would to be pursued, optimization of the flow field should become a priority. Moreover, in a stackable design the size of cathode and anodic chambers, and of the $CO_2$ supply strategy need to be optimized. Utilizing computational modelling, predictions can be made on their optimal size. Preliminary results showed no limiting steps with regard to the anodic chamber at the moment, but this is likely to change in the future as current densities continue to increase (data not shown). Therefore, the anodic chamber has to be studied further, although this part of the MES process was out of scope of this thesis.

In summary, successfully upscaling a new reactor will necessitate an optimal balance between all processes within the system. Stackability is at the moment the scaling strategy most likely to succeed, albeit further research and pilot-scale testing is required. As previously proposed, mathematical models will allow to quickly assess these considerations and move towards industrial application on a more streamlined way.

### 5.3.2. Operational Stability and Long-Term Complications

For long-term operating MES reactors utilizing porous cathodes, fouling is a phenomenon that has to be taken into consideration. In this thesis, it was observed that an overpressure within the liquid phase was generated. Even though increased pressures on their own might benefit mass transfer (e.g., increased $CO_2$ solubility) and be of potential interest for product spectrum diversification, pressures induced by fouling will become serious issues at larger scales [74–76]. Hence, it is clear that pressure within the liquid phase should be closely monitored, especially in biofilm-based reactors utilizing highly dense porous electrodes. This is even more important

**5**

when new designs or pilot-scale setups are being tested. Since the formation of a dense biofilm is a requirement for high rates, the allowable pressure gradient (i.e., shear stress on biofilm) will determine the maximum HRT through the porous cathode, hence the achievable biofilm thickness in that specific reactor.

A point rarely discussed is the reproducibility of MES results, as the utilization of fibrous materials can potentially lead to low predictability. The random nature of their 3-dimensional structure, together with relatively low mechanical stability is a risk for sustaining sufficient internal electrical connections within the electrode. The importance of said connections was observed by abiotically testing multiple carbon felt pieces. Noticeable differences in conductivity of the cathode/current collector pair, as well as deviations on cathodic overpotentials between similarly identical cathodes were observed (data not shown). Thus, careful handling and testing of the cathode before use should be taken seriously and be properly reported, as small differences at laboratory scale can easily scale out of hand when moving towards industrial sized setups.

Similarly, the use of mixed microbial cultures must be assessed. Incidents reported in literature, as well as in this thesis prove the resilience of such mixed cultures [77–79]. Although this can generally be considered an advantage over pure microbial cultures, it can also come along with negative effects regarding reproducibility and stability. Competing strains make such cultures already less predictable and are therefore a risk for constant and reliable results [69]. A successful industrial MES operation might require a simplified mixed culture, by means of identifying and isolating the key species involved on high-rate $CO_2$ reduction and chain elongation. A clear advantage of such an approach is obtaining a culture of well-known and understood microbes, opening the door for potential genetic engineering, strain improvement, and synthetic biology [80–83].

## 5.4. General Conclusion

Tackling the anthropogenic climate crisis necessitates the capture, utilization and valorization of $CO_2$. For this to occur in time, developing technologies like microbial electrosynthesis will have to become economically feasible and scalable in the upcoming years. The work presented in this thesis demonstrates that it is possible to tackle key challenges of a MES reactor and obtain improved performances closer to those needed at an industrial level. This was achieved by combining theoretical, experimental, and computational work in a rational design strategy focusing on main limiting steps. Even though great progress has been made, when compared with established commercial-scale fermentations too many unknowns and uncertainties

remain. Successful MES reactor scale-up will hence necessitate more research on the topics discussed in this chapter, as well as on new challenges that may arise in the future while further developing the technology. A multiscale and multidisciplinary approach is a must in order to effectively tackle all biological, electrochemical, and engineering challenges to scale up MES.

## 5.5. References

[1]     P. Izadi, J.-M. Fontmorin, A. Godain, E.H. Yu, I.M. Head, Parameters influencing the development of highly conductive and efficient biofilm during microbial electrosynthesis: the importance of applied potential and inorganic carbon source, NPJ Biofilms Microbiomes 6 (2020) 40. https://doi.org/10.1038/s41522-020-00151-x.

[2]     M. del P.A. Rojas, M. Zaiat, E.R. González, H. De Wever, D. Pant, Enhancing the gas–liquid mass transfer during microbial electrosynthesis by the variation of CO2 flow rate, Process Biochemistry 101 (2021) 50–58. https://doi.org/10.1016/j.procbio.2020.11.005.

[3]     C.W. Marshall, D.E. Ross, E.B. Fichot, R.S. Norman, H.D. May, Long-term Operation of Microbial Electrosynthesis Systems Improves Acetate Production by Autotrophic Microbiomes, Environ Sci Technol 47 (2013) 6023–6029. https://doi.org/10.1021/es400341b.

[4]     F. Mayer, F. Enzmann, A.M. Lopez, D. Holtmann, Performance of different methanogenic species for the microbial electrosynthesis of methane from carbon dioxide, Bioresour Technol 289 (2019) 121706. https://doi.org/10.1016/j.biortech.2019.121706.

[5]     Q. Liang, Y. Gao, Z. Li, J. Cai, N. Chu, W. Hao, Y. Jiang, R.J. Zeng, Electricity-driven ammonia oxidation and acetate production in microbial electrosynthesis systems, Front Environ Sci Eng 16 (2022) 42. https://doi.org/10.1007/s11783-021-1476-5.

[6]     M.W. Reij, J.T.F. Keurentjes, S. Hartmans, Membrane bioreactors for waste gas treatment, J Biotechnol 59 (1998) 155–167. https://doi.org/10.1016/S0168-1656(97)00169-7.

[7]     M. Stanojević, Bojan Lazarević, Dejan Radić, Review of membrane contactors designs and applications of different modules in industry., FME Transactions 31 (2003) 91–98.

[8]     S. Bajracharya, A. Krige, L. Matsakas, U. Rova, P. Christakopoulos, Dual cathode configuration and headspace gas recirculation for enhancing microbial electrosynthesis using Sporomusa ovata, Chemosphere 287 (2022) 132188. https://doi.org/10.1016/j.chemosphere.2021.132188.

[9]     P. Dessì, C. Buenaño-Vargas, S. Martínez-Sosa, S. Mills, A. Trego, U.Z. Ijaz, D. Pant, S. Puig, V. O'Flaherty, P. Farràs, Microbial electrosynthesis of acetate from CO2 in three-chamber cells with gas diffusion biocathode under moderate saline conditions, Environmental Science and Ecotechnology 16 (2023) 100261. https://doi.org/10.1016/j.ese.2023.100261.

[10]    M.F. Alqahtani, K.P. Katuri, S. Bajracharya, Y. Yu, Z. Lai, P.E. Saikaly, Porous Hollow Fiber Nickel Electrodes for Effective Supply and Reduction of Carbon Dioxide to Methane through Microbial Electrosynthesis, Adv Funct Mater 28 (2018). https://doi.org/10.1002/adfm.201804860.

[11]    S. Bajracharya, K. Vanbroekhoven, C.J.N. Buisman, D. Pant, D.P.B.T.B. Strik, Application of gas diffusion biocathode in microbial electrosynthesis from carbon dioxide, Environmental Science and Pollution Research 23 (2016) 22292–22308. https://doi.org/10.1007/s11356-016-7196-x.

**5**

[12]   B. Bian, M.F. Alqahtani, K.P. Katuri, D. Liu, S. Bajracharya, Z. Lai, K. Rabaey, P.E. Saikaly, Porous nickel hollow fiber cathodes coated with CNTs for efficient microbial electrosynthesis of acetate from $CO_2$ using *Sporomusa ovata*, J Mater Chem A Mater 6 (2018) 17201–17211. https://doi.org/10.1039/C8TA05322G.

[13]   Y. Shen, R. Brown, Z. Wen, Syngas fermentation of Clostridium carboxidivoran P7 in a hollow fiber membrane biofilm reactor: Evaluating the mass transfer coefficient and ethanol production performance, Biochem Eng J 85 (2014) 21–29. https://doi.org/10.1016/j.bej.2014.01.010.

[14]   D. Higgins, C. Hahn, C. Xiang, T.F. Jaramillo, A.Z. Weber, Gas-Diffusion Electrodes for Carbon Dioxide Reduction: A New Paradigm, ACS Energy Lett 4 (2019) 317–324. https://doi.org/10.1021/acsenergylett.8b02035.

[15]   E.W. Lees, B.A.W. Mowbray, F.G.L. Parlane, C.P. Berlinguette, Gas diffusion electrodes and membranes for CO2 reduction electrolysers, Nat Rev Mater 7 (2021) 55–64. https://doi.org/10.1038/s41578-021-00356-2.

[16]   L. Jourdin, M. Winkelhorst, B. Rawls, C.J.N. Buisman, D.P.B.T.B. Strik, Enhanced selectivity to butyrate and caproate above acetate in continuous bioelectrochemical chain elongation from CO2: Steering with CO2 loading rate and hydraulic retention time, Bioresour Technol Rep 7 (2019) 100284. https://doi.org/10.1016/j.biteb.2019.100284.

[17]   L. Jourdin, S.M.T. Raes, C.J.N. Buisman, D.P.B.T.B. Strik, Critical Biofilm Growth throughout Unmodified Carbon Felts Allows Continuous Bioelectrochemical Chain Elongation from CO2 up to Caproate at High Current Density, Front Energy Res 6 (2018). https://doi.org/10.3389/fenrg.2018.00007.

[18]   S.M. de Smit, J.J.H. Langedijk, J.H. Bitter, D.P.B.T.B. Strik, Alternating direction of catholyte forced flow-through 3D-electrodes improves start-up time in microbial electrosynthesis at applied high current density, Chemical Engineering Journal 464 (2023) 142599. https://doi.org/10.1016/j.cej.2023.142599.

[19]   L. Jourdin, J. Sousa, N. van Stralen, D.P.B.T.B. Strik, Techno-economic assessment of microbial electrosynthesis from CO2 and/or organics: An interdisciplinary roadmap towards future research and application, Appl Energy 279 (2020) 115775. https://doi.org/10.1016/j.apenergy.2020.115775.

[20]   E. Molina, J. Fernández, F.G. Acién, Y. Chisti, Tubular photobioreactor design for algal cultures, J Biotechnol 92 (2001) 113–131. https://doi.org/10.1016/S0168-1656(01)00353-4.

[21]   J.P. Díaz, C. Inostroza, F.G. Acién Fernández, Fibonacci-type tubular photobioreactor for the production of microalgae, Process Biochemistry 86 (2019) 1–8. https://doi.org/10.1016/j.procbio.2019.08.008.

[22]   Z. Pan, Y. Hui, X. Hu, J. Yu, H. Zhang, X. Feng, K. Guo, A novel electrolytic gas lift reactor for efficient microbial electrosynthesis of acetate from carbon dioxide, Bioresour Technol 393 (2024) 130124. https://doi.org/10.1016/j.biortech.2023.130124.

[23]   M. Llorente, S. Tejedor-Sanz, A. Berná, C. Manchón, A. Esteve-Núñez, Novel electrochemical strategies for the microbial conversion of $CO_2$ into biomass and volatile fatty acids using a fluid-like bed electrode in a three-phase reactor, Microb Biotechnol 17 (2024). https://doi.org/10.1111/1751-7915.14383.

[24]     K. Cui, K. Guo, J.M. Carvajal-Arroyo, J. Arends, K. Rabaey, An electrolytic bubble column with an external hollow fiber membrane gas–liquid contactor for effective microbial electrosynthesis of acetate from $CO_2$, Chemical Engineering Journal 471 (2023) 144296. https://doi.org/10.1016/j.cej.2023.144296.

[25]     T. La Haye, Design and characterization of new $CO_2$ supply strategies for microbial electrosynthesis, Master's thesis, Delft University of Technology, 2021.

[26]     J. Philips, Extracellular Electron Uptake by Acetogenic Bacteria: Does $H_2$ Consumption Favor the $H_2$ Evolution Reaction on a Cathode or Metallic Iron?, Front Microbiol 10 (2020). https://doi.org/10.3389/fmicb.2019.02997.

[27]     B. Acharya, A. Dutta, P. Basu, Ethanol production by syngas fermentation in a continuous stirred tank bioreactor using *Clostridium ljungdahlii*, Biofuels 10 (2019) 221–237. https://doi.org/10.1080/17597269.2017.1316143.

[28]     F.R. Bengelsdorf, M.H. Beck, C. Erz, S. Hoffmeister, M.M. Karl, P. Riegler, S. Wirth, A. Poehlein, D. Weuster-Botz, P. Dürre, Bacterial Anaerobic Synthesis Gas (Syngas) and $CO_2 + H_2$ Fermentation, in: Adv. Appl. Microbiol. 2018: pp. 143–221. https://doi.org/10.1016/bs.aambs.2018.01.002.

[29]     A. Groher, D. Weuster-Botz, General medium for the autotrophic cultivation of acetogens, Bioprocess Biosyst Eng 39 (2016) 1645–1650. https://doi.org/10.1007/s00449-016-1634-5.

[30]     Y. Lu, F.R. Slater, Z. Mohd-Zaki, S. Pratt, D.J. Batstone, Impact of operating history on mixed culture fermentation microbial ecology and product mixture, Water Science and Technology 64 (2011) 760–765. https://doi.org/10.2166/wst.2011.699.

[31]     N. Rai, L. Huynh, M. Kim, I. Tagkopoulos, Population collapse and adaptive rescue during long-term chemostat fermentation, Biotechnol Bioeng 116 (2019) 693–703. https://doi.org/10.1002/bit.26898.

[32]     M. Lin, X. Dai, P.J. Weimer, Shifts in fermentation end products and bacterial community composition in long-term, sequentially transferred in vitro ruminal enrichment cultures fed switchgrass with and without ethanol as a co-substrate, Bioresour Technol 285 (2019) 121324. https://doi.org/10.1016/j.biortech.2019.121324.

[33]     M. Duperray, M. Delvenne, J.M. François, F. Delvigne, J.-P. Capp, Genomic and metabolic instability during long-term fermentation of an industrial Saccharomyces cerevisiae strain engineered for C5 sugar utilization, Front Bioeng Biotechnol 12 (2024). https://doi.org/10.3389/fbioe.2024.1357671.

[34]     Y. Bian, A. Leininger, H.D. May, Z.J. Ren, $H_2$ mediated mixed culture microbial electrosynthesis for high titer acetate production from $CO_2$, Environmental Science and Ecotechnology 19 (2024) 100324. https://doi.org/10.1016/j.ese.2023.100324.

[35]     I. Vassilev, P. Dessì, S. Puig, M. Kokko, Cathodic biofilms – A prerequisite for microbial electrosynthesis, Bioresour Technol 348 (2022) 126788. https://doi.org/10.1016/j.biortech.2022.126788.

[36]     L. Puiman, B. Abrahamson, R.G.J.M. van der Lans, C. Haringa, H.J. Noorman, C. Picioreanu, Alleviating mass transfer limitations in industrial external-loop syngas-to-ethanol fermentation, Chem Eng Sci 259 (2022) 117770. https://doi.org/10.1016/j.ces.2022.117770.

**5**

[37]    L. Puiman, E. Almeida Benalcázar, C. Picioreanu, H.J. Noorman, C. Haringa, Downscaling Industrial-Scale Syngas Fermentation to Simulate Frequent and Irregular Dissolved Gas Concentration Shocks, Bioengineering 10 (2023) 518. https://doi.org/10.3390/bioengineering10050518.

[38]    E. Blanchet, F. Duquenne, Y. Rafrafi, L. Etcheverry, B. Erable, A. Bergel, Importance of the hydrogen route in up-scaling electrosynthesis for microbial $CO_2$ reduction, Energy Environ Sci 8 (2015) 3731–3744. https://doi.org/10.1039/C5EE03088A.

[39]    J. Philips, K. Rabaey, D.R. Lovley, M. Vargas, Biofilm Formation by Clostridium ljungdahlii Is Induced by Sodium Chloride Stress: Experimental Evaluation and Transcriptome Analysis, PLoS One 12 (2017) e0170406. https://doi.org/10.1371/journal.pone.0170406.

[40]    J. Dolfing, Syntrophy in microbial fuel cells, ISME J 8 (2014) 4–5. https://doi.org/10.1038/ismej.2013.198.

[41]    A. Al-Mamun, W. Ahmed, T. Jafary, J.K. Nayak, A. Al-Nuaimi, A. Sana, Recent advances in microbial electrosynthesis system: Metabolic investigation and process optimization, Biochem Eng J 196 (2023) 108928. https://doi.org/10.1016/j.bej.2023.108928.

[42]    M.T. Knoll, E. Fuderer, J. Gescher, Sprayable biofilm – Agarose hydrogels as 3D matrix for enhanced productivity in bioelectrochemical systems, Biofilm 4 (2022) 100077. https://doi.org/10.1016/j.bioflm.2022.100077.

[43]    F. Ammam, P.-L. Tremblay, D.M. Lizak, T. Zhang, Effect of tungstate on acetate and ethanol production by the electrosynthetic bacterium Sporomusa ovata, Biotechnol Biofuels 9 (2016) 163. https://doi.org/10.1186/s13068-016-0576-0.

[44]    L.-A. Philipp, K. Bühler, R. Ulber, J. Gescher, Beneficial applications of biofilms, Nat Rev Microbiol 22 (2024) 276–290. https://doi.org/10.1038/s41579-023-00985-0.

[45]    A.C.L. de Lichtervelde, A. ter Heijne, H.V.M. Hamelers, P.M. Biesheuvel, J.E. Dykstra, Theory of Ion and Electron Transport Coupled with Biochemical Conversions in an Electroactive Biofilm, Phys Rev Appl 12 (2019) 014018. https://doi.org/10.1103/PhysRevApplied.12.014018.

[46]    F. Kracke, A.B. Wong, K. Maegaard, J.S. Deutzmann, M.A. Hubert, C. Hahn, T.F. Jaramillo, A.M. Spormann, Robust and biocompatible catalysts for efficient hydrogen-driven microbial electrosynthesis, Commun Chem 2 (2019) 45. https://doi.org/10.1038/s42004-019-0145-0.

[47]    H. Ooka, M.C. Figueiredo, M.T.M. Koper, Competition between Hydrogen Evolution and Carbon Dioxide Reduction on Copper Electrodes in Mildly Acidic Media, Langmuir 33 (2017) 9307–9313. https://doi.org/10.1021/acs.langmuir.7b00696.

[48]    J.R. Kim, S. Cheng, S.-E. Oh, B.E. Logan, Power Generation Using Different Cation, Anion, and Ultrafiltration Membranes in Microbial Fuel Cells, Environ Sci Technol 41 (2007) 1004–1009. https://doi.org/10.1021/es062202m.

[49]    R.A. Rozendal, H.V.M. Hamelers, C.J.N. Buisman, Effects of Membrane Cation Transport on pH and Microbial Fuel Cell Performance, Environ Sci Technol 40 (2006) 5206–5211. https://doi.org/10.1021/es060387r.

[50]    L. Jourdin, T. Grieger, J. Monetti, V. Flexer, S. Freguia, Y. Lu, J. Chen, M. Romano, G.G. Wallace, J. Keller, High Acetic Acid Production Rate Obtained by Microbial Electrosynthesis from Carbon Dioxide, Environ Sci Technol 49 (2015) 13566–13574. https://doi.org/10.1021/acs.est.5b03821.

[51]  S.A. Patil, F. Harnisch, C. Koch, T. Hübschmann, I. Fetzer, A.A. Carmona-Martínez, S. Müller, U. Schröder, Electroactive mixed culture derived biofilms in microbial bioelectrochemical systems: The role of pH on biofilm formation, performance and composition, Bioresour Technol 102 (2011) 9683–9690. https://doi.org/10.1016/j.biortech.2011.07.087.

[52]  I. Vassilev, F. Kracke, S. Freguia, J. Keller, J.O. Krömer, P. Ledezma, B. Virdis, Microbial electrosynthesis system with dual biocathode arrangement for simultaneous acetogenesis, solventogenesis and carbon chain elongation, Chemical Communications 55 (2019) 4351–4354. https://doi.org/10.1039/C9CC00208A.

[53]  P. Izadi, J.-M. Fontmorin, S.S. Lim, I.M. Head, E.H. Yu, Enhanced bio-production from $CO_2$ by microbial electrosynthesis (MES) with continuous operational mode, Faraday Discuss 230 (2021) 344–359. https://doi.org/10.1039/D0FD00132E.

[54]  L. Jourdin, T. Burdyny, Microbial Electrosynthesis: Where Do We Go from Here?, Trends Biotechnol 39 (2021) 359–369. https://doi.org/10.1016/j.tibtech.2020.10.014.

[55]  S.C. Saccomano, M.P. Jewell, K.J. Cash, A review of chemosensors and biosensors for monitoring biofilm dynamics, Sensors and Actuators Reports 3 (2021) 100043. https://doi.org/10.1016/j.snr.2021.100043.

[56]  S.M. de Smit, J.J.H. Langedijk, L.C.A. van Haalen, S.H. Lin, J.H. Bitter, D.P.B.T.B. Strik, Methodology for In Situ Microsensor Profiling of Hydrogen, pH, Oxidation–Reduction Potential, and Electric Potential throughout Three-Dimensional Porous Cathodes of (Bio)Electrochemical Systems, Anal Chem 95 (2023) 2680–2689. https://doi.org/10.1021/acs.analchem.2c03121.

[57]  N. Faraghiparapari, K. Zengler, Production of organics from $CO_2$ by microbial electrosynthesis (MES) at high temperature, Journal of Chemical Technology & Biotechnology 92 (2017) 375–381. https://doi.org/10.1002/jctb.5015.

[58]  W.A. Smith, T. Burdyny, D.A. Vermaas, H. Geerlings, Pathways to Industrial-Scale Fuel Out of Thin Air from $CO_2$ Electrolysis, Joule 3 (2019) 1822–1834. https://doi.org/10.1016/j.joule.2019.07.009.

[59]  Y. Song, X. Zhang, K. Xie, G. Wang, X. Bao, High-Temperature $CO_2$ Electrolysis in Solid Oxide Electrolysis Cells: Developments, Challenges, and Prospects, Advanced Materials 31 (2019). https://doi.org/10.1002/adma.201902033.

[60]  H.-P. Iglesias van Montfort, T. Burdyny, Mapping Spatial and Temporal Electrochemical Activity of Water and $CO_2$ Electrolysis on Gas-Diffusion Electrodes Using Infrared Thermography, ACS Energy Lett 7 (2022) 2410–2419. https://doi.org/10.1021/acsenergylett.2c00984.

[61]  J.B.A. Arends, S.A. Patil, H. Roume, K. Rabaey, Continuous long-term electricity-driven bioproduction of carboxylates and isopropanol from $CO_2$ with a mixed microbial community, Journal of CO2 Utilization 20 (2017) 141–149. https://doi.org/10.1016/j.jcou.2017.04.014.

[62]  W. Zhang, T. Sileika, A.I. Packman, Effects of fluid flow conditions on interactions between species in biofilms, FEMS Microbiol Ecol 84 (2013) 344–354. https://doi.org/10.1111/1574-6941.12066.

[63]  A. Ceballos-Escalera, N. Pous, L. Bañeras, M.D. Balaguer, S. Puig, Advancing towards electro-bioremediation scaling-up: On-site pilot plant for successful nitrate-contaminated groundwater treatment, Water Res 256 (2024) 121618. https://doi.org/10.1016/j.watres.2024.121618.

**5**

[64] F. Kong, H.-Y. Ren, S.G. Pavlostathis, J. Nan, N.-Q. Ren, A. Wang, Overview of value-added products bioelectrosynthesized from waste materials in microbial electrosynthesis systems, Renewable and Sustainable Energy Reviews 125 (2020) 109816. https://doi.org/10.1016/j.rser.2020.109816.

[65] F. Harnisch, Dirk Holtmann, eds, Bioelectrosynthesis, New York: Springer 490 (2019).

[66] S. Wu, H. Li, X. Zhou, P. Liang, X. Zhang, Y. Jiang, X. Huang, A novel pilot-scale stacked microbial fuel cell for efficient electricity generation and wastewater treatment, Water Res 98 (2016) 396–403. https://doi.org/10.1016/j.watres.2016.04.043.

[67] K.S. Madiraju, D. Lyew, R. Kok, V. Raghavan, Carbon neutral electricity production by Synechocystis sp. PCC6803 in a microbial fuel cell, Bioresour Technol 110 (2012) 214–218. https://doi.org/10.1016/j.biortech.2012.01.065.

[68] C. Geipel, K. Hauptmeier, K. Herbrig, F. Mittmann, M. Münch, M. Pötschke, L. Reichel, T. Strohbach, T. Seidel, A. Surrey, C. Walter, Stack Development and Industrial Scale-Up, ECS Trans 91 (2019) 123–132. https://doi.org/10.1149/09101.0123ecst.

[69] P. Dessì, L. Rovira-Alsina, C. Sánchez, G.K. Dinesh, W. Tong, P. Chatterjee, M. Tedesco, P. Farràs, H.M.V. Hamelers, S. Puig, Microbial electrosynthesis: Towards sustainable biorefineries for production of green chemicals from CO2 emissions, Biotechnol Adv 46 (2021) 107675. https://doi.org/10.1016/j.biotechadv.2020.107675.

[70] B. Endrődi, E. Kecsenovity, A. Samu, F. Darvas, R. V. Jones, V. Török, A. Danyi, C. Janáky, Multilayer Electrolyzer Stack Converts Carbon Dioxide to Gas Products at High Pressure with High Efficiency, ACS Energy Lett 4 (2019) 1770–1777. https://doi.org/10.1021/acsenergylett.9b01142.

[71] D. Huang, Z. Zhong, X. Ai, K. Hu, B. Xiong, Q. Wen, J. Fang, S. Cheng, Size design strategy for scaling up alkaline water electrolysis stack integrated with renewable energy source: A multiphysics modeling approach, Energy Convers Manag 300 (2024) 117955. https://doi.org/10.1016/j.enconman.2023.117955.

[72] N. Cooper, C. Horend, F. Röben, A. Bardow, N. Shah, A framework for the design &amp; operation of a large-scale wind-powered hydrogen electrolyzer hub, Int J Hydrogen Energy 47 (2022) 8671–8686. https://doi.org/10.1016/j.ijhydene.2021.12.225.

[73] M. Carmo, D.L. Fritz, J. Mergel, D. Stolten, A comprehensive review on PEM water electrolysis, Int J Hydrogen Energy 38 (2013) 4901–4934. https://doi.org/10.1016/j.ijhydene.2013.01.151.

[74] F. Meng, S. Zhang, Y. Oh, Z. Zhou, H.-S. Shin, S.-R. Chae, Fouling in membrane bioreactors: An updated review, Water Res 114 (2017) 151–180. https://doi.org/10.1016/j.watres.2017.02.006.

[75] S.E. Coetser, T.E. Cloete, Biofouling and Biocorrosion in Industrial Water Systems, Crit Rev Microbiol 31 (2005) 213–232. https://doi.org/10.1080/10408410500304074.

[76] A. Drews, Membrane fouling in membrane bioreactors—Characterisation, contradictions, cause and cures, J Memb Sci 363 (2010) 1–28. https://doi.org/10.1016/j.memsci.2010.06.046.

[77] M. del Pilar Anzola Rojas, M. Zaiat, E.R. Gonzalez, H. De Wever, D. Pant, Effect of the electric supply interruption on a microbial electrosynthesis system converting inorganic carbon into acetate, Bioresour Technol 266 (2018) 203–210. https://doi.org/10.1016/j.biortech.2018.06.074.

[78]    D.L. Baho, H. Peter, L.J. Tranvik, Resistance and resilience of microbial communities – temporal and spatial insurance against perturbations, Environ Microbiol 14 (2012) 2283–2292. https://doi.org/10.1111/j.1462-2920.2012.02754.x.

[79]    A. Prokhorova, K. Sturm-Richter, A. Doetsch, J. Gescher, Resilience, Dynamics, and Interactions within a Model Multispecies Exoelectrogenic-Biofilm Community, Appl Environ Microbiol 83 (2017). https://doi.org/10.1128/AEM.03033-16.

[80]    Y. Li, M. Cao, V.K. Gupta, Y. Wang, Metabolic engineering strategies to enable microbial electrosynthesis utilization of $CO_2$ : recent progress and challenges, Crit Rev Biotechnol 44 (2024) 352–372. https://doi.org/10.1080/07388551.2023.2167065.

[81]    F. Harnisch, J.S. Deutzmann, S.T. Boto, M.A. Rosenbaum, Microbial electrosynthesis: opportunities for microbial pure cultures, Trends Biotechnol (2024). https://doi.org/10.1016/j.tibtech.2024.02.004.

[82]    A. Prévoteau, J.M. Carvajal-Arroyo, R. Ganigué, K. Rabaey, Microbial electrosynthesis from CO2: forever a promise?, Curr Opin Biotechnol 62 (2020) 48–57. https://doi.org/10.1016/j.copbio.2019.08.014.

[83]    E.M. Klein, M.T. Knoll, J. Gescher, Microbe–Anode Interactions: Comparing the impact of genetic and material engineering approaches to improve the performance of microbial electrochemical systems (MES), Microb Biotechnol 16 (2023) 1179–1202. https://doi.org/10.1111/1751-7915.14236.

**5**

# Acknowledgements

# Acknowledgements

*És tan subtil la ratlla que separa*
*la llum de l'ombra, que em confonc sovint*
*i de sobte camino a les palpentes.*
*Més que perdut, distant, no goso fer*
*preguntes a l'estrany que m'acompanya.*
*¿Si el vell espill consuetudinari*

*no reflecteix la imatge que voldria,*
*qui sinó jo pot sentir-se'n culpable?*
*Assegut i en silenci, faig recompte*
*de dubtes i mancances per no perdre*
*ni el goig de viure ni la confiança.*

*Túmul de vent*
**Miquel Martí i Pol**

Journeys are a funny thing. We wonder and get lost, we experience, we learn about the new and the old, about ourselves and about each other. We laugh, and sometimes we cry. Nevertheless, no matter how long or difficult a journey is, we always find our way. If one is feeling particularly cynical, one might say we are all slaves to destiny. Stating the obvious and quoting every thinker who ever thought, the destination does not matter because it is how we get there that truly shapes us. "Journey before destination", one could say.

On that note, it would only be fair to acknowledge (see what I did there?) everyone who, in one way or another, by being there or by wanting to be, has become a part of this story. Do not fret, dear reader, if you cannot find yourself within these pages; it only means a future journey awaits your name.

**ACK**

First of all, I would like to thank my promotors for their supervision over these years. **Ludovic**, thank you for giving me the chance to embark on this journey. You introduced me to the world of microbial electrosynthesis and helped me see how much potential this technology has (pun intended). I finish this journey having learned a lot, and much of that learning is thanks to you. **Adrie**, thank you for all your contributions to the project. Your sharp and practical mind helped me focus on the bigger picture whenever I got lost in the details. Your ability to summarize long paragraphs with ease is something that definitely helped keep this thesis from doubling in length. Overall, my stay at BPE with you two will always be an important step in my career, and a period I will never forget.

To my paranymphs **Marijn** and **Joan**, nerdy geeks the two of them. **Olger,** I do not even know where to begin when it comes to thanking you. You have been a rock throughout my PhD. When I saw your picture for the first time, I thought you were going to be the typical sorority-type dude. Honor knows I could not have been more wrong. Yours is a kind soul. Not only did you become one of my best friends, you are also the main reason the work in this thesis even exists to begin with. You taught me the ins and outs of working with MES reactors, and basically assembled the lab from scratch. Following your trail in the lab made it much easier to get my experiments going. I mean, your name appears in two of the chapters of this book. That says it all really. Your passion is contagious, and made me keep going even when the bright flames became smoldering embers. Working together in the office and in the lab, drinking beers with the rest, and going to conferences. Talking about videogame design, listening to metal (I may potentially recognize you might have introduced me to some very nice bands), going to concerts, and sometimes showing up at the gym. The list goes on and on, but I guess it is obvious by now that you are just that important. Thank you very much for being there since the beginning, but most importantly for staying during the hard times. Through mud and dirt, we emerged victorious. The fight never ends, and the dark always awaits. Climbing the mountain of our inner self is not easy task, but it is definitely not a lonely endeavor with people like you close by. My friend, say the words. Life before death, strength before weakness, journey before destination.

**Joan,** ya que podemos, hablemos en la lengua de nuestro señor. En ti encontré el tipo de persona que siempre quise ser. Alguien fuerte, independiente, a quien le preocupa más ser feliz que lo que piensen los demás. Alguien que ve a la gente por quienes son, no por como lucen. Alguien libre. Me enseñaste, de forma voluntaria o no, a ser más yo mismo. Eso es algo que nunca podré agradecerte suficiente. Verte viajar entre Sanquin y Delft, trabajando sin parar en tus artículos mientras cultivabas zumo de tomate en el laboratorio fue una gran inspiración para mí. Eres sin lugar a duda una de las personas más trabajadoras que he conocido jamás (bajo peligro de desheredación, no puedo quitarle el primer puesto a mi madre). Y, aun así, conseguiste encontrar tiempo para todo aquello que te apasiona, cosa que a día de hoy sigo sin saber muy bien cómo lograste. Are you a time wizard perchance? Ambos somos unos frikis de manual, pero en ello triunfamos. Empezamos hablando de juegos, pasamos por el anime y la música (¡Toryanse, toryanse!), terminando con las Cartas Mágicas: El Encuentro. Al lanzarte de cabeza al Magic conmigo, muy probablemente sin darte cuenta, te convertiste en unas de las piezas claves que me ayudaron a superar la oscuridad. Será cierto que hay que creer en el corazón de las

cartas. Por gente como tú no me importaría abrazar la Instrumentalidad y convertirnos en fanta. Por cierto, mantengo la esperanza que los "nunca tocan juntos" terminen, al fin, tocando juntos. Sea como fuere, si me he puesto demasiado cursi lánzame un counterspell.

Here comes the biggest group thanks, and definitely the most important one when arguing who had a bigger impact on me surviving these years. Along with **Marijn** and **Joan**, whom I mentioned earlier, as well as **Mariana**, **Tiago**, **Marina**, **Song**, **Raquel**, **David** and **Daniela**, you all form that royal group:

Even though I do not condone a system where supreme rule is vested into a single individual by the right of some imaginary metaphysical being, there is but one monarch I recognize. **Mariana**, our queen and supreme leader, the passion you show for the things you like is dangerously contagious. You were the first person in the group I made friends with, helped me buy my first bike in Den Haag and all. I fondly look back at all the times I came into your office to chat and, occasionally, gossip a little bit. I remember all the conversations we had, some serious and some less so. It is also a must to mention how your organizational skills were the responsible for most of the birthday parties, lunches and dinners to always be on time. Most importantly, you were a safe space that allowed me to feel that everything would be alright, even during the darkest moments. Thank you so much!

**Tiago**, the third bro in our bromance triangle. Whenever I think about pure discipline and matureness, your ugly face is the first thing that comes to mind. You taught me to persevere and keep going, even when all seemed lost. Together we survived NMST, staying until late at the office trying to understand where that "Failed to evaluate variable" error was coming from. In the end, we somehow managed. I would say part of the energy that kept us going was coming from our shared interest in the proper way metal music is supposed to take "Because tonight will be the night…". We started FACC-BPE and successfully organized multiple events for the whole group. Even the pandemic was no match for our Secret Santa! But jokes aside, I had so much fun sharing these years with you and will always look fondly at all the moments we spent together. You helped me appreciate myself more, and even got angry on my behalf when I failed to do so. Thank you for being such an amazing friend. Also, I will make sure to send you a *cagatió* picture every year.

**Marina**, you are energy incarnate. There is no one in the whole world that shows more interest and proactiveness towards meeting with friends. When I first met you, I soon realized how true the Catalan saying "*Al pot petit hi ha la bona confitura*" is. Your energy pushed me to be more active myself, pulling me out of the darkness

whenever I felt complacent with staying home alone. The beer meetings, together with our queen, at your place during the pandemic truly helped me not succumb to the loneliness so many people suffered from. The passion for what you do is very contagious, and from you I learned how to be more professional when needed. I still find myself using expressions and mannerisms I saw you use at BPE, even though sometimes they might not be all that pertinent. No matter how far down I have to look, you will always be there little Marina. Thank you for everything.

**Song**, without you the experimental work presented in this thesis would just not have been possible. When something broke, you were there to fix it. When I did not know something, you were there to explain it to me. "Don't worry, it will work out". Indeed, in the end it did always work out. Our MES lab was basically running on your back. But it was not just about work. Your legendary cheesecake and those filling hotpots gave me comfort when I needed it most, and I will forever treasure the times you took us to those amazing Chinese restaurants. Really looking forward to visiting your hometown one of these days. From the bottom of my heart, thank you for being there for me. I am forever grateful.

**David**, mi señor caldero. Como en una buena telenovela, cuando tú vas, yo ya vengo de allí. Después de años sin ningún contacto, fue un placer enorme poder reencontrarme contigo. Algo que siempre he admirado en ti es esa facilidad que tienes para iluminar cualquier conversación. Es imposible estar triste demasiado tiempo a tu lado, pues siempre terminas haciendo que uno se ría de algo. Y eso es precisamente lo que ocurría cada vez que íbamos a tu casa. Siempre volvía sonriendo y con los mofletes adoloridos (aunque quizás la buena comida también tenía algo que ver, quién sabe). ¡Mil gracias por todo!

**Raquel**, yours is the brightest laugh. Together with the Little Pig, we also shared the lovely experience that NMST was. What a way to get to know each other. Nonetheless, the willingness you have to share happiness with everyone that needs it is something I will always be very grateful for. Together with **Caya** and **Gullit**, you and your man showed me what true love is. Thank you!

**Daniela**, gracias por ser siempre fiel a ti misma! Admiro cómo esa seguridad que proyectas se contagia a los que te rodean, ya sea con tu infinita sonrisa o tu potente (y a veces ensordecedora) risa. Tu forma de ser y de ver la vida es una inspiración para mí, y sin duda me ayudaste a afrontar la mía con menos seriedad, y con mucha más alegría. Estoy muy agradecido por todo lo que me has enseñado sin siquiera proponértelo. Por cierto, sin duda voy a ir a visitaros a Colombia. ¡Gracias por todo!

To those who know me well, it is no secret that dealing with bureaucracy has never been my strong suit. **Kawieta**, your constant support, efficiency, and willingness to help turned what could have been a daunting process into something manageable and even reassuring. Your kindness, especially during the more challenging moments, meant the world to me. Thank you!

This work would have been much harder without the invaluable technical support I received both in and out of the lab. **Stef** and **Max**, your constant willingness to help me at every stage was essential. Your carefree personalities and open mindedness allowed me to relax during stress peaks. **Christiaan**, not only did you support me with lab work, but also shared a nerdy love for video games. Our chats about Final Fantasy and Monster Hunter made lab days feel less monotonous, and even fun at times! May you ever walk in the light of the crystal.

I would like to sincerely thank **Kunal** for his generosity in letting me and my students use his lab to 3D print our reactors. His patience and expertise during the entire process were invaluable. We might have had a few print failures along the way, but his support never "warped" under pressure. On the topic of lab challenges, huge thanks to **Rozanne** for tackling the messy job of extracting DNA from our biofilms and turning her lab into a stinky bomb in the process!

To my students, without whom this dissertation would not have been possible: **Katja**, **Thijmen**, **Marika**, **Okyanus**, **Roderick**, **Loek**, and **Arthike**. From all our meetings, discussions and time spent together, I was the one that learned the most. Some of you had to endure doing a thesis on a topic you were not familiar with during a pandemic. Some had to deal with old (sometimes ancient) computers for your modeling efforts. Others had to help finish a lab that was still being assembled, or had to move between buildings every day to print resin cubes. At times, the reactors would decide to stop working, and panic ensued. You were all great students, but most importantly, amazing people to talk and share jokes with. Thank you for deciding to pursue your projects with me. I wish you all the best.

To those who shared the office with me: **Chema**, el señor andaluz. Mi estancia en la C0.220 estuvo llena de divertidos y, a veces, ruidosos momentos gracias a ti. Aunque la primera semana me costó entender tu acento, tardamos poco en compartir chistes y reírnos de (o con) tu vecino de la derecha. Gracias por enseñarme que no todo en la vida se reduce al trabajo. **Debby**, even though our time together was limited, I must thank you for all the support you gave me when I started. Having to deal with three metalheads, you also managed to become part of our unhinged conversations. One of us, as we used to say. **Mona**, you were the new voice of

reason. Although our time together was marked by life and its circumstances, I must thank you for all those words of encouragement and wisdom you gave me in my lowest moments. I also owe you big time for helping me during those situations. Talking with you helped me deal with everything, thanks! **Eduardo**, loco, compadre. Verte trabajar sin parar, con tus peques y adolescente en casa, mientras ayudábamos en ODBP a la vez que terminabas tu PhD fue una inspiración. Aún en los peores momentos, debemos seguir adelante. Gracias por todo amigo.

To the old (or classic, depends on how you look at it) BPE generation, **Mónica**, **Joana**, **Bianca**, and **Rita**, thank you for welcoming me like you did. I was a lost lamb, and you showed me how things were done and advised me on how to deal with the uphill battle of a PhD's first year. I also want to thank **Marcel**, **Marieke**, and **Cees** for always helping me with your insightful feedback, as well as for making sure BPE works and stays welcoming to all.

To my own (and the best, no discussion possible here) generation: **Lars**, the *Koning van Delluft* and our personal weekly alarm. Whenever you entered the office with a big smile in your face and asked "Drinks?", we all knew the week was over. Our talks about modelling (damn you COMSOL!) and politics were always a pleasure. I wish you the best in Australia, mate! **Marteen**, you are a hardworking and practical mind, but also very sweet and understanding. Whenever we talked about everything that was going on, I somehow always felt at ease. Thank you for that, and of course for picking up the torch of FACC-BPE. **Tim**, the image of drunk you tearing your own jeans apart lives in my head rent-free. Thankfully we managed to attend a metalcore concert together, how crazy would have been for me to forget a second time? Thanks for always being so authentic! **Roxana**, my German colleague and favorite bread baker. I remember all the times we cooked together, either making dumplings at my place or *spaetzle* at yours. Thank you for all the good times, the chats during the coffee breaks, and our little excursions to Den Haag. **Daphne**, I truly admire your independence and passion for the things you love. Even though our offices were far apart, I enjoyed every moment we talked. The stories of your travels made me keep going, if only to be able to visit some of the places you described. **Zulhaj,** your experience and hardworking attitude towards every aspect of your life is something I envy. Although our time together was limited, I enjoyed all of it!

To the contemporary (gen Z, the younglings) BPE generation, **Marika**, **Mariana**, **Brenda**, **Miki**, **Rik**, **Héctor**, **Ramon**, **Tamara**, and **Robin**. Although we shared few moments together, either because life happens or because young people are too cool to mingle with an old person like myself, the ones we did share were fun and

memorable. I hope, from the bottom of my heart, that you can enjoy your time at BPE as much as I did.

**Clara** (de huevo), me acuerdo perfectamente del momento en el que entraste en mi oficina para presentarte y nos quedamos los dos patidifusos (insert Spiderman meme here). Encontrarnos después de tantos años fue un placer, y sin duda uno de esos momentos que nos hacen pensar que el mundo igual si es un pañuelo. Desde las novatas en la UAB a tomar una birra en Delft hablando de la vida, tu sonrisa y forma de ver el mundo es algo que me llevo conmigo para siempre. Gracias por ser como eres, y por aguantar lo pesado que me puedo poner a veces. ¡Te deseo lo mejor, y espero poder encontrarnos otra vez en un futuro no muy lejano!

Ara toca fer una volta i baixar cap a casa. Els Teletubbies o la big family, digueu-li com vulgueu, sou un grup de persones que, tot i la distància, sempre heu estat presents durant aquest llarg procés. **Tutu**, **Felip**, **Sònia**, **Sergi**, **Àngels**, **Laura**, **Anabel**, **Lluís**, **Cristina**, **Roger**, **Alba**, i **Guillermo**. Sempre que tornava a El Vendrell de vacances, vosaltres éreu allà per rebre a "l'holandès". Portem tota una vida junts, hem passat per moments bons i dolents, però aquí seguim. Sense adonar-vos-en, heu estat, sens dubte, una de les principals fonts d'energia que m'han permès seguir endavant durant aquest pelegrinatge que ha estat el doctorat. Moltes gràcies per ser com sou. Us desitjo el millor en tot el que està per vindre, i que ho puguem gaudir tots plegats. A la pròxima toca paella!

La sang és un concepte literari utilitzat per a descriure aquella gent lligada a nosaltres per llaços invisibles, que, per més distància i temps que passi sempre formaran part del nostre ésser. Per a mi, la sang són els meus pares i la meva àvia. A mi **Yaya**, mi fan número uno, le debo el haber estado siempre para darme esas palabras de admiración y motivación que me hacían sentir todo este trabajo, tal vez, si valía la pena. De ti aprendí que nada en esta vida está garantizado y que debemos luchar por todo aquello que nos importa. **Mama** i **Papa**, gràcies per tot el que heu fet per mi. El vostre esforç constant per criar de la millor manera possible un nen que ja des de ben petit tenia tendència a fer-se mal no té preu. Gràcies per haver aguantat aquests 9 anys que he passat en aquest país perdut de la mà de Déu. De vosaltres he après que la generositat i el treball constant ens fan millor persones. I que a vegades, tot i que la vida ens faci patir, amb constància i esforç sempre s'arriba a un lloc millor. M'heu ensenyat a formar part d'una comunitat, a estimar la gent que m'envolta i la terra que anomenem casa. Sense vosaltres aquest llibre que teniu a les vostres mans no hagués sigut mai. Gràcies per fer-me la persona que soc, us estimo.

**ACK**

# Curriculum vitae

# Curriculum vitae

**Oriol Cabau Peinado** was born in El Vendrell, Catalonia, on May 1st, 1993. He grew up in the wine producing region of *El Penedès*, surrounded by olive trees and under the shadow of the *Serra del Montmell*. Curious from an early age about how the world works, he quickly developed a strong interest in science. Due to a genetic blood disorder in his family, he became increasingly interested in how biology could be used to treat such conditions. Thus, in 2011 Oriol began his BSc. in Biotechnology at Universitat Autònoma de Barcelona. Simultaneously, he worked as an intern with Dr. José Tomás Matus on the characterization and understanding of gene regulatory networks underlying plant development, where he gained experience in genomic and genetic analytical methods. During the final years of his studies, he discovered the world of bioprocess engineering and quickly developed a burning passion for it. Oriol worked under the supervision of Prof. Carles Solà Ferrando on the design of an industrial bioprocess plant for the production of the equine influenza vaccine.

Eager to broaden his horizons, Oriol took a gap year – ostensibly to improve his English, but mainly to indulge his love of mountain climbing. After deciding to focus on bioprocess engineering, he moved to the Netherlands to pursue a MSc. in Biotechnology at Wageningen University & Research. During his master's thesis, he studied the potential of aqueous two-phase systems for downstream processes under the supervision of Prof. Michel Eppink and Dr. Catalina Suarez Ruiz. In parallel, he worked as student assistant in the Transfer Processes course, which had previously rekindled his passion for process design. Oriol also did an internship at Byondis (Nijmegen, the Netherlands), where he worked on periodic counter-current chromatography. In 2018, he graduated *cum laude*.

Motivated by his need to learn more and challenge himself, Oriol started a PhD project on microbial electrosynthesis reactor design at Delft University of Technology. His research combined experimental and modelling approaches to unravel rate-limiting steps and develop novel and scalable microbial electrosynthesis reactors. Most of the results of his research are presented in this thesis.

**CV**

# List of publications

# List of publications

## Journal articles

- **O. Cabau-Peinado**, M. Winkelhorst, R. Stroek, R. de Kat Angelino, A.J.J. Straathof, K. Masania, J.M. Daran, L. Jourdin, Microbial electrosynthesis from CO2 reaches productivity of syngas and chain elongation fermentations, Trends Biotechnol (2024). https://doi.org/10.1016/j.tibtech.2024.06.005.

- <u>M. Winkelhorst</u>, **O. Cabau-Peinado**, A.J.J. Straathof, L. Jourdin, Biomass-specific rates as key performance indicators: A nitrogen balancing method for biofilm-based electrochemical conversion, Front Bioeng Biotechnol 11 (2023). https://doi.org/10.3389/fbioe.2023.1096086.

- C.A. Suarez Ruiz, **O. Cabau-Peinado**, C. van den Berg, R.H. Wijffels, M.H.M. Eppink, Efficient Fractionation of Lipids in a Multiproduct Microalgal Biorefinery by Polymers and Ionic Liquid-Based Aqueous Two-Phase Systems, ACS Sustain Chem Eng 10 (2022) 789–799. https://doi.org/10.1021/acssuschemeng.1c06017.

- **O. Cabau-Peinado**, A.J.J. Straathof, L. Jourdin, A General Model for Biofilm-Driven Microbial Electrosynthesis of Carboxylates From CO2, Front Microbiol 12 (2021). https://doi.org/10.3389/fmicb.2021.669218.

- C.A. Suarez Ruiz, J. Kwaijtaal, **O.C. Peinado**, C. van den Berg, R.H. Wijffels, M.H.M. Eppink, Multistep Fractionation of Microalgal Biomolecules Using Selective Aqueous Two-Phase Systems, ACS Sustain Chem Eng 8 (2020) 2441–2452. https://doi.org/10.1021/acssuschemeng.9b06379.

**PL**

## Conference contributions

Presenting author is indicated <u>underlined</u>.

- <u>O. Cabau-Peinado</u>, A.J.J. Straathof, L. Jourdin. Multiscale computational modelling as enabler for the rational design of microbial electrosynthesis for $CO_2$ reduction to C2-C6 organics. **8th ISMET Global conference**. Chania, Greece (September 2022). Oral presentation.

- O. Cabau-Peinado, A.J.J. Straathof, L. Jourdin. Multiscale computational modelling as enabler for the rational design of microbial electrosynthesis for $CO_2$ reduction to C2-C6 organics. **4th MEEP Symposium**. Lucerne, Switzerland (July 2022). Oral presentation.

- O. Cabau-Peinado, A.J.J. Straathof, L. Jourdin. A general model for biofilm-driven microbial electrosynthesis. **NWO CHAINS 2021**. Virtual (December 2021). Oral presentation.

- O.M. Winkelhorst, O. Cabau-Peinado, L. Jourdin. $CO_2$ electrolysis: How about microbes as catalysts. **ECCM Research Day**. Eindhoven, Netherlands (November 2021). Poster.

- O. Cabau-Peinado, A.J.J. Straathof, L. Jourdin. A general model for biofilm-driven microbial electrosynthesis of carboxylates from $CO_2$. **Electromicrobiology 2021 conference.** Aarhus, Denmark (November 2021). Oral presentation.

- O. Cabau-Peinado, A.J.J. Straathof, L. Jourdin. A general model for biofilm-driven microbial electrosynthesis of carboxylates from $CO_2$. **5th ISMET European meeting**. Virtual (September 2021). Oral presentation.

## Patents

- Jourdin, L & **Cabau-Peinado, O.** (2023). *WO 2023/249484 A2*. World Intellectual Property Organization.